THESIS ON POWER ENGINEERING,
ELECTRICAL ENGINEERING, MINING ENGINEERING D85

Mathematical Modeling and Analysis of a Battery Energy Storage System for Microgrids

AHMAD RAHMOUN

TTÜ PRESS

TALLINN UNIVERSITY OF TECHNOLOGY
School of Engineering
Department of Electrical Power Engineering and Mechatronics

This dissertation was accepted for the defence of the degree of Doctor of Philosophy in Electrical Engineering on October 20, 2017.

Supervisor: Senior Research Scientist, Argo Rosin, Dr.Sc.Eng., Department of Electrical Power Engineering and Mechatronics, Tallinn University of Technology, Tallinn, Estonia

Co-supervisor: Prof. Dr.-Ing. Dr. h.c. Helmuth Biechl, Institute of Electrical Power Systems (IEES), Faculty of Electrical Engineering, University of Applied Sciences Kempten, Germany

Opponents: Professor/Researcher Unai Iraola Iriondo, Dr.-Ing., Department of Electronics and Computing Science, Faculty of Engineering, Mondragon University, Spain

Professor Ilja Galkin, Dr.Sc.Ing., Institute of Power Electronics and Electrical Engineering, Riga Technical University, Latvia

Defence of the thesis: December 15, 2017, Tallinn

Declaration:
Hereby I declare that this doctoral thesis, my original investigation and achievement, submitted for the doctoral degree at Tallinn University of Technology has not been submitted for doctoral or equivalent academic degree.

Ahmad Rahmoun .....

ISSN 1406-474X
ISBN 978-9949-83-171-5 (publication)
ISBN 978-9949-83-172-2 (PDF)

ENERGEETIKA. ELEKTROTEHNIKA. MÄENDUS D85

Mikrovõrkude energiasalvestussüsteemi matemaatiline modelleerimine ja analüüs

AHMAD RAHMOUN

TTÜ
KIRJASTUS

TABLE OF CONTENTS

ACKNOWLEDGEMENTS

First of all, I would like to express my thanks to my co-supervisor Prof. Dr.-Ing. Dr.h.c. Helmuth Biechl for encouraging my research and for allowing me to grow as a research scientist.

I am also deeply grateful to my supervisor Dr.Sc.Eng. Argo Rosin for his invaluable insights and suggestions. I really appreciate having time and advise for me during my short visits to Estonia.

Moreover, I would like to thank Mare-Anne Laane for revising the English texts in this thesis.

Next, I would like to thank my colleagues at the Institute of Electrical Power Systems (IEES), they have been a source of friendship as well as good advise and collaboration.

Last but not least, I would like to thank my family for their endless support, patience and love.

Thank you!
Ahmad Rahmoun

LIST OF PUBLICATIONS

The thesis research is based on the following publications:

PAPER- I A. Rahmoun and H. Biechl, "Modelling of Li-ion batteries using equivalent circuit diagrams," Prz. Elektrotechniczny, vol. 2012, no. 7b, pp. 152–156, 2012.

PAPER- II A. Rahmoun, H. Biechl, and A. Rosin, "SOC estimation for Li-Ion batteries based on equivalent circuit diagrams and the application of a Kalman filter," in 2012 Electric Power Quality and Supply Reliability, 2012, pp. 1–4.

PAPER- III A. Rahmoun, H. Biechl, and A. Rosin, "Evaluation of Equivalent Circuit Diagrams and Transfer Functions for Modeling of Lithium-Ion Batteries," Electr. Control Commun. Eng., vol. 2, no. 1, pp. 34–39, May 2013.

PAPER- IV A. Rahmoun, A. Armstorfer, J. Helguero, H. Biechl, and A. Rosin, "Mathematical modeling and dynamic behavior of a Lithium-Ion battery system for microgrid application," in 2016 IEEE International Energy Conference (ENERGYCON), 2016, pp. 1–6.

PAPER- V A. Rahmoun, A. Armstorfer, H. Biechl, and A. Rosin, "Mathematical Modeling of a Battery Energy Storage System in Grid Forming Mode," in 58^{th} International Scientific Conference of Riga Technical University on Power and Electrical Engineering RTUCON2017, 2017.

OTHER RELATED PUBLICATIONS

PAPER- VI A. Rahmoun, M. Loske, and A. Rosin, “Determination of the Impedance of Lithium-ion Batteries Using Methods of Digital Signal Processing,” Energy Procedia, vol. 46, pp. 204–213, 2014.

PAPER- VII N. Beg, A. Rahmoun, A. Armstorfer, A. Rosin, and H. Biechl, “Determination methods for controller parameters of back-to-back converters in electric power grids,” in 2016 Electric Power Quality and Supply Reliability (PQ), 2016, pp. 157–164.

PAPER- VIII A. Armstorfer, N. Beg, A. Rahmoun, A. Rosin, and H. Biechl, “Mathematical Modeling and Evaluation of a Microgrid Demonstrator in Island Mode,” in Conference on Sustainable Energy Supply and Energy Storage Systems NEIS 2017, 2017.

AUTHOR'S CONTRIBUTIONS TO THE PUBLICATIONS

Author's contributions to the papers in this thesis are:

PAPER- I Ahmad Rahmoun as the main author of the paper discussed theoretically and experimentally the application of different equivalent circuit model (ECM) structures for modeling the electrical dynamics of a Li-Ion cell.

PAPER- II Ahmad Rahmoun as the main author of the paper discussed theoretically and experimentally the application of extended Kalman filter for state of charge (SOC) estimation of a Li-Ion.

PAPER- III Ahmad Rahmoun as the main author of the paper reviewed several mathematical structures for modeling the electrical dynamics of a Li-Ion cell and compared between parameter identification in time and frequency domains.

PAPER- IV Ahmad Rahmoun co-authored the paper, analyzed the impact of the ECM complexity on the dynamic performance of a BESS and investigated the influence of the high frequency (HF) model of a Li-Ion cell on the evaluation of current harmonics of the dc side of the BESS. He presented the paper at the IEEE International Energy Conference (ENERGYCON), April, 2016, Leuven, Belgium.

PAPER- V Ahmad Rahmoun, as the main author of the paper, explained the structure of the BESS. He showed the procedure to develop detailed and amplified models for the BESS with comparisons and verifications using real measurements.

PAPER- VI Ahmad Rahmoun co-authored the paper, developed of a mathematical method for identifying the electrochemical impedance spectrum of a Li-Ion cell based on time domain measurements. He presented the paper at the 8th International Renewable Energy Storage Conference and Exhibition (IRES 2013), November, 2013, Berlin, Germany.

PAPER- VII Ahmad Rahmoun co-authored the paper, supported with the comparisons of different control algorithms for the ac and the

dc of back-to-back voltage source converter (B2B-VSC). He presented the paper at the 2016 Electric Power Quality and Supply Reliability (PQ), August, 2016, Tallinn, Estonia.

PAPER- VIII Ahmad Rahmoun co-authored the paper, developed the simplified model of the BESS which is used for the simulation of the microgrid demonstrator. He also participated in the setup and the evaluation of the measurements.

ABBREVIATIONS

B2B-VSC	back-to-back voltage source converter
BESS	battery energy storage system
BMS	battery management system
CAES	compressed air energy storage
CHP	combined heat and power
CNLS	complex nonlinear least squares
DG	distributed generation
DOD	depth of discharge
DPM	dynamic phasor modeling
DTC	three time constants
ECM	equivalent circuit model
EIS	electrochemical impedance spectroscopy
EKF	extended Kalman filter
EMI	electromagnetic interference
EP	evaluation point
ESS	energy storage system
FES	flywheel energy storage
GF	grid forming
GRS	generator reference-arrow system
HF	high frequency
HSR	high sampling rate
ISEA	Institut für Stromrichtertechnik und Elektrische Antriebe RWTH
LCO	lithium cobalt oxide
LF	low frequency
LFP	lithium iron phosphate
Li-Ion	lithium-ion
LIB	lithium-ion battery
LPF	low pass filter

LS	least squares
LSR	low sampling rate
NCA	nickel cobalt aluminum oxide
NCM	nickel cobalt manganese oxide
OCV	open circuit voltage
OTC	one time constant
PCC	point of common coupling
PHS	pumped hydro storage
PI	proportional-integral
PWM	pulse width modulation
QSS	quasi steady state
RES	renewable energy source
RFC	rain flow counting
SMES	super-conducting magnetic energy storage
SNR	signal to noise ratio
SOC	state of charge
SOE	state of energy
SOF	state of function
SOH	state of health
SOP	state of power
THD	total harmonic distortion
TSO	transmission system operator
TTC	two time constants
VRB	vanadium redox-flow battery

SYMBOLS

A	Arrhenius law factor
A_i	real positive coefficient
A_{QSS}	state matrix of QSS model
B_{QSS}	control matrix of QSS model
C_{cap}	capacitance of the supercapacitor
C_{dtci}	dynamic capacitance of DTC model with index i
C_e	energy installation cost
C_{obj}	heat capacity of the object
C_p	power installation cost
C_{QSS}	output matrix of QSS model
C_{rate}	cell rating current
C_w	heat capacity of water
δ_1	angle between voltage phasors of inv1 and PCC
δ_2	angle between voltage phasors of inv2 and PCC
ΔI	actual current difference
ΔI_m	measured current difference
ΔV	actual voltage difference
ΔV_m	measured voltage difference
DOD_r	relative depth of discharge
$< \overrightarrow{I_1} >_1$	first dynamic phasor of current phasor for inv1
$< \overrightarrow{V} >_1$	first dynamic phasor of voltage phasor at PCC
$< \overrightarrow{V_1} >_1$	first dynamic phasor of voltage phasor for inv1
$< x >_k (t)$	the k^{th} dynamic phasor of signal x
D_{QSS}	feedforward matrix of QSS model
ΔSOH_{ca}	SOH reduction due to calendric aging
ΔSOH_{cy}	SOH reduction due to cycling
Δt	time duration
Δt_c	converted time duration
E_{cap}	stored energy in a super capacitor

E_{smes}	stored energy in a SMES system
E_{fes}	stored energy in a FES system
E_m	specific energy
E_{phs}	stored energy in a PHS system
E_{rms}	relative rms error
η	round-trip efficiency
E_v	energy density
f_1	smoothed frequency of inv1
$\widetilde{f_1}$	instantaneous frequency of inv1
f_{ca}	nonparametric function describes the dependency of SOH reduction on time and SOC
f_{ro}	frequency at which ohmic resistane is measured
f_s	sampling frequency
f^*	no load frequency
f_{sw}	switching frequency
g	gravitational acceleration
h_d	height difference between upper and lower reservoirs
i	integer variabel for indexing
I_1^d	real part of $< \overrightarrow{I_1} >_1$
I_1^q	imaginary part of $< \overrightarrow{I_1} >_1$
I_{cell}	Li-Ion cell acual current
I_m	moment of inertia
I_{smes}	inductor current of a SMES
K_f	f/P droop gain
K_p	P/f droop gain
K_q	Q/V droop gain
K_v	V/Q droop gain
L_{ca}	calendar lifetime
λ_{QSS}	eigenvalues of the QSS model
L_{smes}	inductor of a SMES
N_{cm}	number of full cycles for capacity measurement
N_{cyc}	cycle lifetime
N_{dc}	number of drift compansations
N_{mc}	number of micro-cycles
ω_c	LPF cut-off frequency
ω_f	angular velocity of flywheel
P	active power
P_1	active power at output of inv1

P_{ref}	active power setpoint
P_v	power density
Q_1	reactive power at output of inv1
Q_{ref}	reactive power setpoint
r	Pearson's correlation coefficient
R_1	equivalent resistance between inv1 and PCC
R_{dtci}	dynamic resistance of DTC model with index i
ρ	water density
R_{mc}	percentage of Ah-throughput caused by capacity measurement and drift compansation
R_o	actual ohmic resistance
R_{om}	measured ohmic resistance
$\underline{S}_1$	complex apparent power at the output of inv1
S_d	self discharge rate
SOC_{avg}	average SOC_r of one cycle
SOC_{r0}	initial relative state of charge
SOH_0	initial state of health
t_0	initial time
T_a	ambient temperature
τ	response time
τ_i	time constant with index i
T_c	smoothing time constant
T_{cell}	cell temperature
T_{eq}	equilibrium temperature
θ	voltage phasor angle at PCC
θ_1	voltage phasor angle at output of inv1
θ_2	voltage phasor angle at output of inv2
T_i	itegral time constant
$t_{immersion}$	immersion moment of object in water
T_{obj}	object temperature
T_{ref}	reference temperature
t_s	switching time
T_w	water temperature
V	voltage phasor length at PCC
V_1	voltage phasor length at output of inv1
V_1^d	real part of $< \overrightarrow{V_1} >_1$
$\hat{V}_1$	smoothed output voltage of inv1
V_1^q	imaginary part of $< \overrightarrow{V_1} >_1$
$\widetilde{V}_1$	instantaneous output voltage of inv1

V_2	voltage phasor length at output of inv2
V_1^d	real part of $< \overrightarrow{V} >_1$
V_1^q	imaginary part of $< \overrightarrow{V} >_1$
V_{cap}	capacitor's voltage
V_{cell}	Li-Ion cell output voltage
V_d	dynamic part of cell's output voltage
V^*	no load voltage
V_w	water volume
X_1	equivalent reactance between inv1 and PCC
X_{QSS}^0	state vector at equilibrium point of the QSS model
$\underline{Z}_1$	equivalent impedance between inv1 and PCC

INTRODUCTION

The microgrid concept is becoming more important particularly for developing and rural areas where connection to a traditional grid is not always available. In these areas the microgrid has some advantages over traditional grid regarding investment costs, scalability and environmental aspects [1]. A microgrid can be defined as a small-scale low voltage distribution grid consisting of distributed generation (DG) systems, energy storage systems (ESSs) and loads. The microgrid can be operated either as a grid connected or as an autonomous system (island mode) [2]. The intermittent nature and high penetration of inverter-connected renewable energy sources (RESs) in low voltage microgrids replacing the conventional generators and their rotating machinery have led to a significant reduction in system inertia. Therefore the BESS is an essential component in the islanded microgrid to ensure generation adequacy and to increase the security and reliability of the microgrid [3]. The fast response of BESS improves also microgrid transient stability for different types of disturbances like fast changes of solar irradiation, loss of one DG and three phase short circuit cases [4]. This means that having a BESS in a microgrid contributes to avoid large deviations of voltage and frequency during such contingencies in the microgrid. For these reasons an accurate model of the BESS that describes both the state of energy (SOE) and the electrical dynamics is essential for analyzing the microgrid transients and stability.

The feedback and coupling between the parallel connected DG's can cause stability issues when large disturbances are applied or control parameters are not properly selected. Stability issues in microgrids are classified in detail in [5, 6]. This research work focuses also on the stability analysis of a microgrid in island operation for small disturbances, whereas the control structure and parameters of each DG play an important role for defining stability margins of the microgrid. The standard control structure that uses two cascaded synchronous controllers working in dq reference frame is extensively analyzed in literature [2, 7–12]. However, in industrial applications, a different control structure is used and will therefore be discussed in this thesis.

Main objectives and activities of research

The main objectives of the thesis research are:

- To develop a mathematical model of Li-Ion battery for dynamic analysis of BESS in a microgrid. The battery model should take into account the dependency on SOC, temperature and the state of health (SOH).
- To develop an aging algorithm for the prediction of the service life of a lithium-ion battery (LIB) based on experimental tests.
- To develop a detailed model of the BESS including dc and ac dynamics for short time transient analysis and a simplified model to reduce the complexity of the detailed model for microgrid simulations.
- To develop a new procedure for small signal stability analysis which allows to determine stability margins depending on droop parameters, smoothing time constant and load parameters. This is not not possible by applying the classical method.

Main hypothesis of research

- Electrical dynamics of a Li-Ion cell are a function of its SOC, temperature, SOH and current rate during charging and discharging.
- Aging of a Li-Ion cell can be divided into calendrical aging and aging due to cycling.
- The electrical dynamics of the BESS in the grid forming (GF) mode are influenced by droop control parameters, smoothing time constants and serial impedances between parallel connected inverters and point of common coupling (PCC).
- Stability margins of the BESS in GF mode depends on both electrical and control parameters.

Novelty

The following novel approaches are proposed and presented in the thesis:

- A new approach for identification of the ohmic resistance of the Li-Ion battery based on time domain measurements.
- A new approach to identify and verify the low frequency model parameters of a Li-Ion cell based on time domain measurements.
- A new approach to extend the low frequency model with a high frequency part in order to describe cell's electrical dynamics in high frequency range.

- Design and implementation of an algorithm for service life prediction of a Li-Ion battery using laboratory tests.
- Development of the detailed and simplified models of the BESS for evaluating the electrical dynamics of the BESS in fast resp. slow transients.
- A new procedure for the stability analysis of the BESS in a microgrid for ohmic load case based on dynamic phasor modeling (DPM) approach.

Contribution of the thesis and dissemination

This research can be recommended for reading especially for BESS developers who wish to optimize their system based on a specific microgrid application. It is also valuable for researchers who are interested in improving SOC, SOH and state of function (SOF) estimation algorithms. The results of the thesis are internationally introduced. Author's research is disseminated in **6** international conferences and **5** doctoral schools in the form of oral and poster presentations. Total number of author's papers published in this field is **13**, including **10** published in conference proceedings and **3** in peer-reviewed journals.

1 ELECTRICAL ENERGY STORAGE SYSTEMS

The share of renewable energies in the energy sector of the European countries has noticeably increased as shown in Figure 1.1 since the European Union issued ”DIRECTIVE 2009/28/EC OF THE EUROPEAN PARLIAMENT AND OF THE COUNCIL of 23 April 2009”. It is an ambitious policy towards environmentally compatible and sustainable energy. The target is to increase the share of the renewable energy sources in gross final energy consumption for each European country by 2020 [13]. Following that directive Germany reoriented its policy and initiated the energy transition (Energiewende) in 2011 [14]. The Energiewende aims to shut down all the nuclear power plants in Germany by the year 2022 and to increase the share of the renewable energies up to 35% in the gross electricity consumption and up to 18% in the final energy consumption by the year 2020.

This step shifts the power system from centralized and fossil-based generation towards regenerative and distributed generation which is accompanied with several challenges. The ESSs can be installed at different levels in the electrical power system to overcome these challenges; at generation level they can be used for energy arbitrage and for frequency regulation. At transmission level, they can be used for voltage control and at the distribution level, for peak shaving and for supporting grid capacity.

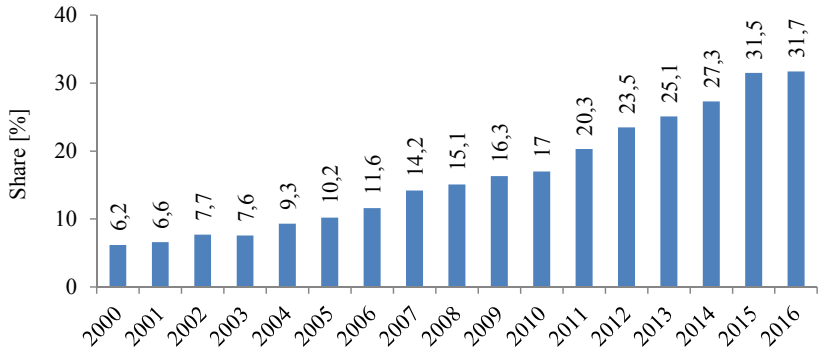

Figure 1.1 Development of renewable energy share of gross electricity consumption in Germany [15].

The next section covers the classification of different electrical energy storage technologies based on [16–22].

1.1 Electrical energy storage technologies

Electrical energy can be stored in one of the following forms:

1.1.1 Mechanical energy

1. **Pumped hydro storage (PHS)**: it consists of two interconnected water reservoirs located at different heights ($h_d = h_{upper} - h_{lower}$). During the charging process water is pumped up from the lower reservoir to the upper reservoir using an electric pump, and during discharging the falling water rotates a turbine that drives the electrical generator. The energy E_{phs} in a PHS depends mainly on the water volume (V_w) and height difference (h_d) between the reservoirs as expressed by Eq. (1.1):

$$E_{phs} = \rho g V_w h_d \tag{1.1}$$

2. **Compressed air energy storage (CAES)**: the electrical energy is stored in the form of compressed air in underground caverns. During charging the air is compressed by a compressor driven by an electric motor, the emerged heat due to compression is dissipated in non-adiabatic CAES using a radiator. During discharging a turbine fed with the compressed air rotates an electrical generator. The required heat during discharging is generated by burning fuel or gas in none-adiabatic CAES. The largest CAES systems worldwide are in Germany and US with $320MW$ and $110MW$ respectively.

3. **Flywheel energy storage (FES)**: it is made up of a rotating cylinder driven by an electric motor, which functions as a motor during charging and as a generator during discharging. The electrical energy E_{fes} is stored in the form of kinetic energy depending on the moment of inertia of the rotating part (I_m) and its angular velocity ω_f according to Eq. (1.2). The frictional effects are minimized by using vacuum and magnetic bearings.

$$E_{fes} = \frac{1}{2} I_m \omega_f^2 \tag{1.2}$$

1.1.2 Electrical energy

1. **Supercapacitor**: it consists of two electrodes, electrolyte and a separator which allows the ions to move between the electrodes during charging and discharging. The stored electrical energy E_{cap} in a capacitor depends on its capacitance (C_{cap}) and voltage (V_{cap}), as expressed in Eq. (1.3). The supercapacitor has a very high cycle lifetime and high power density with low

energy density. Therefore it is suitable for applications which require high power for a short term.

$$E_{cap} = \frac{1}{2} C_{cap} V_{cap}^2 \tag{1.3}$$

2. **Super-conducting magnetic energy storage (SMES)**: the electrical energy is stored using a superconducting coil cooled down below $-260\,^{\circ}C$ with helium. During charging the coil is fed with a direct current (I_{smes}) and during discharging the coil is connected to a load by a switching system. The stored energy E_{smes} is given in Eq. (1.4) where (L_{smes}) is the inductance of the coil. The SMES is considered as a short term energy storage system.

$$E_{smes} = \frac{1}{2} L_{smes} I_{smes}^2 \tag{1.4}$$

1.1.3 Thermal energy

Thermal energy storage systems are classified into high and low temperature energy storage systems.

1. **High temperature thermal energy storage system**: the heat is stored during charging in a thermal storage like magnesium oxide bricks or molten salt at the temperature of about $500\,^{\circ}C$. During discharging the heat in the thermal storage is used to heat up water to produce steam. The steam drives a turbine and an electric generator.

2. **Low temperature thermal energy storage system**: it uses materials that can be kept at low temperature insulated containments. The temperature range is below $-18\,^{\circ}C$ for industrial cooling and $0\,-\,12\,^{\circ}C$ for building cooling.

1.1.4 Chemical energy

the electrical energy is stored as chemical energy in one of the various battery technologies:

1. **Lithium-ion battery**: The Li-Ion cell consists of a positive electrode (cathode) made of lithiated metal oxide such as lithium cobalt oxide (LCO), lithium iron phosphate (LFP), lithium nickel cobalt manganese oxide (NCM), lithium nickel cobalt aluminum oxide (NCA) or lithium titanium oxide (LTO). The negative electrode (anode) is composed of layered graphite, coke, hard carbon or lithium titanate. The electrolyte consists of lithium salts dissolved in organic carbonates [28]. During charging the lithium-ions move from cathode to the anode where they are intercalated in the carbon layers. At the anode lithium ions are oxidized according to Eq. (1.5).

$$Li_x C_6 \leftrightarrow Li^+ + e^- + C_6 \tag{1.5}$$

where $0 \leq x \leq 1$ is a fractional measure of amount of lithium stored withing the electrode, normalized by the saturation (maximum) value, and is refered to as degree of lithiation. During discharging the lithium-ions move back to the cathode where they are intercalated into the crystal structure. At the cathode lithium ions are reduced and they gain more electrons through the chemical reaction in Eq. (1.6).

$$Li^+ + e^- + M \leftrightarrow Li_yM \tag{1.6}$$

where y has a similar definition like x but refers to the cathode. M refers generally to metal oxide or phosphate compounds [29–31]. The sturcture of a Li-Ion cell including charging and discharging processes is depicted in Figure 1.2. Lithium-ion batteries can be used for medium-term and short-term energy storage, therefore they are widely used in the area of portable applications (e.g. laptop, cell phone, etc.), in electric vehicles and in stationary applications.

2. **Flow battery**: The electrolyte of a flow battery is stored in tanks in fluid state. During charging and discharging the electrolyte is pumped through the a cell stack where a current is applied or delivered. The energy capacity is determined by the size of the tanks and the power rating is determined by the area of the cell stack. The main advantage of this battery type is the independent power and energy scaling. The available types of flow battery are the vanadium redox-flow battery (VRB) and Zinc-bromine batteries [26].

3. **Lead-acid battery**: one of the oldest and most widely used battery technologies. It consists of a positive electrode made of lead dioxide (PbO_2), a negative electrode built of sponge lead (pb) and an electrolyte composed of sulfuric acid (H_2SO_4) [23].

4. **High temperature battery (ZEBRA battery)**: it uses a solid state electrolyte melted at high temperature in the range of $270 - 350\,°C$.

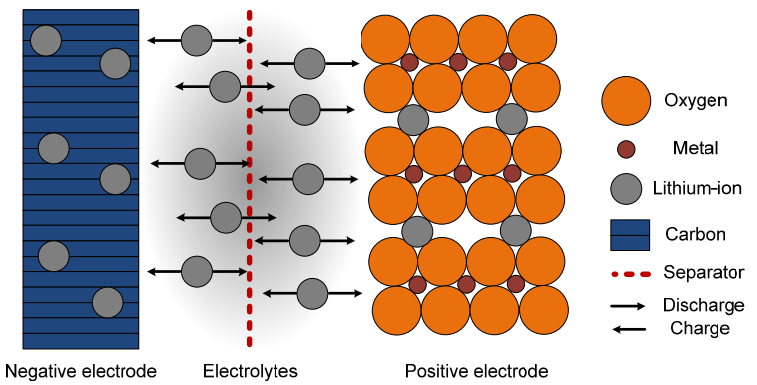

Figure 1.2 Basic structure of a Li-Ion cell showing the charge discharge process based on $LiMeO_2$ cathode material and a carbon-based anode [22].

The commercial ZEBRA batteries are classified into two types based on their chemicals:

- **Sodium-sulphur battery (**NaS**)**: it is composed of molten sodium for the anode and liquid sulphur for the cathode separated by a beta-alumina ceramic electrolyte. During charging the positive sodium ions (Na^+) pass through the electrolyte and combine with sulphur to form a sodium polysulphide (Na_2S_4) according to Eq. (1.7). The inverse reaction happens during discharging [24].

$$2Na + 4S \leftrightarrow Na_2S_4 \tag{1.7}$$

- **Sodium-nickel-chloride battery (**$NaNiCl$**)**: it uses nickel powder and plain salt for electrode material, the electrolyte and separator is a beta-alumina ceramic which is conductive for Na^+ ions but an insulator for electrons. During charging $NaCl$ reacts with Ni resulting in $NiCl_2$ and molten Na (Eq. 1.8). The chemical reaction is reversed during discharging [25].

$$2NaCl + Ni \leftrightarrow NiCl_2 + 2Na \tag{1.8}$$

5. **Hydrogen fuel cell**: it produces electrical power by combining hydrogen and oxygen in the fuel cell stack without the emission of any environmentally damaging pollutants such as CO_2. Furthermore the exothermic nature of the electrochemical reaction makes fuel cells ideal candidates for combined heat and power (CHP) applications. During charging the hydrogen is produced from water using an electrolyzer. During discharging the hydrogen is used as fuel and oxygen as an oxidant to produce electricity and water [27].

1.2 Evaluation parameters

Round-trip efficiency $\eta[\%]$: is the ratio of output energy to input energy.

Energy density $E_v[Wh/l]$: it expresses the amount of energy that can be stored per unit volume.

Specific energy $E_m[Wh/kg]$: it is the amount of energy that can be stored per unit mass.

Power density $P_v[W/l]$: it is the ratio between the available power of a system and it's volume.

Cycle lifetime $N_{cyc}[cycles]$: the maximum number of full cycles that can be achieved by a storage system before it fails (end of lifetime according to a specific criterion).

Calendar lifetime $L_{ca}[y]$: the lifetime of unused storage system until it fails according to a specific criterion.

Self discharge $S_d[\%/\text{time unit}]$: it represents the energy loss due to an internal process in the energy storage system.

Power installation cost $C_p[€/kW]$: the costs of installing certain amount of output power.

Energy installation cost $C_e[€/kWh]$: the costs of installing a certain amount of energy capacity.

Response time τ[time unit]: the time required to reach the full power of the system since it was requested.

1.3 Main applications

Frequency control : system frequency is maintained at its set-point ($50Hz$ in the European electricity grid) by controlling the demand and supply of an electrical energy. If the energy demand is higher than the supply, the frequency drops and in the opposite case it rises. Therefore, energy storage systems can help to balance between energy demand and supply by charging or discharging. The frequency control is divided as shown in Figure 1.3 into three types according to the response time:

- **primary**: it is activated in response to the frequency deviation from the set-point. It allows balancing between generation and demand at a system frequency close to the set-point.
- **secondary**: it is activated to restore the system frequency to its set-point value replacing the primary control.
- **tertiary**: it needs a request from the transmission system operator (TSO) to the energy supplier to change in the set-points of generators or loads. The tertiary control replaces the secondary control.

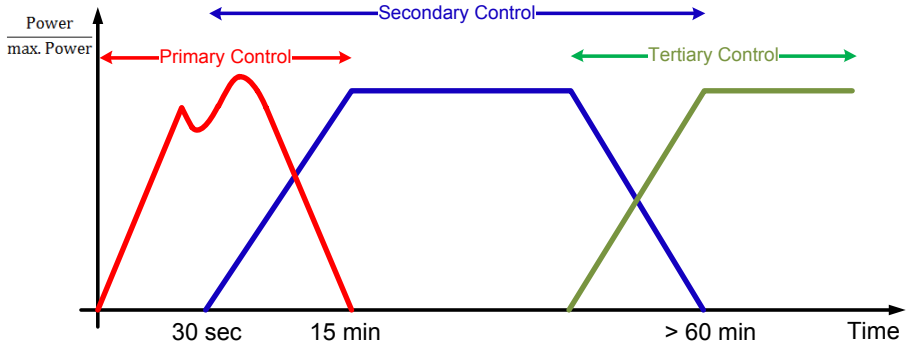

Figure 1.3 Time scale of frequency control (activating times are for Germany) [22].

Voltage control : it is activated to keep the voltage on the transmission and distribution lines within certain limits. Energy storage systems support the voltage control by injecting or absorbing the reactive power.

Peak shaving : the capability of an energy storage system to contribute to the reduction of the peaks under generation and demand.

Island Grids : there is no connection to a stiff grid, therefore the energy storage system should be able to react quickly to any strongly varying energy supply or demand in order to regulate the system frequency.

Electromobility : the energy storage system should be suitable to be installed on an electric vehicle.

1.4 Classification of energy storage technologies

Figure 1.4 shows an overview of the different storage technologies classified according to their energy and power density. More detailed classification is depicted in Tables 1.1 and 1.2, where a comparison between the different energy storage technologies based on the evaluation parameters in section 1.2 and according to application areas in section 1.3 is carried out. Based on this classification, Li-Ion battery is the only energy storage technology, which fulfill system requirements regarding cycle and calendar lifetime, efficiency, response time, energy and power density for smart grids and electric mobility. The major challenges facing Li-Ion is the battery cost. A recent scientific study by Institut für Stromrichtertechnik und Elektrische Antriebe RWTH (ISEA) for solar storage systems show that the end customer system price of a PV storage system with Li-Ion battery has more than $45\,\%$ decreased since the mid of 2013 through the subsidy program of KfW bank. At the moment many Li-Ion battery storage systems are available with end customer system price less than $1000\,€/kWh$. In comparison to lead acid storage systems, where the prices are decreased of about $16\,\%$ over the same period. The actual average end customer system price of PV storage systems with lead acid batter is about $700\,€/kWh$ [32].

1.5 Conclusion

The most common electrical energy storage technologies were reviewed in this chapter. They were classified based on the evaluation parameters and according to application areas. Among these technologies, the Li-Ion is a promising solution to assure the flexibility and security of power supply in microgrid and electric mobility applications.

Table 1.1 Evaluation of mechanical and electrical energy storage technologies.

Parameter	**PHS**	**CAES**	**FES**	**Supercapacitor**	**SMES**
$\eta[\%]$	75-82	70-70	80-95	90-94	80-90
$E_v[kWh/m^3]$	0.27($h_d = 100m$)	3($100bar$)	80-200	2-10	0.5-10
$E_m[Wh/kg]$	0.5-1.5	30-60	5-80	2.5-15	0.5-5
$P_v[kW/m^3]$	n.a.	n.a.	10000	15000	1000-4000
$N_{cyc}[cycles]$	n.a.	not limited	several millions	million	not limited
$L_{ca}[y]$	80	25	15	15	20
S_d	0.005-0.02 [%/day]	0.5-1 [%/day]	5-15[%/h]	10-15[%/h]	10-15[%/h]
$C_p[€/kW]$	500-1000	1000	300	10-20	n.a.
$C_e[€/kWh]$	5-20	40-80	1000	10000-20000	n.a.
τ	min	min	ms	ms	ms
Application					
Frequency control	secondary	secondary	primary	primary	primary
Voltage control	y	y	y	y	y
Peak shaving	y	y	y	y	y
Island grid	n	n	n	n	n
Electromobility	n	n	n	n	n

Table 1.2 Evaluation of electrochemical energy storage technologies.

Parameter	**Lead-Acid**	**ZEBRA**	**VRB**	**Fuel cell**	**Li-ion**
$\eta[\%]$	75-80	75-80	60-70	34-40	83-86
$E_v[Wh/l]$	50-100	150-250	20-70	n.a.	200-350
$E_m[Wh/kg]$	30-50	100-140	10-30	600-1200	75-250
$P_v[W/l]$	10-500	n.a.	n.a.	n.a.	100-3500
$N_{cyc}[cycles]$	500-2000	5000-10000	>10000	n.a.	1000-5000
$L_{ca}[y]$	5-15	15-20	10-15	5-15	5-20
$S_d[\%/day]$	0.1-0.4	10	0.1-0.4	0.03	0.1-0.2
$C_p[€/kW]$	150-200	150-200	1000-1500	1500-2000	150-200
$C_e[€/kWh]$	100-250	500-700	300-500	n.a.	300-800
τ	ms	ms	s	min	ms
Application					
Frequency control	primary	primary	(secondary, tertiary)	n	primary
Voltage control	n	n	n	n	y
Peak shaving	y	y	n	n	y
Island grid	y	y	y	y	y
Electromobility	n	y	n	n	y

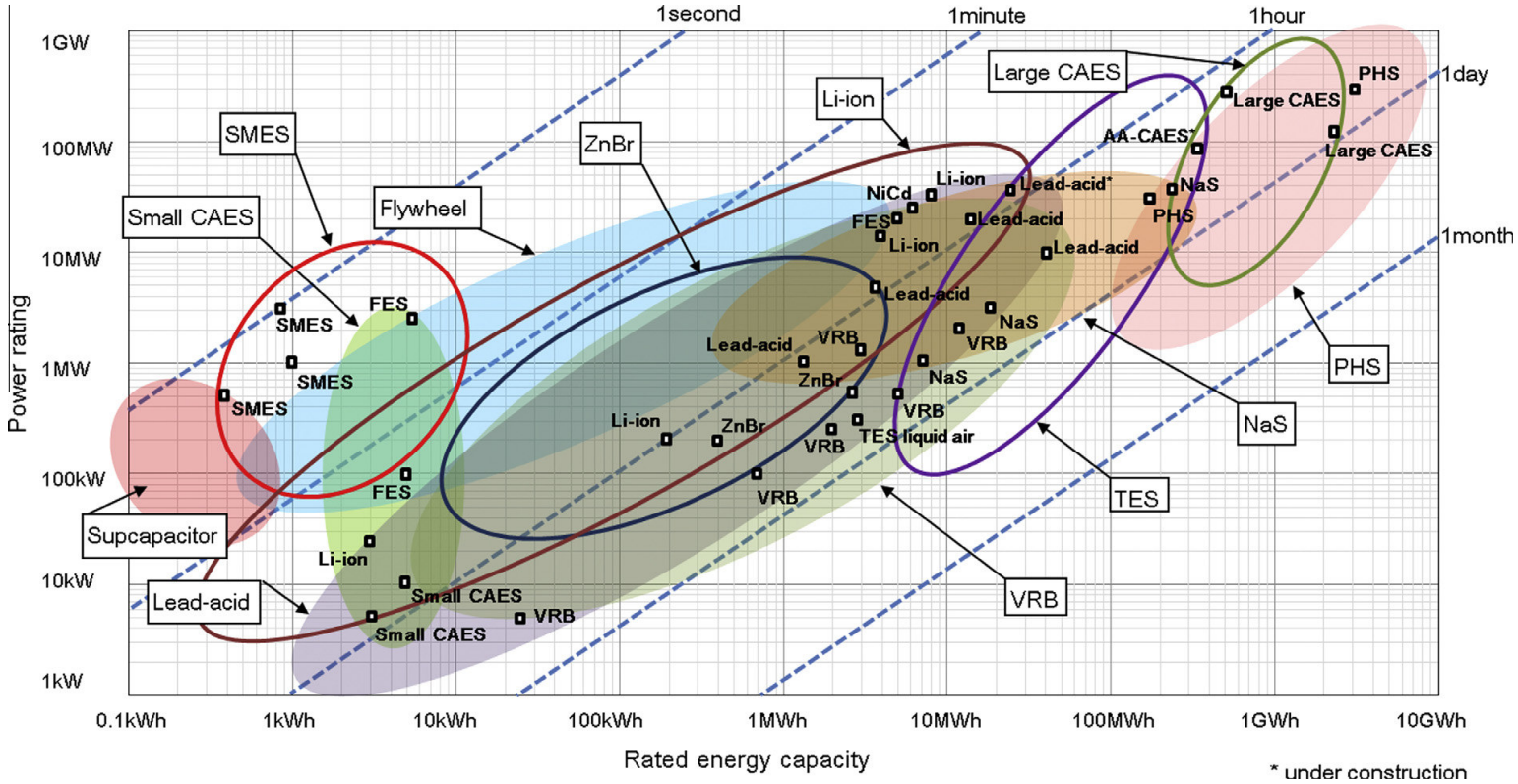

Figure 1.4 Classification of energy storage technologies according to their energy and power densities [17].

2 MODELING OF A LI-ION BATTERY

Li-Ion cells are very complex electrochemical systems due to the coupling between their electrical, thermal and aging dynamical behavior. These dynamics are determined by the state variables of the cell: SOC, temperature (T_{cell}) and SOH. In order to analyze and optimize systems with Li-Ion batteries, such as microgrids with BESSs or electrical vehicles, it is necessary to have a mathematical model that can accurately represent the complete dynamics of the cell. Availability of battery models that can fulfill all the previous requirements, will enable storage system designers to predict and optimize system performance under different conditions just by simulation. As a result they can reduce the experimental efforts and time. However this process is not easy because of the following reasons:

- Li-Ion batteries are not stationary systems due to SOC variation, diffusion phenomenon and several aging effects [33–35].
- They are highly nonlinear systems regarding to current density, SOC, temperature and aging [36, 37].

The complete model structure of a Li-Ion cell is shown in Figure 2.1. The model inputs are the cell actual current I_{cell}, ambient temperature T_a (it is assumed that the cell's initial temperature is equal to $T_{ambient}$), the initial relative state of charge SOC_{r0} ($SOC_{r0} = 0$ when the cell is empty; $SOC_{r0} = 1$ when the cell is full) and the initial state of health SOH_0 ($SOH_0 = 1$ for an unused cell; $SOH_0 = 0.8$ defines the cell's end of lifetime). The model outputs are the cell's terminal voltage V_{cell}, SOC, temperature and SOH.
The complete model of a Li-Ion cell consists mainly of three sub models for modeling the electrical, thermal and aging behavior. The three models are discussed in detail in sections 2.1, 2.2 and 2.3 respectively. The central block is for adapting the electrical model parameters depending on the cell's state variables using trilinear interpolation [38].

2.1 Electrical model

As shown in Figure 2.1, the electrical model of a Li-Ion cell should generate accurately the following main outputs under different operation conditions over the whole service life of the cell:

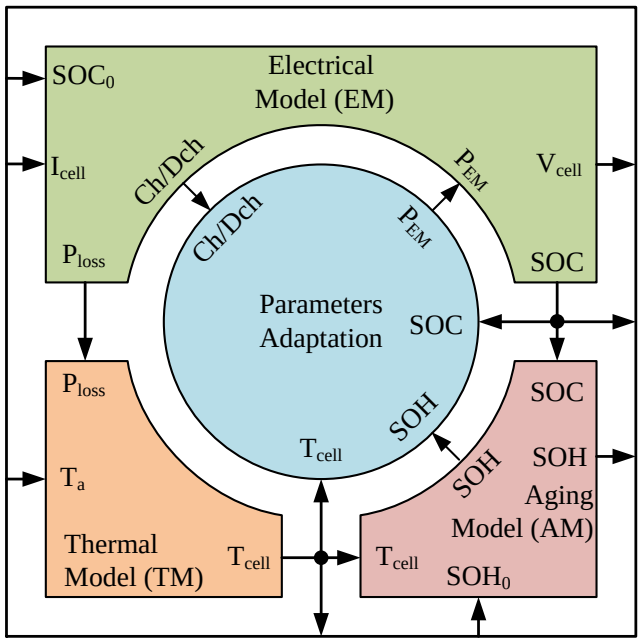

Figure 2.1 Complete model block diagram of a Li-Ion cell.

1. **Prediction of the output voltage (V_{cell})**: the complexity of the model structure defines the accuracy of the output voltage calculation. Therefore in [PAPER- III], some of the common model structures are reviewed and the ECM is selected to describe the relationship between the current and the output voltage of the cell. The ECMs are considered to be a compromise between mathematical complexity and accuracy and they are explained in [PAPER- I] in detail and used for the rest of the thesis as the standard structure for the electrical model. Electrochemical models are not used in this work since the determining parameters of the cell's chemistry and its detailed internal structure usually are unknown and kept as a business secret by the cell manufactures.

2. **Detection of the SOC**: the application of the ECMs and extended Kalman filter (EKF) for estimating the SOC of a Li-Ion cell is explained in detail in [PAPER- II].

3. **Estimation of power losses (P_{loss})**: since that the electrical model parameters have no physical representation of the Li-Ion cell. Accurate estimation of the power losses based only on the electrical model parameters is very challenging. Therefore a further research is required to develop an additional model for power losses.

2.1.1 Equivalent circuit model (ECM)

The ECMs use linear elements to describe the relationship between I_{cell} and V_{cell}. It is composed of four parts, as shown in Figure 2.2.

- **Ohmic resistance (R_o)**: it is the frequency independent part of cell's electrochemical impedance, which is equal to the real part of the electrochemical impedance at the frequency f_{ro}, at which the imaginary part is zero.
- **Capacitive part**: it represents the electrical dynamics of the Li-Ion cell in the low frequency (LF) range $0 \leq f < f_{ro}$ and it consists of a series connection of $(R \parallel C)$ networks. The number of $(R \parallel C)$ networks defines the model's complexity e.g. the one time constant (OTC) and the two time constants (TTC) models are explained in detail in [PAPER- I].
- **Inductive part**: it extends the representation of the electrical dynamics of the cell to the HF range ($f > f_{ro}$) and it is necessary to analyze the harmonic content of the cell's current. It consists of a series connection of $(R \parallel L)$ networks [39].
- **Open circuit voltage**: it is modeled using an ideal voltage source to represent the cell's no-load output voltage in steady state.

In the author's paper [PAPER- IV] the impact of ECM's complexity on the dynamic behavior of the stationary BESS is analyzed. It was found that at least two time constants are required to represent the electrical dynamics in the LF range and one time constant for the HF range in order to analyze the electrical dynamics of a BESS accurately. Based on these conclusions the three time constants (DTC) model combined with the $1RL$ model form, as shown in Figure 2.7, the complete structure of the electrical model to be used for the rest of the thesis.

2.1.2 Identification of equivalent circuit model parameters

The electrical model parameters are the values of the R, C, L and V_{OC} in the ECM and they are functions of SOC, temperature, and SOH.

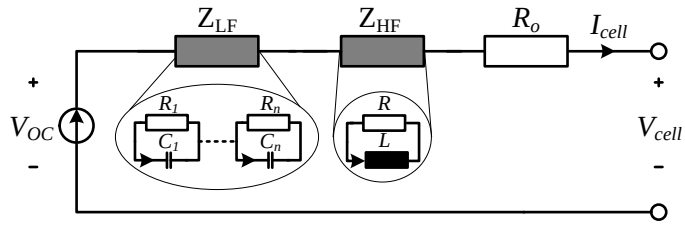

Figure 2.2 ECM structure of a Li-Ion cell for slow (low freq.) and fast (high freq.) dynamical operation.

Ohmic resistance

The ohmic resistance (R_o) is one of the important physical properties of a Li-Ion cell. It can be identified using measurements either in the frequency domain or in the time domain. In the frequency domain it can be identified by measuring the electrochemical impedance at frequency f_{ro} [40, 41]. The impedance measurement is an accurate and simple method but it requires an expensive and complex device such as an impedance spectrum analyzer which is normally restricted for low voltage applications ($V < 10V$) under laboratory conditions. Hence it is not suitable for real applications where high battery voltage is expected.
In order to overcome the previous issues, the voltage and current measurements in the time domain are used to identify the ohmic resistance using two different approaches. The first approach is based on measuring the voltage drop caused by a current impulse and using Ohm's law to calculate the ohmic resistance [42–45]. This approach is explained later in detail in this section. The second approach is to estimate the value of the ohmic resistance as a parameter of the ECM. The estimation can be done either off-line using curve fitting methods like least squares (LS) [46] or on-line using recursive LS or Kalman filter [47, 48]. The second approach implies that the value of R_o does not represent anymore the ohmic resistance in the ECM, but an equivalent resistance, which might include other real parts of the electrochemical impedance that are frequency dependent. In this case the accuracy of identifying R_o is influenced by model complexity, the weights used for the curve fitting and by sampling frequency.
Back to the voltage drop approach, a dc current pulse is applied on the cell and the output voltage V_{cell} and the current I_{cell} are simultaneously measured. The voltage and current difference ΔV resp. ΔI at the switching moment t_s as shown in Figure 2.3, are needed to apply Ohm's law in Eq. (2.1) to calculate the ohmic resistance:

$$R_o = \left|\frac{\Delta V}{\Delta I}\right| = \left|\frac{V_{cell}(t_{k+1}) - V_{cell}(t_k)}{I_{cell}(t_{k+1}) - I_{cell}(t_k)}\right| \tag{2.1}$$

In real application, ΔV and ΔI can not be accurately measured due to the following reasons:

1. Detection of the switching moment t_s is not normally possible because the measurement device is not synchronized with the power supply or electronic load. That leads to a random time delay between t_s and t_{k+1}.

2. Current oscillations caused by the resonance frequency of the RLC circuit composed of the output capacitor of the power supply and electronic load on the one side, and the inductance of the connection cables on the other side.

A novel approach developed to overcome the previous issues is based on applying a sequence of current pulses instead of one pulse in order to increase

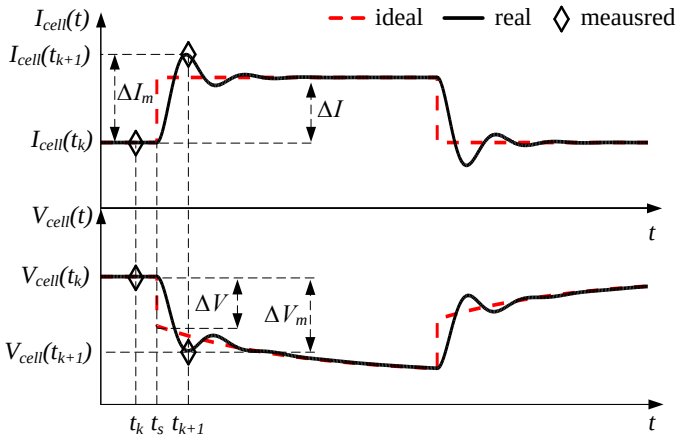

Figure 2.3 Voltage and current signals of Li-Ion cell during applying a current pulse for identifying the ohmic resistance.

the number of switching moments. The sequence is applied before and after each modeling pulse in order to evaluate the ohmic resistance change due to the temperature increase caused by the losses during applying modeling pulse. The modeling pulse together with the pulse sequences are shown in Figure 2.4 (d) and (e). The pulse sequence applied before the modeling pulse is zoomed in and cell's voltage V_{cell} and current I_{cell} are plotted in Figure 2.5 (a) and (b). The cell's output voltage and current are shown at the first switching moment of the pulse sequence in Figure 2.5 (e) and (f). The first step in the new approach is to calculate the voltage and current difference ΔV_m resp. ΔI_m for each pulse sequence as depicted in Figure 2.5 (d) and (e).
The second step is to apply Ohm's law in Eq. (2.1) on the measured signals ΔV_m and ΔI_m and to express them as a linear relationship with the measured ohmic resistance R_{om} as a linear coefficient in Eq. (2.2).

$$|\Delta V_m| = R_{om} \, |\Delta I_m| \tag{2.2}$$

The value of R_{om} is calculated in order to obtain the best correlation between ΔV_m and ΔI_m, as it is mathematically described in Eq. (2.3).

$$R_{om} = \frac{cov(dV_m, dI_m)}{var(dI_m)} \tag{2.3}$$

where:

$$\begin{aligned} var(dV_m) &= \frac{1}{n}\sum dV_m^2 - (\overline{dV_m})^2 && : \overline{dV_m} = \frac{1}{n}\sum dV_m \\ var(dI_m) &= \frac{1}{n}\sum dI_m^2 - (\overline{dI_m})^2 && : \overline{dI_m} = \frac{1}{n}\sum dI_m \\ cov(dV_m, dI_m) &= \frac{1}{n}\sum dI_m * dV_m - \overline{dV_m} * \overline{dI_m} \end{aligned} \tag{2.4}$$

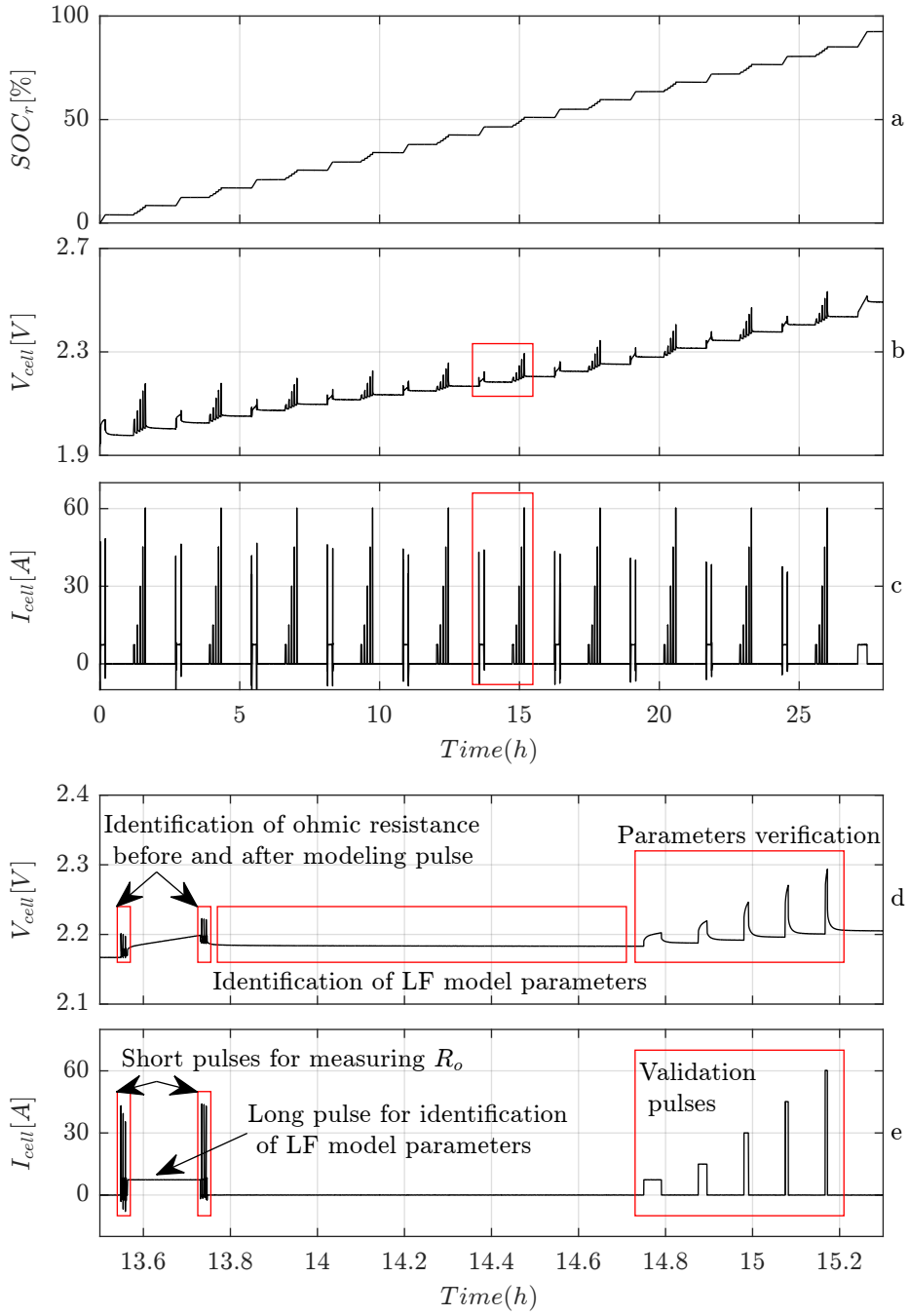

Figure 2.4 Output voltage and current of Li-Ion cell at $20\,^{\circ}C$ *and* $SOH = 1$*: a)relative state of charge; b) measured output voltage; c)measured current; d)output voltage for applying modeling and verification current pulses; e) modeling and verification current pulses.*

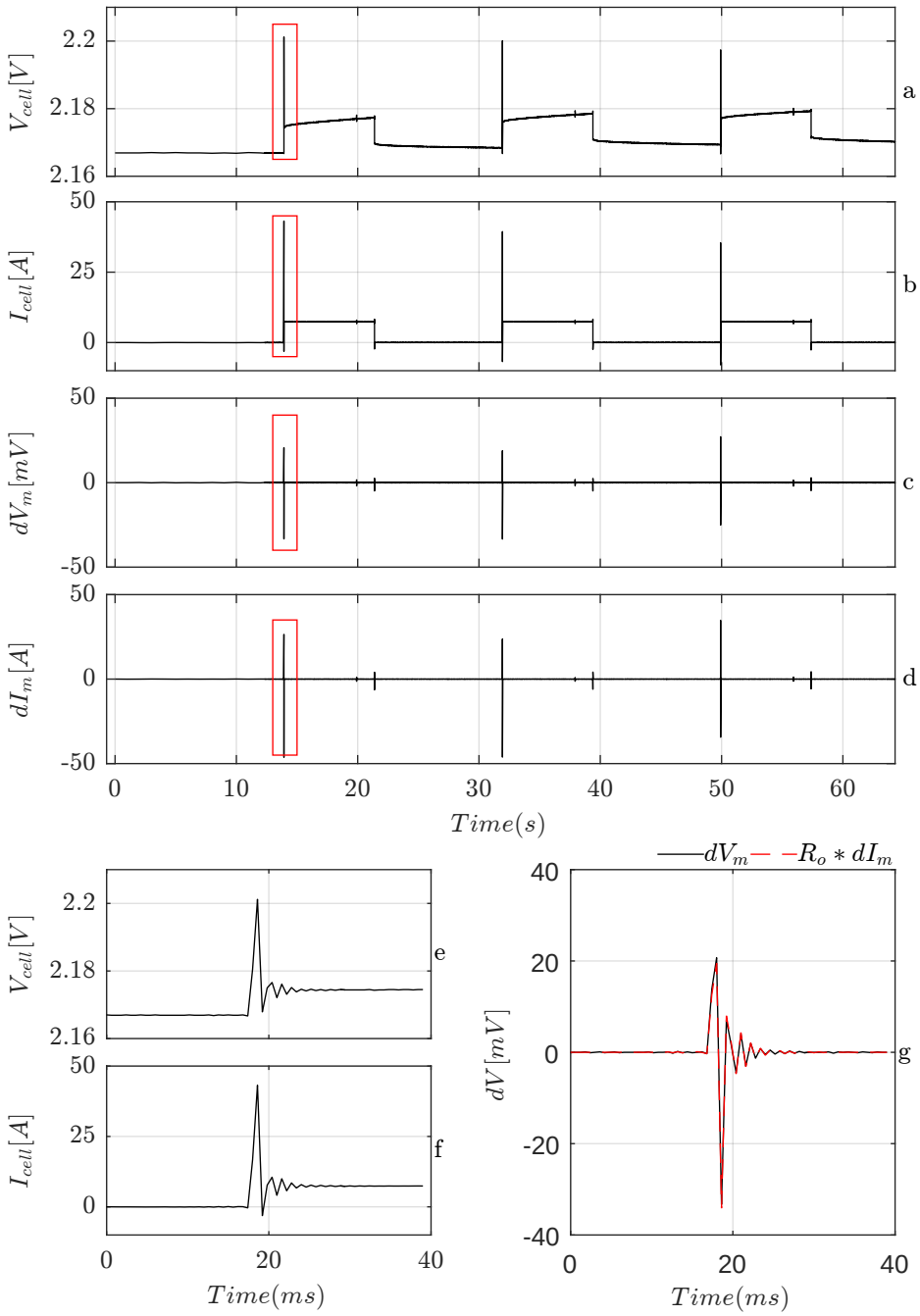

Figure 2.5 Measurement of Li-Ion cell ohmic resistance (R_{om}): a)cell output voltage; b)cell current; c)voltage difference; d)current difference; e)zoom in cell output voltage; f)zoom in cell current; g)matching between dV_m and $R_{om} * dI_m$.

The quality of the fitting (Pearson's correlation coefficient) $0 \leq r \leq 1$ is calculated using Eq. (2.5). This coefficient represents how linear the relationship between ΔV_m and ΔI_m is. So for low values of r the value of R_{om} can not be trusted anymore to represent the ohmic resistance:

$$r = \frac{cov(dV_m, dI_m)}{\sqrt{var(dV_m) * var(dI_m)}} \tag{2.5}$$

The matching results between ΔV_m and $R_{om}\Delta I_m$ are shown in Figure 2.5 (g) for the first switching moment in the current sequence.

Electrical model parameters in low frequency range

The parameters of the capacitive part (R_{dtci} and C_{dtci} for $i = 1 \ldots 3$) are identified using voltage and current measurements in the time domain. After applying each modeling pulse, the cell output voltage is measured for one hour, as shown in Figure 2.6 (b). The open circuit voltage (OCV) V_{OC} is firstly identified at the end of the exponential decay (2.6 (b)), then it is subtracted from the output voltage resulting in V_d the dynamic voltage part shown in Figure 2.6 (a).
The information about the dynamical characteristics of a Li-Ion cell is hidden in V_d, which can be mathematically described in Eq. (2.6) as a sum of exponential functions with real positive time constants τ_i and coefficients A_i.

$$S(t) = \sum_{i=1}^{M} A_i e^{-\frac{t}{\tau_i}} \quad A_i, \tau_i > 0 \quad and \quad 0 < t < \infty \tag{2.6}$$

Determination of the time constants and the amplitudes of the exponential decays from experimental data is a common task in many research fields like:

- semiconductor physic (deep level transient spectroscopy)

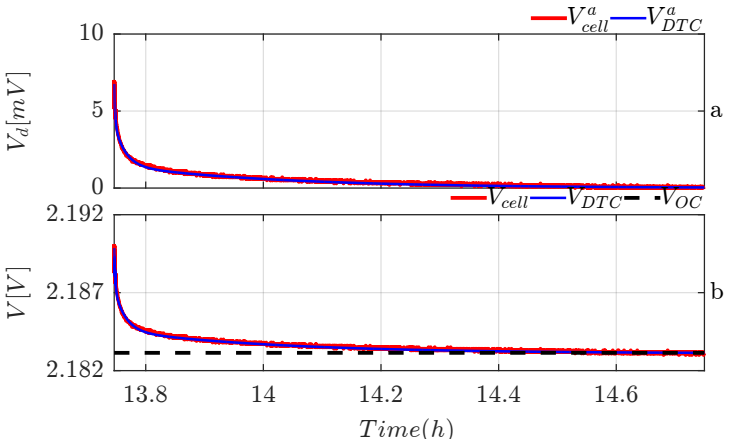

Figure 2.6 Comparison between the cell and the DTC model for: dynamic voltage V_d (a); output voltage (b).

- biophysics (fluorescence decay analysis)
- nuclear physics and chemistry (reaction kinetics)
- medical imaging
- chemistry and electrochemistry

In addition, it is always combined with the following challenges:

- The major problem with the analysis of this class of signals is their strong nonorthogonal property
- If we attempt to determine the unknown parameters A_i, τ_i and M from a finite time samples of the signal V_d, the distribution function of the decay rates will not be unique.
- We are dealing with a series of nonlinear functions
- System theoretical model is not known then the number of the exponential functions M is not known.
- Signal to noise ratio (SNR) limits the maximum number of exponential functions that can be determined

This problem has been tackled by many researchers and several methods have been developed. The methods can be classified under the following categories:

- **Parametric methods**: they can be used to directly identify the parameters of the multi-exponential functions for predefined number of the exponential functions.
  - **Algebraic methods**: early methods that apply an analytical procedure for the parameter identification. The advantage of these methods is that they need no guess point to start the search for parameters. These methods require measurements with a high signal to noise ratio (SNR) in order to achieve a good accuracy for parameter identification. Prony's method for an example is considered to be one of the first methods that devised an algebric scheme which can separate a small number of exponentials with similar amplitudes but with substantially different time constants [49].
  - **Numerical integration methods**: They differentiate the sum of exponential functions in order to convert the problem into a differential equation and they use the numerical integration to solve the problem and identify the parameters. For these methods the initial guess is not required. The methods are more noise resistant than the algebraic method. One of these methods is the Foss' Method and is explained in detail in [50–52].

– **Nonlinear least squares (NLS) methods**: These are general optimization methods that search for an optimum solution which minimizes chi-squared error (goodness-of-fit). Their pros are that they are standard methods in Matlab, whereas it is possible to bound the parameter range, and they can afford good accuracy even for measurements with low SNR. The only disadvantage is that the solution depends on the initial guess; this might lead to a solution that converges to a local minima which differs from the global one. The well known methods are Levenberg-Marquardt (LM) method, Gradient Descent Method, The Gauss-Newton Method and Nelder-Mead simplex method (NMS).

- **Nonparametric methods**: these methods remove the nonorthognality by converting the signal in Eq. (2.6) into a convolution model.

  – **Gardner transformation(GT)**: it applies a nonlinear change of variables to convert the original signal in Eq. (2.6) into a convolution integral which can be deconvolved by using Fourier transform technique [53–57].

Table 2.1 shows a comparison between the different methods. Based on this comparison the Foss' method is selected as a compromise between accuracy and complexity and above all, it is independent of the initial guess. The parameters of the DTC model shown in Figure 2.7 are identified and the comparison between the DTC model and the cell is plotted in 2.6 (a) and (b) for both dynamic voltage and output voltage respectively. The accuracy of the parameter identification is evaluated using the verification pulses. Figure 2.8 (a) shows the comparison between the cell's and DTC model's output voltage during the verification pulses and Figure 2.8 (b) shows the relative error in percentage, which is always less than 1%. The parameters of the DTC model are identified for SOC range: $0-100\%$, Temperature range: $10-40\,°C$, SOH: $1-0.8$. The parameters are displayed in 3D plots for charging and discharging in Figure 2.9 and Figure 2.10.

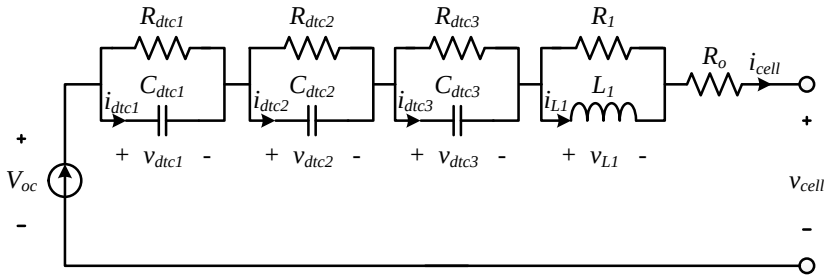

Figure 2.7 Equivalent circuit model of a Li-Ion cell with three time constants (DTC) for the low frequency model and one time constant for the high frequency model.

Table 2.1 Evaluation of different identification methods of multi exponential function.

method	Initial guess	Model order	Complexity	Accuracy
Prony	not required	required	simple	low
Foss	not required	required	simple	good
NLS-NMS	required	required	complex	good
NLS-LM	required	required	complex	good
GT	not required	not required	very complex	very good

Electrical model parameters in the high frequency range

Due to the usage of the pulse width modulation (PWM) technique with a switching frequency of $f_{sw} = 7.95kHz$ for the inverters in the BESS, a high frequency voltage and current harmonics have emerged. Therefore, the evaluation of the dc-side signals in the BESS requires knowledge of the battery dynamics in the HF range. For this reason, the behavior of the cell within the HF range was investigated.

The impact of the HF model's complexity on the dynamic analysis of the BESS has been investigated in [PAPER- IV]. The electrochemical impedance spectroscopy (EIS) measurement technique is used to inspect the cell's dynamic characteristics within the $[2kHz, 50kHz]$ frequency range, though several impedance measurements have been performed for different operation conditions describing the dependency of the cell's dynamics on the SOC, the temperature and the SOH. The 1RL-model is adapted to the complex impedance measurements using the Levenberg-Marquardt complex nonlinear least squares (CNLS) algorithm.

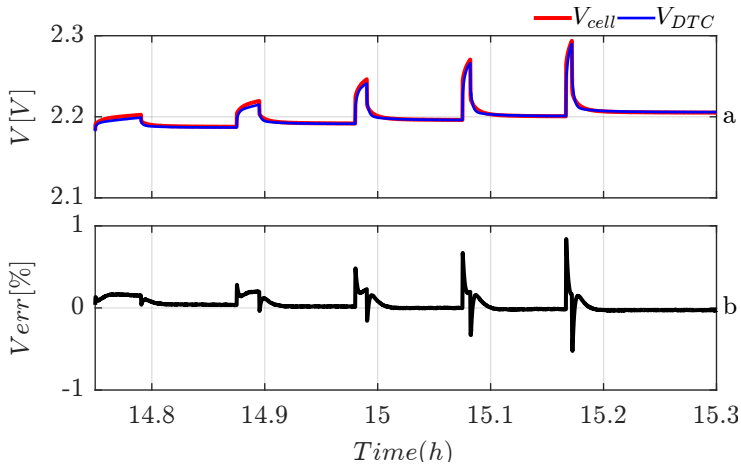

Figure 2.8 Evaluation of the DTC model: comparison between the output voltage of the cell and the DTC model (a); relative error in percentage (b).

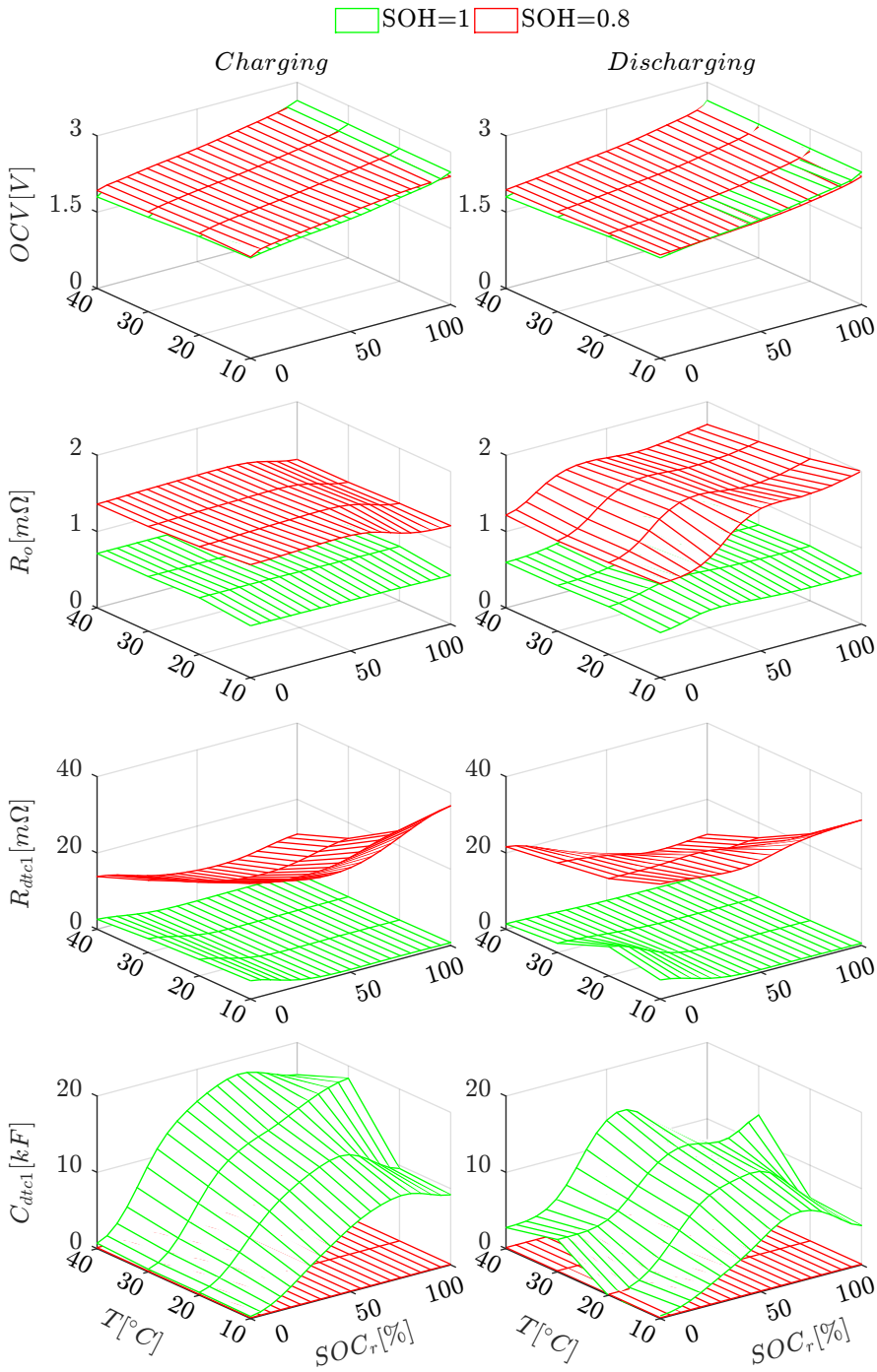

Figure 2.9 Parameters of the DTC model in low frequency range for the tested Li-Ion cell plotted for different SOC, temperatures and SOH (part1).

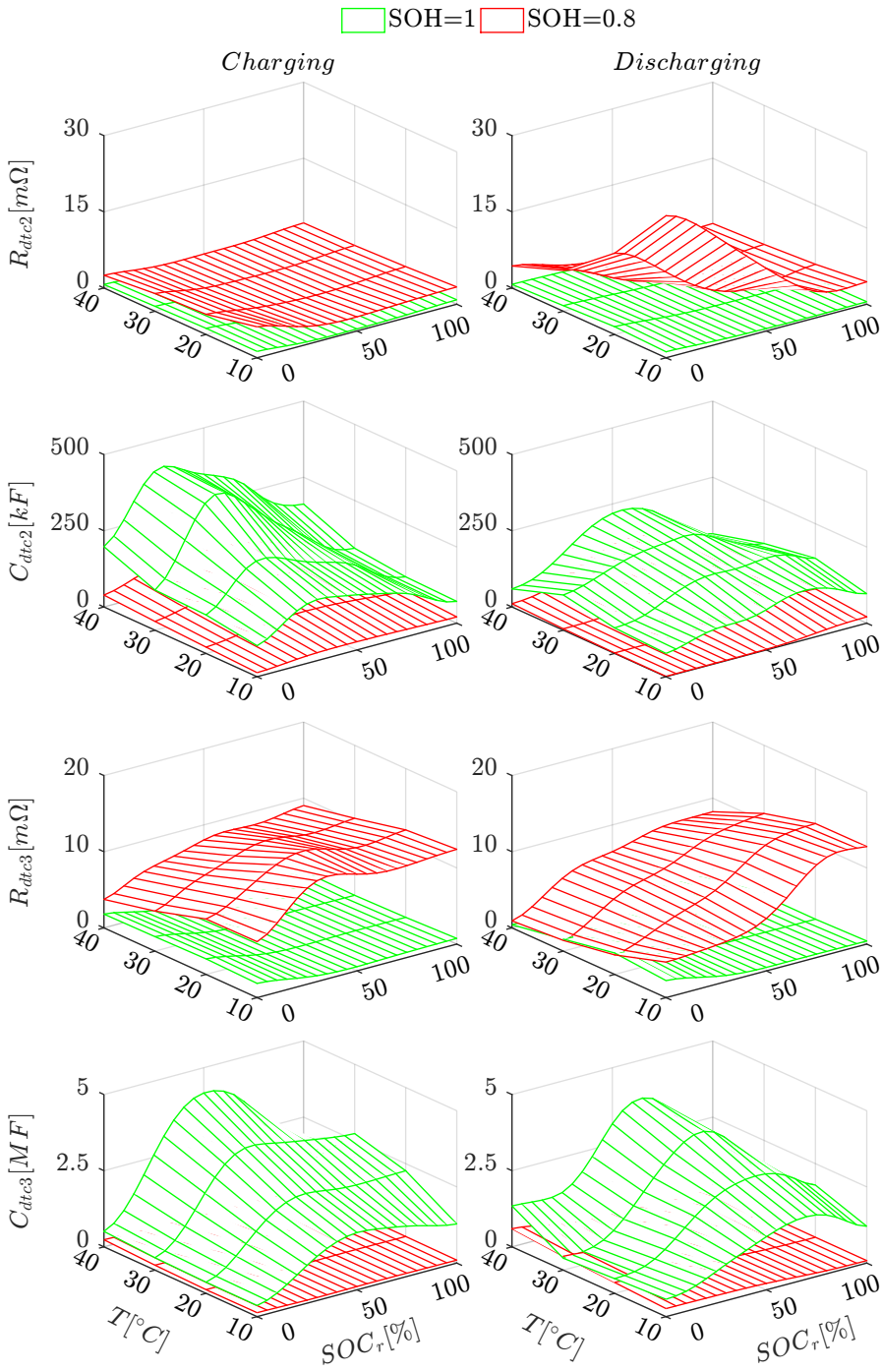

Figure 2.10 Parameters of the DTC model in low frequency range for the tested Li-Ion cell plotted for different SOC, temperatures and SOH (part2).

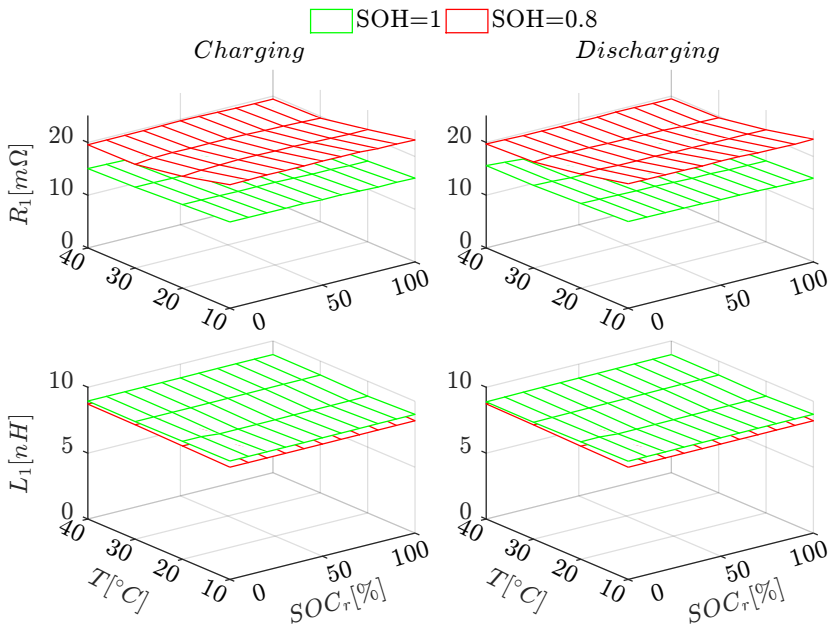

Figure 2.11 Parameters of the 1RL-model model in high frequency range for the tested Li-Ion cell plotted for different SOC, temperatures and SOH.

2.1.3 Test plan

The test plan describes the sequence of the stages of the modeling test and the parameters of each stage. The modeling test consists of two main stages as shown in Figure 2.12:

- **Capacity measurement**: a full charge followed by a full discharge with one C rate are performed in order to measure the cell's capacity.
- **Characteristic measurements**: in this stage, the measurements are generated to be used later for the parameter identification, and they can be divided into two types depending on the measured signals:

Time domain measurements

A current profile is designed to stimulate the cell and generate the desired voltage response to identify and verify the ECM parameters. The profile is built by repeating a pattern ten times, in each time a ΔSOC_r of 10% is achieved so that the parameters of the ECM are identified at ten equal SOC_r steps. The pattern consists of three parts as it is shown in Figure 2.4 (a,b and c):

- **Pulse sequence for the identification of the ohmic resistance**: it consists of three consecutive pulses with a $5\,sec$ on and off periods, as shown in Figure 2.5 (b).

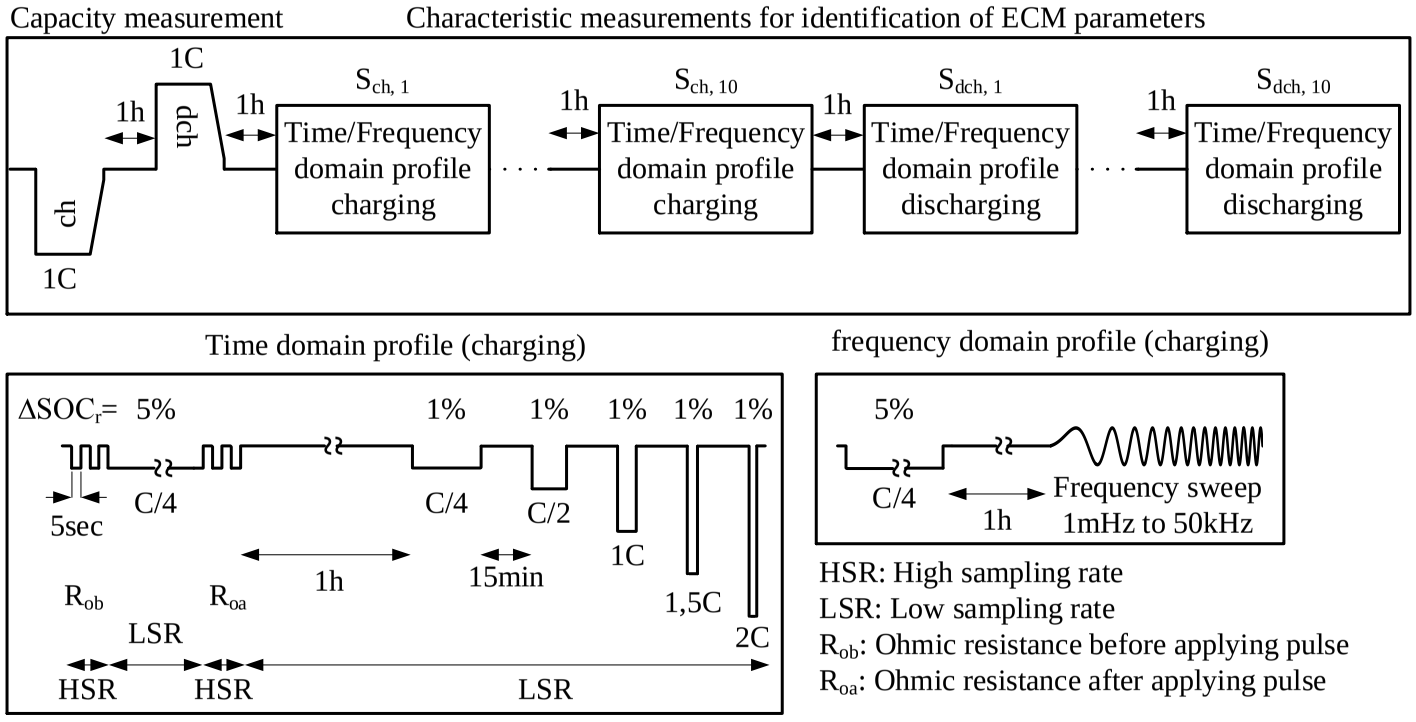

Figure 2.12 Description of the test plan applied for modeling tests in time and frequency domain.

This sequence is applied before and after each modeling pulse in order to evaluate the change of ohmic resistant due to the temperature increase during the modeling pulse. During this sequence, the voltage and current signals are acquired using a high sampling rate (HSR) with $f_s = 1.666\,kHz$.

- **Modeling pulse**: it is used to excite the cell so that the voltage response after the modeling pulse can be used for identifying the parameters of the ECM in the LF range. The modeling pulse duration is controlled in order to achieve $\Delta SOC_r = 5\,\%$. The amplitude of the modeling pulse is constant and equals $1Crate/4 = 7.5\,A$. This value of the pulse amplitude is selected based on experimental results shown in Figure 2.13 where three modeling tests are applied on an unused Li-Ion cell for three different current amplitudes $1C_{rate}, C_{rate}/2$ and $_{rate}/4$. All tests were performed at $T_a = 10\,°C$ during charging and discharging. The parameters of the DTC model are identified and the DTC model output is evaluated for each current amplitude by comparing it with the cell's output voltage. The absolute value of the relative error which indicates the accuracy of the model is displayed in Figure 2.13 for charging and discharging. The error results confirm that the best accuracy can be achieved at the current amplitude of $C_{rate}/4$.

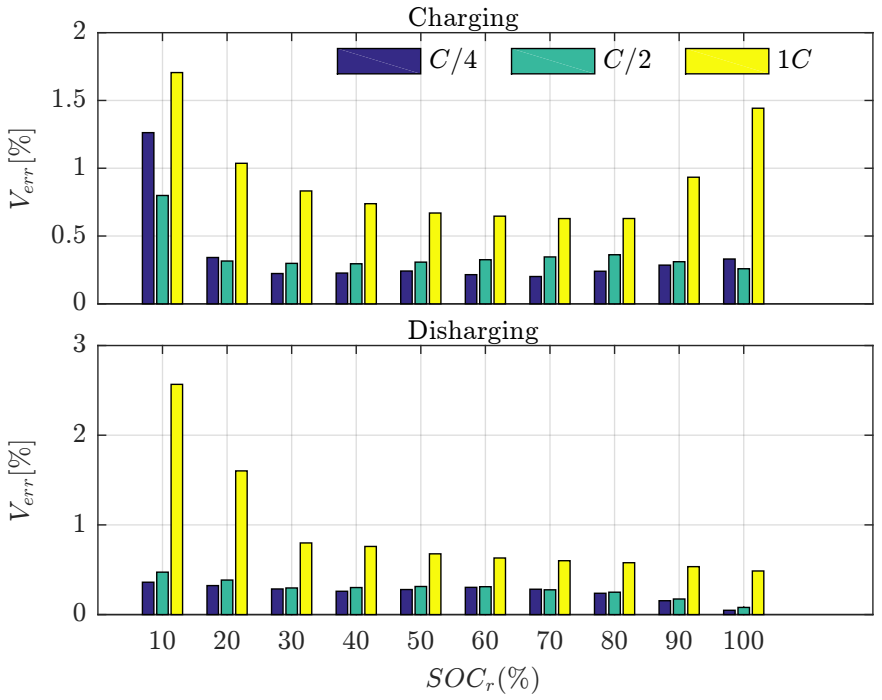

Figure 2.13 Evaluation of different current rates for modeling of a Li-Ion cell.

During the modeling pulse, the voltage and current signals are acquired using a low sampling rate (LSR) with $f_s = 1\,Hz$.

- **Verification pulses**: These pulses are applied for two purposes: the first goal is to verify the ECM parameters using data set different from the one used for the parameter identification. The second goal is to measure the maximum power that can be applied on the cell at each operation point, in other words, to identify the state of power (SOP) under different operation conditions. The verification pulses are five pulses with following amplitudes: $I_1 = C/4, I_2 = C/2, I_3 = 1C, I_4 = 3.5C$ and $I_5 = 2C$. The maximum current amplitude is chosen according to the maximum current in the real BESS when the maximum active power of $P = 55\,kW$ is applied for each of both parallel connected inverters. The voltage and current signals of the verification pulses are acquired using a LSR with $f_s = 1\,Hz$.

Frequency domain measurements

A profile similar to that used for time domain measurement is used. The pattern consists only of the modeling pulse with a constant amplitude that causes each time $\Delta SOC = 10\,\%$. The EIS technique is employed after a waiting period of one hour to measure the complex impedance of the cell over the frequency range of $[2\,kHz, 50\,kHz]$. The measured impedance is fed to a parameter identification algorithm to obtain the HF model parameters.

2.1.4 Experimental setup

The experiments for identifying the parameters of the electrical model were performed under the best possible laboratory conditions. The experimental setup for the modeling tests in the time and frequency domains is shown in Figure 2.14. It consists of the following equipment:

Computer

During the modeling test the following tasks were run by the computer:

1. Control and monitoring of the ambient temperature in temperature chamber during the modeling test.
2. Control of programmable power supply and electronic load in order to apply the predefined current profile on the Li-Ion cell.
3. Configuration of the measurement devices.
4. Real time acquisition and storage of measured data by the measurement devices.

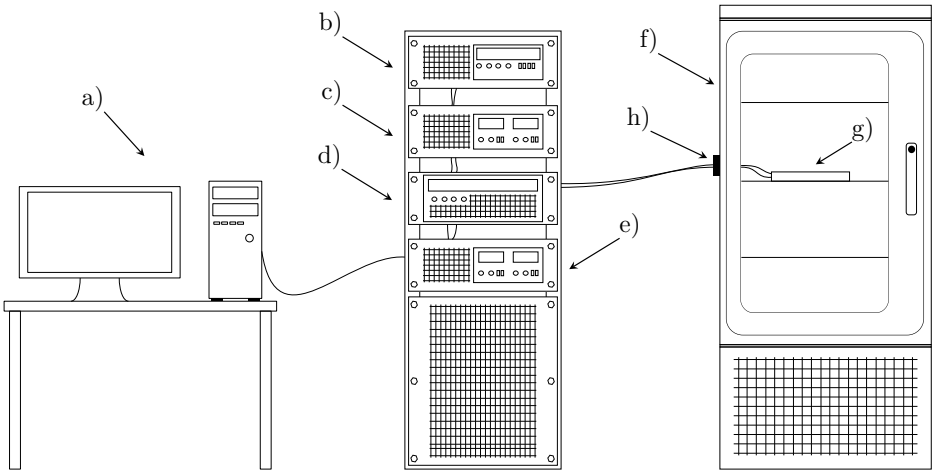

Figure 2.14 Experimental setup consisting of: a) computer; b) programmable power supply; c) programmable electronic load; d) measurement device; e) impedance spectrum analyzer; f) temperature chamber; g) device under test (Li-Ion battery); h) cable hole with low thermal conductivity.

5. Control and configuration of the EIS meter.
6. Real time acquisition and storage of measured data by the EIS meter.

Programmable power supply and electronic load

The power supplies and the electronic loads are modular units manufactured by the company Elektro-Automatik. They can be connected in series or parallel when higher voltage or current is required respectively. LabView VI is developed and implemented in order to configure and control these devices and to acquire and store their measured data in real time.

Measurement devices

The cell's output voltage and current were measured simultaneously using the NI 9215 measurement module. The NI 9215 offers a low voltage range of $\pm 10\,V$, a high accuracy of 16 Bit and a high sampling rate of $100\,kS/s/ch$ simultaneously. The NI 9215 module is plugged in one of the 4 slots of the Ethernet NI CompactDAQ chassis NI cDAQ-9184.

Impedance Spectrum Analyzer

The TrueData-EIS impedance analyzer is a diagnostic tool designed by FuelCon for measuring the electrochemical impedance spectrum of Li-Ion batteries and fuel cells during operation under different load conditions. It is based on the single-sine-method and have the following specifications:

- Impedance range: $5\,\mu\Omega$ to $15\,\Omega$
- Impedance accuracy: Up to $0.1m\,\Omega$
- Frequency, voltage, current accuracy: $\pm 1\,\%$
- Frequency range: from $200\,\mu Hz$ up to $100\,kHz$
- Maximum dc current of $100\,A$ and maximum ac modulation current of $5\,A$
- Maximum dc voltage of $10\,V$

The TrueData-EIS is combined with the electronic load modules TrueData-Load and is controlled using TestWork environment.

Temperature chamber

Li-Ion cells are always tested under controlled ambient temperature according to the predefined test specifications. The temperature chamber manufactured by firm Binder was used to keep the required ambient temperature constant in the range from $-25\,°C$ up to $+60\,°C$. The temperature chamber is controlled by $APT-COM^{TM}3$ Data Control System software over RS422 interface.

Device under test

The laboratory experiments were applied on the cells similar to those used for building the BESS. The cell specifications are given in Table 2.2.

2.2 Thermal characteristics of a Li-Ion cell

This section describes the process used for the thermal characterization of a Li-Ion cell including the experimental set-up and the procedure for accurate measurement of the heat capacity.

Table 2.2 LecCell 30Ah High Energy specifications.

Nominal capacity	$30\,Ah$
Nominal voltage	$2.3\,V$
Cathode	Lithium nickel cobalt oxide (NCO)
Anode	Lithium Titanate oxide (LTO)
Max. charge voltage	$2.7\,V$
End of discharge voltage	$1.7\,V$
Max. charge current	$120\,A(4C)$
Max. discharge current	$120\,A(4C)$
Max. temperature range	$-20\,°C$ to $+55\,°C$
Dimensions ($L \times W \times T$)	$287 \times 178.5 \times 12\,mm$

The heat capacity of a Li-Ion cell is an important part of the thermal model which is independent of module structure or system conditions. Therefore a measurement device is built for measuring the heat capacity of a Li-Ion cell in order to be used later in future research projects for developing a complete thermal model based on a specific battery module design and cooling system specifications.

2.2.1 Calorimeter

A laboratory prototype of a calorimeter was built from a thermally insulating compound known as extruded polystyrene foam (XPS) with the dimensions shown in Figure 2.15, including the walls of a thickness of $5\,cm$ and the room inside with dimensions of 30 x 30 x 6 cm able to hold 5.4 liters. The thermal specifications of the insulation material are shown in Table 2.3.

2.2.2 Measurement of heat capacity

The heat capacity C_p of a substance is defined by the amount of energy needed to rise the temperature of one gram of it by one degree at constant pressure. The heat capacity is an important parameter in the thermal characteristics because the temperature of the object will develop according to its initial temperature, heat caused by the power applied on the object and the heat capacity of the object, as expressed in Eq. (2.7).

$$T(t) = T(t_0) + \frac{1}{C_p}\int_{t_0}^{t} P(t)dt \tag{2.7}$$

Table 2.3 Specifications of the insulation material.

Heat conductivity $[W/mK]$	Specific heat capacity $[Jkg^{-1}K^{-1}]$	Density $[kg/m^3]$
0.065	1200	33

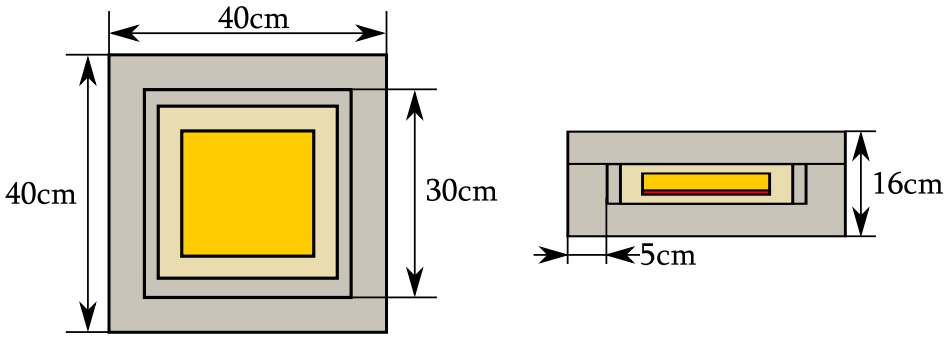

Figure 2.15 Structure of the calorimeter [38].

In order to measure the heat capacity of an object, the calorimeter is filled with a specific amount of water with known thermal characteristics at ambient temperature T_a. Then the object is heated in the temperature chamber to a certain temperature $T_{obj} > T_a$. After that the object is immersed in the water and the water temperature starts to increase due to heat transfer from the heated object until reaching a balance point $T_a < T_w = T_{obj}$. The heat capacity can be calculated when knowing the water temperature at the balance point. Due to the fact that the calorimeter is not an adiabatic system, the heat transfer to the ambient during the immersion of the heated object in water cannot be neglected and can cause a major error in the calculation of the heat capacity. Therefore, the calorimeter is modeled as a first order system, and the model parameters are identified by applying experiments using objects of materials with known specific heat capacity like copper and aluminum. The parameters of the calorimeter listed in Table 2.4 are identified using the common temperature of object and water after balancing, as depicted in stage 2 in Figure 2.16. The model of the calorimeter was used to compensate the error in water temperature caused by the heat transfer to the ambient and to estimate the equilibrium temperature at the immersion moment as shown in stage 1 in Figure 2.16. The equilibrium temperature is used to calculate the heat capacity of the object using Eq. (2.8).

Table 2.4 Specifications of the insulation material.

Parameter	Value	Unit
Total heat capacity of calorimeter+water+ object	9305	Ws/K
Time constant	40900	s
Equivalent thermal resistance to the ambient	4.4	K/W

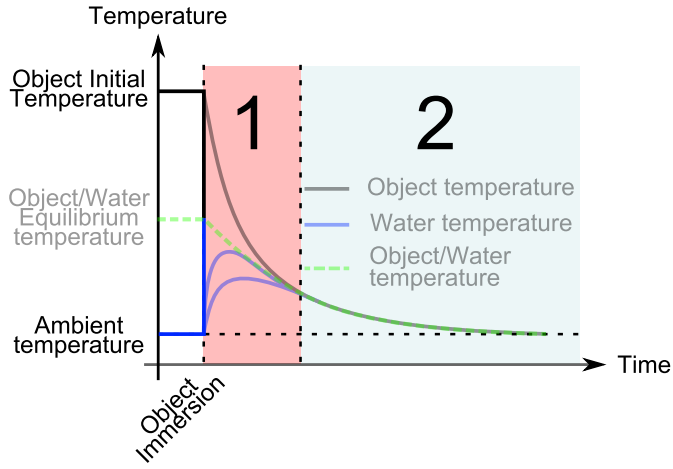

Figure 2.16 Estimation of the equilibrium point based on the thermal model of the calorimeter [38].

$$C_{obj} = \frac{C_w(T_{eq} - T_w)(t_{immersion})}{(T_{obj} - T_{eq})(t_{immersion})} \tag{2.8}$$

The heat capacity of several test objects was measured according to this procedure with the maximum relative error of 5%. Then the heat capacity of the Li-Ion cell of the same type used to build the BESS is measured using the calorimeter and a specific heat capacity of $948 Jkg^{-1}K^{-1}$ is measured.

2.3 Aging model

Battery lifetime prognosis under real operation conditions is a key issue for a reliable integration of Li-Ion batteries into electric vehicle and stationary applications. The accurate prediction of the residual capacity for a Li-Ion battery is very important for determining the available energy and power of the battery system. This information is a prerequisite for precise estimation of the driving range for electrical vehicles and for setting the warranty conditions of a battery system [58–61]. This chapter explains the aging effects of a Li-Ion battery and proposes an algorithm for the prediction of the lifetime of a Li-Ion battery based on laboratory tests.

2.3.1 Aging algorithm

The goal of the aging algorithm is to predict the lifetime of a Li-Ion cell as precise as possible by taking into account the individual stress of the past (”stress biography“). Dependencies include: temperature, SOC, number of cycles, depth of discharge (DOD). The lifetime is defined by the time span starting after manufacturing the cell and ending when $SOH = 0.8$. The algorithm calculates iteratively the reduction in SOH during the service life of the cell. The parameters of the algorithm are identified based on the laboratory tests. The SOH of a Li-Ion cell at the time instant t is denoted by Eq. (2.9).

$$\begin{aligned} SOH(t) &= SOH(t_0) - \Delta SOH(t_0 : t) \\ \Delta SOH(t_0 : t) &= \Delta SOH_{ca}(t_0 : t) + \Delta SOH_{cy}(t_0 : t) \end{aligned} \tag{2.9}$$

where $(t_0 : t) = \{t_0, t_1, t_2, \ldots, t_N = t : t_i = t_0 + i * \Delta t, i = 0 \ldots N\}$ is the time span between t_0 and t.
The calculation of reductions in SOH due to calendrical and cyclic aging ΔSOH_{ca} resp. ΔSOH_{cy} is explained in subsections 2.3.2 and 2.3.3 respectively.

2.3.2 SOH reduction due to calendrical aging

The calendrical aging of a Li-Ion cell is caused by many reasons like decomposition of electrolyte and parasitic chemical reactions between almost all components. In order to quantify the reduction of SOH caused by

calendrical aging, the time span $(t_0 : t)$ is divided into N equal time slices $\{t_0 : t_1, t_1 : t_2, \ldots, t_{N-1} : t_N\}$ with a time duration of Δt, which is small enough to ensure that the temperature $T_{cell}(t_{i-1} : t_i)$ and $SOC_r(t_{i-1} : t_i)$ are constant during each time slice. The $\Delta SOH_{ca}(t_0 : t)$ over the whole time span is calculated as the sum of reductions during each slice using Eq. (2.10):

$$\Delta SOH_{ca}(t_0 : t) = \sum_{i=0}^{N-1} \Delta SOH_{ca}(t_i : t_{i+1}) \tag{2.10}$$

The reduction of SOH during each time slice is calculated using the nonparametric function f_{ca}. The f_{ca} describes the dependency of SOH reduction on the converted time duration Δt_c at a reference temperature T_{ref} and on SOC_r, as expressed in Eq. (2.11). The values of f_{ca} are identified based on the experimental results of tests in Table 2.5. In each of these tests, a Li-Ion cell is stored with a constant SOC_r at a high temperature in order to accelerate the degradation process based on the Arrhenius law. The capacity of each cell is regularly measured according to the procedure in Figure 2.17 in order to evaluate the degradation of its SOH which is mainly caused by calendrical aging.

$$\Delta SOH_{ca}(t_i : t_{i+1}) = f_{ca}(\Delta t_c, SOC_r(t_i)) \tag{2.11}$$

The actual time duration Δt of each time slice at the cell temperature $T_{cell}(t_i)$ is converted into time duration Δt_c at a reference temperature e.g. $T_{ref} = 25\,^{\circ}C$ based on the Arrhenius law factor A using Eq. (2.12):

$$\Delta t_c = A^{\frac{\Delta T}{10}} \Delta t \quad : \Delta T = T_{cell}(t_i) - T_{ref} \tag{2.12}$$

The results of the calendrical aging test were plotted using the real test time (no conversion is applied) in Figure 2.18 for the different SOC_r and temperatures. Figure 2.18 (a) show that the $SOH = 0.8$ is already reached for some cells like L_{03} at $50\,^{\circ}C$ and L_{06} at $55\,^{\circ}C$ for $SOC_r = 100\,\%$, but for the other six cells, the SOH reduction is not yet enough to predict the future trend of each of these cells accurately.

Table 2.5 Plan of calendrical aging tests.

Cell#	Temperature[$^{\circ}C$]	SOC [%]
L01	40	100
L02	40	30
L03	50	100
L04	50	60
L05	50	30
L06	60	100
L07	60	60
L08	60	30

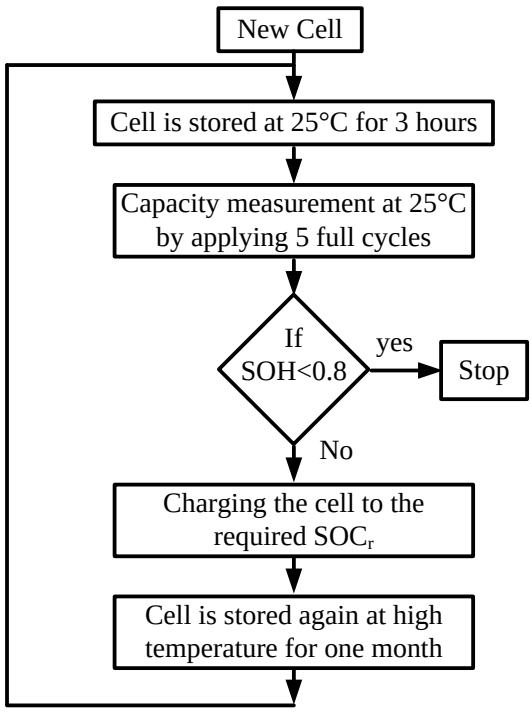

Figure 2.17 Procedure of the calendrical aging test.

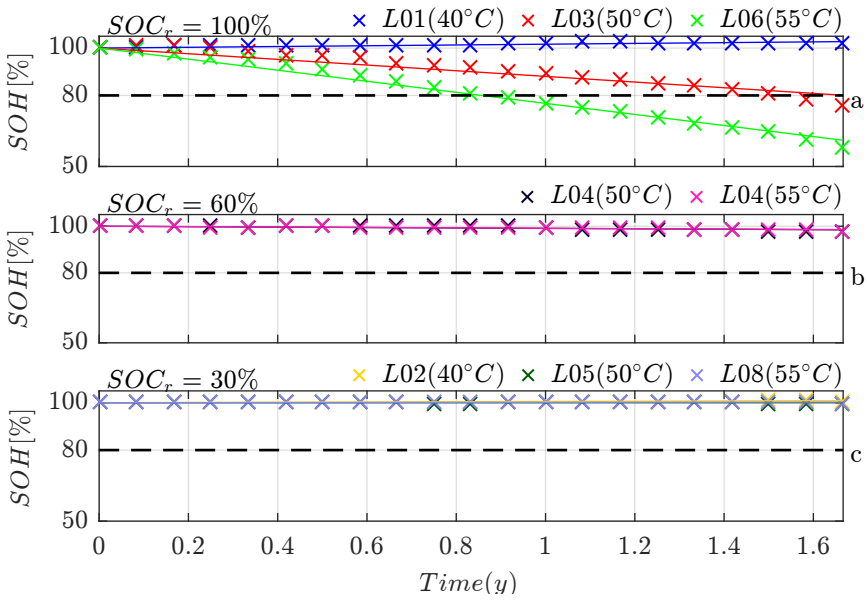

Figure 2.18 Evaluation of SOH reduction for different temperatures and SOCs using real test time.

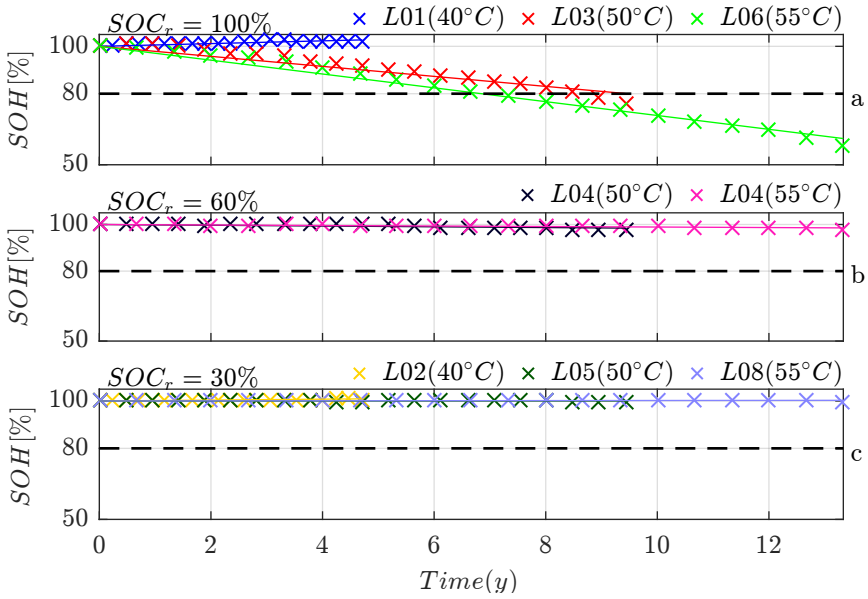

Figure 2.19 Evaluation of SOH for different temperatures and SOCs using converted time with Arrhenius law factor of 2.

These tests are still running and in the next six months, new results can be added to describe the SOH reduction for mid and low SOC_r values. The time of the experimental results in Figure 2.18 was converted using an Arrhenius law factor of $A = 2$ resulting in new SOH curves shown in Figure 2.19.

The end of lifetime as it is predicted in Figure 2.19 for a fully charged cell at $T_{ref} = 25\,°C$ is about 8 years. This value is relatively high compared with other Li-Ion cell types which were tested for other projects.

2.3.3 SOH reduction due to cycling

Cycling causes mechanical stress to the active material in the Li-Ion cell due to stretching/contraction during the intercalation process. A cycle is defined by one charge and one discharge sequence which leads to the return to the same SOC level. In order to evaluate the reduction of SOH due to cycling, the cycle lifetime of the cell is described based on laboratory tests. Then the reduction of SOH during a specific time span $(t_0 : t)$ is evaluated.

Cycle lifetime of Li-Ion cell: The cycle lifetime of a Li-Ion cell is defined by the maximum number of cycles which can be achieved using a certain DOD and SOC_{avg} until reaching $80\,\%$ of the initial capacity at the beginning of the test. It can be identified according to the following steps:

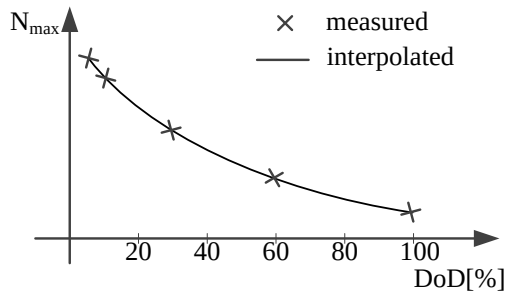

Figure 2.20 Cycle lifetime as a function of DOD value at a specific SOC_{avg}.

- Identification of the maximum number of cycles $N_{max}(DOD, SOC_{avg})$ as a function of cycle depth of discharge and the average SOC (operation point) at a controlled ambient temperature, as shown in Figure 2.20.

- Compensation of the SOH reduction due to calendrical aging during each cycling test.

The first step is achieved by running a set of cycling tests at the ambient temperature of $T_a = 25\,°C$ with different DOD_r values and with constant SOC_{avg}, as listed in Table 2.6. The dependency on the SOC_{avg} is neglected. The cycling tests with a $DOD_r < 100\,\%$ are called micro-cycling and they are performed according to the procedure shown in Figure 2.21.

In order to ensure that the SOH reduction is mainly caused by micro-cycling, a condition has to be set on the number of micro-cycles N_{mc} depending on the number of full cycles used for the capacity measurement N_{cm}, number of drift compensations N_{dc} and a ratio factor $R_{mc} = 5\,\%$ which determines the amount of SOH reduction caused by the capacity measurement and drift compensation in relation to the whole SOH reduction during the cycling test.

$$N_{mc} \geq \frac{N_{cm} \times 100\% + N_{dc} * SOC_{avg}}{R_{mc} * N_{dc} * DOD_r} \tag{2.13}$$

Table 2.6 Plan of cyclic aging tests.

Cell#	$DOD[\%]$	$SOC_{avg}[\%]$	N_{mc}	N_{dc}	N_{cm}
L15	100	50	-	-	-
L14	60	50	50	5	5
L13	30	50	100	5	5
L12	10	50	300	5	5
L11	5	50	600	5	5

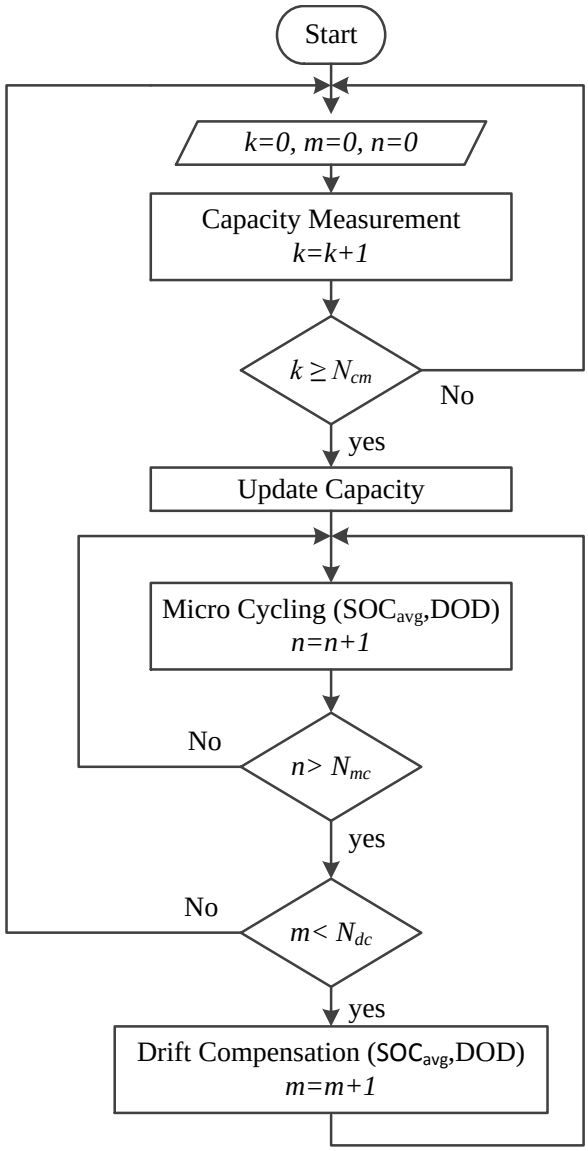

Figure 2.21 Procedure of the micro-cycling test.

Based on the experimental results of tests listed in Table 2.6, the SOH reduction was calculated as a function of the number of cycles for each test. As shown in Figure 2.22 the test with cell $L15$ reached the end of lifetime already at about 1700 full cycles. But the micro-cycling tests have to be run for more time in order to know the maximum number of cycles when the end of lifetime is reached. The micro cycles were added linearly and the SOH reduction was plotted again as a function of equivalent full cycles in Figure 2.23.

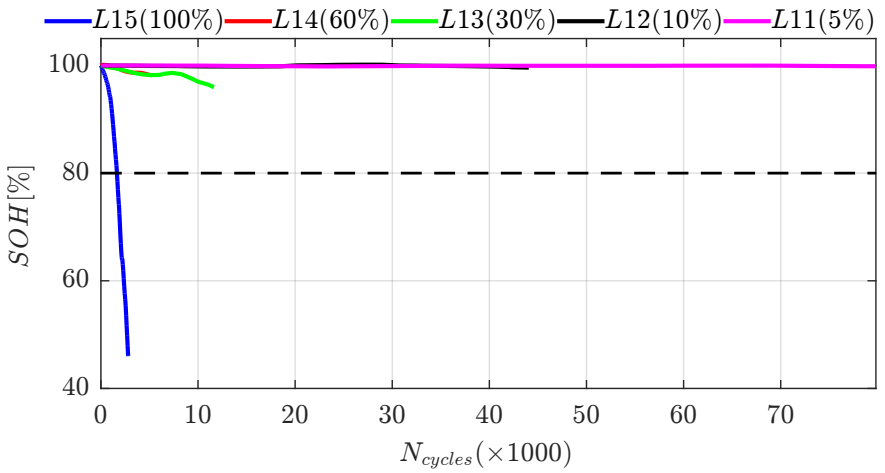

Figure 2.22 Evaluation of SOH as a function of the number of cycles for cycling tests with different DOD values.

It can be seen that equivalent full cycles with $DOD_r < 100\,\%$ cause less SOH reduction compared to the real full cycles of L_{15} cycling test.

The time duration of a cycling test with a specific DOD_r and SOC_{avg} is defined by $t_{cy}(DOD_r, SOC_{avg})$ at ambient temperature of $T_a = T_{ref}$. The SOH reduction due to calendrical aging during the cycling test can be calculated using Eq. (2.14):

$$\Delta SOH_{cacy} = f_{ca}(t_{cy}(DOD_r, SOC_{avg}), SOC_{avg}) \tag{2.14}$$

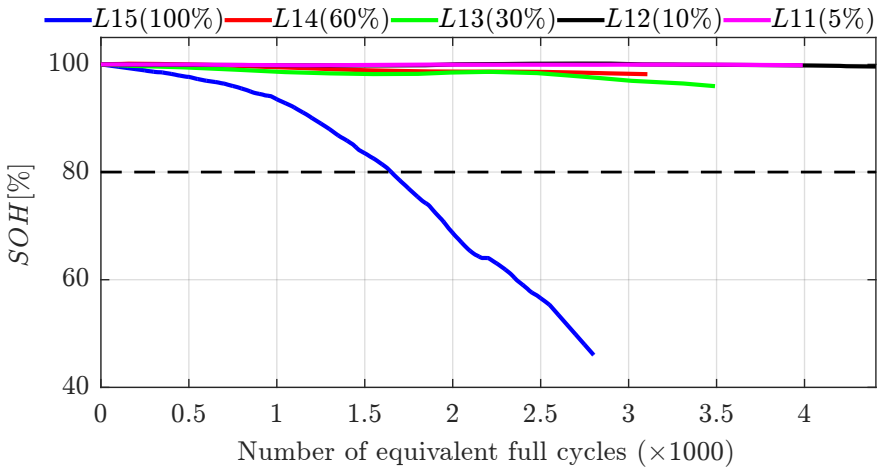

Figure 2.23 Evaluation of SOH as a function of the number of equivalent full cycles for cycling tests with different DOD values.

The reduction of SOH due to calendrical aging ΔSOH_{cacy} is converted into the number of cycles using Eq. (2.15):

$$\Delta N_{cy}(DOD_r, SOC_{avg}) = \frac{\Delta SOH_{cacy} * N_{max}(DOD_r, SOC_{avg})}{0.2} \tag{2.15}$$

The maximum number of cycles $N_{max}(DOD_r, SOC_{avg})$ is compensated by adding $\Delta N_{cy}(DOD_r, SOC_{avg})$, as shown in Eq. (2.16):

$$N^c_{max}(DOD_r, SOC_{avg}) = N_{max}(DOD_r, SOC_{avg}) + \Delta N_{cy}(DOD_r, SOC_{avg}) \tag{2.16}$$

Determination of the actual number of cycles: The history of $SOC_r(t_0 : t)$ is used as an input to the rain flow counting (RFC) method which identifies and counts the individual stress cycles. The output of the RFC method is a table $N_{cy}(DOD_i)$ containing the number of cycles for each DOD and their corresponding average SOC_r [62–64]. The total reduction of SOH due to cycling can be calculated then using Eq. (2.17):

$$\Delta SOH_{cy} = 0.2 * \sum_{i=1}^{M} \frac{N_{cy}(DOD_i)}{N^c_{max}(DOD_i, SOC_{avg})} \tag{2.17}$$

where:
M: number of DOD ranges
DOD_i: DOD range with index i.

2.4 Conclusion

An accurate battery model has been developed for Li-Ion battery in order to optimally integrate it in simulations of the BESSs. The tests setup and the procedure on how to identify the model parameters of a Li-Ion were explained in detail. New approaches for measuring the ohmic resistance and for identifying the parameters of the LF model were introduced introduced in section 2.1. Then the parameters of the electrical model were shown in Figures 2.9, 2.10 and 2.11 for LF and HF models respectively. The influence of the cell model on the electrical dynamics of the BESS was evaluated in [PAPER- IV] and the following results were made:

1. Battery ECM with one time constant (OTC) does not represent the fast battery's dynamics accurately mainly when the battery is aged. Therefore, at least two time constants (TTC model) are needed in order to represent the slow and fast dynamics of the battery over the whole service life of the cell ([PAPER- IV] Figure 4).

2. Temperature deviation within the range of $20\,°C$ to $35\,°C$ as well as aging has a significant effect on the voltage drop at the dc-side and needs to be taken into account.

3. The SOC, the aging and the temperature have no significant effect on the total harmonic distortion (THD) on the grid side ([PAPER- IV] Table II).

4. In order to calculate correctly the harmonics of I_{bat}, it is required to extend the usual ECM for low frequencies by an HF model with one time constant (1RL-model).

5. The effects of SOC, cell temperature and aging on the harmonic content of I_{dc} and I_{bat} can be neglected.

The first step on developing a thermal model of Li-Ion cell was done in section 2.2 by measuring its heat capacity using a students made calorimeter.
Since that aging influences the electrical dynamics of Li-Ion cell significantly, an aging algorithm for prediction of service life of Li-Ion battery using laboratory tests was also introduced in section 2.3. Furthermore, the actual results of calendar and cyclic aging results were shown in Figures 2.19 and 2.23 respectively.

It should be underlined that our results are only valid for the cells used in this investigation. Other cells might have different behavior.

3 MODELING OF BATTERY ENERGY STORAGE SYSTEM (BESS)

3.1 Introduction

In the frame of the research project IREN2 (Future Oriented Electricity Grids for Integration of Renewable Energy Systems) a microgrid has been set up in the village of Wildpoldsried in the south of Germany [65]. The microgrid consists of renewable energy sources, a stationary 300kVA/170kWh battery system with Lithium Nickel Cobalt Oxide (NCO) - Lithium Titanate cells, a 100kVA Genset with vegetable oil fueling for secondary control, a 500kVA back to back station between the 20kV and the 400V grid to emulate volatile photovoltaic generation as well as a battery of infinite energy or to create real disturbances. Further, a 3x 50kW controllable unsymmetrical load bank is available. One of the important goals of IREN2 is to develop a mathematical model of the BESS for the two operation modes of a microgrid, i.e. the synchronous mode and the island mode. In the synchronous mode BESS synchronizes itself to an external grid and tracks given reference setpoints P_{ref} and Q_{ref}, whereas fast responses are avoided in order not to cause large disturbances to the grid. All the details about the mathematical modeling of BESS in this operation mode are described in [66].

In the island operation mode, the droop control forms a decentralized control method which is based on the communication between the different DGs over frequency and voltage providing an expandable system without extra communication requirements [67]. This approach implies that every DG runs in the GF mode and regulates its active resp. reactive power output depending on the frequency resp. voltage [68].

The next section 3.2 provides a description of the electrical and control structure of the BESS. Section 3.3 deals with setting up a detailed mathematical model which describes the electro dynamical behavior of the real system. Section 3.4 shows the verification of the detailed model by a comparison with the measurement results of the real system. Since that the detailed model is very complex and is causing very high computation time on a computer, section 3.5 focuses on simplification of the detailed model resulting in a simplified model suitable for the simulation of the BESS as a subsystem in a microgrid consisting

also of other power components. The simplified model is validated using simulation results of the detailed model in Section 3.6. Section 3.7 concludes this chapter.

3.2 Structure of the BESS

During operation, some unexpected Li-Ion cell issues had to be solved by a complete replacement of the battery modules. The new cells were available with different geometry having the consequence that only three battery strings with approximately the same total energy could be set up instead of six in the original version. Therefore, every two inverters of the original system had to be connected to one battery string, resulting in a much more complex electrical structure because extra filters and isolating transformers were necessary. The modified structure affects the dynamic behavior that is discussed later in section 3.4.

3.2.1 Electrical structure

As shown in Figure 3.1, the BESS consists of three Li-Ion batteries bat1, bat2 and bat3 which can be operated independently. Each battery is connected to two 3-phase inverters through an electromagnetic interference (EMI) filter for protecting the battery management system (BMS) from the electrical noise due to the unsynchronized switching of the two parallel inverters. Every 3-phase inverter has a rated power of $55\,kVA$ and is followed by an LCL filter in order to reduce the current harmonics injected into the grid. The first three inverters inv1, inv2 and inv3 are connected to the first matching transformer (MT_1) and the next three inverters inv4, inv5 and inv6 are connected to the second matching transformer (MT_2). The three phase two-winding matching transformers are used to adapt the inverters' low output voltage to the grid voltage. Two isolating transformers IT_1, IT_2 are used to avoid circulating currents in the circuit of inv1 and inv6, and of inv2 and inv5 which are connected to the same dc circuit.

3.2.2 Control structure

The input of the control structure are the 3-phase voltage and current measured at the output of the LCL filter. Based on these measurements, the output active and reactive power of the inverter are calculated and fed into the droop controller. The droop controller is composed mainly of two parts. The first part adjusts the inverter frequency based on the active power, the new frequency set-point $\tilde{f}$ is calculated based on the P/f droop formula as shown in Figure 3.2, then $\tilde{f}$ is smoothed using a low pass filter (LPF) with a time constant T_c, resulting in the inverter actual frequency f, which is integrated to obtain the actual angle θ. The second part of the droop controller regulates the amplitude of the inverter voltage depending on the inverter output reactive power. The new set-point of

the voltage amplitude $\tilde{V}$ is calculated using the Q/V droop formula as shown in Figure 3.2. The voltage $\tilde{V}$ is smoothed using a similar LPF filter as it is the case in the first part. The filtered voltage amplitude $\hat{V}$ is used as reference for the proportional-integral (PI) controller which regulates the actual inverter voltage amplitude V_{act} to match the reference voltage $\hat{V}$.

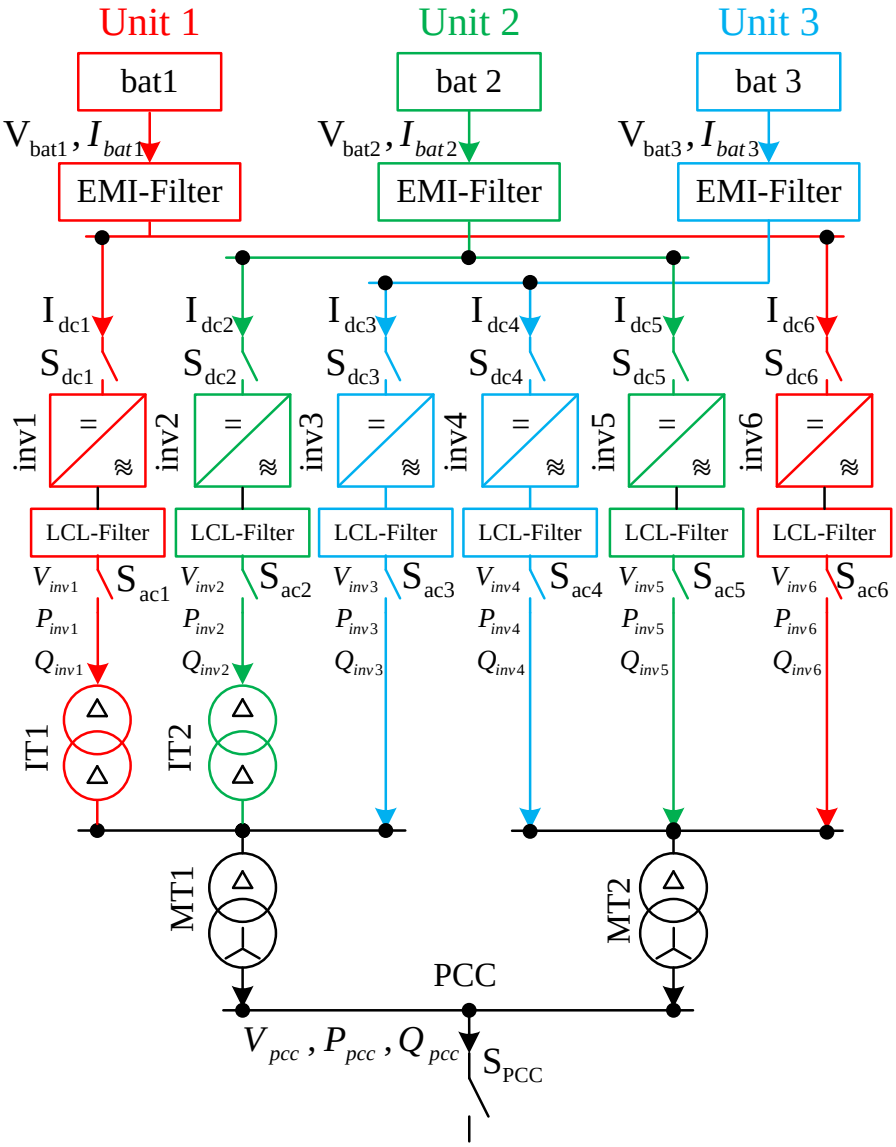

Figure 3.1 Block diagram of the BESS electrical structure

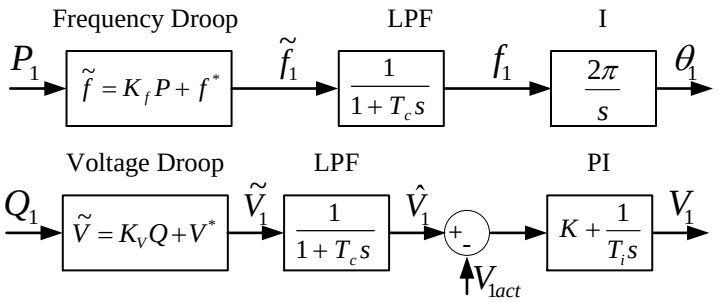

Figure 3.2 Structure of the frequency and voltage droop control

3.3 Detailed model of the BESS

The detailed model considers the dynamics of dc and ac sides and the switching operation of the IGBTs; thus it is appropriate to analyze short time transients and harmonic content. Starting from the dc side, the battery model is implemented by upscaling the Li-Ion cell's model described in section 2.1. The LCL and EMI filters are modeled using their equivalent circuits shown in Figure 3.3 (a) and (b) respectively. The parameters are given in Table 3.1. The IGBTs are modeled using a two-state resistive switches. The transformers are modeled using the standard 3-phase 2-winding transformer model in PSCAD. The specifications of both matching and isolating transformers are given in Table 3.2.

The modular structure of the BESS enables dividing the BESS into three independent units U1(bat1, inv1, inv6 and IT1), U2(bat2, inv2, inv5 and IT2) and U3(bat3, inv3 and inv4) shown in red, green and blue in Figure 3.1. U1 and U2 have an identical structure and they differ from U3 by having an isolating transformer in series to the output of inv1 and inv2 respectively. Therefore, two detailed models are only needed for evaluating the electrical dynamics of the BESS .

3.4 Validation of the detailed model

The detailed model was verified using real measurements of the BESS, where a $60\,kW$ ohmic load step is applied on both U1 and U3 at the PCC.

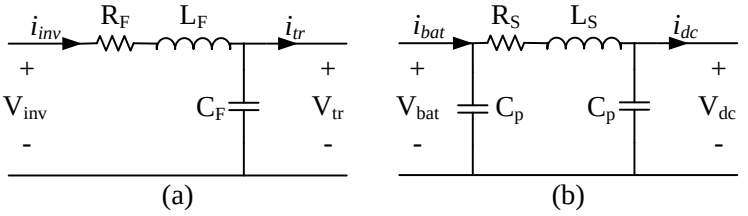

Figure 3.3 Equivalent circuit of: a) LCL filter and b) EMI filter.

Table 3.1 Parameters of the LCL and EMI filter

LCL-Filter equivalent circuit parameters	**Value**
Serial inductance L_F	$160\,\mu H$
Serial resistance R_F	$16.4\,m\Omega$
Parallel capacitor C_F	$3.5\,\mu F$
EMI filter equivalent circuit parameters	**Value**
Serial inductance L_S	$0.1\,\mu H$
Serial resistance R_S	$0.1\,m\Omega$
Parallel capacitor C_P	$8\,\mu F$

Table 3.2 Specifications of the matching and the isolating transformers.

257V/400V Δ-Y Matching transformer	**Value**
Rating [$S_{r,LV}$]	$165\,kVA$
u_k	4.3%
P_{copper}	$0.008484\,pu$
$P_{no-load}$	$0.002424\,pu$
260V/260V Δ-Δ Isolating transformer	**Value**
Rating [$S_{r,MV}$]	$55\,kVA$
u_k	$3.73\,\%$
P_{copper}	$0.021545\,pu$
$P_{no-load}$	$0.0029091\,pu$

The experiments were made with relatively unused batteries at ambient temperature of $25\,^{\circ}C$ and relative state of charge around $50\,\%$. The voltages and currents were measured at three different points in order to evaluate the goodness of the detailed models of U1 and U3. The first evaluation point (EP) is the dc side of each unit. At this point the dc voltages and currents are used directly for the comparison. The second EP is at the inverter output and the third EP is at the PCC. For the second and third EPs, the amplitude of voltage phasor, frequency, active and reactive power were calculated and used for the evaluation. Active and reactive power were calculated with respect to generator reference-arrow system (GRS).

Figures 3.8, 3.6 and 3.4 show the comparison between detailed model's signals of U1 and corresponding measurements. These figures show a fluctuation of the active and reactive power at the moment of switching the load on due to the delay between the different phases of the ohmic load which results in a asymmetrical loading of U1 that finally causes these fluctuations. After these fluctuations as can be seen in Figure 3.6 (b,c) slow oscillations in active and reactive power signals occurred due to the different serial impedances between inv1, inv6 and the PCC.

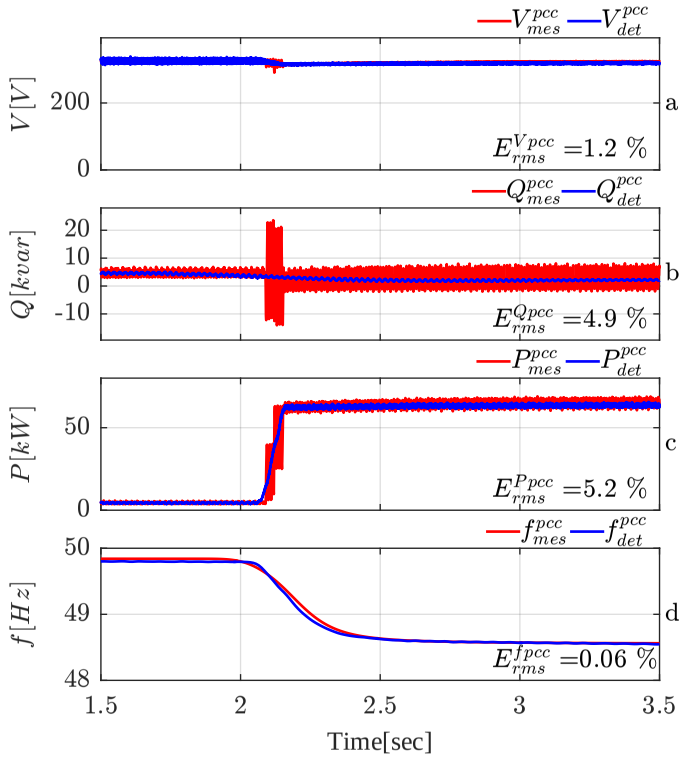

Figure 3.4 U1: Comparison between detailed model and measurements at PCC for: a) amplitude of voltage phasor; b) reactive power; c) active power; d) frequency.

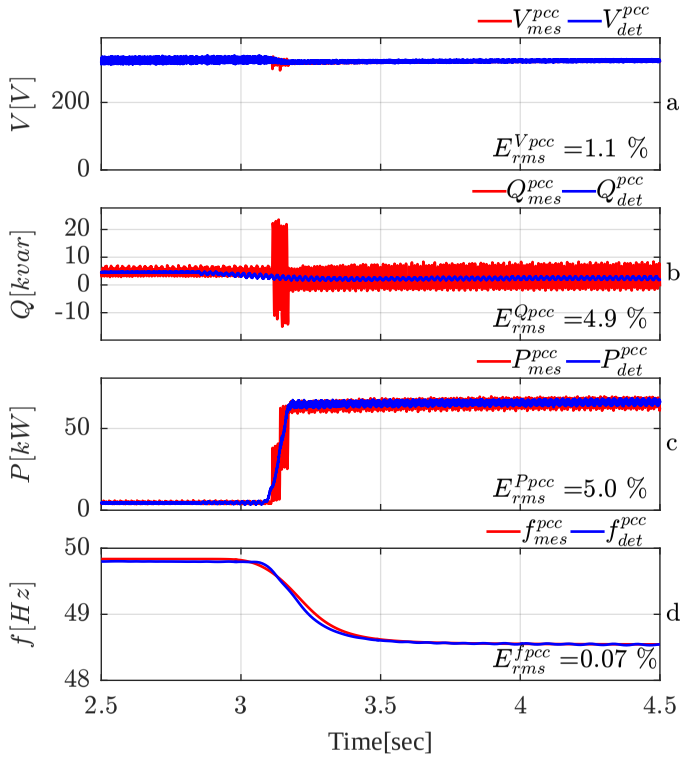

Figure 3.5 U3: Comparison between detailed model and measurements at PCC for: a) amplitude of voltage phasor; b) reactive power; c) active power; d) frequency.

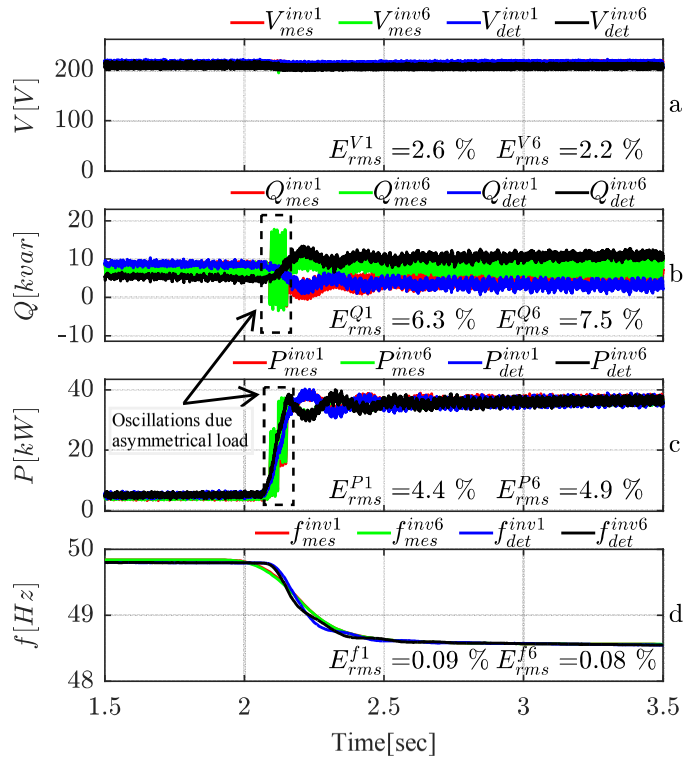

Figure 3.6 U1: Comparison between detailed model and measurements at the ac side of inv1 and inv6 for: a) amplitude of voltage phasor; b) reactive power; c) active power; d) frequency.

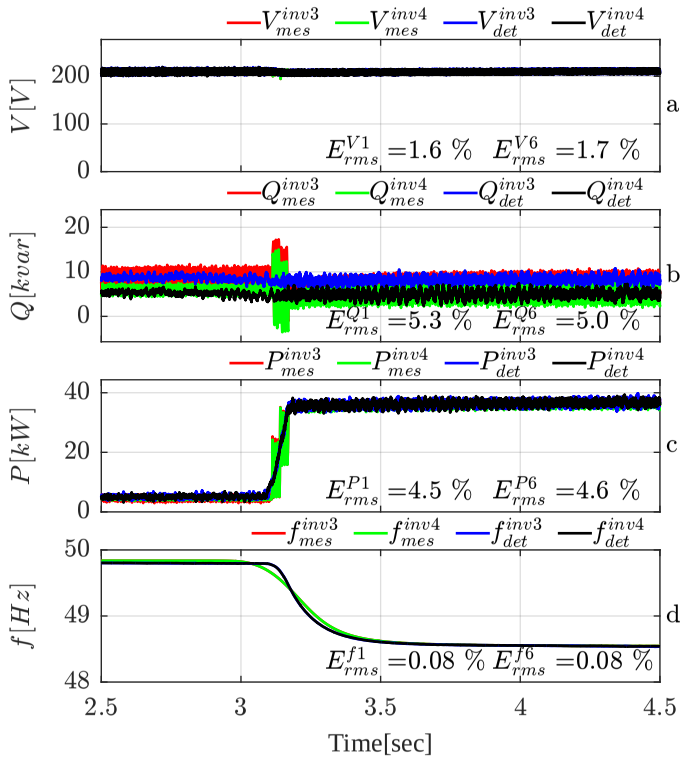

Figure 3.7 U3: Comparison between detailed model and measurements at the ac side of inv3 and inv4 for: a) amplitude of voltage phasor; b) reactive power; c) active power; d) frequency.

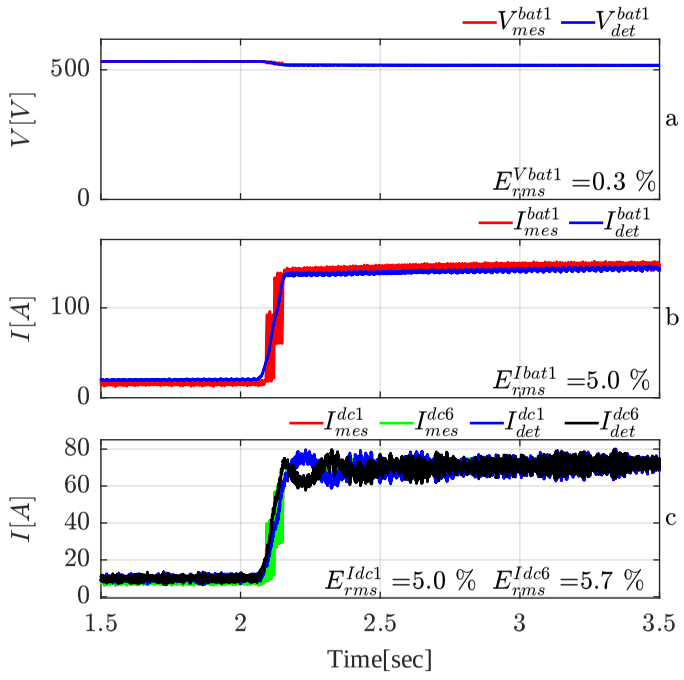

Figure 3.8 U1: Comparison between detailed model and measurements for: a) battery voltage; b) battery current; c) dc currents of inv1 and inv6.

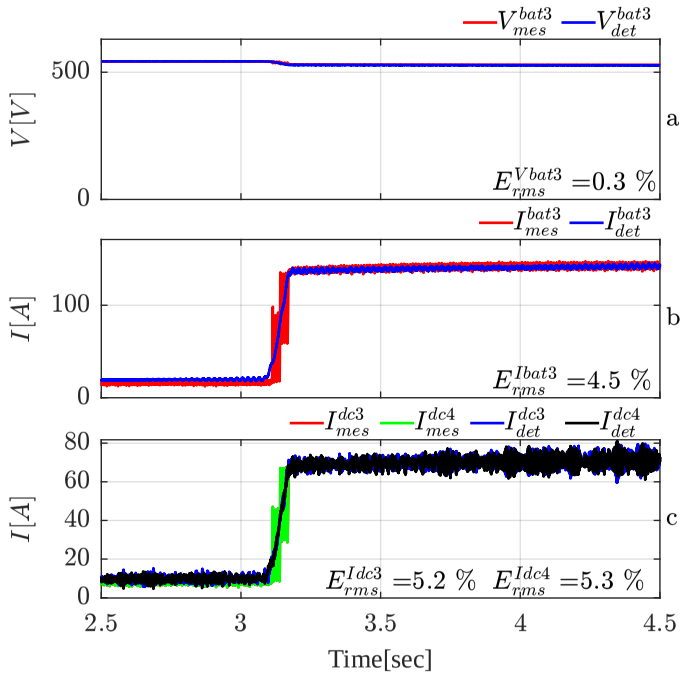

Figure 3.9 U3: Comparison between detailed model and measurements for: a) battery voltage; b) battery current; c) dc currents of inv3 and inv4.

Figures 3.9, 3.7 and 3.5 show the comparison between detailed model signals of U3 and measurements. These figures show only the fluctuations due to the switching of the load but they show no slow oscillations because inv3 and inv4 have the same serial impedance to the PCC. The oscillations in active and reactive power were analyzed mathematically in chapter 4. The numbers displayed on the figures show the relative error values which are calculated according to Eq. (3.1):

$$E_{rms}(X_1, X_2)[\%] = \frac{rms(X_1 - X_2)}{max(X_1, X_2)}.100 \tag{3.1}$$

3.5 Simplified model of the BESS

Due to the complex structure of the BESS the detailed model is not suitable for long time simulations when the BESS is integrated with other microgrid components as it is the case in [PAPER- VIII]. Therefor a simplified model is required which represents the fundamental dynamics of the original system and reduces the complexity of the detailed model. The simplification procedure was performed according to the following steps:

1. The dc side dynamics are ignored as it does not influence the ac side dynamics as it is proofed in [PAPER- IV].
2. Each 3-phase inverter is modelled using an ideal 3-phase voltage source connected to the serial impedance of the LCL filter.
3. All the transformers are replaced with their equivalent serial and parallel impedances $(Z_s^{MT} and Z_s^{IT1})$ resp. $(Z_p^{MT}, Z_p^{IT1} and Z_p^{IT2})$, referred to the high voltage side of matching transformers.
4. The control structure stays the same as for the simplified model.

The simplified electrical structures of U1 and U3 are shown in Figure 3.10 and Figure 3.11 respectively.

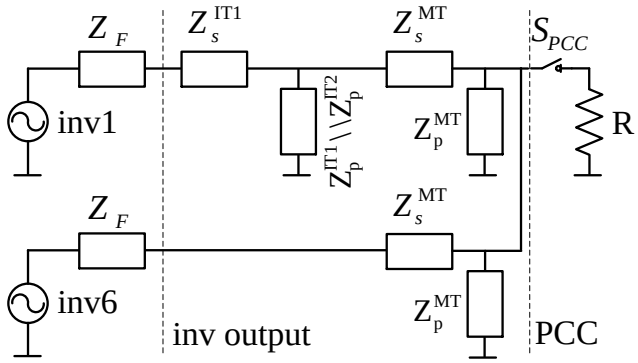

Figure 3.10 Simplified model of Unit 1.

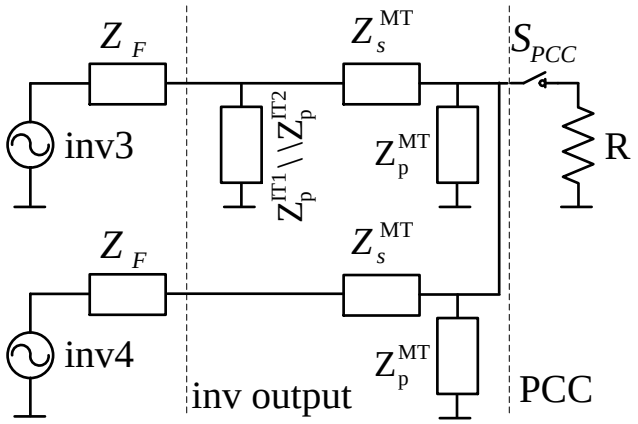

Figure 3.11 Simplified model of Unit 3.

3.6 Validation of the simplified model

In this section, the simulation results of the simplified model are compared with those of detailed model. The compared signals are plotted in Figure 3.14 and Figure 3.12 for U1 at inverter output and at PCC respectively. The simplified model shows also the oscillations in active and reactive power signals similar to the detailed model. Figures 3.15 and 3.13 demonstrate the comparison between the simplified and detailed model for U3 at inverter output and at PCC respectively. The comparison results show a good coincidence between the simplified and detailed model of U3.

3.7 Conclusion

The Li-Ion battery model was integrated with the other components in the BESS like: EMI filter, IGBTs, LCL filter and transformers to establish a detailed model that describes the electrical dynamics of the BESS accurately. The detailed model was used to analyze the short time transients and to evaluate the harmonic contents of dc and ac signals. Figures 3.4, 3.5, 3.6, 3.7, 3.8 and 3.9 show a good coincidence with relative error less than 5 % between the measurements and the simulation results for the detailed model of U1 and U3, respectively. The high error values for dc currents, active power and reactive power are due to the asymmetrical loading at the beginning of the load step.
The complexity of the detailed model is reduced by considering the fundamental electrical dynamics of the BESS. The comparison between the simulation results of the detailed and the simplified models in Figures 3.12, 3.13, 3.14 and 3.15 confirms that using the simplified model, the fundamental dynamics are accurately represented for U1 resp. U3.

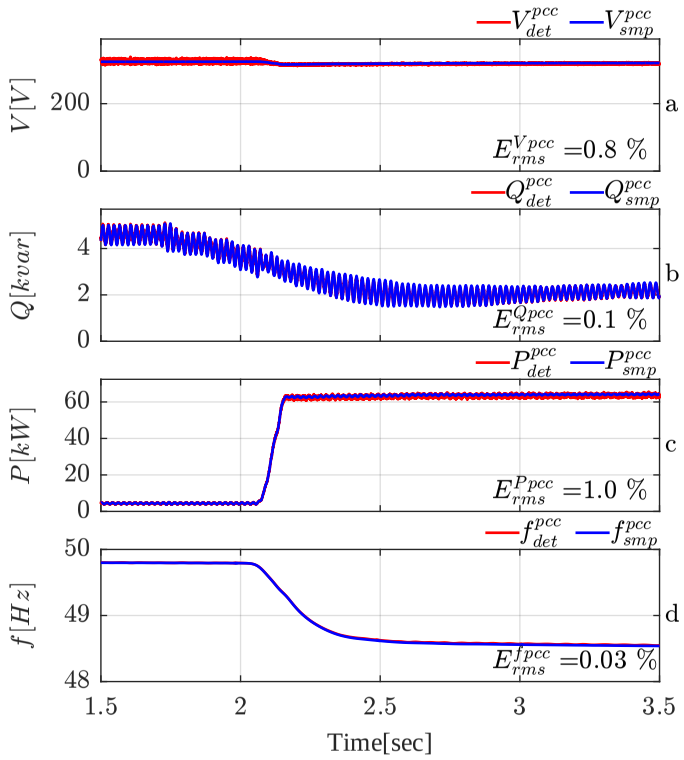

Figure 3.12 U1: Comparison between detailed model and measurements at PCC for: a) amplitude of voltage phasor; b) reactive power; c) active power; d) frequency.

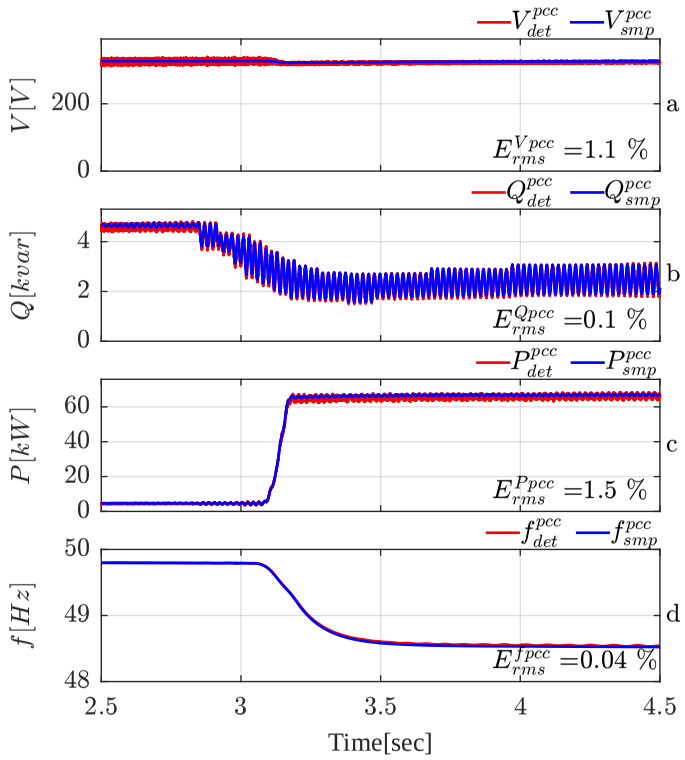

Figure 3.13 U3: Comparison between detailed model and measurements at PCC for: a) amplitude of voltage phasor; b) reactive power; c) active power; d) frequency.

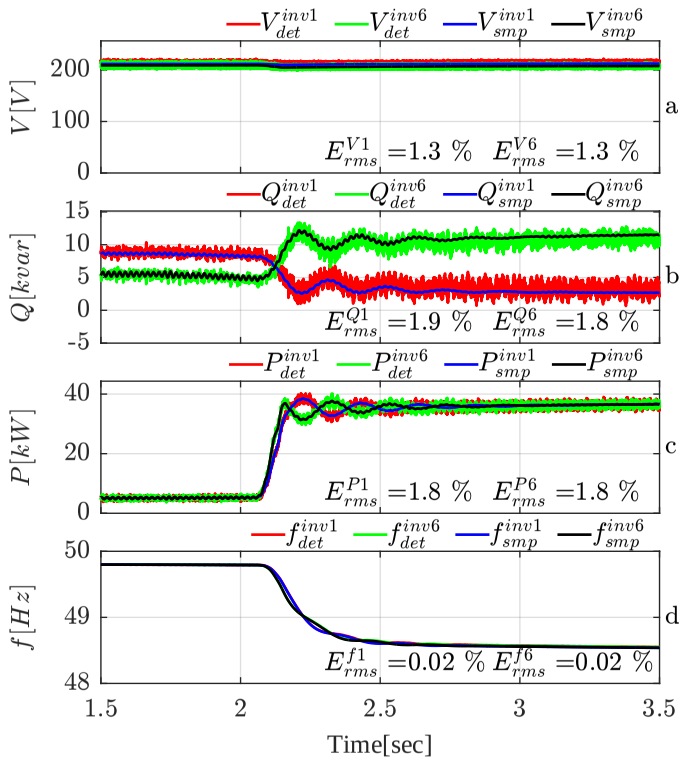

Figure 3.14 U1: Comparison between detailed and simplified model at the ac side of inv1 and inv6 for: a) amplitude of voltage phasor; b) reactive power; c) active power; d) frequency.

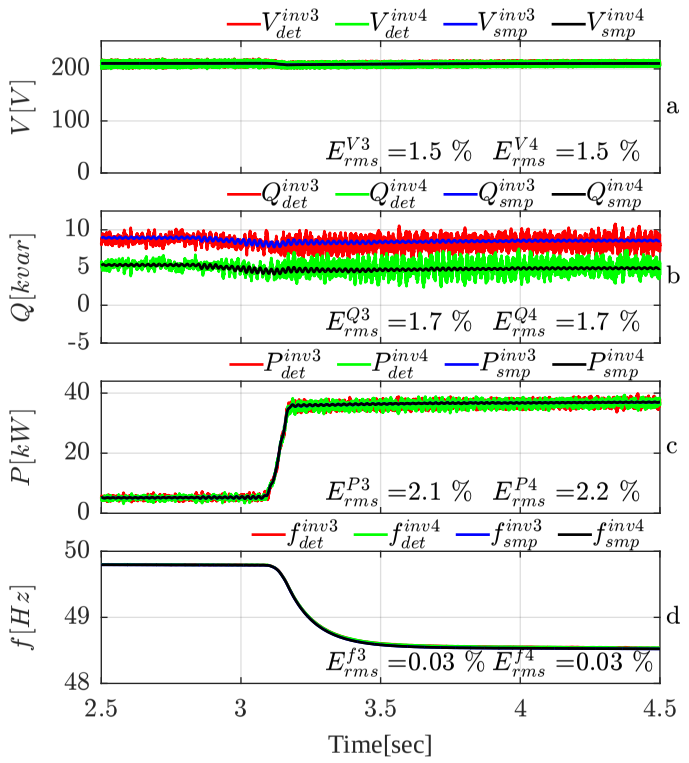

Figure 3.15 U3: Comparison between detailed and simplified model at the ac side of inv3 and inv4 for: a) amplitude of voltage phasor; b) reactive power; c) active power; d) frequency.

4 STABILITY ANALYSIS OF THE BESS IN A MICRO-GRID

4.1 Introduction

This chapter focuses on the theoretical and experimental analysis of small signal stability of a microgrid consisting of one unit of a stationary BESS and an 3-phase ohmic load connected at PCC. The microgrid including electrical and control structures is explained in detail in section 4.2. The small signal stability of parallel inverters with a non-standard control structure is firstly analyzed using the quasi steady state (QSS) approach in section 4.3. The real part of the system's eigenvalues calculated using the QSS approach shows no dependency on the droop gains, i.e. no information about microgrid stability can be derived. Hence, a new approach based on DPM is introduced in section 4.4, which enables us to take the dynamic effects of the electrical elements into consideration without having to go through the complex differential equations. A comparison between the results of both approaches is shown in section 4.5 and an evaluation of system stability dependency on control and load parameters is also discussed.

4.2 Microgrid structure

As shown in Figure 3.10, the microgrid consists of U1 and an 3x 50kW unsymmetrical load bank connected at the PCC. The U1 is selected as it represents the basic unit in the BESS, where the impedances between parallel connected inverters and the PCC are unequal.

The simplified model of U_1 has to be prepared before using it for the stability analysis. In the first step the parallel impedances in the simplified model of U_1 are neglected. In the second step the serial impedances are added together resulting in an equivalent impedance for every inverter. In the last step the model structure is generalized by resetting the indexes of inverters inv1 and inv6 to inv1 and inv2, respectively. The simplified electrical structure shown in Figure 4.1 together with the control structure of each inverter shown in Figure 3.2 covers the whole microgrid dynamics required for the stability analysis.

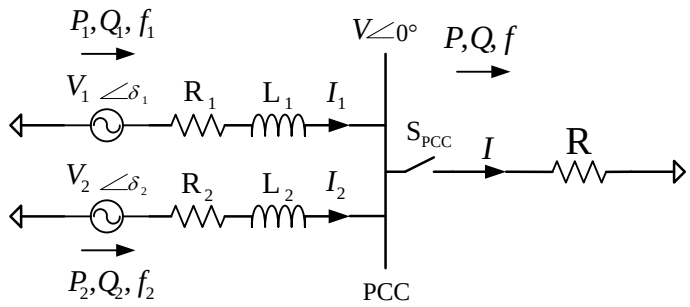

Figure 4.1 Single line diagram of the equivalent circuit model of U1 used for stability analysis.

4.3 Quasi steady state approach

This approach is used traditionally to analyze the stability of a synchronous machine connected to a stiff ac system. It was firstly used for stability analysis of a single phase inverters connected to a stiff ac system in [69]. Later it has been applied for the stability analysis of parallel connected 3-phase inverters [9]. The simplicity of this approach makes it the first choice for the stability analysis of a microgrid; however, this approach shows some issues regarding stability dependency on droop gains discussed in [70, 71]. In this section, the stability analysis of two inverters connected in parallel to an ohmic load, as shown in Figure 4.1, using the QSS approach is recalled. This approach implies that the system should satisfy the following conditions:

1. Balanced 3-phase sinusoidal system
2. Fundamental frequency is only considered
3. Power change in the system is much slower than the fundamental frequency
4. No large changes in the voltage amplitude ($V_1 \approx V_2 \approx V$)
5. Droop parameters are the same for Inv1 and Inv2 (Extension of the solution for different droop parameters is also possible)

The voltages at the output of inverters and PCC are defined by their space phasors in Eq. (4.1), where V_1, V_2 and V are the time varying voltage amplitudes and θ_1, θ_2 and θ are the phasor angles of inv1, inv2 resp. PCC. The angle differences δ_1 and δ_2 defined in Eq. (4.2) play an important role for determining the power flow in the system.

$$\overrightarrow{V_1} = V_1 e^{j\theta_1}, \quad \overrightarrow{V_2} = V_2 e^{j\theta_2} \quad \text{and} \quad \overrightarrow{V} = V e^{j\theta} \tag{4.1}$$

$$\delta_1 = \theta_1 - \theta \quad \text{and} \quad \delta_2 = \theta_2 - \theta \tag{4.2}$$

The complex apparent power $\underline{S}_1$ at the output of inv1 in steady state is defined according to Eq. (4.3) in two parts, the real part defines the active power and the imaginary part defines the reactive power:

$$\underline{S}_1 = P_1 + jQ_1 = \frac{3}{2}\overrightarrow{V_1}.\overrightarrow{I_1}^* = \frac{3(V_1^2 - V_1 V e^{j(\theta_1-\theta)})\underline{Z}_1}{2Z_1^2} \tag{4.3}$$

Using Eq. (4.2) and the fact that $\underline{Z}_1 = R_1 + jX_1$, the active and reactive power can be then calculated in the quasi steady state using Eq. (4.4):

$$\begin{aligned} P_1 &= \frac{3}{2}\frac{R_1V_1^2 - R_1V_1Vcos(\delta_1) + X_1V_1Vsin(\delta_1)}{R_1^2 + X_1^2} \\ Q_1 &= \frac{3}{2}\frac{X_1V_1^2 - X_1V_1Vcos(\delta_1) + R_1V_1Vsin(\delta_1)}{X_1^2 + X_1^2} \end{aligned} \tag{4.4}$$

Since $\delta_1, \delta_2 << 1$ for the whole power range of the system, the approximation of $cos(\delta_1) \approx 1$ and $sin(\delta_1) \approx \delta_1$ is valid for δ_1 resp. δ_2. Based on the 4^{th} condition that ($V_1 \approx V_2 \approx V$) leading to active and reactive power formulas in Eq. (4.5) for inv1. Similar ones can be obtained for inv2.

$$\begin{aligned} P_1 &= \frac{3}{2}\frac{R_1V_1^2 - R_1V_1V + X_1V_1V\delta_1}{R_1^2 + X_1^2} = \frac{3X_1V_1^2\delta_1}{2Z_1^2} \\ Q_1 &= \frac{3}{2}\frac{X_1V_1^2 - X_1V_1V + R_1V_1V\delta_1}{X_1^2 + X_1^2} = \frac{-3R_1V_1^2\delta_1}{2Z_1^2} \end{aligned} \tag{4.5}$$

4.3.1 Frequency control

Based on the control diagram of the inverter frequency shown in Figure 3.2 the differential equation of the frequency f_1 at the output of the LPF can be written in Eq. (4.6), by substituting P_1 from Eq. (4.5) yields to Eq. (4.7) where f^* is the no-load frequency.

$$\begin{aligned} \dot{f}_1 &= -\omega_c f_1 + \omega_c \widetilde{f}_1 \\ \dot{f}_1 &= -\omega_c f_1 + \omega_c(K_f P_1 + f^*) \end{aligned} \tag{4.6}$$

where $K_f = -\frac{1}{K_p}$ and $\omega_c = \frac{2\pi}{T_c}$.

$$\dot{f}_1 = -\omega_c f_1 + \frac{3\omega_c K_f X_1}{2Z_1^2}V_1^2\delta_1 + \omega_c f^* \tag{4.7}$$

The steady state frequency f is the average value of both f_1 and f_2 weighted by their droop gains as it is given in Eq. (4.8):

$$f = \left.\frac{K_{p1}f_1 + K_{p2}f_2}{K_{p1} + K_{p2}}\right|_{K_{p1}=K_{p2}} = \frac{f_1 + f_2}{2} \tag{4.8}$$

The change of angles θ_1, θ_2 and θ is determined by their frequencies f_1, f_2 and f respectively through the differential equations in Eq. (4.9), then the change of the angle differences δ_1 and δ_2 can be obtained directly by calculating the derivative of Eq. (4.2) with respect to time and using Eq. (4.9) leading to Eq. (4.10).

$$\dot{\theta}_1 = 2\pi f_1, \quad \dot{\theta}_2 = 2\pi f_2 \quad \text{and} \quad \dot{\theta} = 2\pi f \tag{4.9}$$

$$\dot{\delta}_1 = \frac{2\pi(f_1 - f_2)}{2} = -\dot{\delta}_2 \tag{4.10}$$

4.3.2 Voltage control

The closed loop of the voltage control of inv1 consists mainly of three stages as shown in Figure 3.2, In the first stage, the reactive power Q_1 is used to calculate the voltage amplitude $\tilde{V}_1$, this output voltage is smoothed in the second stage using first order LPF giving out $\hat{V}_1$, the reference value for the PI controller. In the third stage, the output of PI V_1 tracks the reference voltage $\hat{V}_1$. The output of the PI V_1 is used combined with angle θ_1 from the frequency control to calculate the output voltage phasor $\overrightarrow{V_1}$. The dynamics of LPF can be expressed in Eq. (4.11), the value of the reactive power Q_1 can be taken from Eq. (4.5) and be substituted in Eq. (4.11), leading to Eq. (4.12). Since that the proportional gain of the PI is zero, the dynamics of the PI can be described by Eq. (4.13) where T_i is the integral time constant:

$$\begin{aligned} \dot{\hat{V}}_1 &= -\omega_c \hat{V}_1 + \omega_c \tilde{V}_1 \\ \dot{\hat{V}}_1 &= -\omega_c \hat{V}_1 + \omega_c K_v Q_1 + \omega_c V^* \end{aligned} \tag{4.11}$$

where $K_v = -\frac{1}{K_q}$.

$$\dot{\hat{V}}_1 = -\omega_c \hat{V}_1 - \frac{3\omega_c K_v R_1}{Z_1^2} V_1^2 \delta_1 + \omega_c V^* \tag{4.12}$$

$$\dot{V}_1 = \frac{1}{T_i}\hat{V}_1 - \frac{1}{T_i} V_1 \tag{4.13}$$

Differential equations Eq. (4.12) and (4.13) describe the dynamics of the voltage closed loop for inv1. Similar differential equations can be also obtained for inv2.

4.3.3 System linearization

The four differential equations in Eq. (4.7), Eq. (4.10), Eq. (4.12) and Eq. (4.13) of inv1 are repeated for inv2 and grouped together in a vector form in Eq. (4.14)

building a nonlinear state space model of the system.

$$\begin{aligned} \dot{X}_{QSS} &= H(X_{QSS}, u) \\ y &= G(X_{QSS}, u) \end{aligned} \tag{4.14}$$

where $X_{QSS} = [f_1, \delta_1, \hat{V}_1, V_1, f_2, \delta_2, \hat{V}_2, V_2]^T$ is the state vector and $u = [f^*, V^*]^T$ is the input vector. The state vector QSS is chosen so that the system can be easily extended to more than two inverters. The nonlinear system in Eq. (4.14) is linearized for small perturbations ΔX_{QSS} and Δu at an equilibrium point (X^0_{QSS}, u_0) which fulfills the condition Eq. (4.15), resulting in the linearized system defined by Eq. (4.16) [72].

$$\dot{X}^0_{QSS} = H(X^0_{QSS}, u_0) = 0 \tag{4.15}$$

Table 4.1 Electrical and control parameters of U1.

$R_1[\Omega]$	$X_1[\Omega]$	$R_2[\Omega]$	$X_2[\Omega]$	$T_c[s]$	$T_i[s]$
0.112	0.253	0.048	0.163	0.15	0.5

where $X^0_{QSS} = [f_{10}, \delta_{10}, \hat{V}_{10}, V_{10}, f_{20}, \delta_{20}, \hat{V}_{20}, V_{20}]^T$ and $u_0 = [f^*_0, V^*_0]^T$ are determined by solving the set of nonlinear equation in Eq. (4.15) numerically for the system parameters given in Table 4.1, specific droop gains (K_p, K_q), and specific total load active and reactive power P resp. Q, e.g., when $P = 1kW$, $Q = 0kvar$, $K_p = 25kW/Hz$ and $K_q = 2.5kvar/V$ this leads to X^0_{QSS} given in Table 4.2.

Table 4.2 The X^0_{QSS} calculated for $P = 1kW$, $Q = 0kvar$, $K_p = 25kW/Hz$ and $K_q = 2.5kvar/V$.

i	$f_{i0}[Hz]$	$\delta_{i0}[rad]$	$\hat{V}_{i0}[V]$	$V_{i0}[V]$
1	49.98	0.00095	326.7	326.7
2	49.98	0.00055	326.7	326.7

$$\begin{aligned} \Delta\dot{X}_{QSS} &= A_{QSS}\Delta X_{QSS} + B_{QSS}\Delta u \\ \Delta y_{QSS} &= C_{QSS}\Delta X_{QSS} + D_{QSS}\Delta u \end{aligned} \tag{4.16}$$

According to Lyapunov's first method, the stability of a nonlinear system for small perturbations is determined by its eigenvalues. The system is said to be asymptotically stable when its eigenvalues have negative real parts [72]. Therefore, the eigenvalues of the state matrix A_{QSS}, which are the roots of the characteristic equation Eq. (4.17), have to be calculated at each equilibrium point (X^0_{QSS}, u_0).

$$det(A_{QSS} - \lambda_{QSS} I) = 0 \tag{4.17}$$

The system stability is first evaluated for a small ohmic load case ($P = 1kW$ and $Q = 0kvar$). The dominant eigenvalues are plotted in Figures 4.2 and 4.3 for different values of droop gains K_p and K_q, respectively.
Figure 4.2 shows that the imaginary parts of the eigenvalues change according to K_p value, but the real parts which determines system stability, remain constant, i.e., the system stays stable independent of the K_p value which is in conflict with the real system behavior. In Figure 4.3, both imaginary and real parts are independent of K_q.
These results and other findings in literature in [70, 71] confirm that using the QSS approach, the original system is oversimplified, so that the electrical dynamics are completely ignored, which leads to a loss of the information about the stability of the microgrid. A novel approach based on the DPM concept is introduced in the next section in order to overcome these issues.

4.4 Dynamic phasor modeling approach

4.4.1 Dynamic phasors

The concept of DPM is based on the calculation of a time varying Fourier coefficient of the fundamental frequency for a sinusoidal signal [70, 73, 74]. A complex periodic signal $x(\tau)$ can be represented in the interval $(t - T, t]$ using the Fourier series of the form:

$$x(\tau) = \sum_{k=-\infty}^{\infty} X_k(t) e^{jk\omega\tau} \tag{4.18}$$

where $\omega = \frac{2\pi}{T}$.
X_k are the complex time varying Fourier coefficients referred to as dynamic phasors. The k^{th} dynamic phasor at time t is determined by:

$$X_k(t) = \frac{1}{T} \int_t^{t+T} x(\tau) e^{-j\omega\tau} d\tau = < x >_k (t) \tag{4.19}$$

There are three important properties for dynamic phasors:

Differential Property: an important property for analyzing differential equations of dynamic phasors. The derivative with respect to the time of the k^{th} dynamic phasor is given in Eq. (4.20).

$$< \frac{dx}{dt} >_k = \frac{d < x >_k}{dt} + j\omega < x >_k \tag{4.20}$$

Phasor Property of Product: the k^{th} phasor of the product of the two time domain signals, $x_1(t)$ and $x_2(t)$, is equal to the discrete time convolution of their dynamic phasors, which is given by Eq. (4.21):

$$< x_1 x_2 >_k = \sum_{i=-\infty}^{\infty} < x_1 >_{k-i} < x_2 >_i \tag{4.21}$$

Property of Conjugation: in the case of complex signal $x(t)$, the k^{th} dynamic phasor of the conjugated signal $x^*(t)$ can be calculated using Eq. (4.22):

$$< x^* >_k = < x >^*_{-k} \tag{4.22}$$

The dynamics of the electrical components in the power system shown in Figure 4.1 for inv1 is given by the differential equation in Eq. (4.23):

$$L_1 \frac{d\overrightarrow{I_1}}{dt} + R_1 \overrightarrow{I_1} = \overrightarrow{V_1} - \overrightarrow{V} \tag{4.23}$$

4.4.2 Electrical system

By replacing the voltage and current signals in Eq. (4.23) with their dynamic phasors based on the definition in Eq. (4.18) during time interval $(t-T, t]$ and considering only the first dynamic phasor (fundamental frequency) yields to Eq. (4.24), the following is obtained:

$$L_1 < \frac{d\overrightarrow{I_1}}{dt} >_1 + R_1 < \overrightarrow{I_1} >_1 = < \overrightarrow{V_1} >_1 - < \overrightarrow{V} >_1 \tag{4.24}$$

The derivative property of DPM is used to simplify the differential equation in Eq. (4.24), resulting in Eq. (4.25):

$$\begin{aligned} L_1 \frac{d < \overrightarrow{I_1} >_1}{dt} + j\omega < \overrightarrow{I_1} >_1 + R_1 < \overrightarrow{I_1} >_1 \\ = < \overrightarrow{V_1} >_1 - < \overrightarrow{V} >_1 \end{aligned} \tag{4.25}$$

The complex coefficients $< \overrightarrow{I_1} >_1$, $< \overrightarrow{V_1} >_1$, and $< \overrightarrow{V} >_1$ are then written using there real and imaginary parts in Eq. (4.26).

$$\begin{aligned} < \overrightarrow{V_1} >_1 &= (V_1^d + jV_1^q) \quad = V_1 e^{j\delta_1} \\ < \overrightarrow{V} >_1 &= (V_1^d + jV_1^q) \quad = V e^{j\delta} \\ < \overrightarrow{I_1} >_1 &= (I_1^d + jI_1^q) \end{aligned} \tag{4.26}$$

By substituting voltage and current dynamic phasors in Eq. (4.25) using their definitions in Eq. (4.26) and splitting the differential equation to real and imaginary parts, Eq. (4.27) is expressed as follows:

$$\begin{aligned} \dot{I}_1^d &= -\frac{R_1}{L_1} I_1^d + \omega_1 I_1^q + \frac{1}{L_1}(V_1^d - V^d) \\ \dot{I}_1^q &= -\frac{R_1}{L_1} I_1^q - \omega_1 I_1^d + \frac{1}{L_1}(V_1^q - V^q) \end{aligned} \tag{4.27}$$

$V_1^d = V_1 cos(\delta_1)$ and $V_1^q = V_1 sin(\delta_1)$ real and imaginary parts of $< \overrightarrow{V_1} >_1$ can be replaced in Eq. (4.27) leading to Eq. (4.28):

$$\begin{aligned} \dot{I}_1^d &= -\frac{R_1}{L_1} I_1^d + \omega_1 I_1^q + \frac{1}{L_1}(V_1 cos(\delta_1) - V^d) \\ \dot{I}_1^q &= -\frac{R_1}{L_1} I_1^q - \omega_1 I_1^d + \frac{1}{L_1}(V_1 sin(\delta_1 - V^q) \end{aligned} \tag{4.28}$$

Information about the load type is required at this point in order to define the relationship between the voltage at PCC $\overrightarrow{V}$ and the output current $\overrightarrow{I}$. In the special case of an ohmic load, it can be written in Eq. (4.29):

$$\overrightarrow{V} = R\overrightarrow{I} = R(\overrightarrow{I_1} + \overrightarrow{I_2}) \tag{4.29}$$

Replacing signals in Eq. (4.29) with their dynamic phasors and considering only the fundamental frequency results in Eq. (4.30).

$$< \overrightarrow{V} >_1 e^{j\omega t} = R(< \overrightarrow{I_1} >_1 e^{j\omega t} + < \overrightarrow{I_2} >_1 e^{j\omega t}) \tag{4.30}$$

Using definitions in Eq. (4.26) yields to:

$$V^d + jV^q = R[I_1^d + I_2^d + j(I_1^q + I_2^q)] \tag{4.31}$$

Dividing Eq. (4.31) into real and imaginary parts gives:

$$\begin{aligned} V^d &= R(I_1^d + I_2^d) \\ V^q &= R(I_1^q + I_2^q) \end{aligned} \tag{4.32}$$

Substituting V^d and V^q in Eq. (4.28) using Eq. (4.32) leads to the differential equations in Eq. (4.33), which describe the electrical dynamics of inv1:

$$\begin{aligned} \dot{I}_1^d &= -\frac{(R_1 + R)}{L_1} I_1^d + \omega I_1^q - \frac{R}{L_1} I_2^d + \frac{V_1}{L_1} cos(\delta_1) \\ \dot{I}_1^q &= -\frac{(R_1 + R)}{L_1} I_1^q - \omega I_1^d - \frac{R}{L_1} I_2^q + \frac{V_1}{L_1} sin(\delta_1) \end{aligned} \tag{4.33}$$

Similarly, the differential equations Eq. (4.34) for inv2 can be obtained:

$$\begin{aligned} \dot{I}_2^d &= -\frac{(R_2 + R)}{L_2} I_2^d + \omega I_2^q - \frac{R}{L_2} I_1^d + \frac{V_2}{L_1} cos(\delta_2) \\ \dot{I}_2^q &= -\frac{(R_2 + R)}{L_2} I_2^q - \omega I_2^d - \frac{R}{L_2} I_1^q + \frac{V_2}{L_1} sin(\delta_2) \end{aligned} \tag{4.34}$$

4.4.3 Calculation of active and reactive power

The definition of the apparent power in Eq. (4.3) can be extended to cover also the system transient as follows:

$$\underline{S}_1 = \frac{3}{2}\overrightarrow{V_1}.\overrightarrow{I_1}^* \tag{4.35}$$

The zero order dynamic phasor which corresponds to the dc part of the apparent power is only considered in Eq. (4.36).

$$< \underline{S}_1 >_0 = \frac{3}{2} < \overrightarrow{V_1}.\overrightarrow{I_1}^* >_0 \tag{4.36}$$

Active and reactive power can be now defined as the real and imaginary parts of the dc component of the apparent power, and the multiplication between voltage and current phasors is converted into convolution product using the second property leading to Eq. (4.37):

$$< \underline{S}_1 >_0 = P_1 + jQ_1 = \frac{3}{2} \sum_{i=-\infty}^{\infty} < \overrightarrow{V_1} >_{0-i} < \overrightarrow{I_1}^* >_i \tag{4.37}$$

The third property of conjugation is applied on Eq. (4.37) leading to Eq. (4.38). The fundamental frequency is only considered for voltage and current phasors, as shown in Eq. (4.39) and (4.40) for inv1. The infinite sum of Eq. (4.38) can then be reduced to only one product between the first order dynamic phasors of voltage and current given in Eq. (4.41).

$$< \underline{S}_1 >_0 = P_1 + jQ_1 = \frac{3}{2} \sum_{i=-\infty}^{\infty} < \overrightarrow{V_1} >_{-i} < \overrightarrow{I_1} >^*_{-i} \tag{4.38}$$

$$< \overrightarrow{V_1} >_k = \begin{cases} (V_1^d + jV_1^q) & \text{if } k = 1 \\ 0 & \text{elsewhere} \end{cases} \tag{4.39}$$

$$< \overrightarrow{I_1} >_k = \begin{cases} (I_1^d + jI_1^q) & \text{if } k = 1 \\ 0 & \text{elsewhere} \end{cases} \tag{4.40}$$

$$< \underline{S}_1 >_0 = P_1 + jQ_1 = \frac{3}{2} < \overrightarrow{V_1} >_1 < \overrightarrow{I_1} >^*_1 \tag{4.41}$$

Replacing $< \overrightarrow{V_1} >_1$ and $< \overrightarrow{I_1} >_1$ by their real and imaginary parts from Eq. (4.26) leads to active and reactive power equations in Eq. (4.42) for inv1:

$$\begin{aligned} P_1 &= \frac{3}{2}(V_1 cos(\delta_1) I_1^d + V_1 sin(\delta_1) I_1^q) \\ Q_1 &= \frac{3}{2}(V_1 sin(\delta_1) I_1^d - V_1 cos(\delta_1) I_1^q) \end{aligned} \tag{4.42}$$

4.4.4 Frequency and voltage control

Differential equations similar to Eq. (4.7), Eq. (4.10), Eq. (4.12), and Eq. (4.13) in the QSS approach can be developed based on the frequency and voltage control diagrams in Figure 3.2. The new formulas of active and reactive power were used, resulting in the new frequency and voltage differential equations Eq. (4.43) for inv1:

$$\begin{aligned}
\dot{I}_1^d &= -\frac{(R_1+R)}{L_1} I_1^d + \frac{(\omega_1+\omega_2)}{2} I_1^q - \frac{R}{L_1} I_2^d + \frac{V_1}{L_1} cos(\delta_1) \\
\dot{I}_1^q &= -\frac{(R_1+R)}{L_1} I_1^q - \frac{(\omega_1+\omega_2)}{2} I_1^d - \frac{R}{L_1} I_2^q + \frac{V_1}{L_1} sin(\delta_1) \\
\dot{\omega}_1 &= -\omega_c \omega_1 + 3\pi\omega_c K_f V_1 [I_1^d cos(\delta_1) + I_1^q sin(\delta_1)] + \omega_c \omega^* \\
\dot{\delta}_1 &= \frac{\omega_1 - \omega_2}{2} \\
\dot{\hat{V}}_1 &= -\omega_c \hat{V}_1 + \frac{3}{2}\omega_c K_v V_1 [I_1^d sin(\delta_1) - I_1^q cos(\delta_1)] + \omega_c V^* \\
\dot{V}_1 &= \frac{1}{T_i}\hat{V}_1 - \frac{1}{T_i} V_1
\end{aligned} \tag{4.43}$$

4.4.5 System linearization

Differential equations similar to those in Eq. (4.43) are also obtained for inv2. Then a nonlinear state space system is defined, where the state and input vectors are defined in Eq. (4.44) similar to that in the QSS approach to be easily extended.

$$\begin{aligned}
X^T &= [I_1^d, I_1^q, \omega_1, \delta_1, \hat{V}_1, V_1, I_2^d, I_2^q, \omega_2, \delta_2, \hat{V}_2, V_2] \\
u^T &= [\omega^*, V^*]
\end{aligned} \tag{4.44}$$

The system is linearized at the equilibrium point given in Eq. (4.45). The equilibrium point for the DPM approach is determined by the system parameters given in Table 4.1, droop gains (K_p, K_q), and load resistance. The equilibrium point is calculated by solving the system nonlinear equations similar to those in Eq. (4.15) numerically, e.g. for $K_p = 25\,kW/Hz$, $K_q = 2.5\,kvar/V$, $R = 160\,\Omega (P = 1\,kW)$ leads to X_0^T given in Table 4.3.

Table 4.3 Equilibrium point of the DPM for $P = 1kW$ and $Q = 0kvar$.

i	$I_{i0}^d[A]$	$I_{i0}^q[A]$	$\omega_{i0}[rad/s]$	$\delta_{i0}[rad]$	$\hat{V}_{i0}[V]$	$V_{i0}[V]$
1	1.0	0.3	0.13	314.1	326.6	326.6
2	1.0	0.0	0.13	314.1	326.6	326.6

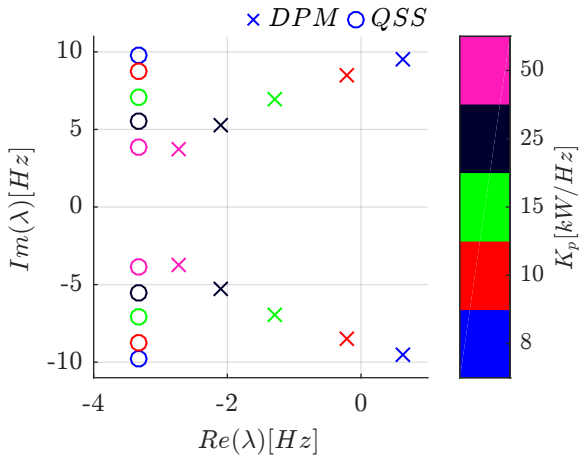

Figure 4.2 Evaluation of eigenvalues dependency on P/f droop gain K_p for QSS and DPM approaches.

$$\begin{aligned} X_0^T &= [I_{10}^d, I_{10}^q, \omega_{10}, \delta_{10}, \hat{V}_{10}, V_{10}, I_{20}^d, I_{20}^q, \omega_{20}, \delta_{20}, \hat{V}_{20}, V_{20}] \\ u_0^T &= [\omega_0^*, V_0^*] \end{aligned} \tag{4.45}$$

The dominant eigenvalues of the linearized system at different equilibrium points are then compared with those of the QSS approach in Figure 4.2 and Figure 4.3 for different values of droop gains K_p and K_q respectively. It can be clearly seen in Figure 4.2 that the real part of the eigenvalues shifts right when reducing the droop gain K_p until it becomes positive, meaning that the system becomes unstable.

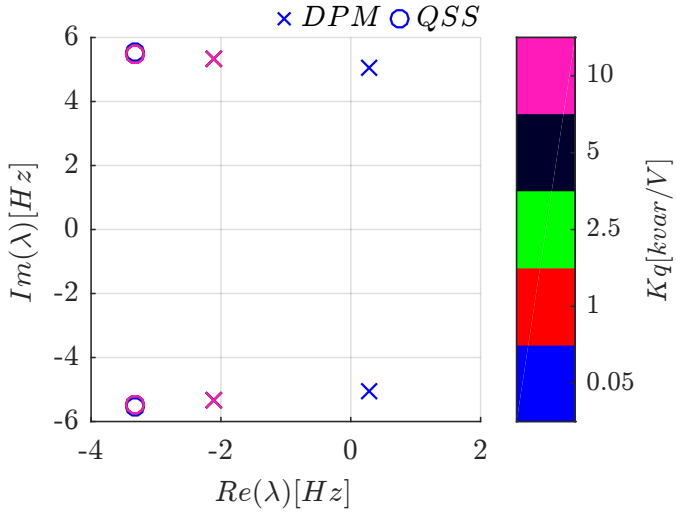

Figure 4.3 Evaluation of eigenvalues dependency on Q/V droop gain K_q for QSS and DPM approaches.

In Figure 4.3 the real part of the eigenvalues shows less sensitivity to the droop gain K_q compared to K_p, nevertheless when K_q is very small the system becomes unstable. These results are totally consistent with the experimental findings of the real system. The verification of the results using the DPM approach and further evaluations are described in the next section.

4.5 Evaluation of microgrid stability

In this section the linearized system model developed using the DPM approach is used to analyze the influence of different system parameters on the stability margins. The linearized model is also verified using simulations and measurements of the real system. The simulation setup is based on the simplified model of U_1 shown in Figure 3.10 implemented in PSCAD. The measurement setup consists of only one unit of the BESS connected to the ohmic load bank at PCC.

4.5.1 Dependency on droop gains

The dominant eigenvalues of the linearized system model are plotted in Figure 4.2 to evaluate the influence of droop gain K_p on stability margins for a constant load. It can be clearly seen that the stability limit lies between $8 \leq K_p \leq 10kW/Hz$. In order to verify these analytical results, a simulation scenario was designed so that the simulation starts using a high value of the droop gain K_p and then gradually decreasing its value until reaching the stability limit as shown in Figure 4.4. During the simulation, the load remains constant in order to avoid applying large disturbances on the system.

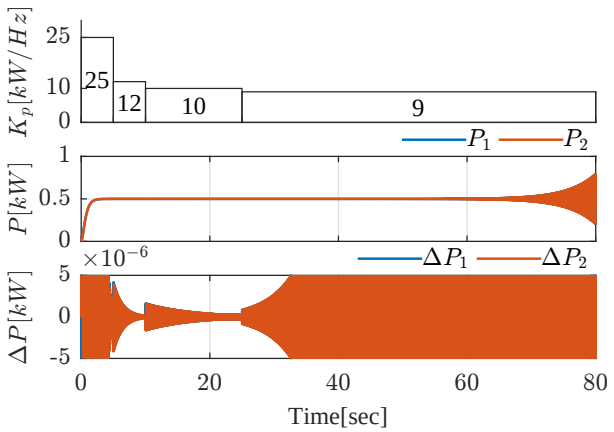

Figure 4.4 Simulation results for the evaluation of the influence of droop gain K_p on system stability.

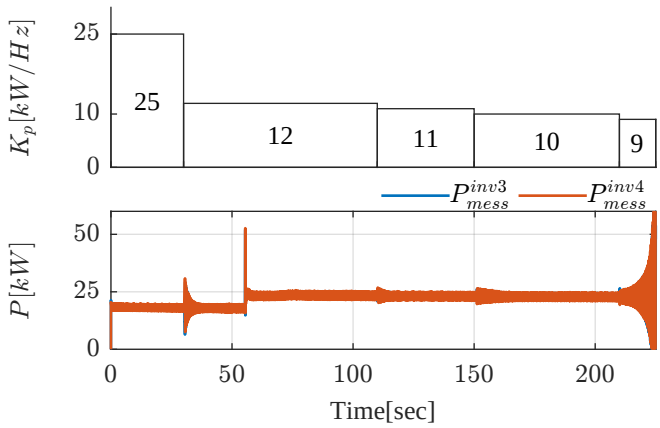

Figure 4.5 Measurement results for the evaluation of the influence of droop gain K_p on system stability.

The active power at the output of both inverters P_1 resp. P_2 and their deviations from the average power ΔP_1 resp. ΔP_2 together with droop gain K_p are depicted. It can be clearly seen that ΔP_1 resp. ΔP_2 converge to zero for large values of K_p up to $K_p = 10\,kW/Hz$, meaning that the system is still stable, after that when $K_p = 9\,kW/Hz$, they start to diverge indicating that the system is unstable. These simulation results comply totally with the analytical ones.
A similar scenario was applied on the real system by connecting a constant ohmic load and decreasing the value of K_p until reaching the stability limit of the real system. Experimental results plotted in Figure 4.5 show that the real system stay stable until reaching $K_p = 9\,kW/Hz$ which confirms both analytical and simulation results.

Since that the Q/V droop gain K_q does not have a significant influence on the system stability for the typical values $1 \leq K_q \leq 10\,kvar/V$, it will not be considered in the evaluation.

4.5.2 Dependency on load resistance

The load influence on the stability margin is only significant when the system is close to the stability limit, i.e., for low values of P/f droop gain K_p, as shown in Figure 4.6. The large, middle and small crosses represent the system eigenvalues for the maximum active power ($P = 100\,kW$), $P = 50\,kW$ and $P = 1\,kW$, respectively. The different colors refer to K_p values. A comparison between the analytical and the simulation results was carried out for two load values when $K_p = 10\,kW/Hz$. The first load value $P = 1\,kW$ shows a stable operation in Figure 4.4 for $K_p = 10\,kW/Hz$ on the opposite to the second load value $P = 50\,kW$ where the system becomes unstable for the same droop value, as shown in Figure 4.7.

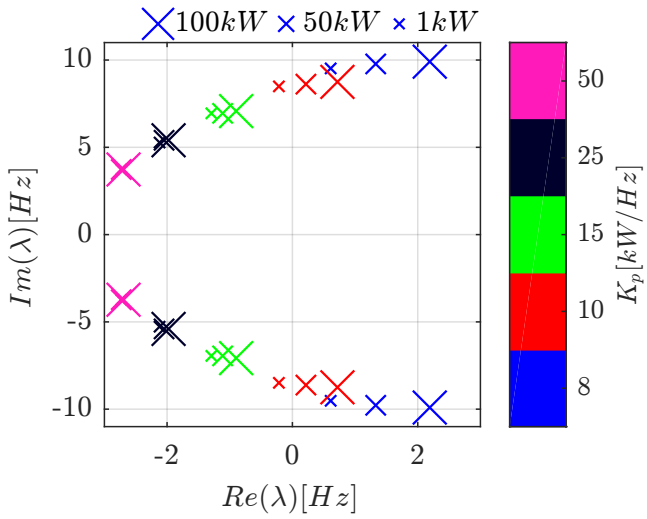

Figure 4.6 Evaluation of eigen values dependency on load resistance (active power) for different values of P/f droop gain K_p.

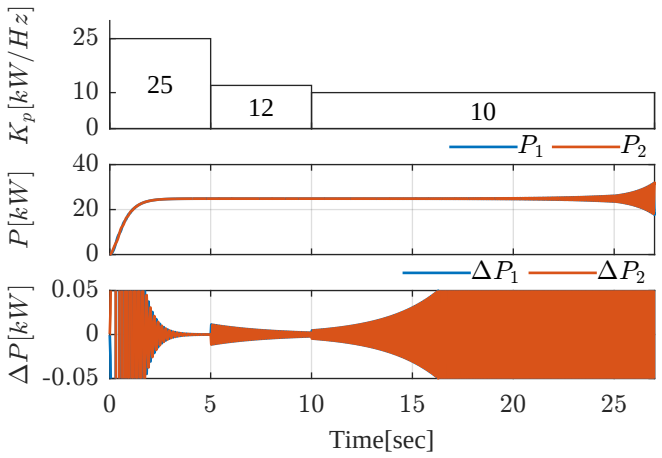

Figure 4.7 Simulation results for the evaluation of the load influence ($P = 50\,kW$) on the stability margin.

4.5.3 Dependency on smoothing time constant

The dominant eigenvalues of the linearized system are plotted in Figure 4.8 as a function of the smoothing time constant T_c for constant droop gain $K_p = 25\,kW/Hz$ and constant load $P = 1\,kW$.

Figure 4.8 shows that the absolute value of the real part of the eigenvalues depends proportionally on the cut off frequency ω_c.

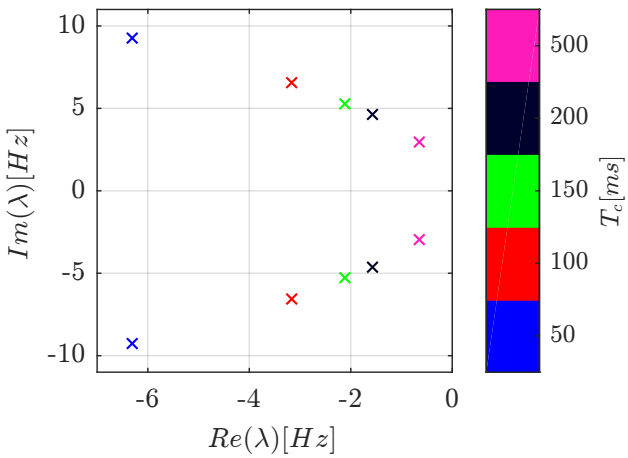

Figure 4.8 Evaluation of eigenvalues dependency on smoothing time constant T_c using the DPM approach.

The reason behind this dependency is that the low values of T_c enable the system to respond faster to disturbances resulting in a larger stability margin. Similar results could be observed at the real system, as shown in Figure 4.9. Where the system is operated close to the stability limit by reducing the droop gain to $K_p = 9\,kW/Hz$ and then changing the smoothing time constant. The experimental results in Figure 4.9 show that the system is more resistant to disturbances when using a low value of $T_c = 50ms$, on the opposite the system tends to go unstable when using a high value of $T_c = 300\,ms$.

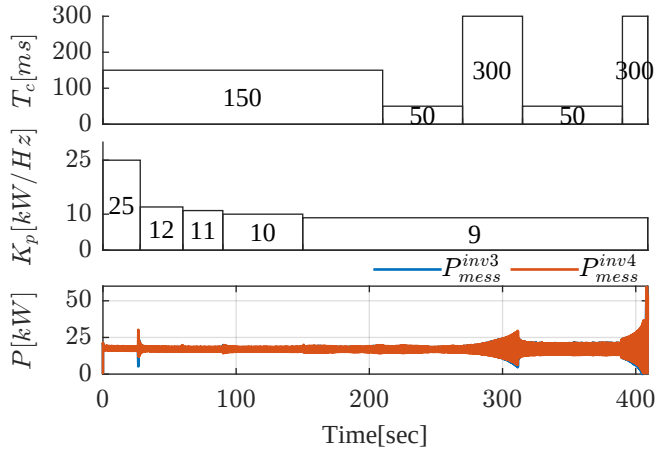

Figure 4.9 Measurement results for the evaluation of the influence of smoothing time constant T_c on system stability.

4.6 Conclusion

Focus in this chapter was on the stability analysis of a microgrid consisting of a BESS and an ohmic load carried out using QSS and DPM approaches. The following conclusions are made base on the thesis research:

1. The system model developed using the traditional QSS approach shows a limitation in determining the system stability.
2. A new mathematical model was developed using the DPM approach considering the electrical dynamics of the system in order to identify the stability limit accurately.
3. The stability limit of the system depends significantly on both P/f droop gain K_p and smoothing time constant T_c.
4. The load resistance plays a significant role only for low values of the P/f droop gain K_p.
5. The Q/V droop gain K_q has almost no influence on the system stability for its typical range.

The comparisons between analytical, simulation and measurement results in section 4.5 confirm that the system stability for small disturbances can be accurately analyzed using the analytical model developed in section 4.4 using the DPM approach.

5 CONCLUSIONS AND FUTURE WORK

5.1 Conclusions

This Thesis has presented a classification of different electrical ESSs and their possible role in microgrids with high share of RESs. This study indicates that the Li-Ion battery properties regarding high power and energy density, high efficiency, short response time and long service life make them appropriate for short and medium term applications. An accurate battery model has been developed for Li-Ion battery in order to optimally integrate it in simulations of stationary and mobile BESSs. The influence of the cell model on the electrical dynamics of the BESS was evaluated and the following results were made:

- Battery ECM with one time constant (OTC) does not represent the fast battery's dynamics accurately mainly when the battery is aged. Therefore, at least two time constants (TTC model) are needed in order to represent the slow and fast dynamics of the battery over the whole service life of the cell ([PAPER- IV] Figure 4).
- Temperature deviation within the range of $20\,°\text{C}$ to $35\,°\text{C}$ as well as aging has a significant effect on the voltage drop at the dc-side and needs to be taken into account.
- The SOC, the aging and the temperature have no significant effect on the THD on the grid side ([PAPER- IV] Table II).
- In order to calculate correctly the harmonics of I_{bat}, it is required to extend the usual ECM for low frequencies by an HF model with one time constant (1RL-model).
- The effects of SOC, cell temperature and aging on the harmonic content of I_{dc} and I_{bat} can be neglected.

It should be underlined that our results are only valid for the cells used in this investigation. Other cells might have different behavior.

The Li-Ion battery model was integrated with the models of other components in the BESS like: EMI filter, IGBTs, LCL filter and transformers to establish a detailed model that describes the electrical dynamics of the BESS accurately.

The detailed model is used to analyze the short time transients and to evaluate the harmonic contents of dc and ac signals. Figures 3.4, 3.5, 3.6, 3.7, 3.8 and 3.9 show a good coincidence with a relative error lower than 5% between measurements and simulation results for the detailed model of U1 and U3 respectively. The complexity of the detailed model is reduced by considering the fundamental electrical dynamics of the BESS. The comparison between the simulation results of the detailed and simplified models in Figures 3.12, 3.13, 3.14 and 3.15 confirms that using the simplified model, the fundamental dynamics are accurately represented for U1 resp. U3.

The modular structure of the BESS composed of six parallel connected inverters can cause stability issues when large disturbances are applied or control parameters are not properly selected. Therefore, the stability analysis of a microgrid consisting of the U1 and an ohmic load was carried out using the QSS and DPM approaches. The following conclusions were made:

- System model developed using the traditional QSS approach shows a limitation in determining the system stability.
- A new model was developed using the DPM approach considering the electrical dynamics of the system in order to detect the stability limit accurately.
- The stability limit of the system depends significantly on both P/f droop gain K_p and smoothing time constant T_c.
- The Q/V droop gain K_q has almost no influence on the system stability for its typical range.

The comparisons between analytical, simulation and measurement results in section 4.5 confirm that the system stability for small disturbances can be accurately analyzed using the analytical model developed in section 4.4 using the DPM approach.

5.2 Future research

The author proposes the following topics for further research:

- Development of a thermal model for Li-Ion cell taking into account the actual structure of battery modules and the cooling system.
- Evaluation of the SOH degradation of the Li-Ion cells in the BESS using the proposed aging algorithm and the current aging tests results.
- Extending the stability analysis of the BESS in a microgrid to also consider ohmic inductive loads.

REFERENCES

[1] E. Hittinger, T. Wiley, J. Kluza, and J. Whitacre, "Evaluating the value of batteries in microgrid electricity systems using an improved Energy Systems Model," *Energy Conversion and Management*, vol. 89, pp. 458–472, jan 2015. [Online]. Available: http://dx.doi.org/10.1016/j.enconman.2014.10.011http://linkinghub.elsevier.com/retrieve/pii/S0196890414008929

[2] J. Rocabert, A. Luna, F. Blaabjerg, and P. Rodríguez, "Control of power converters in AC microgrids," *IEEE Transactions on Power Electronics*, vol. 27, no. 11, pp. 4734–4749, 2012.

[3] N. Shi and Y. Luo, "Energy Storage System Sizing Based on a Reliability Assessment of Power Systems Integrated with Wind Power," *Sustainability*, vol. 9, no. 3, p. 395, mar 2017. [Online]. Available: http://www.mdpi.com/2071-1050/9/3/395

[4] J. Stanojevic, A. Djordjevic, and M. Mitrovic, "Influence of battery energy storage system on generation adequacy and system stability in hybrid micro grids," in *2016 4th International Symposium on Environmental Friendly Energies and Applications (EFEA)*. IEEE, sep 2016, pp. 1–6. [Online]. Available: http://ieeexplore.ieee.org/document/7748813/

[5] Z. Shuai, Y. Sun, Z. J. Shen, W. Tian, C. Tu, Y. Li, and X. Yin, "Microgrid stability: Classification and a review," *Renewable and Sustainable Energy Reviews*, vol. 58, pp. 167–179, may 2016. [Online]. Available: http://linkinghub.elsevier.com/retrieve/pii/S1364032115015841

[6] R. Majumder, "Some Aspects of Stability in Microgrids," *IEEE Transactions on Power Systems*, vol. 28, no. 3, pp. 3243–3252, aug 2013. [Online]. Available: http://ieeexplore.ieee.org/document/6412768/

[7] C. L. Chen, J.-s. Lai, D. Martin, and Y.-s. Lee, "State-space modeling, analysis, and implementation of paralleled inverters for microgrid applications," in *2010 Twenty-Fifth Annual IEEE Applied Power Electronics Conference and Exposition (APEC)*. IEEE, feb 2010, pp. 619–626. [Online]. Available: http://ieeexplore.ieee.org/document/5433605/

[8] M. Zhu, H. Li, and X. Li, "Improved state-space model and analysis of islanding inverter-based microgrid," in *2013 IEEE International Symposium*

on Industrial Electronics. IEEE, may 2013, pp. 1–5. [Online]. Available: http://ieeexplore.ieee.org/document/6563600/

[9] E. A. A. Coelho, P. C. Cortizo, and P. F. D. Garcia, "Small-signal stability for parallel-connected inverters in stand-alone ac supply systems," *IEEE Transactions on Industry Applications*, vol. 38, no. 2, pp. 533–542, 2002.

[10] N. Pogaku, M. Prodanović, and T. C. Green, "Modeling, analysis and testing of autonomous operation of an inverter-based microgrid," *IEEE Transactions on Power Electronics*, vol. 22, no. 2, pp. 613–625, 2007.

[11] S. Tabatabaee, H. R. Karshenas, A. Bakhshai, and P. Jain, "Investigation of droop characteristics and X/R ratio on small-signal stability of autonomous Microgrid," *2011 2nd Power Electronics, Drive Systems and Technologies Conference, PEDSTC 2011*, pp. 223–228, 2011.

[12] J. Vasquez, J. Guerrero, A. Luna, P. Rodriguez, and R. Teodorescu, "Adaptive Droop Control Applied to Voltage-Source Inverters Operating in Grid-Connected and Islanded Modes," *IEEE Transactions on Industrial Electronics*, vol. 56, no. 10, pp. 4088–4096, oct 2009. [Online]. Available: http://ieeexplore.ieee.org/lpdocs/epic03/wrapper.htm?arnumber=5175493

[13] T. E. P. UNION and T. C. O. T. EUROPEAN, "on the promotion of the use of energy from renewable sources and amending and subsequently repealing Directives 2001/77/EC and 2003/30/EC of 23 April 2009," 2009.

[14] M. Lang and A. Lang, "Clear Bundestag Majority for 2022 Nuclear Phase-Out and Coalition Party Approval for Energy Package," 2011.

[15] BMWi, "Anteil Erneuerbarer Energien am Bruttostromverbrauch in Deutschland in den Jahren 1990 bis 2016." [Online]. Available: https://de.statista.com/statistik/daten/studie/2142/umfrage/erneuerbare-energien-anteil-am-stromverbrauch/

[16] A. Dekka, R. Ghaffari, B. Venkatesh, and Bin Wu, "A survey on energy storage technologies in power systems," in *2015 IEEE Electrical Power and Energy Conference (EPEC)*. IEEE, oct 2015, pp. 105–111. [Online]. Available: http://ieeexplore.ieee.org/document/7379935/

[17] X. Luo, J. Wang, M. Dooner, and J. Clarke, "Overview of current development in electrical energy storage technologies and the application potential in power system operation," *Applied Energy*, vol. 137, pp. 511–536, jan 2015. [Online]. Available: http://dx.doi.org/10.1016/j.apenergy.2014.09.081http://linkinghub.elsevier.com/retrieve/pii/S0306261914010290

[18] S. Sabihuddin, A. Kiprakis, and M. Mueller, "A Numerical and Graphical Review of Energy Storage Technologies," *Energies*, vol. 8, no. 1, pp.

172–216, dec 2014. [Online]. Available: http://www.mdpi.com/1996-1073/8/1/172/

[19] M. S. Guney and Y. Tepe, "Classification and assessment of energy storage systems," *Renewable and Sustainable Energy Reviews*, vol. 75, no. November 2016, pp. 1187–1197, aug 2017. [Online]. Available: http://linkinghub.elsevier.com/retrieve/pii/S1364032116308218

[20] M. Aneke and M. Wang, "Energy storage technologies and real life applications – A state of the art review," *Applied Energy*, vol. 179, pp. 350–377, 2016. [Online]. Available: http://dx.doi.org/10.1016/j.apenergy.2016.06.097

[21] D. Akinyele and R. Rayudu, "Review of energy storage technologies for sustainable power networks," *Sustainable Energy Technologies and Assessments*, vol. 8, pp. 74–91, dec 2014. [Online]. Available: http://dx.doi.org/10.1016/j.seta.2014.07.004http://linkinghub.elsevier.com/retrieve/pii/S2213138814000708

[22] G. Fuchs, B. Lunz, M. Leuthold, and D. U. Sauer, "Technology Overview on Electricity Storage - Overview on the potential and on the deployment perpectives of electric storage technologies," *Institute for Power Electronics and Electrical Drives (ISEA), RWTH Aachen University*, no. June, p. 66, 2012.

[23] D. Linden and T. B. Reddy, *Handbook Of Batteries*. McGraw-Hill Professional, 2001.

[24] E. Rodrigues, G. Osório, R. Godina, A. Bizuayehu, J. Lujano-Rojas, J. Matias, and J. Catalão, "Modelling and sizing of NaS (sodium sulfur) battery energy storage system for extending wind power performance in Crete Island," *Energy*, vol. 90, pp. 1606–1617, oct 2015. [Online]. Available: http://linkinghub.elsevier.com/retrieve/pii/S0360544215008725

[25] C.-H. Dustmann, "Advances in ZEBRA batteries," *Journal of Power Sources*, vol. 127, no. 1-2, pp. 85–92, mar 2004. [Online]. Available: http://linkinghub.elsevier.com/retrieve/pii/S0378775303009418

[26] B. Li and J. Guo, "Scaled VRB system modeling and simulating," *Power System Technology (POWERCON), 2012 ...*, pp. 1–6, oct 2012. [Online]. Available: http://ieeexplore.ieee.org/lpdocs/epic03/wrapper.htm?arnumber=6401395http://ieeexplore.ieee.org/xpls/abs{_}all.jsp?arnumber=6401395

[27] T. Elmer, M. Worall, S. Wu, and S. B. Riffat, "Fuel cell technology for domestic built environment applications: State of-the-art review," *Renewable and Sustainable Energy Reviews*, vol. 42, pp. 913–931, feb

2015. [Online]. Available: http://dx.doi.org/10.1016/j.rser.2014.10.080http://linkinghub.elsevier.com/retrieve/pii/S1364032114009058

[28] N. Nitta, F. Wu, J. T. Lee, and G. Yushin, "Li-ion battery materials: Present and future," *Materials Today*, vol. 18, no. 5, pp. 252–264, 2015. [Online]. Available: http://dx.doi.org/10.1016/j.mattod.2014.10.040

[29] M. K. Gulbinska, *Lithium-ion Battery Materials and Engineering*, ser. Green Energy and Technology, M. K. Gulbinska, Ed. London: Springer London, 2014. [Online]. Available: http://link.springer.com/10.1007/978-1-4471-6548-4

[30] R. Korthauer, Ed., *Handbuch Lithium-Ionen-Batterien*. Berlin, Heidelberg: Springer Berlin Heidelberg, 2013. [Online]. Available: http://link.springer.com/10.1007/978-3-642-30653-2

[31] M. Yoshio, R. J. Brodd, and A. Kozawa, Eds., *Lithium-Ion Batteries*. New York, NY: Springer New York, 2009. [Online]. Available: http://link.springer.com/10.1007/978-0-387-34445-4

[32] J. Figgener, D. Haberschusz, K.-P. Kairies, O. Wessels, B. Tepe, M. Ebbert, R. Herzog, and D. U. Sauer, "Wissenschaftliches Mess- und Evaluierungsprogramm Solarstromspeicher 2.0," Institut für Stromrichtertechnik und Elektrische Antriebe der RWTH, Aachen, Tech. Rep., 2017. [Online]. Available: http://www.speichermonitoring.de/

[33] M. Montaru and S. Pelissier, "Frequency and Temporal Identification of a Li-ion Polymer Battery Model Using Fractional Impedance," *Oil & Gas Science and Technology – Revue de l'Institut Français du Pétrole*, vol. 65, no. 1, pp. 67–78, jan 2010. [Online]. Available: http://ogst.ifp.fr/10.2516/ogst/2009056http://ogst.ifpenergiesnouvelles.fr/10.2516/ogst/2009056

[34] H. Al Jed, A. Mieze, J.-M. Vinassa, and R. Simon, "Mathematical modeling of aging factors for Li-ion battery cells," in *2010 IEEE Vehicle Power and Propulsion Conference*. IEEE, sep 2010, pp. 1–4. [Online]. Available: http://ieeexplore.ieee.org/document/5729124/

[35] H. He, R. Xiong, and J. Fan, "Evaluation of Lithium-Ion Battery Equivalent Circuit Models for State of Charge Estimation by an Experimental Approach," *Energies*, vol. 4, no. 12, pp. 582–598, mar 2011. [Online]. Available: http://www.mdpi.com/1996-1073/4/4/582/

[36] S. Buller, M. Thele, R. De doncker, and E. Karden, "Supercapacitors and lithium-ion batteries for power electronic applications," *IEEE Industry Applications Magazine*, vol. 11, no. 2, pp. 62–67, mar 2005. [Online]. Available: http://ieeexplore.ieee.org/document/1405828/

[37] S. Buller, M. Thele, E. Karden, and R. W. De Doncker, "Impedance-based non-linear dynamic battery modeling for automotive applications," *Journal of Power Sources*, vol. 113, no. 2, pp. 422–430, jan 2003. [Online]. Available: http://linkinghub.elsevier.com/retrieve/pii/S037877530200558X

[38] L. F. H. Mesa, "Simulation of a battery storage system taking into account a thermal-electric model for lithium-ion cells," Master of Engineering, University of Applied Sciences Kempten, 2014.

[39] J. Wang, K. Zou, C. Chen, and L. Chen, "A high frequency battery model for current ripple analysis," *2010 Twenty-Fifth Annual IEEE Applied Power Electronics Conference and Exposition (APEC)*, no. 1, pp. 676–680, feb 2010. [Online]. Available: http://ieeexplore.ieee.org/lpdocs/epic03/wrapper.htm?arnumber=5433598

[40] A. Eddahech, O. Briat, and J.-M. Vinassa, "Lithium-ion battery heat generation investigation based on calorimetric entropy measurements," in *2013 IEEE International Symposium on Industrial Electronics*. IEEE, may 2013, pp. 1–5. [Online]. Available: http://ieeexplore.ieee.org/lpdocs/epic03/wrapper.htm?arnumber=6563807

[41] D. Andre, M. Meiler, K. Steiner, H. Walz, T. Soczka-Guth, and D. Sauer, "Characterization of high-power lithium-ion batteries by electrochemical impedance spectroscopy. II: Modelling," *Journal of Power Sources*, vol. 196, no. 12, pp. 5349–5356, jun 2011. [Online]. Available: http://dx.doi.org/10.1016/j.jpowsour.2010.07.071http://linkinghub.elsevier.com/retrieve/pii/S0378775310012942

[42] X. Lin, H. E. Perez, S. Mohan, J. B. Siegel, A. G. Stefanopoulou, Y. Ding, and M. P. Castanier, "A lumped-parameter electro-thermal model for cylindrical batteries," *Journal of Power Sources*, vol. 257, pp. 1–11, jul 2014. [Online]. Available: http://dx.doi.org/10.1016/j.jpowsour.2014.01.097http://linkinghub.elsevier.com/retrieve/pii/S0378775314001244

[43] B. Schweighofer, K. Raab, and G. Brasseur, "Modeling of high power automotive batteries by the use of an automated test system," *IEEE Transactions on Instrumentation and Measurement*, vol. 52, no. 4, pp. 1087–1091, aug 2003. [Online]. Available: http://ieeexplore.ieee.org/lpdocs/epic03/wrapper.htm?arnumber=1232350

[44] S. Abu-Sharkh and D. Doerffel, "Rapid test and non-linear model characterisation of solid-state lithium-ion batteries," *Journal of Power Sources*, vol. 130, no. 1-2, pp. 266–274, may 2004. [Online]. Available: http://linkinghub.elsevier.com/retrieve/pii/S0378775303011455

[45] R. Benger, H. Wenzl, H.-p. Beck, M. Jiang, and D. Ohms, "Electrochemical and thermal modeling of lithium-ion cells for use in HEV or EV application," vol. 3, pp. 1–10, 2009.

[46] K. Uddin, A. Picarelli, C. Lyness, N. Taylor, and J. Marco, "An Acausal Li-Ion Battery Pack Model for Automotive Applications," *Energies*, vol. 7, pp. 5675–5700, 2014. [Online]. Available: http://www.mdpi.com/1996-1073/7/9/5675/

[47] J. Remmlinger, M. Buchholz, M. Meiler, P. Bernreuter, and K. Dietmayer, "State-of-health monitoring of lithium-ion batteries in electric vehicles by on-board internal resistance estimation," *Journal of Power Sources*, vol. 196, no. 12, pp. 5357–5363, jun 2011. [Online]. Available: http://linkinghub.elsevier.com/retrieve/pii/S0378775310013534

[48] X. Hu, F. Sun, Y. Zou, and H. Peng, "Online estimation of an electric vehicle Lithium-Ion battery using recursive least squares with forgetting," *Proceedings of the 2011 American Control Conference*, pp. 935–940, 2011.

[49] F. Hildebrand, *Introduction to numerical analysis*. New York: McGraw-Hill, 1973.

[50] S. D. Foss, "A Method of Exponential Curve Fitting by Numerical Integration," *Biometrics*, vol. 26, no. 4, p. 815, dec 1970. [Online]. Available: http://www.jstor.org/stable/2528726?origin=crossref

[51] J. L. Fresen and J. M. Juritz, "A Note on Foss's Method of Obtaining Initial Estimates for Exponential Curve Fitting by Numerical Integration," *Biometrics*, vol. 42, no. 4, p. 821, dec 1986. [Online]. Available: http://www.jstor.org/stable/2530696?origin=crossref

[52] P. Zaikin and M. Ufimtsev, "Development of integro-differential methods of parameter determination for a sum of exponential functions," *Computational Mathematics and Modeling*, vol. 8, no. 2, pp. 165–171, 1997. [Online]. Available: http://link.springer.com/article/10.1007/BF02405168

[53] D. G. Gardner, J. C. Gardner, G. Laush, and W. W. Meinke, "Method for the Analysis of Multicomponent Exponential Decay Curves," *The Journal of Chemical Physics*, vol. 31, no. 4, p. 978, 1959. [Online]. Available: http://scitation.aip.org/content/aip/journal/jcp/31/4/10.1063/1.1730560

[54] M. R. Smith, S. Cohn-Sfetcu, and H. A. Buckmaster, "Decomposition of Multicomponent Exponential Decays by Spectral Analytic Techniques," *Technometrics*, vol. 18, no. 4, p. 467, nov 1976. [Online]. Available: http://www.jstor.org/stable/1268663?origin=crossref

[55] M. SALAMI and S. SIDEK, "PARAMETER ESTIMATION OF MULTICOMPONENT TRANSIENT SIGNALS USING DECONVOLUTION AND ARMA MODELLING TECHNIQUES," *Mechanical Systems and Signal Processing*, vol. 17, no. 6, pp. 1201–1218, nov 2003. [Online]. Available: http://linkinghub.elsevier.com/retrieve/pii/S0888327002914962

[56] A. U. Jibia, M. J. E. Salami, and O. O. Khalifa, “Effect of sampling on the parameter estimates of multicomponent transients,” *2010 The 2nd International Conference on Computer and Automation Engineering, ICCAE 2010*, vol. 5, pp. 704–708, 2010.

[57] A. U. Jibia and M.-J. E. Salami, “Parameter Estimation of Transient Multiexponential Signals Using SVD-ARMA and Multiparameter Deconvolution Techniques,” *International Journal of Computer Theory and Engineering*, vol. 4, no. 5, pp. 751–757, 2012. [Online]. Available: http://www.ijcte.org/show-44-523-1.html

[58] S. F. Schuster, T. Bach, E. Fleder, J. Müller, M. Brand, G. Sextl, and A. Jossen, “Nonlinear aging characteristics of lithium-ion cells under different operational conditions,” *Journal of Energy Storage*, vol. 1, no. 1, pp. 44–53, jun 2015. [Online]. Available: http://www.sciencedirect.com/science/article/pii/S2352152X15000092http://linkinghub.elsevier.com/retrieve/pii/S2352152X15000092

[59] V. Agubra and J. Fergus, “Lithium Ion Battery Anode Aging Mechanisms,” *Materials*, vol. 6, no. 4, pp. 1310–1325, mar 2013. [Online]. Available: http://www.mdpi.com/1996-1944/6/4/1310/

[60] M. Ecker, J. B. Gerschler, J. Vogel, S. Käbitz, F. Hust, P. Dechent, and D. U. Sauer, “Development of a lifetime prediction model for lithium-ion batteries based on extended accelerated aging test data,” *Journal of Power Sources*, vol. 215, pp. 248–257, oct 2012. [Online]. Available: http://linkinghub.elsevier.com/retrieve/pii/S0378775312008671

[61] M. Ecker, N. Nieto, S. Käbitz, J. Schmalstieg, H. Blanke, A. Warnecke, and D. U. Sauer, “Calendar and cycle life study of Li(NiMnCo)O2-based 18650 lithium-ion batteries,” *Journal of Power Sources*, vol. 248, pp. 839–851, feb 2014. [Online]. Available: http://linkinghub.elsevier.com/retrieve/pii/S0378775313016510

[62] H. Beltran, J. Barahona, R. Vidal, J. C. Alfonso, C. Ariño, and E. Pérez, “Ageing of different types of batteries when enabling a PV power plant to enter electricity markets,” *IECON Proceedings (Industrial Electronics Conference)*, pp. 1986–1991, 2016.

[63] H. Beltran, M. Swierczynski, N. Aparicio, E. Belenguer, R. Teodorescu, and P. Rodriguez, “Lithium ion batteries ageing analysis when used in a PV power plant,” *2012 IEEE International Symposium on Industrial Electronics*, pp. 1604–1609, may 2012. [Online]. Available: http://ieeexplore.ieee.org/lpdocs/epic03/wrapper.htm?arnumber=6237330

[64] A. International and F. Indexed by mero, “Standard Practices for Cycle Counting in Fatigue Analysis 1,” pp. 1049–85, 1997.

[65] "IREN2 official website." [Online]. Available: www.iren2.de

[66] J. L. H. Cruz, "Modelling and Simulation of a Big Battery Storage System of a Smart Grid including Power Electronics," Master of Engineering, University of Applied Sciences Kempten, 2013. [Online]. Available: http://www.ncbi.nlm.nih.gov/pubmed/21365933

[67] A. Engler, "Applicability of droops in low voltage grids," *International Journal of Distributed Energy Resources and Smart Grids*, no. 1, pp. 1–5, 2005.

[68] S. V. Iyer, M. N. Belur, and M. C. Chandorkar, "A generalized computational method to determine stability of a multi-inverter microgrid," *IEEE Transactions on Power Electronics*, vol. 25, no. 9, pp. 2420–2432, 2010.

[69] E. Coelho, P. Cortizo, and P. Garcia, "Small signal stability for single phase inverter connected to stiff\nAC system," *Conference Record of the 1999 IEEE Industry Applications Conference. Thirty-Forth IAS Annual Meeting (Cat. No.99CH36370)*, vol. 4, pp. 2180–2187, 1999. [Online]. Available: http://ieeexplore.ieee.org/articleDetails.jsp?arnumber=798756

[70] L. Wang, X. Q. Guo, H. Gu, W. Wu, and J. M. Guerrero, "Precise modeling based on dynamic phasors for droop-controlled parallel-connected inverters," in *2012 IEEE International Symposium on Industrial Electronics*. IEEE, may 2012, pp. 475–480. [Online]. Available: http://ieeexplore.ieee.org/document/6237133/

[71] X. Guo, Z. Lu, B. Wang, X. Sun, L. Wang, and J. M. Guerrero, "Dynamic phasors-based modeling and stability analysis of droop-controlled inverters for microgrid applications," *IEEE Transactions on Smart Grid*, vol. 5, no. 6, pp. 2980–2987, 2014.

[72] P. Kundur, *Power system stability and control*. New York: McGraw-Hill, 1994.

[73] M. Calabria and W. Schumacher, "Modeling power inverter interactions in a low voltage grid," *2014 IEEE 15th Workshop on Control and Modeling for Power Electronics, COMPEL 2014*, pp. 1–9, 2014.

[74] W. Ru, J. Sun, M. Gao, X. Zha, F. Liu, and C. Lin, "Modeling and Simulation of Micro-grid including Inverter-interfaced Distributed Resources Based on Dynamic Phasors," no. 51177113, pp. 686–690, 2013.

ABSTRACT

The share of the renewable energy sources (RESs) have recently rapidly increased shifting the power system from centralized and fossil-based power generation towards regenerative and distributed power generation. The intermittent nature and high penetration of inverter-connected RESs in low voltage micro grids replacing conventional generators and their rotating machinery led to a significant reduction in system inertia.

This PhD thesis presents a classification of different electrical ESSs in Chapter 1 and their possible role in microgrids with high share of RESs. Chapter 1 indicates that battery energy storage systems (BESSs) can play a key role to ensure generation adequacy and to increase the reliability and security of the microgrid under the new conditions.

The procedure on how to develop a mathematical model of a Li-ion based BESS for microgrid applications is introduced in Chapters 2 and 3. Focus in Chapter 2 is on the development of a mathematical model of a Li-Ion cell for the evaluation of the electrical dynamics of the BESS. The cell model considers the effects of the state of charge (SOC), cell temperature, and aging. An empirical aging algorithm is introduced for the prediction of service life of the Li-Ion battery based on laboratory tests in Chapter 2.

Chapter 3 covers the development of two mathematical models for the BESS in grid forming (GF) mode. The first model is a detailed model that describes accurately the electrical dynamics of the BESS including the switching operation of the IGBTs, which makes it appropriate for the evaluation of short time transients. For long time simulations of the BESS along with other microgrid components a simplified model is also implemented, which represents only the fundamental dynamics of the system. The verification of the detailed and the simplified model was carried out using measurements of the real system. The feedback and coupling between parallel connected inverters in GF mode can cause stability issues when large disturbances are applied or control parameters are not properly selected.

Therefore, Chapter 4 introduces a new approach for the stability analysis of the BESS in a microgrid. The new approach is based on the dynamic phasor modeling (DPM) concept. The comparison between the DPM approach and the traditional quasi steady state (QSS) approach shows that the DPM approach is capable to represent not only the slow dynamics of the control system but also the fast dynamics of the electrical system. The validation of the QSS and the

DPM was performed with real experiments considering the influence of droop gains, smoothing time constant and load parameters on the stability margin of the BESS.
This research is valuable for BESS developers who wish to optimize their system based on specific microgrid application, and for researchers who are interested in improving BESS diagnostics algorithms.

KOKKUVÕTE

Taastuvate energiaallikate laialdane kasutuselevõtt on kiirendanud elektrisüsteemi üleminekut tsentraliseeritud ja fossiilkütusel põhinevalt elektritootmiselt taastuvenergiaallikatel põhinevale hajatootmisele. Madalpinge mikrovõrkudes traditsiooniliste pöörlevate masinatega generaatoreid asendavate muundurite kaudu võrku ühendatud taastuvenergiaallikate suur hulk ja nende ilmast sõltuv tootmine vähendab oluliselt süsteemi inertsi.

Doktoritöö esimene osa annab ülevaate energiasalvestite klassifikatsioonist ja nende rollist suure osakaaluga taastuvenergiaallikatega mikrovõrkudes. Akudel põhinevad energiasalvestussüsteemid on põhilahendused, mis aitavad ühtlustada energiatootmise kõikumisi ja tagada uutes tingimustes elektrivõrgu töö- ja varustuskindlus.

Järgmises kahes töö peatükis on kirjeldatud Li-Ion akudel põhineva mikrovõrgu energiasalvesti matemaatilise mudeli väljatöötamist. Teise peatüki rõhk asetseb täpsemalt Li-Ion elemendi matemaatilise mudeli väljatöötamisel, et hinnata selle mõju energiasalvesti töö dünaamikale. Elemendi mudel võtab arvesse selle laetust, temperatuuri ja vananemist. Lisaks kirjeldatakse ka uut laborikatsete alusel väljatöötatud empiirilist energiasalvesti kasutusea hindamise algoritmi.

Töö kolmandas peatükis kirjeldatakse kahte aku-energiasalvesti matemaatilise mudeli väljatöötamist võrku toetavatele (*grid –forming, GF*) muunduritele. Esimene mudel kirjeldab detailselt energiasalvesti elektriosa dünaamikat sh IGBT lülitusi, et uurida lühiajalisi transiente. Pikaajaliseks energiasalvesti ja mikrovõrgu komponentide koostöö analüüsiks on välja töötatud teine ehk lihtsustatud matemaatiline mudel, mis kirjeldab ainult süsteemi üldist ehk põhidünaamikat. Mõlemad mudelid on valideeritud mõõtmistega reaalses süsteemis. Tagasiside ja sidestus paralleelselt ühendatud muundurite vahel võib võrku toetavas talitluses suurte häiringute või ebatäpsete juhtimisseadete korral põhjustada stabiilsusprobleeme.

Töö neljandas peatükis kirjeldatakse uut aku-energiasalvestiga varustatud mikrovõrgu stabiilsusanalüüsi meetodit. Uus meetod põhineb dünaamilisel vektormodelleerimisel (*dynamic phasor modeling, DPM*). Võrreldes dünaamilist vektormodelleerimist traditsioonilise kvaasistabiilse (*quasi steady state, QSS*) modelleerimisega, võimaldab see lisaks juhtimissüstemi aeglastele muutustele analüüsida ka elektrisüsteemi kiireid muutusi. Mõlemaid modelleerimise tulemusi katsetati reaalsetes tingimustes, võttes aku-energiasalvesti stabiilsusvaru hindamisel arvesse statismi tegurit (*droop gains*), silumise ajakonstanti ja

koormuse parameetreid.
Käesolev uurimistöö on oluline aku-energiasalvestite arendajatele, kes soovivad optimeerida oma rakendusi mikrovõrkudes ja teadlastele, kelle eesmärk on parendada energiasalvestite diagnostikaalgoritme.

CURRICULUM VITAE

Personal data

Name:	Ahmad Rahmoun
Citizenship:	German/Syrian

Contact data

Aadress:	Freudenberg 9, 87435 Kempten, Germany
E-mail:	rahmad83@gmail.com

Education

Period	Educational institution	Eduction (field of study/degree)
2013 – 2017:	Tallinn University of Technology (TUT)	PhD studies
2010 – 2012:	University of Applied Sciences Kempten (HKE)	Master of Electrical Engineering
2000 – 2006:	Higher Institute for Applied Sciences and Technology (HIAST)	Diploma of Engineering

Professional employment

Period	Organization	Position
2011 – 2013:	Institute for Applied Battery Research (IABF), University of Applied Sciences Kempten	Researcher
2009 – 2012:	Institute for Electrical Power Systems (IEES), University of Applied Sciences Kempten	Researcher

Research work

Period	Research project
Mar. 2011 – Sept. 2011:	eE-Tour Allgäu
Apr. 2011 – Dec. 2013:	IRENE (Integration of Renewable Energies and Electromobility)
Oct. 2012 – Dec. 2015:	E-Lieferungen im Allgäu
July 2014 – Dec. 2017:	IREN2 (Future Oriented Electricity Grids for Integration of Renewable Energy Systems)
Sept. 2012 – Dec. 2016:	SF0140016s11 (Topologies and control methods for active power distribution network converters), Dmitri Vinnikov, Tallinn University of Technology , Faculty of Power Engineering

Defended theses

M.Eng.: SOC Estimation for Li-Ion Batteries Based on Equivalent Circuit Diagrams and the Application of Kalman Filter, 2012, Supervisor Prof. Dr.-Ing. Dr.h.c. Helmuth Biechl, University of Applied Sciences Kempten

Dipl.-Ing.: Real Time Image Labeling Using FPGA: Application On Mobile Robot for Object Positioning, 2006, Higher Institute for Applied Sciences and Technology (HIAST)

Honours and awards

2012: DAAD Prize for outstanding achievements of international students at German universities

Language competence

Language	Level
Arabic:	Native speaker
English:	Fluent
German:	Fluent
French:	Basic

ELULOOKIRJELDUS

Isikuandmed

Nimi: Ahmad Rahmoun
Kodakondsus: Saksa/Süüria

Kontaktandmed

Aadress: Freudenberg 9, 87435 Kempten, Germany
E-mail: rahmad83@gmail.com

Hariduskäik

Õppimise aeg	Õppeasutus (nimetus lõpetamise ajal)	Haridus (eriala/kraad)
2013 – 2017:	Tallinn University of Technology	PhD studies
2010 – 2012:	University of Applied Sciences Kempten (HKE)	Master of Electrical Engineering
2000 – 2006:	Higher Institute for Applied Sciences and Technology (HIAST)	Diploma of Engineering

Teenistuskäik

Töötamise aeg	Tööandja nimetus	Ametikoht
2011 – 2013:	Institute for Applied Battery Research (IABF), University of Applied Sciences Kempten	Researcher
2109 – 2112:	Institute for Electrical Power Systems (IEES), University of Applied Sciences Kempten	Researcher

Teadustegevus

Töötamise aeg	Uuringuprojekt
Mar. 2011 – Sept. 2011:	eE-Tour Allgäu
Apr. 2011 – Dec. 2013:	IRENE (Integration of Renewable Energies and Electromobility)
Oct. 2012 – Dec. 2015:	E-Lieferungen im Allgäu
July 2014 – Dec. 2017:	IREN2 (Future Oriented Electricity Grids for Integration of Renewable Energy Systems)
Sept. 2012 – Dec. 2016:	SF0140016s11 (Topologies and control methods for active power distribution network converters), Dmitri Vinnikov, Tallinn University of Technology , Faculty of Power Engineering

Kaitstud lõputööd

M.Eng.: SOC Estimation for Li-Ion Batteries Based on Equivalent Circuit Diagrams and the Application of Kalman Filter, 2012, Supervisor Prof. Dr.-Ing. Dr.h.c. Helmuth Biechl, University of Applied Sciences Kempten

Dipl.-Ing.: Real Time Image Labeling Using FPGA: Application On Mobile Robot for Object Positioning, 2006, Higher Institute for Applied Sciences and Technology (HIAST)

Teaduspreemiad ja tunnustused

2012: DAADi auhind Saksa ülikoolide rahvusvaheliste üliõpilaste suurepäraste saavutuste eest.

Keelteoskus

Keel	Tase
Araabia keel:	Emakeel
Inglise:	Kõrgtase
Saksa:	Kõrgtase
Prantsuse:	Algtase

APPENDIXES

PAPER- I A. Rahmoun and H. Biechl, “Modelling of Li-ion batteries using equivalent circuit diagrams,” Prz. Elektrotechniczny, vol. 2012, no. 7b, pp. 152–156, 2012.

Ahmad RAHMOUN, Helmuth BIECHL

University of Applied Sciences Kempten

Modelling of Li-ion batteries using equivalent circuit diagrams

Abstract. *This paper presents the fundamentals of a method how to determine the state of charge (SOC) of lithium-ion batteries on the basis of two different equivalent circuit diagrams and an extended Kalman filter (EKF). It describes how to identify the parameters of these circuits by characteristic measurements. The comparison between measurement and computation results shows a good accordance. In the first step the dependency of these parameters on the temperature and on the battery age is neglected.*

Streszczenie. *W artykule przedstawiono podstawy metody pozwalającej określić stan naładowania (SOC) akumulatorów litowo-jonowych na podstawie dwóch różnych schematów zastępczych i rozszerzonego filtru Kalmana (EKF). Opisano, jak zidentyfikować parametry akumulatorów na podstawie pomiarów ich charakterystyk. Porównanie wyników pomiarów z wynikami symulacji wykazuje zgodność. W pierwszym etapie pominięto zależność parametrów akumulatorów od temperatury i od czasu użytkowania.(* ***Modelowanie akumulatorów litowo-jonowych z wykorzystaniem schematów zastępczych)***

Keywords: Li-ion battery, equivalent circuit diagrams, battery modelling, parameters identification.
Słowa kluczowe: akumulator Li-Ion, schematy zastępcze, modelowanie baterii, identyfikacja parametrów.

Introduction

If a defined full charge of a battery takes place regularly it is possible to determine the state of charge (SOC) by the so-called Ampere-counting method. This method is basing on the charge that is transferred into the battery respectively taken out of the battery. In case where a defined full charge of the battery cannot happen regularly the error in the SOC estimation can become inacceptable high and a better method has to be found. The SOC is a function of the open circuit voltage (OCV) of a lithium-ion battery, $SOC=f(V_{OC})$, but this method involves the problem of its dynamics as Figures 3 (c) and (d) demonstrate. The electrochemical processes which take place in a cell result in the fact that the OCV cannot be measured at the battery terminals. The dynamics needs to be modeled mathematically in a way that the OCV respectively SOC can be calculated by measuring only the battery voltage and current at the terminals of the battery. For this purpose an equivalent circuit diagram for the battery cell has to be used, and the parameters need to be identified by characteristic measurements.

In this paper at first the internal resistance model (IR) is presented, then the one time constant model (OTC), and finally the two time constants model (TTC). Further, comparisons between the model-based simulation data and the measured data are carried out to evaluate the validity of the demonstrated models, which provide a foundation for the model based SOC estimation [4].

Equivalent Circuit models

IR Model, the IR model as shown in Figure 1 (a), and described by Equation 1 implements an ideal voltage source V_{OC} that represents the open-circuit voltage (OCV) of the battery, and an ohmic resistance in order to describe the internal resistance. Both, resistance and open-circuit voltage V_{OC} are functions of SOC, state of health (SOH) and temperature. i_{Batt} is the battery output current with a positive value when discharging, and a negative value when charging, v_{Batt} is the battery terminal voltage [1].

$$v_{Batt} = V_{OC} - R_0 i_{Batt} \tag{1}$$

As the IR model does not represent the transient behavior of lithium-ion cells, it is not suitable for the accurate estimation of SOC during any dynamical operation (non-constant load).

OTC Model, The OTC model adds a parallel RC network in series to the internal resistance R_0 of the IR model, in order to approximate the dynamic behaviour of the lithium-ion battery. As shown in Figure 1 (b), it mainly consists of three parts including the voltage source V_{OC}, the ohmic resistance R_0, and R_{OTC},C_{OTC} to describe the battery transient response during charging or discharging. v_{OTC} is the voltage across C_{OTC}; i_{OTC} is the current that flows in C_{OTC}. The electric behaviour of the OTC model can be expressed by Equations 2 and 3 in continuous time [1]:

$$\dot{v}_{OTC} = \frac{-1}{R_{OTC} * C_{OTC}} v_{OTC} + \frac{1}{C_{OTC}} i_{Batt}, \tag{2}$$

$$v_{Batt} = V_{OC} - v_{OTC} - R_0 i_{Batt}. \tag{3}$$

The description in discrete time is shown by Equations 4 and 5.

$$v_{OTC,k+1} = v_{OTC,k} e^{\frac{-T_S}{\tau_{OTC}}} + R_{OTC}\left(1 - e^{\frac{-T_S}{\tau_{OTC}}}\right) i_{Batt,k} \tag{4}$$

$$v_{Batt,k} = V_{OC}(SOC_k) - v_{OTC,k} - R_0 i_{Batt,k} \tag{5}$$

where: T_S – sampling period, τ_{OTC} – OTC time constant.

TTC Model, Basing on the observation of the battery output voltage when the battery output current is zero (no-load) it has been found out that the battery shows a big difference between the short time and the long time transient behavior. That means the dynamic characteristics cannot be represented very accurately by the OTC model.

To improve the flexibility of the OTC model an extra RC network is added in series to the OTC circuit to get the TTC circuit model. As shown in Figure 1 (c), the TTC circuit is composed of four parts: voltage source V_{OC}, ohmic resistance R_0, R_{TTC1} and C_{TTC1} to describe the short term characteristics, R_{TTC2} and C_{TTC2} to describe the long term characteristics. v_{TTC1} and v_{TTC2} are the voltages across C_{TTC1} and C_{TTC2} respectively. i_{TTC1} and i_{TTC2} are the outflow currents of C_{TTC1} and C_{TTC2} respectively [1].

The electrical behavior of the TTC circuit can be expressed by Equations 6, 7 and 8 in continuous time:

$$\dot{v}_{TTC1} = \frac{-1}{C_{TTC1} R_{TTC1}} v_{TTC1} + \frac{1}{C_{TTC1}} i_{Batt}, \tag{6}$$

$$\dot{v}_{TTC2} = \frac{-1}{C_{TTC2} R_{TTC2}} v_{TTC2} + \frac{1}{C_{TTC2}} i_{Batt}, \tag{7}$$

(8) $$v_{Batt} = V_{OC} - v_{TTC1} - v_{TTC2} - R_0 i_{Batt}\,.$$

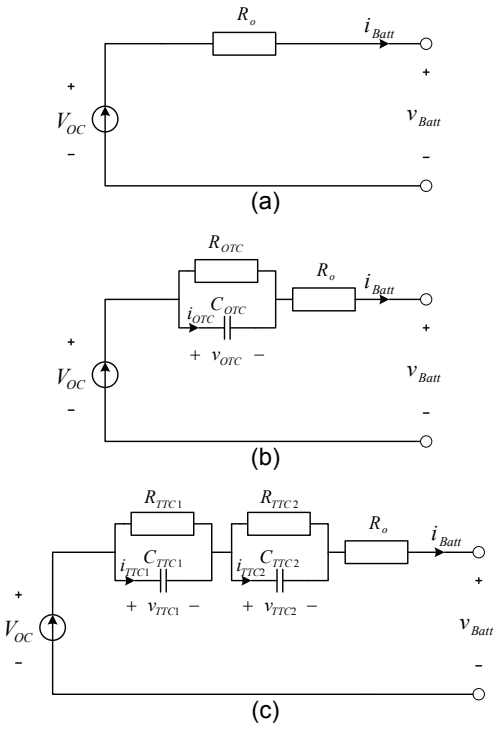

Fig.1. Battery equivalent circuit diagrams. (a) internal resistance model (IR), (b) one time constant model (OTC), (c) two time constants model (TTC).

The description in discrete time is given by Equations 9, 10 and 11:

$$v_{TTC1,k+1} = v_{TTC1,k} e^{\frac{-T_S}{\tau_{TTC1}}} + R_{TTC1}\left(1 - e^{\frac{-T_S}{\tau_{TTC1}}}\right) i_{Batt,k}\,, \tag{9}$$

$$v_{TTC2,k+1} = v_{TTC2,k} e^{\frac{-T_S}{\tau_{TTC2}}} + R_{TTC2}\left(1 - e^{\frac{-T_S}{\tau_{TTC2}}}\right) i_{Batt,k}\,, \tag{10}$$

$$v_{Batt,k} = V_{OC}(SOC_k) - v_{TTC1,k} - v_{TTC2,k} - R_0 i_{Batt}\,. \tag{11}$$

Estimation of Model Parameters

In this section the procedure of estimating the model parameters basing on battery measurements is demonstrated. In a first approach temperature and aging effects are neglected. The experimental parameter identification of the battery has been performed at the constant temperature of 25°C with relatively new and unused cells. The temperature and aging effects will be taken into account in a continuation of this work.

Charging and Discharging Process. Figure 2, shows characteristic curves of the battery output voltage and current when charging and discharging. In the following the different subintervals of the curves are described:

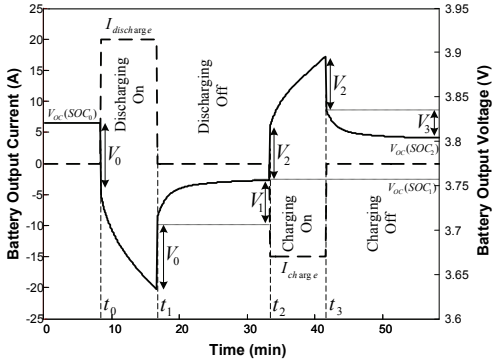

Fig. 2. Characteristic waveforms for battery output voltage and current during charging and discharging of lithium-ion cells.

- Subinterval S_0($t < t_0$): In this subinterval the battery output current can be assumed to zero over a sufficient time, though the output voltage can reach the open circuit voltage value $V_{OC}(SOC_0)$, and while the output current is zero the SOC value is constant.
- Subinterval S_1($t_0 \le t \le t_1$): In this subinterval the battery is discharged with a constant current $I_{discharge} > 0$, first a steep decrease of the battery output voltage can be seen due to the internal resistance R_0, and then it continues to decrease exponentially controlled by the OCV (as the SOC is decreasing).
- Subinterval S_2($t_1 \le t \le t_2$): In this subinterval the battery output current $i_{Batt} = 0$, so the battery output voltage at first will have a steep increase due to R_0, and then it shows an exponential increase until it reaches $V_{OC}(SOC_1)$.
- Subinterval S_3($t_2 \le t \le t_3$): In this subinterval the battery is charged with a constant current $I_{charge} < 0$; at first a steep increase of the battery output voltage can be seen due to internal resistance R_0, and then it continues to increase exponentially controlled by the OCV (as the SOC is increasing).
- Subinterval S_4($t \ge t_3$): In this time subinterval the battery output current $i_{Batt} = 0$, so the battery output voltage at first will have a steep decrease due to R_0, and then it has an exponential decrease until it reaches $V_{OC}(SOC_2)$.

Ohmic Resistance. The voltage drop across R_0 at the first time instant when charging (V_2) respectively discharging (V_0) can be taken to calculate R_0 [2], according to Equation 12:

$$R_0 = \begin{cases} \dfrac{V_0}{I_{discharge}} : for\ discharging \\ \dfrac{-V_2}{I_{charge}} : for\ charging \end{cases}. \tag{12}$$

Estimation of OTC Model Parameters. in this step battery output voltage measurements during the subintervals S_2 and S_4 are used, as in these subintervals OCV is constant, and the battery output voltage is just driven by the dynamic characteristics of the battery. The output voltage v_{Batt} during S_2 and S_4 can be calculated according to the OTC model by setting i_{Batt} to zero in Equations 2 and 3, then solving the differential equation as shown in Equation 13:

$$\begin{cases} S_2 : v_{Batt}(t) = V_{OC}(SOC_1) - v_{OTC}(t_1) e^{\frac{-t}{\tau_{OTC}}} \\ S_4 : v_{Batt}(t) = V_{OC}(SOC_2) - v_{OTC}(t_3) e^{\frac{-t}{\tau_{OTC}}} \end{cases}, \tag{13}$$

where:

(14) $$\tau_{OTC} = R_{OTC} C_{OTC} .$$

The identification of OTC model parameters necessitates the estimation of the values $V_{OC}(SOC_1)$, $V_{OC}(SOC_2)$, $v_{OTC}(t_1)$, $v_{OTC}(t_3)$ and τ_{OTC} in Equations 13 and 14. In order to estimate these parameters a nonlinear least squares algorithm is applied (nonlinear data fitting) to search for the values which lead to the best fit between the given measurements and the nonlinear function (in this case an exponential function $f(t)=A+Be^{-\alpha t}$ is used).

The output of the nonlinear least squares algorithm is a vector of the coefficients A, B and α. These coefficients will be used to calculate the OTC model parameters through Equations 15 to 19:

(15) $$\begin{cases} S_2 : V_{OC}(SOC_1) = A,\ v_{OTC}(t_1) = B \\ S_4 : V_{OC}(SOC_2) = A,\ v_{OTC}(t_2) = B \end{cases},$$

(16) $$\tau_{OTC} = \frac{1}{\alpha},$$

(17) $$\begin{cases} T_{discharge} = t_1 - t_0 \\ T_{charge} = t_3 - t_2 \end{cases},$$

(18) $$\begin{cases} S_2 : R_{OTC} = \dfrac{v_{OTC}(t_1)}{\left(1 - e^{\frac{-T_{discharge}}{\tau_{OTC}}}\right) I_{discharge}} \\ S_4 : R_{OTC} = \dfrac{v_{OTC}(t_3)}{\left(1 - e^{\frac{-T_{charge}}{\tau_{OTC}}}\right) I_{charge}} \end{cases},$$

(19) $$C_{OTC} = \frac{\tau_{OTC}}{R_{OTC}}.$$

Estimation of TTC Model Parameters. TTC model parameters can be estimated the same way as for the OTC model, by taking into consideration the two RC networks instead of one in the OTC model. The TTC model output voltage can be expressed during the subintervals S_2 and S_4 by Equations 20 and 21:

(20) $$\begin{cases} S_2 : v_{Batt} = V_{OC}(SOC_1) - v_{TTC1}(t_1) e^{\frac{-t}{\tau_{TTC1}}} - v_{TTC2}(t_1) e^{\frac{-t}{\tau_{TTC2}}} \\ S_4 : v_{Batt} = V_{OC}(SOC_2) - v_{TTC1}(t_3) e^{\frac{-t}{\tau_{TTC1}}} - v_{TTC2}(t_3) e^{\frac{-t}{\tau_{TTC2}}} \end{cases},$$

Table 1. SLPB120216216 Cell Data

Typical Capacity		53 Ah
Nominal Voltage		3.7 V
Charge Condition	Max. Current	53A
	Voltage	4.2 ± 0.03 V
Discharge Condition	Continuous Current	159 A
	Peak Current	260 A
	Cut-off Voltage	3.0 V

where:

(21) $$\begin{cases} \tau_{TTC1} = R_{TTC1} C_{TTC1} \\ \tau_{TTC2} = R_{TTC2} C_{TTC2} \end{cases}.$$

The identification of the TTC model requires to estimate the values $V_{OC}(SOC_1)$, $V_{OC}(SOC_2)$, $v_{TTC1}(t_1)$, $v_{TTC1}(t_3)$, $v_{TTC2}(t_1)$, $v_{TTC2}(t_3)$, τ_{TTC1} and τ_{TTC2} in Equations (20) and (21). In this case an exponential function with two time constants $f(t)=A+Be^{-\alpha t}+Ce^{-\beta t}$ is used.

The output of the nonlinear least squares algorithm is a vector of the coefficients A, B, C, α, and β. These coefficients will be used to calculate all TTC model parameters through Equations 22 to 27:

(22) $$\begin{cases} S_2 : V_{OC}(SOC_1) = A \\ S_4 : V_{OC}(SOC_2) = A \end{cases},$$

(23) $$\begin{cases} S_2 : v_{TTC1}(t_1) = B,\ v_{TTC2}(t_1) = C \\ S_4 : v_{TTC1}(t_3) = B,\ v_{TTC2}(t_3) = C \end{cases},$$

(24) $$\begin{cases} \tau_{TTC1} = \dfrac{1}{\alpha} \\ \tau_{TTC2} = \dfrac{1}{\beta} \end{cases},$$

(25) $$\begin{cases} S_2 : R_{TTC1} = \dfrac{v_{TTC1}(t_1)}{\left(1 - e^{\frac{-T_{discharge}}{\tau_{TTC1}}}\right) I_{discharge}} \\ S_4 : R_{TTC1} = \dfrac{v_{TTC1}(t_3)}{\left(1 - e^{\frac{-T_{charge}}{\tau_{TTC1}}}\right) I_{charge}} \end{cases},$$

(26) $$\begin{cases} S_2 : R_{TTC2} = \dfrac{v_{TTC2}(t_1)}{\left(1 - e^{\frac{-T_{discharge}}{\tau_{TTC2}}}\right) I_{discharge}} \\ S_4 : R_{TTC2} = \dfrac{v_{TTC2}(t_3)}{\left(1 - e^{\frac{-T_{charge}}{\tau_{TTC2}}}\right) I_{charge}} \end{cases},$$

(27) $$\begin{cases} C_{TTC1} = \dfrac{\tau_{TTC1}}{R_{TTC1}} \\ C_{TTC2} = \dfrac{\tau_{TTC2}}{R_{TTC2}} \end{cases}.$$

Experimental and Computational Results

For the experimental tests and modeling lithium polymer battery cells from the manufacturer Kokam have been used. Some important cell data are depicted in Table 1. To identify the model parameters, a battery test bench was set up. In this test bench a current signal with rectangular shape has to be applied to the battery with short and long interrupts. At the same time the battery output voltage has to be measured. The ohmic resistance R_0 of the battery can be calculated during short interrupts of the current signal, while OTC and TTC model parameters need to be estimated during long interrupts.

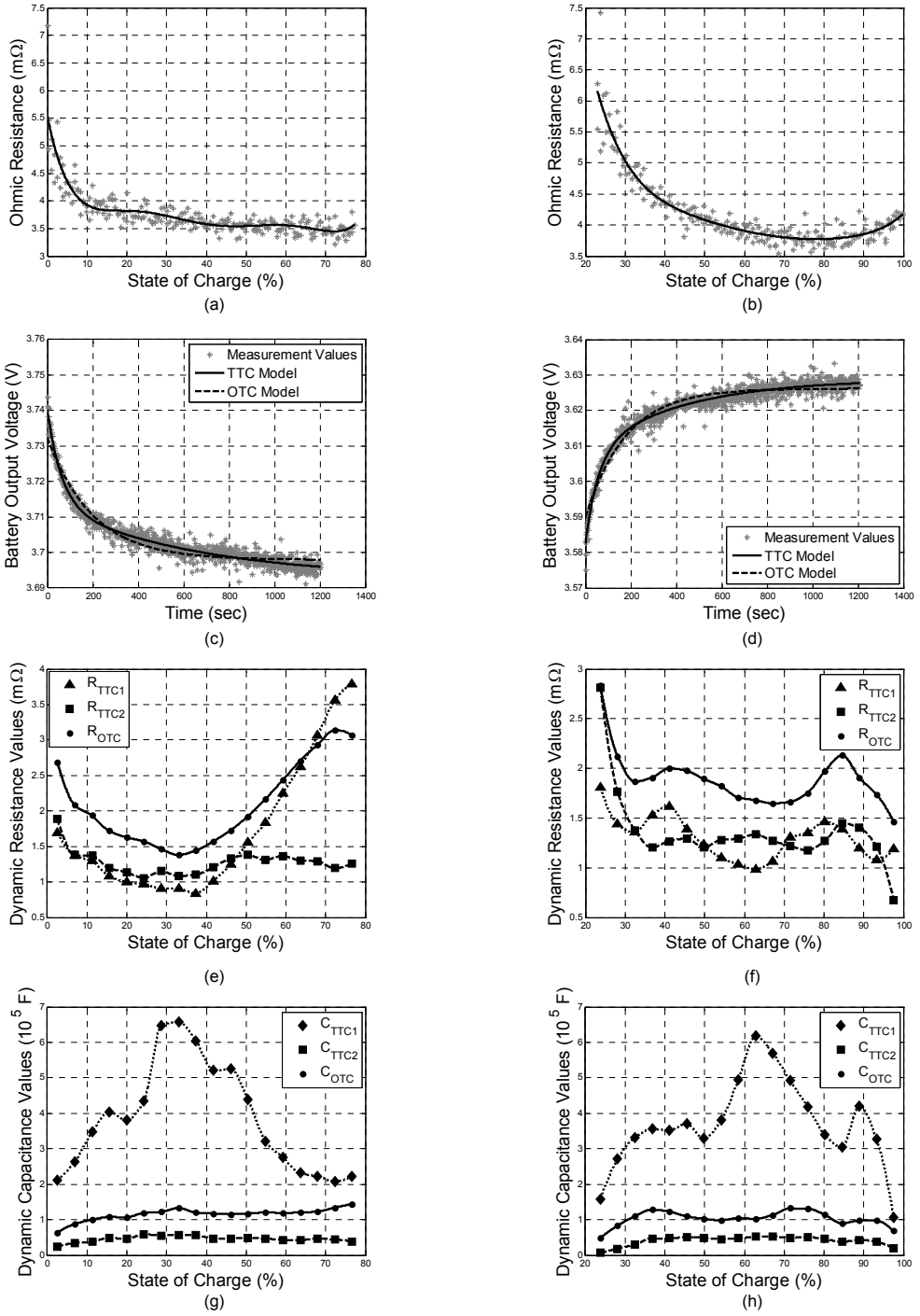

Fig. 3. (a), (b): ohmic resistance R_0 as a function of SOC during charging and discharging processes respectively; (c), (d): output voltage measurement and computational results during charging and discharging processes respectively; (e), (f): dynamic resistance values as a function of SOC during charging and discharging processes respectively; (g), (h): dynamic capacitance values as a function of SOC during charging and discharging processes respectively.

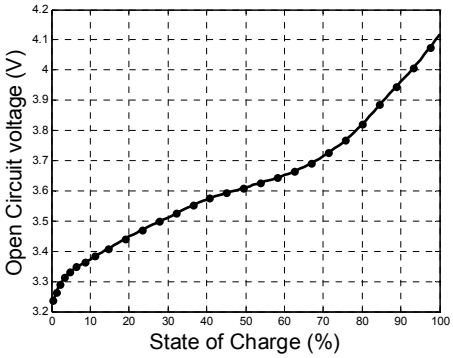

Fig. 4. Battery open circuit voltage as a function of SOC.

Experimental and Computational Results

For the experimental tests and modeling lithium polymer battery cells from the manufacturer Kokam have been used. Some important cell data are depicted in Table 1. To identify the model parameters, a battery test bench was set up. In this test bench a current signal with rectangular shape has to be applied to the battery with short and long interrupts. At the same time the battery output voltage has to be measured. The ohmic resistance R_0 of the battery can be calculated during short interrupts of the current signal, while OTC and TTC model parameters need to be estimated during long interrupts.

Ohmic Resistance Results: Ohmic resistance R_0 results are shown in Figures 3 (a) and (b) for charging and discharging processes respectively. It can be seen that R_0 increases at low SOC values in both, charging and discharging processes.

Values of the RC-Network Elements: Figures 3 (c) and (d). depict the battery output voltage measurement with the OTC and TTC model values for one long interrupt during charging and discharging processes respectively at 25°C. This processes are repeated over all long interrupts. From these two figures it can be seen that the TTC model has a better fit to the measurements than the OTC model, therefore the TTC model gives a better representation of the battery dynamics compared to the OTC model.

Dynamic resistance values are shown in Figures 3 (e) and (f) in both, charging and discharging processes respectively. These two figures demonstrate that there is not such a big deviation in the dynamic resistance values as it is the case with the dynamic capacitances. Dynamic capacitance values are depicted in Figures 3 (g) and (h) during both, charging and discharging processes respectively.

In these figures it can be seen that C_{TTC1} has a value being about 10 times greater than C_{TTC2}, that leads to a greater time constant τ_{TTC1} which is responsible for the long term effects in the battery. Figure 4 shows the battery open circuit voltage in dependence of SOC.

Conclusion

This paper presents three different equivalent circuit diagrams for lithium-ion batteries. The IR model is a very simple model, but it does not represent at all the dynamics of the battery and therefore it is not suitable for an accurate SOC determination during any dynamical operation. The OTC model describes the dynamic characteristics of the battery approximately (Figures 3 (c) and (d)). By adding a second RC network the dynamics of the lithium-ion battery can be approximated very accurately (Figures 3 (c) and (d)), thus a good estimation of SOC can be expected.

This paper demonstrates how to identify the parameters of the equivalent circuit diagrams of lithium-ion cells from characteristic measurements. The next step of this research consists of the application of an Extended Kalman Filter to obtain the optimum estimation of SOC. A comparison of the results with the Ampere-counting method will be shown.

Acknowledgment

The authors wish to thank the Federal Ministry of Economics of Germany for the financial support by the research projects eE-Tour (Electric Mobility) and IRENE (Integration of Renewable Energy and Electric Mobility). Further many thanks to Prof. Dr. R. Schmidt, President of the University of Applied Sciences Kempten, and Prof. Dr.-Ing. A. Rupp, Vice President for R&D, for their continuous support of the Institute for Applied Battery Research.

The publication of this paper was supported by the European Social Fund (project "Doctoral School of Energy and Geotechnology II").

REFERENCES

[1] Hongwen He, Rui Xiong, and Jinxin Fan, "Evaluation of Lithium-Ion Battery Equivalent Circuit Models for State of Charge Estimation by an Experimental Approach," *J. Energies*, vol. 4, pp 582-598, ISSN 1996-1073, March 2011.

[2] Hans-Georg Schweiger et al, "Comparison of Several Methods for Determining the Internal Resistance of Lithium-Ion Cells," *J. Sensors*, vol. 10, pp. 5604-5625, ISSN 1424-8220, June 2010.

[3] G. Plett, "Extended Kalman Filtering for Battery Management Systems of LiPB-Based HEV Battery Packs. Part 1. Background," *J. Power Sources*, vol. 134, pp. 252–261, 2004.

[4] Giacomo Marangoni, "Battery Management System for Li-Ion Batteries in Hybrid Electric Vehicles," M. Sc. thesis, Dept. of Information Engineering, University of Padova, Padua, Italy, 2010.

***Authors**: prof. dr.–ing. Helmuth Biechl, University of Applied Sciences Kempten, Bahnhofstraße 61, 87435 Kempten, Germany, E-mail: biechl@fh-kempten.de; dipl.–ing. Ahmad Rahmoun, University of Applied Sciences Kempten, Bahnhofstraße 61, 87435 Kempten, Germany, E-mail: ahmad.rahmoun@fh-kempten.de.*

PAPER- II A. Rahmoun, H. Biechl, and A. Rosin, “SOC estimation for Li-Ion batteries based on equivalent circuit diagrams and the application of a Kalman filter,” in 2012 Electric Power Quality and Supply Reliability, 2012, pp. 1–4.

SOC Estimation for Li-Ion Batteries Based on Equivalent Circuit Diagrams and the Application of a Kalman Filter

Ahmad Rahmoun, Helmuth Biechl, and Argo Rosin

Abstract-- **Batteries play an essential role in electric vehicles (EV), and obtain more and more importance also in smart grids due to the non-constant power generation of renewable energy sources. In order to achieve an optimum operation of systems with batteries it is necessary to develop accurate mathematical models for the calculation of the state of charge (SOC), taking into account the individual operation by the user. This paper presents the fundamentals of a method how to determine SOC of lithium-ion batteries on the basis of two different equivalent circuit diagrams and an Extended Kalman Filter (EKF). The comparison between measurement and computation results shows a good accordance. The accurate determination of SOC of a battery in an EV is of high importance for the prediction of the distance that can be driven. In the first step the dependency of these parameters on the temperature and on the battery age is neglected.**

Index Terms--**Batteries, Kalman filters, battery management system, state estimation, equivalent circuits.**

I. Introduction

STATE of charge (SOC) detection is one of the main tasks of every battery management system (BMS). This task can be achieved easily by using the Ampere-counting method which is considered to be the most accurate method, but on the other hand it requires some conditions such as an initial SOC value, and a regular full-charge or a regular full-discharge. In some applications these conditions are not always fulfilled (full-charge or full-discharge), therefore SOC computation directly from the current measurements is not possible due to the measurement error accumulation. For such applications the SOC can be estimated by using a mathematical model to represent the dynamic characteristics of the battery, and an estimator which observes the battery output measurements and generates an estimation value of the SOC which minimizes the error between battery and model outputs [1].

This paper is a continuation of a previous work, where two models were presented basing on the equivalent circuit diagrams. These two models will be used together with a Kalman filter in order to estimate the SOC [2].

A Kalman filter is essentially a set of recursive mathematical equations implementing a predictor-corrector type estimator. It generates an optimal estimation of the system state based on the input control and output measurements, therefore it is used mainly when the system state cannot be measured directly, and it needs to be estimated optimally from the output measurements [3].

In this paper at first the discrete Kalman filter for linear systems is presented, then the extended Kalman filter (EKF) for non-linear systems is explained, and finally a state space model for the Li-Ion battery is setup. Further, comparisons between SOC values computed by Ampere-counting and SOC values estimated by EKF are carried out to evaluate the validity of the demonstrated method.

II. The Discrete Kalman Filter

This section describes the basic structure of a Kalman filter where the measurements are taken and the system state is estimated at discrete time values [3]–[4].

A. The Process Model

The discrete Kalman filter handles the problem of estimating the state vector $x_k \in R^n$ of a discrete time controlled process which is governed by the linear difference stochastic equation (1).

$$x_{k+1} = A_k x_k + B_k u_k + w_k \tag{1}$$

where the measurement vector $y_k \in R^m$ is given by (2).

$$y_k = C_k x_k + D_k u_k + v_k \tag{2}$$

Equation (1) is called "state equation" or "process equation". This equation describes the system dynamics, system stability, controllability and sensitivity to disturbance. The control input to the system is $u_k \in R^p$, and $w_k \in R^n$ is a random variable that represents the "process noise". Equation (2) is called the "output equation". This equation defines how the system output depends on the state vector x_k and control input u_k plus $v_k \in R^m$, which models the measurement noise.

The matrix $A_k \in R^{n \times n}$ describes the system dynamics and relates the state at the previous time step $k-1$ to the state at the current time step k when the control input u_k is zero. The matrix $B_k \in R^{n \times p}$ relates the control input u_k to the state x_k. The matrices $C_k \in R^{m \times n}$ and $D_k \in R^{m \times p}$ relate the measurement y_k to the state x_k and control input u_k. All these matrices can be time varying.

The Kalman filter method can give the optimum estimation of the unmeasured state value x_k for a given system model (by knowing all the system matrices), a known control input u_k and the measurement y_k under certain assumptions. First, both w_k and v_k are assumed to be mutually uncorrelated white Gaussian random processes

A. Rahmoun and H. Biechl are with the Institute for Applied Battery Research, University of Applied Sciences Kempten, Kempten, Germany (e-mail: ahmad.rahmoun@fh-kempten.de, biechl@fh-kempten.de).

A. Rosin is with the Department of Electrical Drives and Power Electronics, Tallinn University of Technology, Tallinn, Estonia (e-mail: argo.rosin@ttu.ee).

978-1-4673-1979-9/12/$31.00 ©2012 IEEE

with zero mean and covariance matrices with known values as shown in (3) and (4).

$$P(w) \sim N(0, Q) \tag{3}$$

$$P(v) \sim N(0, R) \tag{4}$$

Process noise covariance Q and measurement noise covariance R might change with each time step, but here we assume that they are constants.

Second, the system must be "Observable" that means it is possible to estimate the state from the output. The system which we work on meets this requirement.

B. The Discrete Kalman Filter Algorithm

The discrete Kalman filter algorithm uses the entire observed data $\{u_0, u_1, \ldots\ldots, u_k\}$ and $\{y_0, y_1, \ldots\ldots, y_k\}$ to find the minimum mean square error estimation $\hat{x}_k$ of the true state x_k taking into consideration the assumptions on w_k and v_k, and the system model as shown in (1) and (2).

The algorithm consists mainly of two stages: "time update" and "measurement update". In the time update stage the first estimation of the state $\hat{x}_k^-$ and error covariance P_k^- are calculated basing on the system model and a prior estimation $\hat{x}_{k-1}^+$ and P_{k-1}^+ from the previous time step as shown in (5) and (6). Both (5) and (6) are computed before any new measurements are made.

$$\hat{x}_k^- = A_{k-1}\hat{x}_{k-1}^+ + B_{k-1}u_{k-1} \tag{5}$$

$$P_k^- = A_{k-1}P_{k-1}^+A_{k-1}^T + Q \tag{6}$$

If the system is stable then $A_{k-1}P_{k-1}^+A_{k-1}^T$ is contractive. This will reduce the uncertainty of the state estimation over the time. The process noise term Q always increases the uncertainty because w_k cannot be measured. The second estimated $\hat{x}_k^+$ tunes up the first estimated $\hat{x}_k^-$ after measuring the system output y_k. The state and error covariance $\hat{x}_k^+$ and P_k^+ are now more accurate than $\hat{x}_k^-$ and P_k^- as they involve the information from the measurement y_k. The new measurement adds a new information through a correction factor which is equal to the measured system output y_k minus the predicted system output $\hat{y}_k = C_k\hat{x}_k^- + D_ku_k$. The new state estimation $\hat{x}_k^+$ is equal to the predicted state estimation plus a weighted correction factor as shown in (7).

$$\hat{x}_k^+ = \hat{x}_k^- + K_k\left[y_k - \left(C_k\hat{x}_k^- + D_ku_k\right)\right] \tag{7}$$

The term K_k in (7) is a gain matrix which is called Kalman gain and given by (8).

$$K_k = P_k^-C_k^T\left(C_kP_k^-C_k^T + R\right)^{-1} \tag{8}$$

If the current state estimation $\hat{x}_k^-$ is very uncertain, then P_k^- tends to be "large" which leads to a large Kalman gain, which means a large update for the state estimation $\hat{x}_k^+$. If the current sate estimation is certain, the Kalman gain tends to be small which means a small update to the state estimation. Also if the measurement noise is large through a high R value, this will lead to a small Kalman gain and the update is small. The Kalman gain also balances the signal to noise ratio (SNR) of the sensor. When the sensor has a high SNR value Kalman gain is small and the Kalman filter converges faster.

The error covariance is also corrected through (9). In this formula the Kalman gain is also used and the state uncertainty is decreased due to the new information provided by the measurement.

$$P_k^+ = \left(I - K_kC_k\right)P_k^- \tag{9}$$

The Kalman filter is initialized with the best available information on the state and error covariance as shown in (10).

$$\hat{x}_0^+ = E[x_0],\ P_0^+ = E\left[\left(x_0 - \hat{x}_0^+\right)\left(x_0 - \hat{x}_0^+\right)^T\right] \tag{10}$$

Often, these quantities are not precisely known, but this is not a problem as the Kalman filter is known to be very robust to poor initialization, and will quickly converge to the true values as it runs.

III. Extended Kalman Filter

The Kalman filter is the optimum state estimator for a linear system with the assumptions as described. If the system is nonlinear, then we may use a linearization process at every time step to approximate the nonlinear system with a linear time varying (LTV) system. This LTV system is then used in the Kalman filter, resulting in an extended Kalman filter (EKF) on the true nonlinear system. The nonlinear system is presented in (11), (12) [3]–[5].

$$x_{k+1} = f(x_k, u_k) + w_k \tag{11}$$

$$y_{k+1} = g(x_k, u_k) + v_k \tag{12}$$

As before, w_k and v_k are assumed to be mutually uncorrelated white Gaussian random processes, with zero mean and covariance matrices Q and R respectively. Now, $f(.,.)$ is a nonlinear state transition function and $g(.,.)$ is a nonlinear measurement function.

At each time step, $f(x_k, u_k)$ and $g(x_k, u_k)$ are linearized by a first-order Taylor-series expansion. We assume that $f(.,.)$ and $g(.,.)$ are differentiable at all operating points (x_k, u_k) as shown in (13) and (14).

$$f(x_k, u_k) \approx f(\hat{x}_k, u_k) + \underbrace{\left.\frac{\partial f(x_k, u_k)}{\partial x_k}\right|_{x_k = \hat{x}_k}}_{\text{defined as } \hat{A}_k}\left(x_k - \hat{x}_k\right) \tag{13}$$

$$g(x_k, u_k) \approx g(\hat{x}_k, u_k) + \underbrace{\left.\frac{\partial g(x_k, u_k)}{\partial x_k}\right|_{x_k = \hat{x}_k}}_{\text{defined as } \hat{C}_k}\left(x_k - \hat{x}_k\right) \tag{14}$$

By combining equations (11) and (12) with (13) and (14) we get the linearized equations (15) and (16) describing the nonlinear system.

$$x_{k+1} \approx \hat{A}_kx_k + \underbrace{f(\hat{x}_k, u_k) - \hat{A}_k\hat{x}_k}_{\text{not a function of } x_k} + w_k \tag{15}$$

$$y_k \approx \hat{C}_kx_k + \underbrace{g(\hat{x}_k, u_k) - \hat{C}_k\hat{x}_k}_{\text{not a function of } x_k} + v_k \tag{16}$$

By using these approximations, the EKF algorithm is developed in a way similar to the discrete Kalman filter. The terms labeled “not a function of x_k” replace the B_ku_k and D_ku_k in the discrete Kalman filter.

IV. Battery State Space Model

A. Battery Models

In a previous work two battery models were investigated. These two models were set up basing on equivalent circuit diagrams [2]. The first model is called "one time constant model (OTC)", as shown in Fig. 1a. It consists of three parts including the voltage source V_{OC}, the ohmic resistance R_0, and R_{OTC}, C_{OTC} to describe the battery transient response during charging or discharging. v_{OTC} is the voltage across C_{OTC}; i_{OTC} is the current that flows in C_{OTC}. The electric behavior of the OTC model can be expressed by (17) and (18) in discrete time:

$$v_{OTC,k+1} = v_{OTC,k} * exp[-T_S /(R_{OTC} * C_{OTC})] + R_{OTC} * \{1 - exp[-T_S /(R_{OTC} * C_{OTC})]\} * i_{Batt,k}, \quad (17)$$

$$v_{Batt,k} = V_{OC}(SOC_k) - v_{OTC,k} - R_0 * i_{Batt,k}, \quad (18)$$

The second model is called "two time constants model (TTC)", as shown in Fig. 1b it is composed of four parts: voltage source V_{OC}, ohmic resistance R_0, R_{TTC1} and C_{TTC1} to describe the short term characteristics, R_{TTC2} and C_{TTC2} to describe the long term characteristics. v_{TTC1} and v_{TTC2} are the voltages across C_{TTC1} and C_{TTC2} respectively. i_{TTC1} and i_{TTC2} are the outflow currents of C_{TTC1} and C_{TTC2} respectively. The electrical behavior of the TTC circuit can be expressed by (19), (20) and (21) in discrete time:

$$v_{TTC1,k+1} = v_{TTC1,k} * exp[-T_S /(R_{TTC1} * C_{TTC1})] + R_{TTC1} * \{1 - exp[-T_S /(R_{TTC1} * C_{TTC1})]\} * i_{Batt,k}, \quad (19)$$

$$v_{TTC2,k+1} = v_{TTC2,k} * exp[-T_S /(R_{TTC2} * C_{TTC2})] + R_{TTC2} * \{1 - exp[-T_S /(R_{TTC2} * C_{TTC2})]\} * i_{Batt,k}, \quad (20)$$

$$v_{Batt,k} = V_{OC}(SOC_k) - v_{TTC1,k} - v_{TTC2,k} - R_0 * i_{Batt}. \quad (21)$$

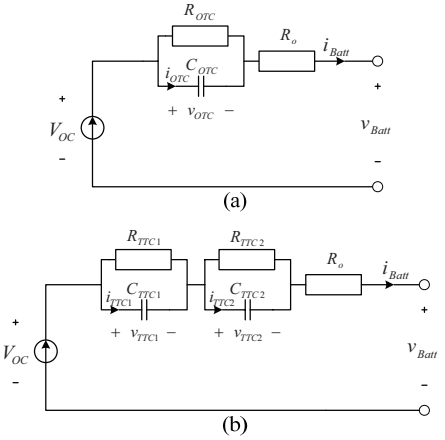

Fig. 1. Battery equivalent circuit diagrams. (a): one time constant model (OTC); (b): two time constants model (TTC).

B. OTC Model State Space Form

For finding the state space model for the OTC model, we define the state vector x_k as shown in (22):

$$x_{OTC,k} = \begin{pmatrix} v_{OTC,k} \\ S_k \end{pmatrix}, \quad (22)$$

where S_k is the abbreviation of SOC at the time step k, S_k is given by (23):

$$S_k = S_{k-1} + \eta i_{Batt,k} T_S / C_N, \quad (23)$$

where T_S is the sampling time, η is the coulombic efficiency, and C_N is the nominal capacity of the battery.

By using (17), (18), (22) and (23) OTC model matrices can be extracted as shown in (24).

$$A_{OTC,k} = \begin{pmatrix} e^{\frac{-T_S}{R_{OTC,k} C_{OTC,k}}} & 0 \\ 0 & 1 \end{pmatrix}$$

$$B_{OTC,k} = \begin{pmatrix} R_{OTC,k}\left(1 - e^{\frac{-T_S}{R_{OTC,k} C_{OTC,k}}}\right) \\ \frac{-\eta T_S}{C_N} \end{pmatrix} \quad (24)$$

$$C_{OTC,k} = \left.\frac{\partial v_{Batt}}{\partial x}\right|_{x=\hat{x}_k} = \left[-1 \quad \left.\frac{\partial V_{OC}(S)}{\partial S}\right|_{x=\hat{x}_k}\right]$$

$$D_{OTC,k} = \left[-R_{0,k}\right]$$

And the discrete time state space form for the OTC model is shown in (25) and (26).

$$x_{OTC,k+1} = A_{OTC,k} x_{OTC,k} + B_{OTC,k} i_{Batt,k} + w_k \quad (25)$$

$$v_{Batt,k} = C_{OTC,k} x_{OTC,k} + D_{OTC,k} i_{Batt,k} + v_k \quad (26)$$

C. TTC Model State Space Form

The state vector of this model consists of three state variables as shown in (27).

$$x_{TTC,k} = \begin{pmatrix} v_{TTC1,k} \\ v_{TTC2,k} \\ S_k \end{pmatrix}, \quad (27)$$

where the matrices A, B, C, D are given by (28).

$$A_{TTC,k} = \begin{pmatrix} e^{\frac{-T_S}{R_{TTC1,k} C_{TTC1,k}}} & 0 & 0 \\ 0 & e^{\frac{-T_S}{R_{TTC2,k} C_{TTC2,k}}} & 0 \\ 0 & 0 & 1 \end{pmatrix}$$

$$B_{TTC,k} = \begin{pmatrix} R_{TTC1,k}\left(1 - e^{\frac{-T_S}{R_{TTC1,k} C_{TTC1,k}}}\right) \\ R_{TTC2,k}\left(1 - e^{\frac{-T_S}{R_{TTC2,k} C_{TTC2,k}}}\right) \\ \frac{-\eta T_S}{C_N} \end{pmatrix}$$

$$C_{TTC,k} = \left.\frac{\partial v_{Batt}}{\partial x}\right|_{x=\hat{x}_k} = \left[-1 \quad -1 \quad \left.\frac{\partial V_{OC}(S)}{\partial S}\right|_{x=\hat{x}_k}\right]$$

$$D_{TTC,k} = \left[-R_{0,k}\right]. \quad (28)$$

The discrete time state space form for the TTC model is shown in (29) and (30).

$$x_{TTC,k+1} = A_{TTC,k} x_{TTC,k} + B_{TTC,k} i_{Batt,k} + w_k \quad (29)$$

$$v_{Batt,k} = C_{TTC,k} x_{TTC,k} + D_{TTC,k} i_{Batt,k} + v_k \quad (30)$$

V. Experimental And Computational Results

A. SOC Estimation with Adaptive Model Parameters

The SOC estimation is done by using an extended Kalman filter with adaptive model parameters. Parameter values are calculated in each time step during the estimation as a function of SOC. In order to do this calculation a linear interpolation is used. Fig. 2 shows SOC estimation results

for both models OTC and TTC in comparison to Ampere counting results. This figure shows approximately identical curves for SOC.

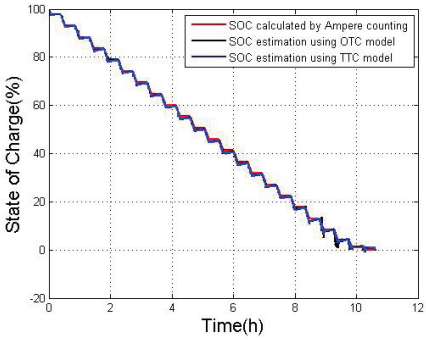

Fig. 2. Battery SOC estimation values using EKF for OTC and TTC models compared to SOC calculated by the Ampere counting method.

The percentage error between SOC values estimated by EKF for both OTC and TTC models and SOC values calculated by the Ampere counting method is depicted in Fig. 3. It shows that the SOC estimation using TTC model gives more accuracy than using the OTC model (see Fig. 3, after 8 hours). The TTC model achieves approximately 20% less absolute average error and approximately three times less absolute maximum error than the OTC error. This was expected because the TTC model represents the Li-Ion battery better than the OTC model.

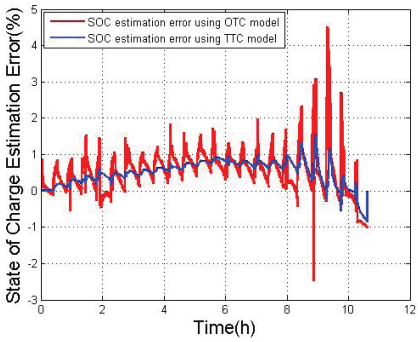

Fig. 3. Battery SOC estimation percentage error for OTC and TTC models.

B. SOC Estimation at Different Initial Values

An accurate SOC estimation depends on two aspects according the definition of SOC given by (23). The first is the initial SOC value, and the second is the calculation method. In order to investigate how the SOC estimation is affected by the initial value for SOC, a value of 90% is used for a fully charged battery, and the result is shown in Fig. 4. It shows very well that SOC estimation starts with wrong values and converges very quick towards the real SOC value.

VI. Conclusion

This paper presents the application of an Extended Kalman filter on Li-Ion batteries to obtain the optimum estimation of SOC. For this purpose Kalman filter and extended Kalman filter methods are applied.

A comparison between the Ampere-counting method and the SOC estimation by using EKF has been shown. The TTC

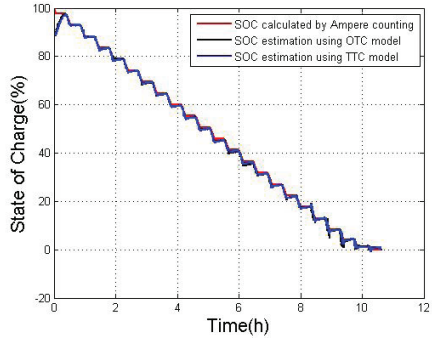

Fig. 4. Battery SOC estimation values using EKF for OTC and TTC models at initial SOC value of 90% for a full battery.

model results in a higher accuracy concerning SOC estimation compared to the OTC model. Further, the effect of incorrect initial values on the SOC estimation has been demonstrated. In a continuation of this research the effect of temperature and aging will be taken into account. Finally the algorithm will be realized by hardware for an online SOC estimation.

VII. Acknowledgment

The authors wish to thank the Federal Ministry of Economics of Germany for the financial support by the research project IRENE (Integration of Renewable Energy and Electric Mobility). Further many thanks to Prof. Dr.-Ing. A. Rupp, Vice President for R&D, for his continuous support of the Institute for Applied Battery Research.

VIII. References

[1] G. Marangoni, "Battery Management System for Li-ion Batteries in Hybrid Electric Vehicles," Padova, 2010.

[2] A. Rahmoun and H. Biechl, "Parameters identification of equivalent circuit diagrams for li-ion batteries," *in Proc.* 2012 11th International Symposium PÄRNU, pp. 37-41.

[3] G. Welch and G. Bishop, "An introduction to the Kalman filter," University of North Carolina at Chapel Hill, Department of Computer Science, Chapel Hill, 2001, pp. 1-41.

[4] G. L. Plett, "Extended Kalman filtering for battery management systems of LiPB-based HEV battery packs Part 1. Background," *Journal of Power Sources 134,* 2004.

[5] G. L. Plett, "Extended Kalman filtering for battery management systems of LiPB-based HEV battery packs Part 2. Modeling and identification," *Journal of Power Sources*, p. 262–276, 28 May 2004.

[6] H. He, R. Xiong and J. Fan, "Evaluation of Lithium-Ion Battery Equivalent Circuit Models for State of Charge Estimation by an Experimental Approach," Energies, pp. 582-598, June 2011.

IX. Biographies

Ahmad Rahmoun M.Eng.(L'2012) was born in Damascus in Syria, on January 20, 1983. He graduated from Higher Institute for Applied Sciences and Technology (HIAST), Damascus, and finished his Master study of Electrical Engineering at the University of Applied Sciences Kempten, Germany. His employment experience included Digital Image and Signal Processing Lab (HIAST), and he is currently a research engineer and a PhD student at the Institute for Applied Battery Research (IABF) at the University of Applied Sciences Kempten.

Helmuth Biechl, PhD, is a professor and the director of the Institute for Applied Battery Research (IABF), University of Applied Sciences Kempten, Kempten, Germany.

Argo Rosin, PhD, is a Senior Research Scientist at the Department of Electrical Drives and Power Electronics, Tallinn University of Technology, Estonia.

PAPER- III A. Rahmoun, H. Biechl, and A. Rosin, “Evaluation of Equivalent Circuit Diagrams and Transfer Functions for Modeling of Lithium-Ion Batteries,” Electr. Control Commun. Eng., vol. 2, no. 1, pp. 34–39, May 2013.

VERSITA
Electrical, Control and Communication Engineering
doi: 10.2478/ecce-2013-0005
2013 / 2

Evaluation of Equivalent Circuit Diagrams and Transfer Functions for Modeling of Lithium-Ion Batteries

Ahmad Rahmoun (*Researcher, Institute for Applied Battery Research – IABF*), Helmuth Biechl (*Director, IABF*) and Argo Rosin (*Senior Research Scientist, Tallinn University of Technology*)

***Abstract* – The rapid developments in the field of electrochemistry, enabled lithium-ion batteries to achieve a very good position among all the other types of energy storage devices. Therefore they became an essential component in most of the modern portable and stationary energy storage applications, where the specific energy and the life time play an important role. In order to analyze and optimize lithium-ion batteries an accurate battery model for the dynamic behavior is required. At the beginning of this paper four different categories of electrical models for li-ion cells are presented. In the next step a comparison between equivalent circuit diagrams and fractional rational functions with the complex variable s is shown for lithium-ion battery modeling. It is described how to identify the parameters of the models in the time domain and also in frequency domain. The validation of the different models is made for high and low dynamic current profiles. In the first step the dependency of all model parameters on the temperature and on the battery age is neglected. These effects will be taken into account in the continuation of this work.**

***Keywords* – Batteries, equivalent circuits, mathematical model, transfer functions.**

I. Introduction

In order to analyze and optimize systems with Li-ion batteries, such as smart grids with big energy storage devices, photovoltaic, and other systems, it is necessary to have accurate electrical models of all the components in the system. Regarding Li-ion cells the dynamic behavior depends on SOC, internal temperature and aging. Therefore all three effects should be taken into account. An accurate model must produce (over the whole life time) a precise prediction of the output voltage during different discharge/charge current rates, and ambient temperatures of the battery. Additional models are needed for the accurate estimation of other battery parameters such as state of charge (SOC), internal temperature and state of health (SOH).

By having battery models that can fulfill all the previous requirements, storage system designers can predict and optimize system performance under different conditions just by simulation, and therefore they can reduce the experimental efforts and time [1], [2].

Modeling of Li-ion batteries is not an easy task due to the following reasons [3] – [6]:

- Li-ion batteries are complex systems due to SOC variation, diffusion phenomenon and different aging effects.
- They are highly nonlinear systems regarding SOC, temperature, and aging.

In the way to develop an accurate model for Li-ion batteries both time and frequency domain behaviors of the model should be investigated thoroughly. For this purpose two groups of models have been investigated in this paper. The first group contains the equivalent circuit models with RLC elements which can be easily identified from the time domain measurements. The second group consists of fractional rational functions representing a good method to fit the battery impedance spectrum curves in frequency domain.

This paper is structured as follows: Section II presents a brief state of art analysis of the different model architectures used to model Li-ion batteries; Section III explains the two types of the identification methods and how to be applied to the selected models. Section IV shows the experimental setup and experimental results used to validate the models, Section V concludes this paper.

The research work which is published in the paper is a step forward on the way to simulate a big energy storage system in the research project "IRENE" (Integration of Renewable Energies and Electromobility). This energy storage system (300kW, 170kWh) includes also inverters, transformers, filters, and other power electronic devices [7].

II. Battery Models

The first step in the modeling process is always to choose the right model structure which is able to represent the physical phenomena which occur inside the battery. However the main difficulty in this process is always how to compromise between model accuracy and complexity. In other words the model must be accurate enough to fit the dynamic requirements of the application, and at the same time it should be as simple as possible.

This compromise between accuracy and complexity has pushed the researchers to find out many model different structures. These structures can be categorized according to the following four aspects:

A. Full Parametric Model

It describes mathematically the whole behavior of the cell including the open circuit voltage (OCV) as a function of SOC, hysteresis and cell temperature. This kind of model is very suitable for parameter and state estimation purposes as shown in [8] – [10], where five mathematical state-space structures have been introduced as follows:

- Combined model

- Simple model
- Zero-State hysteresis model
- One-State hysteresis model
- Enhanced self-correcting (ESC) model

The parameters of these models are identified by the use of Extended Kalman Filter (EKF), and then a comparison between the simulation and measurement results is made by calculating the average of the root mean value of the error (RMSE). Ref. [9] depicts that the simple model has the highest RMSE of 53.8mV over temperature range between 30 and 45°C, the best model according to this study is the ESC model which can achieve a RMSE of 11,8mV over the same temperature range. Similar results can be also extracted from [10]. The main advantage of this type of models is the small number of parameters to model the cell.

B. Equivalent Circuit Model with RLC Elements

It uses a network of R, L and C elements to simulate the dynamic characteristics of the Li-ion cell, and a voltage source to model the OCV as shown in Fig.1, demonstrating one time constant (OTC) model and two time constants (TTC) model [11]. This type of models can afford a better accuracy compared to the full parametric models [12]. On the other hand they need larger memory size to store the model parameters and the OCV look up table. So they are compromising between the model accuracy and memory size.

Ref. [12] introduces a comparative study between twelve model structures for li-ion batteries, the twelve model structures include the five structures which have been already introduced in the last paragraph, beside the equivalent circuit model structures with one, two, three time constants, and taking into account with or without hysteresis effect. The model parameters are identified in time domain using multi-swarm particle swarm optimization (MPSO) method.

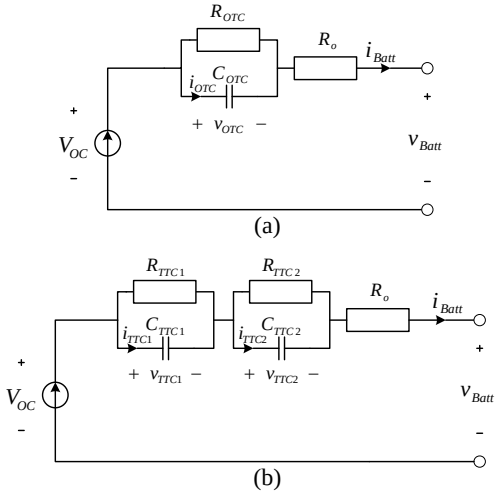

Fig.1. Battery equivalent circuit diagrams: (a) one time constant model (OTC), (b) two time constants model (TTC).

Ref. [12] indicates that the equivalent circuit models with RC elements can afford a lower RMSE than the full parametric models for LiNMC and $LiFePO_4$ cells.

C. Equivalent Circuit Models with Zarc and Warburg Elements

The idea behind this type of models is to simulate the behavior of the Li-ion cell in both time and frequency domains very precisely. To achieve this goal new elements have been introduced in the frequency domain such as the constant phase element (CPE), the Zarc element, and the Warburg element. These elements do not have a Laplace transformation, thus it is not possible to have a representation of them in time domain without approximations [13].

Ref. [13] shows also a comparison between an equivalent circuit model with RLC elements and an equivalent circuit model using Zarc and Warburg elements by applying different test profiles to the cell at different temperatures. Subsequently the measured output voltage is compared to the calculated output of both models. As a result of the comparison both models can produce a very satisfying agreement with the measured values. In opposite the equivalent circuit model with Zarc and Warburg elements is able to reproduce the impedance spectra more accurately than the equivalent circuit model with RLC elements at the cost of double of the computation time.

D. Fractional Rational Functions

This is our new approach to find out an optimum between model accuracy and complexity. This approach imposes that the battery model should match the time and frequency domain behavior of Li-ion battery as accurate as possible without using any complex structures.

Fractional rational functions can be used as a general concept for modeling any linear system in the frequency domain. They have been used extensively in many applications [14]. Therefore one can get benefit from the high number of literature sources and applications in this field. The fractional rational function is defined as shown in (1), n_b and n_a are numerator and denominator orders respectively (where $a_0 \neq 0$ and $b_0 \neq 0$), $\{b_0,b_1,\cdots,b_{nb}\}$ and $\{a_0,a_1,\ldots,a_{na}\}$ are the numerator and denominator coefficients respectively.

$$H(s)=\frac{B(s)}{A(s)}=\frac{b_0 s^{n_b}+b_1 s^{n_b-1}+\cdots+b_{n_b}}{a_0 s^{n_a}+a_1 s^{n_a-1}+\cdots+a_{n_a}}. \qquad (1)$$

The advantage of using fractional rational functions for modeling of Li-ion cells mainly is flexibility. Fractional rational functions do not need complex optimization methods to estimate model parameters. The model parameters can be identified in the frequency domain but also in the time domain where the state space representation is used and the same coefficients occur [15]. Above all the model accuracy can be improved by increasing the order of polynomials in the numerator and denominator. Hence the fractional rational functions are a good choice to model the frequency response of a battery and thus the dynamic behavior in the range where it can be treated as being linear.

III. Identification Methods

Identification methods can be divided mainly into two branches as follows:

A. Time Domain Identification Methods

These methods consist of applying a current signal with a defined profile to the battery, and measuring the output voltage. The current profile can be a pulse with a high current value or it can be a pseudo random binary sequence. These methods have the advantage of the possibility to use high current values during modeling; on the other hand the frequency range might be limited by the sampling frequency and therefore the model at high frequencies cannot be identified accurately enough.

B. Frequency Domain Identification Methods

These methods employ the electrochemical impedance spectroscopy (EIS) technique to extract the complex impedance values over a certain frequency range. Subsequently the impedance curves are fitted to a variety of model structures by using the nonlinear complex least square (NCLS) optimization method. The EIS technique affords a precise impedance measurement in a wide band of frequencies but only for low current values [13], [16].

The next paragraphs show a description of two different model structures, and the identification methods which have been used to adapt the model parameters.

C. Parameters Identification of the RC Elements of an Equivalent Circuit Model

The identification of the model parameters is made by applying a current signal to the battery with rectangular shape with short and long interruptions. At the same time the battery output voltage is measured. The ohmic resistance R_o of the battery is calculated during short interruptions of the current signal, while OTC and TTC model parameters are estimated during long interruptions using nonlinear least squares algorithm [11].

D. Parameters Identification of Fractional Rational Function

By applying the EIS technique to the battery, complex values of the impedance are obtained for discrete frequencies. These values form the battery frequency response. The adaptation of the model parameters is made by using the Matlab function “invfreqs”. This function finds the continuous-time transfer function H(s) corresponding to a given complex frequency response with n frequency pins. “invfreqs” uses the equation error in (2) to optimize the fitting in order to find the best model which fits the data.

$$\min_{a,b} \sum_{k=1}^{n} w_k \left| h_k A(\omega_k) - B(\omega_k) \right|^2 , \qquad (2)$$

where: $\{w_k: k=1,2,\ldots,n\}$ are the weighting factors. After obtaining the transfer function coefficients, $\{b_0,b_1,\ldots,b_{nb}\}$ and $\{a_0,a_1,\ldots,a_{na}\}$ the continuous time transfer function H(s) is converted into discrete time transfer function H(z) by using of the Matlab function “c2d” with the sampling time Ts=100ms. Finally the discrete time transfer function H(z) is simulated by using Matlab function “lsim”.

This identification process has been applied to the battery impedance measurements in order to calculate the parameters of a third order transfer function (TF_3: $n_b = n_a = 3$) and a sixth order transfer function (TF_6: $n_b = n_a = 6$).

IV. Validation of the Models

For the validation experiment a lithium polymer battery cell has been used, the important cell data are depicted in Table I.

The validation criterion consists of two stages. In first stage the EIS meter measurements respectively the current pulse is applied to the battery in order to identify the parameters of models concerning equivalent circuit diagrams respectively fractional rational functions. Fig.2 and Fig.3 show the measured Nyquist and bode plots of the battery impedance and the frequency responses of the models. The sixth order transfer function shows the best fit to the impedance curve. The third order transfer function comes in the second place; it shows a rough approximation of the battery. Both equivalent circuit diagrams OTC and TTC show an analogue behavior of the battery but only for low frequencies.

The second stage includes applying a current profile with two phases (phase-I and phase-II) to the battery. During this time the output voltage is acquired with the same sampling time Ts. The first phase is dedicated to test the transient response of the different models for the high dynamic current profiles, and the second phase is dedicated to test the steady state error of the models.

Phase-I of the current profile is a random pseudo sequence of current pulses with a mean value of zero. The maximum absolute value of the current pulses is 40A. Each current pulse has the duration of 1s, and the number of pulses is 120, which results in 120 seconds for the whole duration of phase-I.

Phase-II consists of a current pulse with constant value of 20A for duration of 10 minutes. This duration is chosen to be long enough to test the models error in the steady state and short enough to hold the deviation of SOC value within appropriate limits (otherwise the models require a SOC adaptation). Phase-I and Phase-II represent the high and low dynamical load with respect to the electrical behavior.

TABLE I
LFP Cell Data

Typical Capacity		40Ah
Rated Voltage		3.2V
Charge Condition	Max. Current	120A
	Voltage	4.0V
Discharge Condition	Continuous Current	120A
	Peak Current	800A
	Cut-off Voltage	2.8V

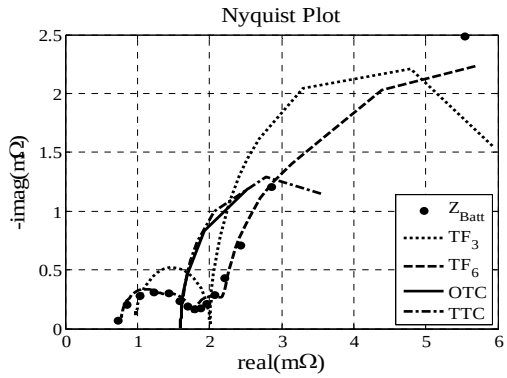

Fig.2. Nyquist plot of the battery electrochemical impedance measurements and the frequency response of the TF_6, TF_3, OTC and TTC models.

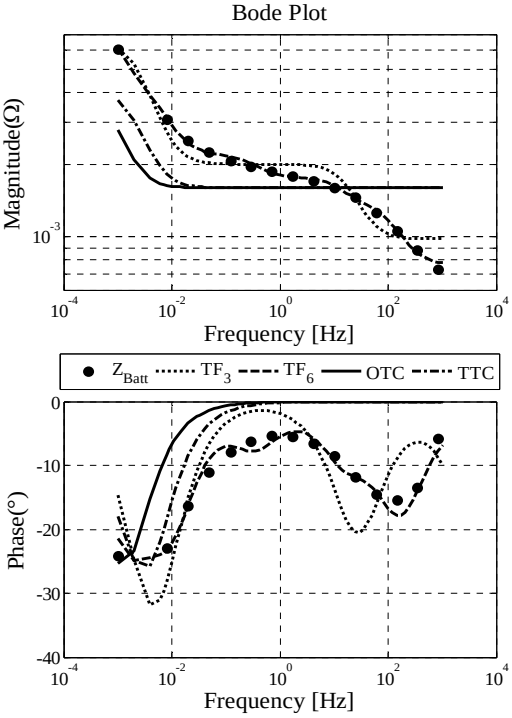

Fig.3. Bode plot of the battery electrochemical impedance and the measurements frequency response of the TF_6, TF_3, OTC and TTC models.

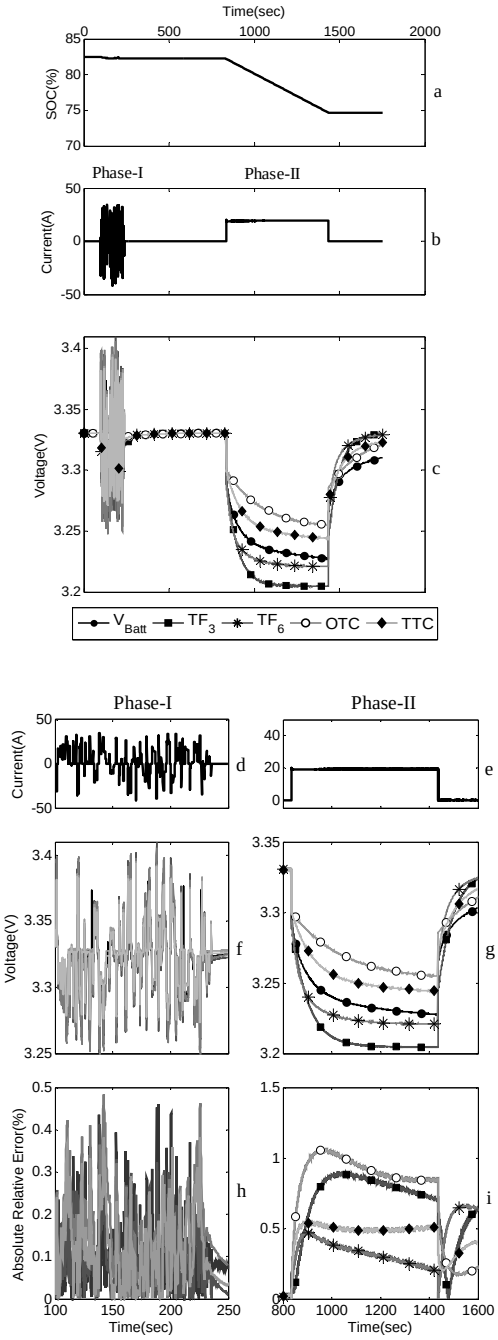

Fig.4. Experimental results for battery model validation: (a) battery state of charge during the test, (b) impressed current profile which is applied to the battery, (c) measured battery output voltage, (d) and (e) - detailed battery current profile during phase-I and phase-II respectively, (f) and (g) - measured battery voltage and calculated model outputs in detail during phase-I and phase-II respectively, (h) and (i) - relative error in percentage calculated for all models during phase-I and phase-II respectively.

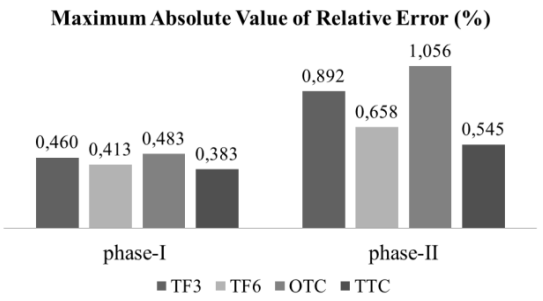

Fig.5. Comparison between the maximum absolute values of the relative error of the TF_6, TF_3, OTC and TTC models during phase-I and phase-II.

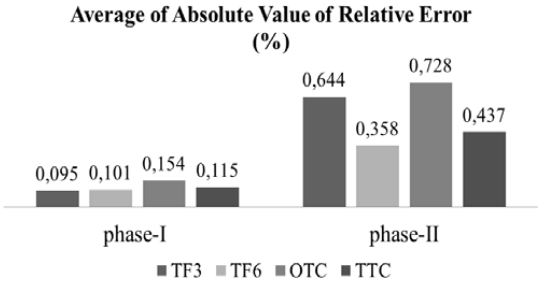

Fig.6. Comparison between the average absolute values of the relative error of the TF_6, TF_3, OTC and TTC models during phase-I and phase-II.

Phase-I and phase-II are repeated sequentially for several SOC values. Fig.4 demonstrates the experimental and calculation results around an SOC value of 80%. Fig.4(a) shows that the SOC value calculated during phase-I and phase-II is changing in the range of less than 5%. Thus it can be assumed to be more or less invariant. The current profile is shown in Fig.4(b), while Fig.4(d) and (e) show the impressed battery output current during phase-I and phase-II respectively. In Fig.4(c) one can see the measured output voltage of the battery and the calculated output voltage resulting from the different models. In Fig.4(f) and (g) the transient behavior during phase-I and phase-II respectively can be seen in detail.

The absolute value of the relative error in Fig.4(h) and 4(i) during phase-I and phase-II respectively shows that the relative error during phase-I is less than 0.5%, and less than 1.5% during phase-II.

V. Conclusion

This paper presents firstly a brief explanation about different types of model structures for Li-ion cells. Secondly a comparison between two different model structures has been carried out. The sixth order and third order transfer functions show a very good fit to the electrochemical impedance measurements of the battery which has resulted in very small relative error values during phase-I as shown in Fig.5 and Fig.6. During phase-II thermal effects grow up and affect the dynamical characteristics of the battery, hence the error increases for both TF_6 and TF_3. Equivalent circuit diagrams show a worse fit to the battery electrochemical impedance measurements of the battery, but they have a stable performance over phase-I and phase-II. This stability in performance is due to the fact that the identification process of the equivalent circuit diagrams is made under similar conditions concerning internal temperature and current value.

In a continuation of this research the effect of current value, internal temperature and aging will be taken into account.

Acknowledgment

The authors wish to thank the Federal Ministry of Economics of Germany for the financial support by the research project IRENE (Integration of Renewable Energy and Electric Mobility). Further many thanks to Prof. Dr.-Ing. A. Rupp, Vice President for R&D of the University of Applied Sciences Kempten, for his continuous support of the Institute for Applied Battery Research.

This Estonian partner research work has been supported by Estonian Ministry of Education and Research (Project SF0140016s11), and Estonian Science Foundation (Grant No. 9350).

References

[1] Huria, T.; Ceraolo, M.; Gazzarri, J.; Jackey, R., "High fidelity electrical model with thermal dependence for characterization and simulation of high power lithium battery cells," Electric Vehicle Conference (IEVC), 2012 IEEE International , vol., no., pp.1,8, 4-8 March 2012

[2] Min Chen; Rincon-Mora, G.A., "Accurate electrical battery model capable of predicting runtime and I-V performance," Energy Conversion, IEEE Transactions on , vol.21, no.2, pp.504,511, June 2006

[3] M. Montaru and S. Pelissier, "Frequency and Temporal Identification of a Li-ion Polymer Battery Model Using Fractional Impedance," in Les Rencontres Scientifiques de l'IFP - Advances in Hybrid Powertrains, Rueil-Malmaison, France, November 2008.

[4] S. Buller, M. Thele, E. Karden and R. W. De Doncker, "Impedance-based non-linear dynamic battery modeling for automotive applications," Journal of Power Sources, vol. 113, no. 2, pp. 422-430, 27 January 2003.

[5] Buller, S.; Thele, M.; De Doncker, R.W.A.A.; Karden, E., "Impedance-based simulation models of supercapacitors and Li-ion batteries for power electronic applications," Industry Applications, IEEE Transactions on , vol.41, no.3, pp.742,747, May-June 2005

[6] Al Jed, H.; Mieze, A.; Vinassa, J. -M; Simon, R., "Mathematical modeling of aging factors for Li-ion battery cells," Vehicle Power and Propulsion Conference (VPPC), 2010 IEEE , vol., no., pp.1,4, 1-3 Sept. 2010

[7] "IRENE," [Online]. Available: http://www.projekt-irene.de/

[8] G. L. Plett, "Extended Kalman filtering for battery management systems of LiPB-based HEV battery packs Part 1. Background," Journal of Power Sources, p. 252–261, 2004.

[9] G. L. Plett, "Extended Kalman filtering for battery management systems of LiPB-based HEV battery packs Part 2. Modeling and identification," Journal of Power Sources, p. 262–276, 2004.

[10] Farag, M. S.; Ahmed, R.; Gadsden, S.A.; Habibi, S.R.; Tjong, J., "A comparative study of Li-ion battery models and nonlinear dual estimation strategies," Transportation Electrification Conference and Expo (ITEC), 2012 IEEE , vol., no., pp.1,8, 18-20 June 2012

[11] A. Rahmoun and H. Biechl, "Parameters Identification of Equivalent Circuit Diagrams for Li-Ion Batteries," in 2012 11th International Symposium PÄRNU, PÄRNU, Estonia, 2012.

[12] X. Hua, S. Li and H. Peng, "A comparative study of equivalent circuit models for Li-ion batteries," Journal of Power Sources, p. 359–367, 2012.

[13] D. Andre, M. Meiler , K. Steiner, H. Walz, T. Soczka-Guth and D. U. Sauer, "Characterization of High-Power Lithium-Ion Batteries by Electrochemical Impedance Spectroscopy. II: Modelling," Journal of Power Sources, p. 5349–5356, 15 June 2011.

[14] Biechl, H.; Lorenzen, H. W.; Lubasch, R.; Prenner, H., "Transient Behaviour of a Current-Source Inverter-Fed Synchronous Motor with a Solid Rotor," Power Engineering Review, IEEE , vol.9, no.9, pp.52,52, Sept. 1989

[15] H. Biechl and H. Bischof, "Meßtechnische Ermittlung von Systemübertragungsfunktionen aus transienten Übertragungsverläufen von Systemanregung und - antwort - Anwendung auf Synchronmaschinen," etzArch.10, pp. 47-51, 1988 (in German).

[16] O. Obeidi and H. G. Schweiger, "Impedance Spectra of Lithium Ion Cells Influence of Temperature, State of Charge and Ageing," in Kronacher Impedanztage 2011, Kronacher, Germany, 2011.

A. Rahmoun M.Eng. received Dipl.Eng. in Electronic Systems from Higher Institute for Applied Sciences and Technology (HIAST), Damascus, Syria, in 2006, and finished his Master study of Electrical Engineering at the University of Applied Sciences Kempten, Germany, in 2012.

His employment experience included Digital Image and Signal Processing Lab (HIAST), and he is currently a research engineer at IABF at the University of Applied Sciences Kempten (Kempten, Germany), and a PhD student at Tallinn University of Technology (Estonia).

Postal address: University of Applied Sciences Kempten, Institute for Applied Battery Research (IABF), Bahnhofstraße 61, 87435 Kempten (Allgäu), Germany.

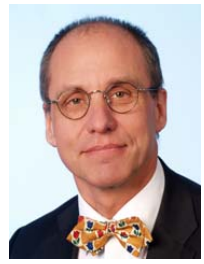

Helmuth Biechl received his Dipl.-Ing. Univ. and M.Sc. degree from the Technical University of Munich (TUM) in 1985 and his Dr.-Ing. and PhD degree in 1989 also from the Technical University of Munich. From 1989 till 1994 he was a developing and planning engineer and a group leader at the companies Siemens and E.ON.

Since 1994 he is a full professor at the University of Applied Sciences Kempten in Germany and working on the field of electrical power systems, mainly electrical machines, drives, power transportation and distribution systems and big batteries. Since 2011 he is the Director of the Institute for Electrical Power Systems. Since 2005 is a Titular Professor at the Universidad Pontificia Bolivariana in Colombia where he got a doctor honoris causa degree in 2012. His main research interests are modelling and simulation of electrical power systems. He has published more than 30 international scientific papers and about 200 articles in technical magazines.

Postal address: University of Applied Sciences Kempten, Institute for Applied Battery Research (IABF), Bahnhofstraße 61, 87435 Kempten (Allgäu), Germany.

Argo Rosin received the Dipl. Eng., M.Sc. and Dr.Sc.techn. degrees in electrical engineering from Tallinn University of Technology, Tallinn, Estonia, in 1996, 1998 and 2005, respectively. He is presently a Senior Researcher in the Department of Electrical Engineering, Tallinn University of Technology. He has published more than 60 papers on energy management, control and diagnostic systems development and is the holder of a Patent in this application field. His research interests include modelling and simulation of power management and industrial control systems. He is member of Estonian Association of Engineers, Estonian Association of Transport and Roads.

Postal address: Faculty of Power Engineering, Tallinn University of Technology, Ehitajate str. 5, 19086 Tallinn, Estonia.

PAPER- IV A. Rahmoun, A. Armstorfer, J. Helguero, H. Biechl, and A. Rosin, “Mathematical modeling and dynamic behavior of a Lithium-Ion battery system for microgrid application,” in 2016 IEEE International Energy Conference (ENERGYCON), 2016, pp. 1–6.

Mathematical Modeling and Dynamic Behavior of a Lithium-Ion Battery System for Microgrid Application

Ahmad Rahmoun[1,2], Andreas Armstorfer[1,2], Jorge Helguero[1], Helmuth Biechl[1,2]
[1]Institute of Electrical Power Systems (IEES)
[1]University of Applied Sciences Kempten
[1]Kempten, Germany
ahmad.rahmoun@hs-kempten.de, andreas.armstorfer@hs-kempten.de,
jorge.helguero@hs-kempten.de, biechl@hs-kempten.de

Argo Rosin[2]
[2]Faculty of Power Engineering
[2]Tallinn University of Technology
[2]Tallinn, Estonia
argo.rosin@ttu.ee

***Abstract*—This paper deals with the analysis and simulation of a stationary battery system for microgrid application, where the system structure including battery cells, inverters, filters, transformers, control system and a simplified grid model is described and modeled mathematically. For the simulation of the whole system the software PSCAD™ is used. In the first part several equivalent circuit models for Lithium-Ion cells will be compared in order to model the dynamic behavior of the battery system. Particularly the evaluation of the effect of the model's complexity on the dynamics of the entire system will be investigated.**

In the second part, the dependency of state of charge (SOC), temperature and aging effects of the Lithium-Ion cells on electrical system quantities will be shown.

It is also investigated the fact that a high frequency battery model has to be taken into account to describe the cells' dynamics if an inverter with Pulse Width Modulation is used.

***Index Terms*—Microgrid, Batteries Energy Storage, Lithium Batteries and Power System Modeling**

I. Introduction

The research project IREN2 (Future Oriented Electricity Grids for Integration of Renewable Energy Systems) runs from 2014 to 2017 and is executed in a cooperation between the German entities Siemens AG, the electricity supplier Allgäuer Überlandwerk GmbH, ID.KOM, the University RWTH Aachen and the University of Applied Sciences Kempten. The main goals are: the development of mathematical models to analyze the dynamic behavior of microgrids including new control concepts on the one hand, and setting up a real system in the village Wildpoldsried in the south of Germany on the other hand. The microgrid consists of renewable energy sources, a stationary 300kVA/170kWh battery system with Lithium Nickel Cobalt Oxide (NCO) - Titanate cells, an 100kVA Genset with vegetable oil fueling for secondary control, a 500kVA back to back station between the 20kV and the 400 V grid for test purposes and a 3x 50kW unsymmetrical load bank.

The Energy Storage System (ESS) which is analyzed in this paper is a modular system consisting of 6 independent strings. Each string consist of a Lithium-Ion (li-ion) battery, an inverter and a filter [1]–[3]. Three strings are connected via a transformer to the grid. For this paper only one string is examined. Fig. 1 shows the block diagram of the system.

978-1-4673-8463-6/16/$31.00

II. Evaluation of the Equivalent Circuit Models' Complexity

In this section three different Equivalent Circuit Model (ECM) are used in order to simulate the electrical dynamics of the li-ion cells which are utilized in the ESS, the One Time Constant (OTC) model, the Two Time Constants (TTC) model and the Three Time Constants (DTC) model. As shown in Fig. 2 the ECM models consist basically of an ideal voltage source representing the cell's Open Circuit Voltage (Voc) and an impedance composed of parallel RC-elements connected with an ohmic serial resistance. The number of the RC-elements defines the order of the ECM and all the model's parameters are functions of State of Charge (SOC), cell's temperature and State of Health (SOH). The ECM's parameters are identified by applying a sequence of current pulses on the cell then employing the voltage and current measurements in time domain. For optimization using multiple exponential functions, the identification procedure is shown in details in [4], [5]. The identified ECM parameters of one cell are stored in Lookup Tables (LuTs) to be accessed and adapted during the simulation run depending on SOC, cell's temperature and SOH, then they are converted based on the number of cells in parallel and series resulting in a battery model of one string.

In order to choose the right battery's model for the simulation of the ESS, the accuracy of the battery models in estimating the battery's output voltage is evaluated, hence a simulation benchmark is designed, in which the OTC, TTC and DTC models are simulated for an active power pulse of Pset=50kW for 5 sec, the initial conditions of the simulation are SOC=60%, T=20°C and SOH=aged/new (new: no cycles, aged: after approx. 640 full cycles). The active power pulse (Pset), battery current (I_{bat}), battery output voltage (V_{bat}) and

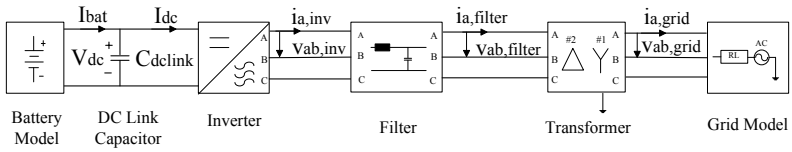

Fig. 1. ESS Structure (for 1 string).

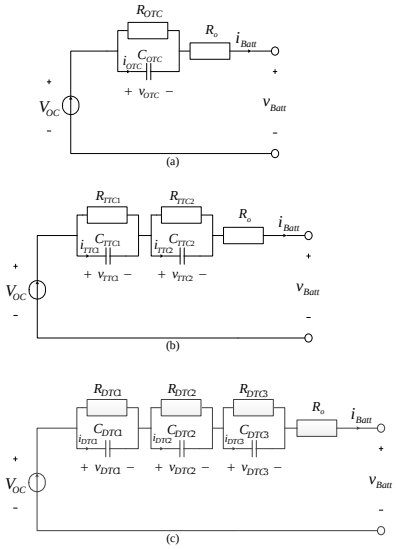

Fig. 2. Battery equivalent circuit diagrams. (a): one time constant model (OTC); (b): two time constant model (TTC); (c): three time constants model (DTC).

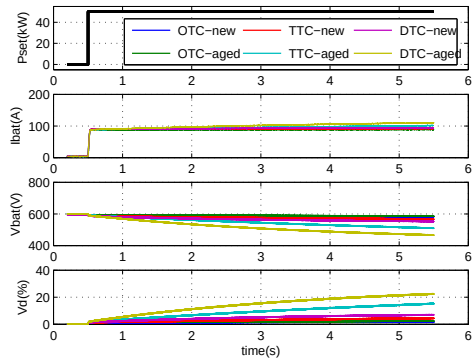

Fig. 3. A comparison between the OTC, TTC and DTC models in estimating the cell output voltage for a new and aged cell.

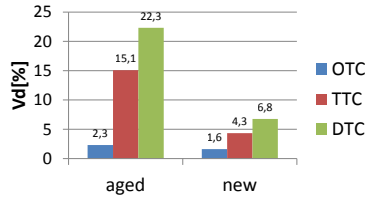

Fig. 4. Voltage difference evaluation of OTC, TTC and DTC models for a new and an aged cell.

the relative voltage difference (V_d) between (V_{bat}) and Voc are plotted in Fig. 3.

The V_d diagram in Fig. 3 shows that the model order plays a bigger roll as the battery ages, so in order to demonstrate the variation between the different models regarding (V_{bat}) calculation, the V_d at the end of the active power pulse is displayed in Fig. 4 for a new and an aged cell. The Fig. 4 manifests that for a new cell, the difference between the three models is about 5 %, but as the cell ages, the difference between the OTC and the TTC models increases faster than the difference between the TTC and DTC models. The reason behind this behavior is that the OTC is very influenced by the long time constants of the cell, thus the TTC and DTC models which include short time constants, lead to bigger voltage drop than the OTC model in the short time range. Based on these evaluation results the DTC model is used for all of the next simulations since it is a capable model to describe the cell behavior for both short and long time ranges.

III. Steady State Analysis

The steady state behavior of the complete system depending on SOC, temperature and aging is analyzed in the following. As described above, the DTC battery model is used for simulation. A reference active power step of 25 kW controlled at the filter output is applied to the system. For variation of SOC, temperature and aging, 9 battery settings are defined and compared (Tab. I). For aging it is distinguished between new cells, aged cells and - to show the effect of dc link voltage drop - an old cell with $SOH \approx 0.87$.

A. Voltage Drop at DC Link

Due to the battery dynamics taken into account by the DTC model, the decrease of the dc link voltage (V_{dc}) depends on: SOC, aging and temperature (Fig. 5). It is illustrated that old cells at the end of their lifetime (setting No. 7) have an early

TABLE I
BATTERY SETTINGS FOR SIMULATION

No.	SOC (%)	Temp. (°C)	Aging
1	30	20	new
2			aged
3	30	35	new
4			aged
5	70	20	new
6			aged
7	70	35	new
8			aged
9	30	20	old

limitation of the maximum power due to the under voltage protection of the system (at $V_{dc} = 450V$). Thus for further analysis it is not taken into account anymore.

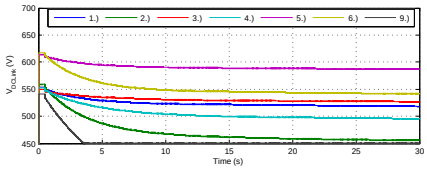

Fig. 5. Battery Voltage Response for a 25kW Active Power Step.

The relative voltage drop at the dc link is investigated as well as the corresponding battery current (rms value).

The relative voltage drop Δv_{dc} is defined as the difference between open circuit voltage V_{OC} and $V_{dc}(30s)$ (1):

$$\Delta v_{dc} = (V_{OC} - V_{dc}(30s))/V_{OC} * 100\% \quad (1)$$

1) Dependency on SOC: For SOC dependency simulation, the settings No. 1,2 are compared with the settings No. 5,6. The temperature is kept at 20°C while SOC and aging is varied.

New cells show a relative voltage drop of approx. 6.6% at $SOC = 30\%$ and approx. 4.7% at $SOC = 70\%$ when applying the mentioned active power step. For aged cells, the relative voltage drop is approx. 19.4% at $SOC = 30\%$ respectively 12.8% at $SOC = 70\%$ (Fig. 6).

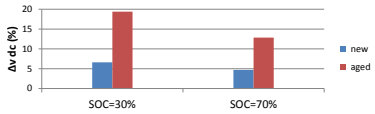

Fig. 6. Relative Voltage Drop at the Battery Terminals after a 30s Power Step.

For the cells used in our ESS it could be shown that the influence of aging has a similar importance than SOC concerning battery voltage dynamics.

Battery currents I_{bat} vary depending on SOC and aging (Fig. 7). As the power at the filter output is controlled to achieve a constant value, a lower dc voltage V_{dc} leads to a higher battery current I_{dc}.

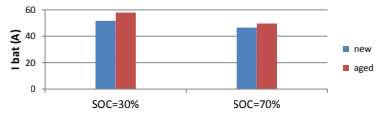

Fig. 7. Battery Current (RMS).

2) Dependency on Temperature: The cell temperature as an influence to the system behavior is analyzed in this section. The SOC is set to 30% while temperature (20°C/35°C) and the aging (new/aged) are varied according settings 1-4 (Tab. I). As a result, a higher temperature leads to a voltage drop reduction. Nevertheless, aging effects play a more dominant role than temperature (Fig. 8) in this range.

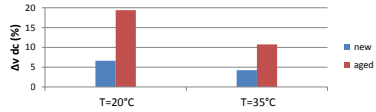

Fig. 8. Relative Voltage Drop after 30s Power Pulse.

B. Harmonics Dependency at the Grid Side

The influence of SOC, temperature and aging of Li-Ion cells on the system's power quality was investigated. Hence the harmonic distortion of the grid current is analyzed. The Fast Fourier Transform (FFT) shows dominant content at order N=1 (50Hz, grid frequency), at order 157 and 161 (7850Hz and 8050Hz, side-bands of switching frequency) as well as at order 317 and 319 (side-bands of the double of switching frequency (15850Hz, 15950Hz). Hence, for current THD determination only these dominant orders (N=157, N=161, N=317, N=319) are taken into account (2):

$$THD_I = \sqrt{\frac{V_{157}^2 + V_{161}^2 + V_{317}^2 + V_{319}^2}{V_1^2}} \quad (2)$$

In mains parallel operation, current harmonic distortion is low and practically independent from the SOC, temperature (20°C ...35°C and aging (Tab. II).

C. Steady State Conclusion

It is shown that due to the power control the ac behavior of the battery storage system at the grid side is independent of the SOC and the cell's temperature. This applies as long as the dc voltage does not fall below the under voltage limit. To reach this minimum voltage depends mainly on the parameters SOC, SOH and active power demand.

TABLE II
TOTAL HARMONICS DISTORTION (THD) OF GRID CURRENT

Case	SOC (%)	Temp. (°C)	Aging	THD_I (%)
1	30	20	new	0.80
2	30	20	aged	0.86
3	70	20	new	0.75
4	70	20	aged	0.78
5	30	35	new	0.80
6	30	35	aged	0.82

IV. EVALUATION OF THE ENEREGY STORAGE SYSTEM IN THE HIGH FREQUENCY RANGE

The usage of the Pulse Width Modulation (PWM) technique with a switching frequency of $f_s = 7.95kHz$ results, in a high frequency voltage and current harmonics. Therefore, the evaluation of the dc-side signals requires knowledge of the battery dynamics within the High Frequency (HF) range. For this reason the battery's behavior within the HF range is investigated in subsection IV-A, next the necessity of using a HF model is explained in subsection IV-B, and finally the influence of SOC, temperature and SOH on the battery's impact is presented in subsection IV-C.

A. High Frequency Battery Model

The Electrochemical Impedance Spectroscopy (EIS) measurement technique is used to inspect the cell's dynamic characteristics within the $[3kHz, 30kHz]$ frequency range, though several impedance measurements have been done for the operation conditions (1-8) mentioned in Table I describing the dependency of the cell's dynamics on the SOC, the temperature and the SOH. At the first step a 1RL-model is adapted to the complex impedance measurements using the Levenberg-Marquardt Complex Nonlinear Least Squares (CNLS) algorithm, the 1RL-model shown in Fig. 11 (a) forms the equivalent circuit diagram of the cell in the HF range, so it consists of an ideal voltage source representing the cell's Voc wired to an impedance consisting of one RL-element and a serial resistance R_o connected in series. The 1RL-model's impedance together with the cell's measured impedance are plotted in Fig. 12 in bode and nyquist diagrams showing that the 1RL-model fits the measurements well, but the error diagram in Fig. 12 shows that the relative error varies within the $[3kHz, 30kHz]$ range, having a local minimum less than 5% around $7kHz$ then increasing in both directions to about 13% at the range limits. In order to reduce the error over the whole frequency range, one more RL-element is connected in series to the 1RL-model resulting in the 2RL-model shown in Fig. 11 (b). The 2RL-model's impedance in Fig. 13 shows clearly with a relative error less than 3% over the whole frequency range that 2RL-model guarantees a very good accuracy.

The 1RL-model resp. 2RL-model parameters are depicted in Fig. 14 and Fig. 15 for the different operation conditions, it can be seen that both models' parameters are influenced mainly by aging. Both models are implemented in PSCAD by extending the Low Frequency (LF) part in the battery's model (consisting of RC-elements) with the HF part (consisting of RL-elements) as it is drawn in Fig. 10. The parameters of the HF models are stored in LuTs in order to be accessed and adapted during the simulation run according to the SOC, the cell's temperature and the SOH.

B. Impact of the Battery Behavior on the DC Currents within the HF Range

In order to show the impact of the battery's HF model on the dc currents in the HF range, the ESS is simulated for three different cases:

1) Without using HF-model
2) Using the 1RL-model
3) Using the 2RL-model

In every case an active power pulse of $P = 50kW$ and a reactive power $Q = 0kvar$ are applied for all the operation conditions (1-8) in Table I. The FFT of both I_{bat} and I_{dc} are plotted in Fig. 9 showing the main current harmonics when using the 2RL-model for (SOH: aged, SOC=70 %, T=35 °C), the dominant frequency components are around the switching frequency ($f_s = 7.95kHz$) and at the double of the switching frequency ($2f_s = 15.9kHz$).

The impact of the battery behavior on the dc currents within the HF range is determined by using the harmonic content (H_I) of the I_{dc} and the I_{bat}. The H_I represents the effective value of the ac part of the current in respect to the effective value of the current, and it's given mathematically in (3).

$$H_I = \frac{\text{effective value of } I_{ac}}{\text{effective value of } I} = \frac{I_{ac,eff}}{I_{eff}} \tag{3}$$

In order to eliminate the influence of any noise on the calculation of the harmonic content (H), only frequency components with an amplitude larger than 1% of the dc component are considered. The H_{Idc} and H_{Ibat} are shown in Fig. 16 for the three different cases, where it can be seen that the use of HF model in the simulation of the ESS has no influence on Idc, but it influences significantly the harmonic content of Ibat. It can be seen also in Fig. 16 that there is almost no difference in the harmonic content calculation of Idc and Ibat when using 1RL-model or 2RL-model, nevertheless, the 2RL-model has a better accuracy in fitting the battery impedance than the 1RL-model. Based on these results the 1RL-model is always used in the next evaluations for representing the battery dynamics in the HF range.

C. Influence of Operation conditions on the Battery dynamics in the HF Range

The 1RL-model simulation results are used in this section to evaluate the dependency of the harmonic content of I_{bat} and I_{dc} on the SOC, the temperature , and the SOH. The H_{Idc} displayed in Fig. 17 shows a slight dependency on SOC, if one compares between H_{Idc} for $SOC = 30\%$ and $SOC = 70\%$. But it shows almost no dependency neither on the temperature nor on the SOH. The change of the H_{Idc} because of the SOC

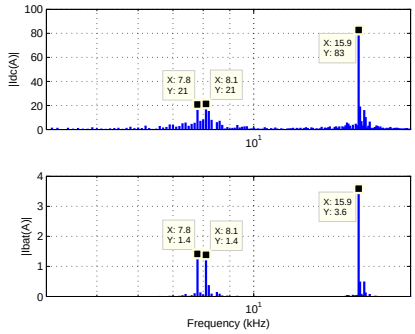

Fig. 9. FFT of I_{dc} and I_{bat} showing the main current harmonic for (SOH: aged, SOC=70 %, T=35 °C) when applying active power pulse of $P = 50kW$ and $Q = 0kvar$ and simulated using the 2RL-model.

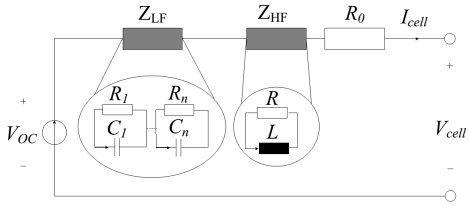

Fig. 10. Li-Ion battery general model structure for high and low frequency application.

is mainly due to the change of the dc component of the Idc as the battery output voltage varies with the SOC.

The H_{Ibat} depicted in Fig. 18 shows almost no dependency neither on temperature nor on SOC. But it shows a slight dependency on SOH, so for an aged battery the H_{Ibat} slightly increases compared to a new battery. This effect is due to the change of HF model parameters when the battery is aged.

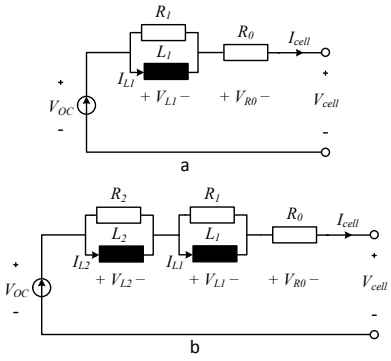

Fig. 11. Battery equivalent circuit models for HF. (a): 1RL-model; (b): 2RL-model.

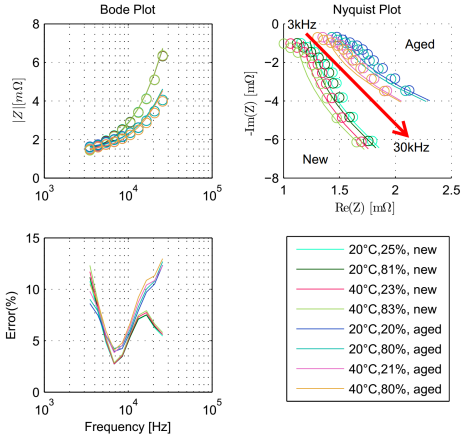

Fig. 12. Bode, Nyquist and error diagrams of cell's measured impedance (circles) and 1RL-model's impedance (line) for various operation conditions.

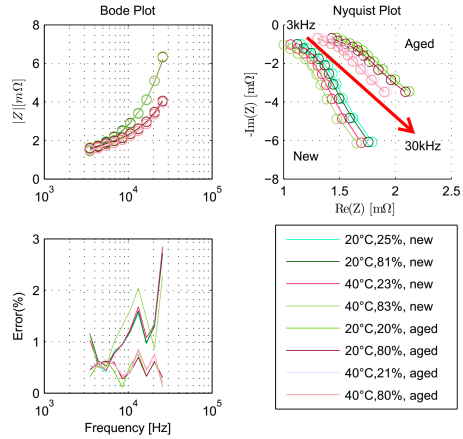

Fig. 13. Bode, Nyquist and error diagrams of cell's measured impedance (circles) and 2RL-model's impedance (line) for various operation conditions.

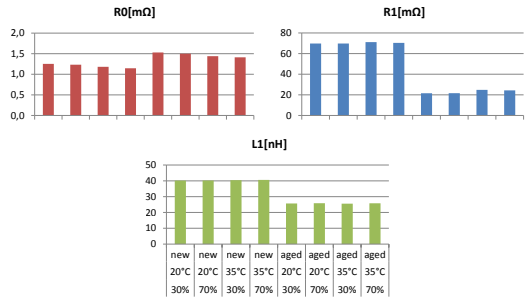

Fig. 14. 1RL-model's parameters dependency on SOC, cell's temperature and SOH.

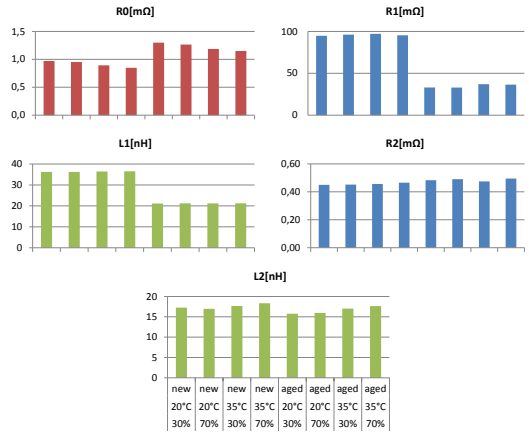

Fig. 15. 2RL-model's parameters dependency on SOC, cell's temperature and SOH.

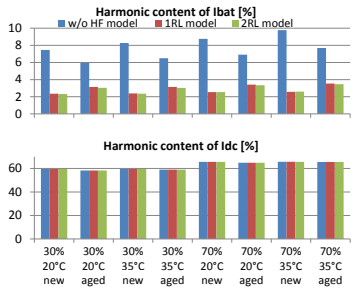

Fig. 16. Harmonic content of I_{dc} and I_{bat} calculated for three different cases and for eight operation conditions.

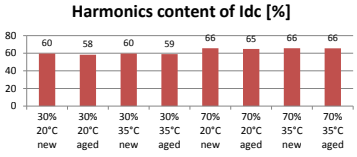

Fig. 17. Harmonic content of I_{dc} calculated based on simulation results when using 1RL-model for the eight operation conditions.

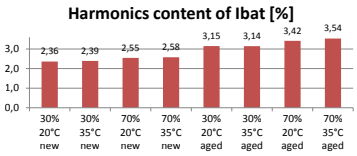

Fig. 18. Harmonic content of I_{bat} calculated based on simulation results when using 1RL-model for the eight operation conditions.

V. Conclusion

The paper is analyzing the usage of electrical models of li-ion batteries for the simulation of the ESS. The following 6 results have been found out:

- Battery ECM with one time constant (OTC) does not represent the fast battery's dynamics accurately mainly when the battery is aged. Therefore, at least two time constants (TTC model) are needed in order to represent the slow and fast dynamics of the battery over the whole service life of the cells (Fig. 4).
- Temperature deviation within 20°C to 35°C range as well as aging has a significant effect on the voltage drop at the dc-side and needs to be taken into account (Fig. 6 and Fig. 8).
- The SOC, the aging and the temperature do not have a significant effect on the Total Harmonics Distortion (THD) on the grid side (Tab. II).
- In order to calculate correctly the harmonics of I_{bat}, the usual ECM for low frequencies need to be extended by an HF model with one time constant (1RL-model).
- The harmonic content of I_{dc} and I_{bat} in Fig. 17 and Fig. 18 depicts that the effects of SOC, cells' temperature and aging on the harmonic content can be neglected.

We would underline that our results are only valid for the cells used in this investigation. Other cells might have different behavior.

Acknowledgment

The authors wish to thank the Federal Ministry for Economic Affairs and Energy of Germany for the financial support by the research project IREN2 (Future Oriented Electricity Grids for Integration of Renewable Energy Systems).

Argo Rosin's research work has been supported by Estonian Ministry of Eduction and Research (Project SF0140016s11).

References

[1] J. L. Helguero, "Modeling and simulation of a big battery storage system of a smart grid including power electronics," master thesis, Hochschule Kempten, March 2013.

[2] T. Khani, "Modeling and simulation of a big battery storage system of a smart grid including power electronics and control," master thesis, Hochschule Kempten, September 2013.

[3] L. F. Hoyos, "Simulation of a battery storage system taking into account a thermal-electric model for lithium-ion cells," master thesis, Hochschule Kempten, July 2014.

[4] A. Rahmoun and H. Biechl, Parameters identification of equivalent circuit diagrams for li-ion batteries, in 11th International Symposium PRNU 2012 TOPICAL PROBLEMS IN THE FIELD OF ELECTRICAL AND POWER ENGINEERING and Doctoral School of Energy and Geotechnology II, 2012, pp. 3537.

[5] A. Rahmoun, H. Biechl, and A. Rosin, Evaluation of Equivalent Circuit Diagrams and Transfer Functions for Modeling of Lithium-Ion Batteries, Sci. J. Riga Tech. Univ. - Electr. Control Commun. Eng., vol. 2, pp. 3439, 2013.

PAPER- V A. Rahmoun, A. Armstorfer, H. Biechl, and A. Rosin, "Mathematical Modeling of a Battery Energy Storage System in Grid Forming Mode," in 58^{th} International Scientific Conference of Riga Technical University on Power and Electrical Engineering RTUCON2017, 2017.

Mathematical Modeling of a Battery Energy Storage System in Grid Forming Mode

Ahmad Rahmoun, Andreas Armstorfer, Helmuth Biechl
Institute of Electrical Power Systems (IEES)
University of Applied Sciences Kempten
Kempten, Germany
ahmad.rahmoun@hs-kempten.de, andreas.armstorfer@hs-kempten.de, biechl@hs-kempten.de

Argo Rosin
School of Engineering: Department of Electrical Power Engineering and Mechatronics
Tallinn University of Technology
Tallinn, Estonia
argo.rosin@ttu.ee

***Abstract*—The paper presents an approach for modelling a Battery Energy Storage System (BESS). This approach consists of four stages. In the first stage a detailed model is developed taking into consideration all the electrical details of the original system. In stage two the detailed model will be validated using real measurements. In the third stage the complexity of the detailed model is reduced resulting in a simplified model which is able to represent the relevant electrical dynamics of the original system and to decrease the simulation time significantly. In the last stage the simplified model is validated by a comparison with simulation results of the detailed model.**

Keywords—Battery energy storage, Power system analysis computing, Power system dynamics, Microgrid

I. INTRODUCTION

The high penetration of inverter-connected Renewable Energy Sources (RESs) in low voltage microgrids replacing the conventional generators and their rotating machinery has led to a significant reduction in rotating system inertia. In island operation where no connection to a stiff grid is available, the BESSs play a very important role to ensure generation adequacy and to increase security and reliability of microgrids [1]. The fast response of BESS improves also microgrid transient stability for different type of disturbances like fast changes of solar irradiation, loss of one Distributed Generation (DG) and three phase short circuit cases [2]. This means that having a BESS in a microgrid contributes to avoid big deviations of voltage and frequency during such contingencies in the microgrid. For these reasons an accurate model of the BESS describing not only the State of Energy (SOE) but also the electrical dynamics is essential for analyzing the microgrid transients and stability. In the frame of the research project IREN2 (Future Oriented Electricity Grids for Integration of Renewable Energy Systems) a microgrid has been set up in the village Wildpoldsried in the south of Germany [3]. The microgrid consists of RESs, a stationary 300kVA/170kWh battery system with Lithium Nickel Cobalt Oxide (NCO) - Lithium Titanate cells, a 100kVA Genset with vegetable oil fueling for secondary control, a 500kVA back to back station between the 20kV and the 400V grid to emulate volatile photovoltaic generation as well as a battery of infinite energy or create real disturbances. Further a 3x 50kW controllable unsymmetrical load bank is available.

One of the important goals of IREN2 is to develop a mathematical model of the BESS for the two operation modes of a microgrid i.e. synchronous mode and island mode. In synchronous mode BESS synchronizes itself to an external grid and tracks given reference setpoints P_{ref} and Q_{ref}, whereas fast responses are avoided in order not to cause big disturbances to the grid. All the details about the mathematical modeling of BESS in this operation mode are described in [4].

In island operation mode the droop control forms a decentralized control method which is based on the communication between the different DGs over frequency and voltage providing an expandable system without extra communication requirements [5]. This approach implies that every DG runs in Grid Forming (GF) mode and regulates its active resp. reactive power output depending on frequency resp. voltage. The dynamic behavior of BESS depends not only on the electrical power components but also on the control structure. The standard control structure using two cascaded synchronous controllers working in dq reference frame is extensively analyzed in literature [6]. However in industrial applications a different control structure is used and will therefore be discussed in this paper.

This research work starts with a description of the electrical system including control structure of the BESS being explained in detail in section II. Section III deals with setting up a detailed mathematical model which describes the electro dynamical behavior of the real system. Section IV shows the verification of the detailed model by a comparison with measurement results of the real system. Due to the fact that the detailed model is very complex and is causing very high computation time on a computer, section V focus on a simplification of the detailed model resulting in a simplified model suitable for the simulation of the BESS as a subsystem in a microgrid which consists also of other power components. The validation of the simplified model using simulation results of the detailed model is carried out in Section VI. Section VII concludes the paper.

II. BESS Structure

During operation some unexpected Lithium-Ion (Li-ion) cell issues had to be solved by a replacement of all battery cells. The new cells were just available with different geometry having the consequence that only three battery strings with approx. the same total energy could be set up instead of six in the original version. Due to this fact every two inverters of the original system had to be connected to one battery string resulting in a much more complex electrical structure because extra filters and isolating transformers were necessary. The modified structure affects the dynamic behavior being discussed later in Section IV.

A. Electrical Structure

As shown in Fig. 1 the BESS consists of three Li-ion batteries Batt1, Batt2 and Batt3 which can be operated independently. Each battery is connected to two 3-phase inverters through an Electromagnetic Interference (EMI) filter for protecting the Battery Management System (BMS) from electrical noise due to the unsynchronized switching of the two parallel inverters.

Every 3-phase inverter has a rated power of 55kVA and is followed by an LCL filter in order to reduce the current harmonics injected into the grid. The first three inverters Inv.1, Inv.2 and Inv.3 are connected to the first matching transformer MT_1 and the next three inverters Inv.4, Inv.5 and Inv.6 are connected to the second matching transformer MT_2.

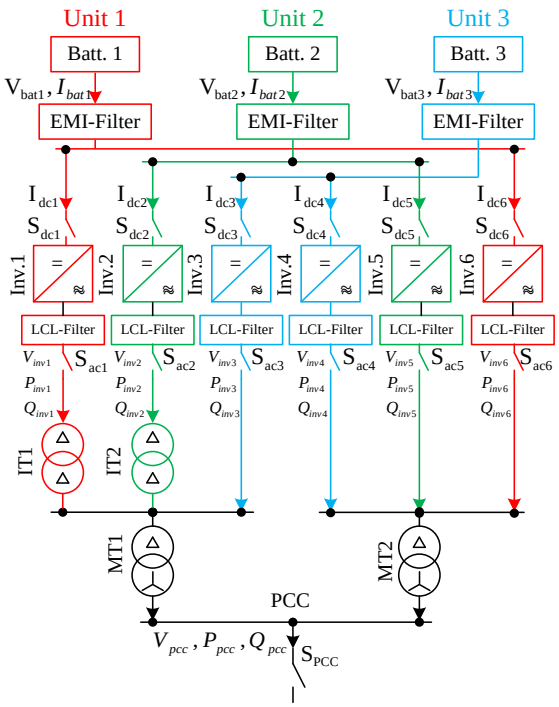

Fig. 1. Block diagram of the BESS electrical structure.

The three phase two-winding matching transformers are used to adapt the inverters' low output voltage to the grid voltage. Two isolating transformers IT_1, IT_2 are used to avoid circulating currents in the circuit of Inv.1 and Inv.6, and of Inv.2 and Inv.5 which are connected to the same dc circuit.

B. Control Structure

The input of the control structure are the 3-phase voltage and current measured at the output of the LCL filter. Based on these measurements the output active and reactive power of the inverter are calculated and fed into the droop controller. The droop controller is composed mainly of two parts. The first part adjusts the inverter frequency based on the active power, the new frequency setpoint $\tilde{f}$ is calculated based on the P/*f* droop formula as shown in Fig. 2, then $\tilde{f}$ is smoothed using a Low Pass Filter (LPF) with a time constant T_c resulting in the inverter actual frequency *f*, which is integrated to get the actual angle θ.

The second part of the droop controller regulates the amplitude of the inverter voltage depending on the reactive power at the output side of the inverter. The new setpoint of the voltage amplitude $\tilde{V}$ is calculated using the Q/V droop formula as shown in Fig. 2. The voltage $\tilde{V}$ is smoothed using a similar LPF filter as it is the case in the first part. The filtered voltage amplitude $\hat{V}$ is used as reference for the Proportional-Integral (PI) controller which regulates the inverter voltage amplitude *V* to match the reference voltage $\hat{V}$.

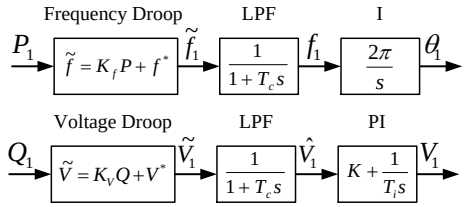

Fig. 2. Structure of frequency and voltage droop control.

III. Detailed Model of the BESS

The detailed model considers the dynamics of dc and ac sides and the switching operation of the IGBTs, thus it is appropriate for analyzing short time transients and harmonic content. Starting from dc side, the battery model is implemented by upscaling a Li-ion cell's model. The cell is modeled in a previous work using a third order Equivalent Circuit Model (ECM) taking into account the dependencies on State of Charge (SOC), temperature and State of Health (SOH) [7], [8]. The EMI and LCL filters are modeled using their equivalent circuits and the parameters are given in Table I. The IGBTs are modeled using two-state resistive switches. The transformers are modeled using the standard 3-phase 2-winding transformer model in PSCAD. The specifications of both matching and isolating transformers are given in Table II.

The modular structure of the BESS enables to split the BESS into three independent units U_1(Batt1, Inv.1, Inv.6 and

IT_1), U_2(Batt2, Inv.2, Inv.5 and IT_2) and U_3(Batt3, Inv.3 and Inv.4) shown in Fig.1 in red, green and blue in Fig. 1 respectively. U_1 and U_2 have an identical structure and they differ from U_3 by having an isolating transformer in series to the output of Inv.1 and Inv.2 respectively. Therefore two detailed models are only needed for evaluating BESS dynamics.

LCL Filter equivalent circuit parameters	**Value**
Serial inductance L_F	160μH
Serial resistance R_F	16.4mΩ
Parallel capacitor C_F	3.5μF
EMI filter equivalent circuit parameters	**Value**
Serial inductance L_S	0.1μH
Serial resistance R_S	0.1mΩ
Parallel capacitor C_P	8 μF

TABLE I. PARAMETERS OF LCL AND EMI FILTER.

257V/400V Δ-Y Matching transformer	**Value**
Rating [$S_{r,LV}$]	165kVA
u_k	4.3%
P_{copper}	0.008484pu
$P_{no\text{-}load}$	0.002424pu
260V/260V Δ-Δ Isolating transformer	**Value**
Rating [$S_{r,LV}$]	55kVA
u_k	3.73%
P_{copper}	0.021545pu
$P_{no\text{-}load}$	0.0029091pu

TABLE II. SPECIFICATIONS OF THE MATCHING AND ISOLATING TRANSFORMERS.

IV. DETAILED MODEL VALIDATION

The verification of the detailed model is carried out using real measurements of the BESS, where a 60kW ohmic load step is applied on both U1 and U3 at the Point of Common Coupling (PCC). The experiments are executed with a new battery at 25°C and relative state of charge around SOCr=50%. The voltages and currents are measured at three different points in order to evaluate the quality of the detailed models of U1 and U3. The first Evaluation Point (EP) is the dc side of each unit. At this point the dc voltages and currents are used directly for the comparison. The second EP is at the inverters' output and the third EP is at the PCC. For the second and third EPs the voltage phasor amplitude, frequency, active and reactive power are calculated and used for the evaluation.

Figures 3, 4 and 5 show the comparison between detailed model's signals of U_1 and corresponding measurements. These figures show a fluctuation of the active and reactive power at the moment of switching the load on due to the delay between the different phases of the ohmic load which results in a asymmetrical loading of U_1 which finally causes these fluctuations. After these fluctuations, slow oscillations in active and reactive power signals due to the different serial impedances between Inv.1, Inv.6 and the PCC can be seen in Fig. 4 (b,c).

Figures 6, 7 and 8 show the comparison between signals of the detailed model of U_3 and measurements. These figures show only the fluctuations due to the switching of the load but they show no slow oscillations because Inv.3 and Inv.4 have the same serial impedance to the PCC. The oscillations in active and reactive power are analyzed mathematically and will be presented in the next research work. The numbers inside the figures show values of the relative error which are calculated according to (1).

$$E_{rms}(X_1, X_2)[\%] = \frac{rms(X_1 - X_2)}{\max(X_1, X_2)} \times 100 \quad (1)$$

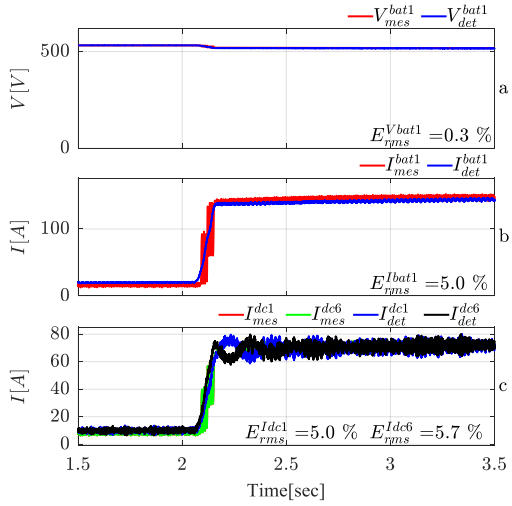

Fig. 3. Unit1: Comparison between detailed model and measurements for: (a) battery voltage; (b) battery current; (c) dc currents of inv1 and inv6.

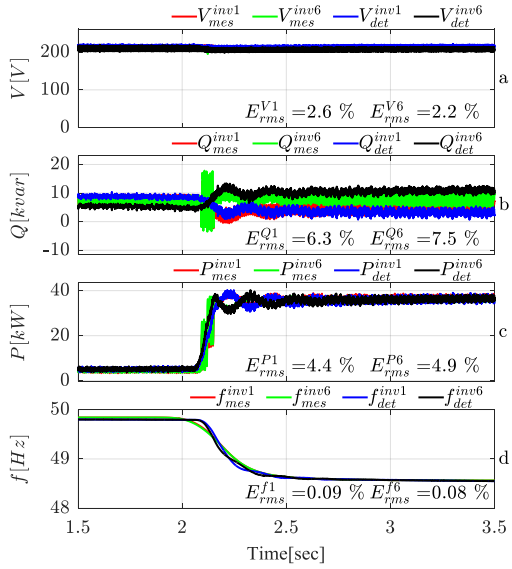

Fig. 4. Unit1: Comparison between detailed model and measurements at the ac side of inv1 and inv6 for: (a) voltage amplitude; (b) reactive power; (c) active power; (d) frequency.

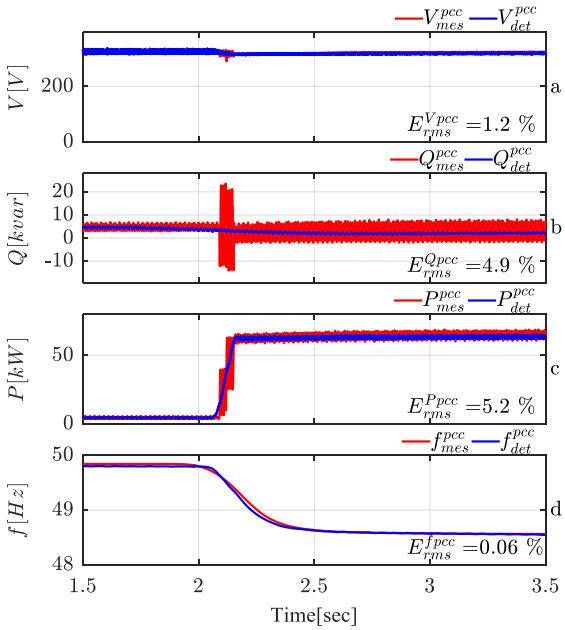

Fig. 5. Unit1: Comparison between detailed model and measurements at PCC for: (a) voltage amplitude; (b) reactive power; (c) active power; (d) frequency.

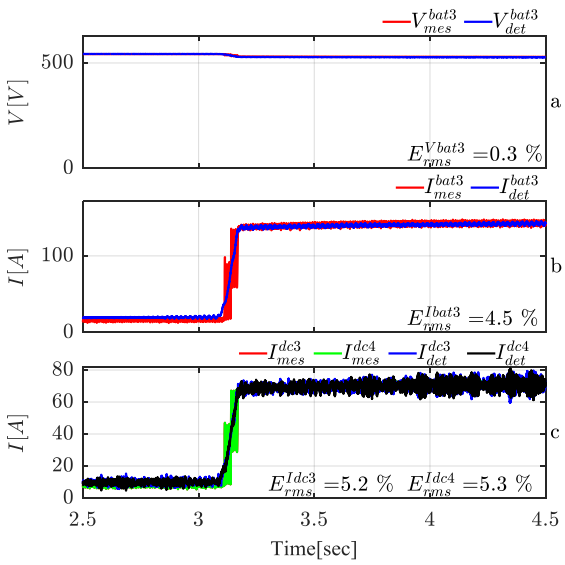

Fig. 6. Unit3: Comparison between detailed model and measurements for: (a) battery voltage; (b) battery current; (c) dc currents of inv3 and inv4.

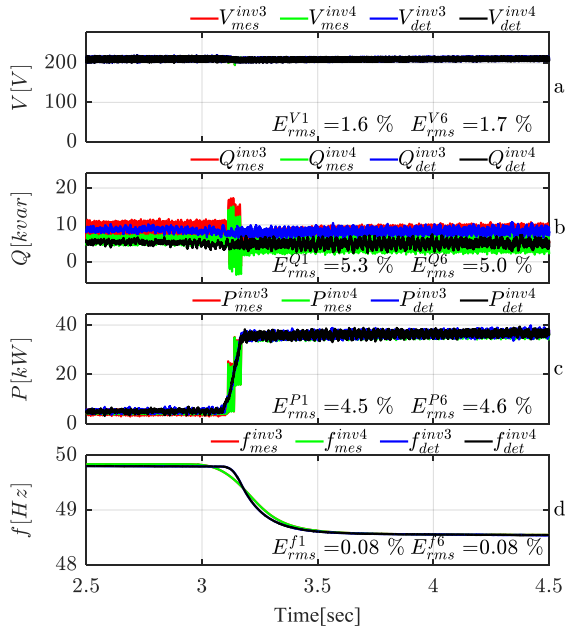

Fig. 7. Unit3: Comparison between detailed model and measurements at the ac side of inv3 and inv4 for: (a) voltage amplitude; (b) reactive power; (c) active power; (d) frequency.

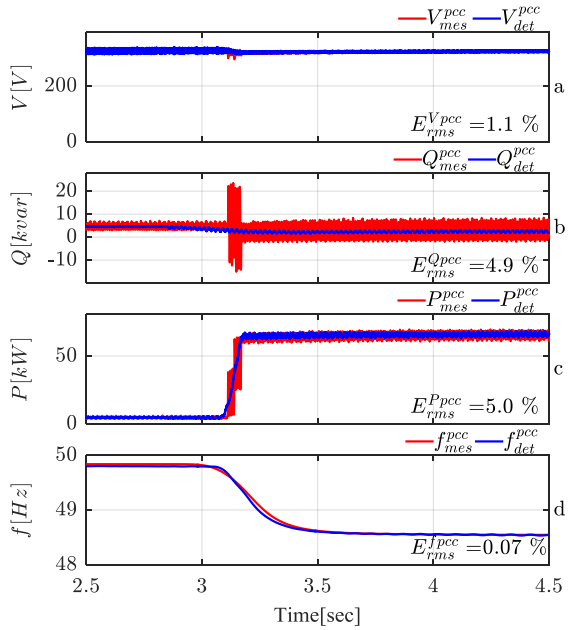

Fig. 8. Unit3: Comparison between detailed model and measurements at PCC for: (a) voltage amplitude; (b) reactive power; (c) active power; (d) frequency.

V. Simplified Model of the BESS

Due to the complex structure of the BESS the detailed model is unsuitable for long time simulations along with other microgrid components. Therefore a simplified model is required which represents the fundamental dynamics of the original system but reduces the complexity of the detailed model.

The simplification procedure is performed according to the following steps:

1. The dc side dynamics are neglected as it does not influence the ac side dynamics significantly [9].
2. Each 3-phase inverter is modelled using an ideal 3-phase voltage source connected to the serial impedance of the LCL filter.
3. All the transformers are replaced with their equivalent serial and parallel impedances (Z_s^{MT} and Z_s^{IT1}) resp. (Z_p^{MT},Z_p^{IT1} and Z_p^{IT2}) referred to the high voltage side of the matching transformers.
4. The control unit for the simplified model remains the same.

The simplified electrical structures of U1 and U3 are shown in Fig. 9 and Fig. 10 respectively.

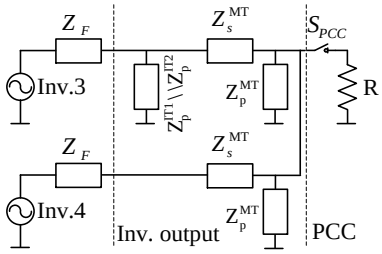

Fig. 9. Simplified model of Unit 1.

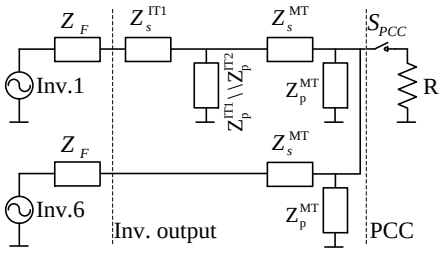

Fig. 10. Simplified model of Unit 3.

VI. Simplified Model Validation

In this section the simplified model simulation results are compared with those of the detailed model and plotted in Fig. 11 and Fig. 12. It is carried out for U_1 at the inverters' output and at PCC respectively. The simplified model shows also the oscillations in active and reactive power signals similarly to the detailed model.

Figures 13 and 14 for U3 at inverters' output and at PCC respectively show that a good coincidence between the simplified and detailed model of U3.

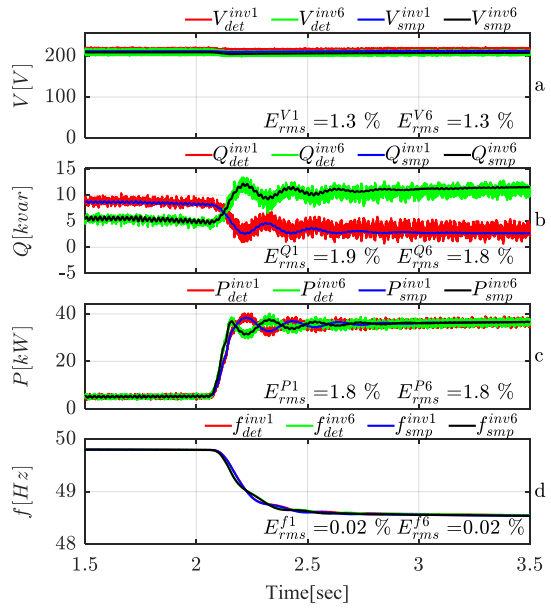

Fig. 11. Unit1: Comparison between detailed and simplified model at the ac side of inv1 and inv6 for: (a) voltage amplitude; (b) reactive power; (c) active power; (d) frequency.

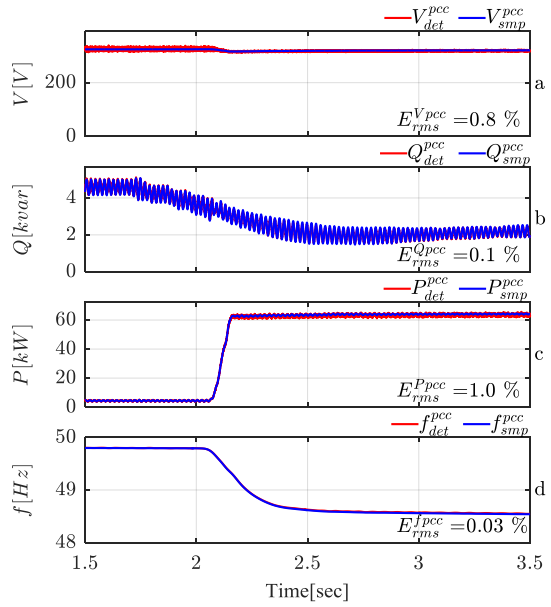

Fig. 12. Unit1: Comparison between detailed model and measurements at PCC for: (a) voltage amplitude; (b) reactive power; (c) active power; (d) frequency.

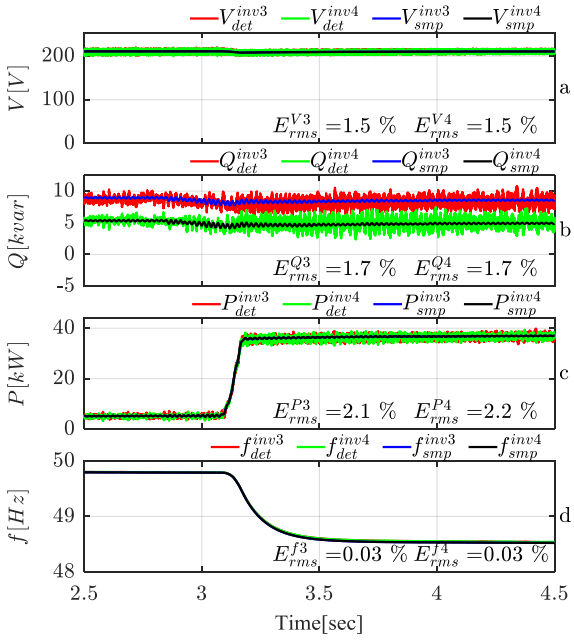

Fig. 13. Unit3: Comparison between detailed and simplified model at the ac side of inv3 and inv4 for: (a) voltage amplitude; (b) reactive power; (c) active power; (d) frequency.

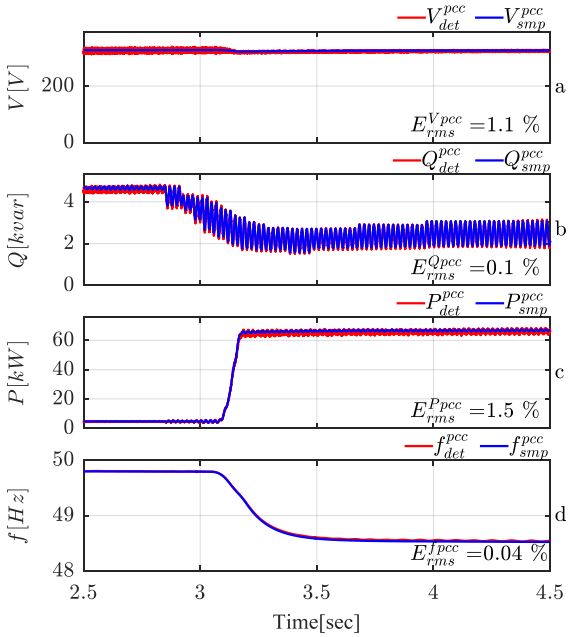

Fig. 14. Unit3: Comparison between detailed model and measurements at PCC for: (a) voltage amplitude; (b) reactive power; (c) active power; (d) frequency.

VII. Conclusion

Figures 3, 4, 5, 6, 7 and 8 show a good coincidence with a relative error less than 5% between measurement and simulation results for the detailed model of U_1 and U_3 respectively. The high error values for dc currents, active power and reactive power are due to the asymmetrical loading at begin of the load step.

The comparison between simulation results for detailed and simplified models in Fig. 11, 12, 13 and 14 confirms that the fundamental dynamic behavior is accurately represented for U_1 resp. U_3 when the simplified models are applied.

Acknowledgment

The authors wish to thank the Federal Ministry for Economic Affairs and Energy of Germany for the financial support by the research project IREN2 (Future Oriented Electricity Grids for Integration of Renewable Energy Systems).

Estonian partner work was supported by the Estonian Research Council grant PUT (PUT1680), and Estonian Centre of Excellence in Zero Energy and Resource Efficient Smart Buildings and Districts ZEBE, grant 2014- 2020.4.01.15-0016 funded by European Regional Development Fund.

References

[1] N. Shi and Y. Luo, "Energy Storage System Sizing Based on a Reliability Assessment of Power Systems Integrated with Wind Power," *Sustainability*, vol. 9, no. 3, p. 395, Mar. 2017.

[2] J. Stanojevic, A. Djordjevic, and M. Mitrovic, "Influence of battery energy storage system on generation adequacy and system stability in hybrid micro grids," in *2016 4th International Symposium on Environmental Friendly Energies and Applications (EFEA)*, 2016, pp. 1–6.

[3] "IREN2 (Future Oriented Electricity Grids for Integration of Renewable Energy Systems)." [Online]. Available: http://www.iren2.de/.

[4] J. L. H. Cruz, "Master thesis.," University of Applied Sciences Kempten, 2013.

[5] A. Engler, "Applicability of droops in low voltage grids," *Int. J. Distrib. Energy Resour. Smart Grids*, no. 1, pp. 1–5, 2005.

[6] J. Rocabert, A. Luna, F. Blaabjerg, and P. Rodríguez, "Control of power converters in AC microgrids," *IEEE Trans. Power Electron.*, vol. 27, no. 11, pp. 4734–4749, 2012.

[7] A. Rahmoun and H. Biechl, "Modelling of Li-ion batteries using equivalent circuit diagrams," *Prz. Elektrotechniczny*, vol. 2012, no. 7b, pp. 152–156, 2012.

[8] A. Rahmoun, H. Biechl, and A. Rosin, "Evaluation of Equivalent Circuit Diagrams and Transfer Functions for Modeling of Lithium-Ion Batteries," *Electr. Control Commun. Eng.*, vol. 2, no. 1, pp. 34–39, May 2013.

[9] A. Rahmoun, A. Armstorfer, J. Helguero, H. Biechl, and A. Rosin, "Mathematical modeling and dynamic behavior of a Lithium-Ion battery system for microgrid application," in *2016 IEEE International Energy Conference (ENERGYCON)*, 2016, pp. 1–6.

Ahmad Rahmoun is a doctoral student and researcher at the Institute of Electrical Power Systems (IEES) of University of Applied Sciences Kempten/Germany. He received his Master degree in the field of Electrical Engineering from the University of Applied Sciences Kempten (HKE) in 2012. His current research interests is mathematical modeling of battery systems for microgrid and e-mobility applications.

PAPER- VI A. Rahmoun, M. Loske, and A. Rosin, “Determination of the Impedance of Lithium-ion Batteries Using Methods of Digital Signal Processing,” Energy Procedia, vol. 46, pp. 204–213, 2014.

Available online at www.sciencedirect.com

SciVerse ScienceDirect

Energy Procedia 00 (2014) 000–000

Energy Procedia

www.elsevier.com/locate/procedia

8th International Renewable Energy Storage Conference and Exhibition, IRES 2013

Determination of the Impedance of Lithium-Ion Batteries using Methods of Digital Signal Processing

Ahmad Rahmoun[a] *, Moritz Loske[a], Argo Rosin[b]

[a]*University of Applied Sciences Kempten, 87435 Kempten, Germany*
[b]*Tallinn University of Technology, 19086 Tallinn, Estonia*

Abstract

This paper presents the design, implementation and verification of methods to determine the electrochemical impedance spectrum of a Lithium-Ion battery by using methods of digital signal processing. The principle is to excite the battery by applying a current step and measuring the voltage response. Both signals, the stimulation and response signal, are the basis of the signal processing algorithm. The method is verified theoretically with a very good accuracy by a computer simulation and was successfully applied to real cells under laboratory conditions. The reference impedance spectra for the evaluation are produced by the electrochemical impedance spectroscopy (EIS) technique.

Selection and peer-review under responsibility of EUROSOLAR - The European Association for Renewable Energy.

Keywords: Digital Signal Processing, Electrochemical Impedance Spectroscopy, Lithium-Ion Batteries,

1. Introduction

Stationary energy storage systems play an important role in Smart Grids and serve as an energy buffer to balance the fluctuating in-feed to the grid. For an ideal integration and control of such temporary energy storages, a detailed and accurate battery model is essential. As the battery behaviour changes with the increasing number of charging cycles, respectively the state of charge (SOC), the state of health (SOH) and the temperature T, it is necessary to adjust these model parameters regularly.

* Corresponding author. Tel.: +49 831 2523 528; fax: +49 831 2523 530.
E-mail address: ahmad.rahmoun@fh-kempten.de

Selection and peer-review under responsibility of EUROSOLAR - The European Association for Renewable Energy.

The electrochemical impedance spectrum or the frequency response characteristic acts like a fingerprint of a battery. It contains information about the SOC, temperature and SOH. From the impedance spectrum the parameters for the desired battery model can easily be obtained. So when knowing the electrochemical impedance, the battery model can be established. The most common method to find out the impedance spectrum is the electrochemical impedance spectroscopy (EIS) method. From this point and forward impedance means the electrochemical impedance until otherwise is mentioned.

This paper presents the design, implementation and verification of a method to determine the impedance of a Li-Ion battery using digital signal processing (DSP) approaches. The goal is to obtain a robust and fast method, which is applicable to both, battery arrays and battery cells, with an average deviation of less than 5% to the reference. In the first and second sections the general idea of the DSP-method is highlighted and adapted for the application to real Li-Ion batteries. Section three deals with algorithms to compensate the errors caused by the fast Fourier transform (FFT). In the next section the DSP-methods are applied to real Li-Ion batteries under laboratory conditions and the results are evaluated in frequency and time domain. At the last sections the results are discussed and a conclusion is presented.

2. General Idea of the DSP method

The theory is based on a paper published by Bischof and Biechl in 1987 [1]. The authors describe a method to determine the impedance spectrum of a system, by using arbitrary transients of system stimulation and response and a combination of analytical and fast Fourier transform. The theory is to apply an arbitrary transient stimulus *e(t)*, from a steady state to another to the system and measure the response *r(t)*. Then the Fourier transform is applied to both, the excitation and response signal. This principle is only valid, if for $\mathcal{F}\{e(t)\}$ and $\mathcal{F}\{r(t)\}$ the Fourier integral exists, which means the signal is integrable in the interval of $\left[-\infty \le t \le +\infty\right]$. To ensure this, the transient excitation signal *e(t)* and the response signal *r(t)* may need to be split up into components, where the Fourier integral exists. This means either an energy-limited signal or a signal which analytically can be transferred into frequency domain [2]. In case of energy-limited signals the fast Fourier transform is applied.

2.1. *Adaption to Li-Ion Batteries*

The definition of the (operational) impedance is only valid within linear system theory (LST). Which implies that the system has to be linear, stationary, time-invariant and causal [3]. As Li-Ion batteries do not fulfill these explicit requirements, except the causality (implied), assumptions have to be made:

- The battery behaves linearly within the certain operating point, time range and the chosen stimulus (current) and response (voltage).
- The temperature is constant during the time range and does not change with amperage.
- The change of parameters due to SOC-change and ageing effects are neglected.

For the analytical investigation this means, the open circuit voltage v_{OC} is constant. When applying to real batteries a linear coherence between v_{OC} and SOC is supposed. It is required to achieve an accuracy of $\geq 95\%$ of the obtained spectrum $\underline{Z}(f)$ compared to the reference spectrum $\underline{Z}_{\mathrm{EIS}}(f)$ (EIS-measurement). The frequency range to be investigated is limited to the span between 1 mHz and 0.5 Hz.

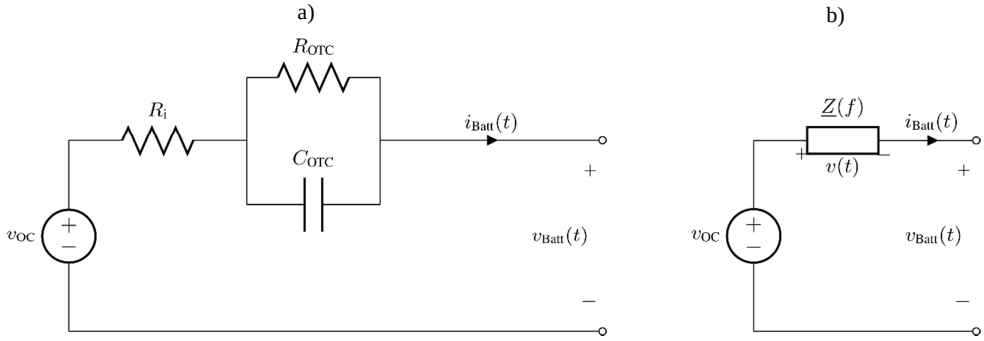

Figure 1. (a):'one time constant' (OTC) battery model, (b): the general and simplified battery model.

2.1.1. Analytical Investigation

As stimulus signal a current step is used. The unit-step function *u(t)* is the integration of the Dirac impulse δ and contains all frequencies [4]. It has therefore ideal conditions for a scientific investigation. Additionally a current step can easily be reproduced in practice by a laboratory power supply or electronic load. The step-function reads as

$$i_{\mathrm{Batt}}(t) = \hat{I} \cdot u(t)\,, \tag{1}$$

where $\hat{I}$ is the height or amplitude of the current step and *u(t)* the unit-step function (Heaviside function). $\hat{I}$ can either be negative for a charging or positive for a discharging of the battery. For the analytical investigation of the method the one time constant (OTC) - model (cf. figure 1(a)) is used. Due to linearity all results can be transferred to models with two or more time constants.

The step-response $v_{\mathrm{Batt}}(t)$ of the OTC-model reads as

$$v_{\mathrm{Batt}}(t) = v_{\mathrm{OC}}(\mathrm{SOC}) - R_{\mathrm{OTC}} \cdot \hat{I} \cdot u(t) \left(1 - e^{-\frac{t}{R_{\mathrm{OTC}} C_{\mathrm{OTC}}}} \right) - R_i \cdot \hat{I} \cdot u(t), \tag{2}$$

in continuous time.

From the simplified equivalent circuit diagram in 1(b) it follows, that only the voltage drop across the impedance $\underline{Z}(f)$ and the change in the current is required to obtain the impedance spectrum of the battery. The voltage drop is calculated by

$$u(t) = v_{OC} - v_{\mathrm{Batt}}(t)\,, \tag{3}$$

and the current through $\underline{Z}(f)$ as

$$i(t) = i_{\mathrm{Batt}}(t)\,. \tag{4}$$

From system theory it follows that, equal directed current and voltages yield in a negative impedance. The impedance $\underline{Z}(f)$ reads

$$\underline{Z}(f) = -\frac{F\{v(t)\}}{F\{i(t)\}}. \tag{5}$$

The excitation signal $i_{Batt}(t)$ and the system (step-) response $v_{Batt}(t)$, exemplified for charging mode, are shown in figure 2(a) and 2(b) respectively. The step height is $\hat{I} = 8$ A. The change in current and voltage is marked with $i(t)$ and $v(t)$. The model parameters R_i, R_{OTC}, C_{OTC} and v_{OC} within this investigation and simulation are chosen from a real battery.

As previously described the response signal $v(t)$ needs to be split up into components, where the Fourier integral exists. As the stimulus $i(t)$ is a step function, which analytically can be transferred into frequency domain, no fragmentation for the current is necessary. The Fourier spectrum of $i(t)$ is donated as $\underline{I}(f)$. Charging is done with a constant negative current $\hat{I}$ (cf. fig.2(a)). The step-response of the model is illustrated in (b). The response signal is split up into a step function $v_1(t)$ (c) together with an energy limited signal component $v_2(t)$ (d).

The step-function $v_1(t)$ is transferred into Fourier space by the CTFT to $\underline{V}_1(f)$ and the energy-limited signal $v_2(t)$ by the FFT to $\underline{V}_2(f)$. The total voltage $v(t)$ to be examined, is set-up of $v_1(t)$ and $v_2(t)$ like

$$v(t) = v_1(t) - v_2(t). \tag{6}$$

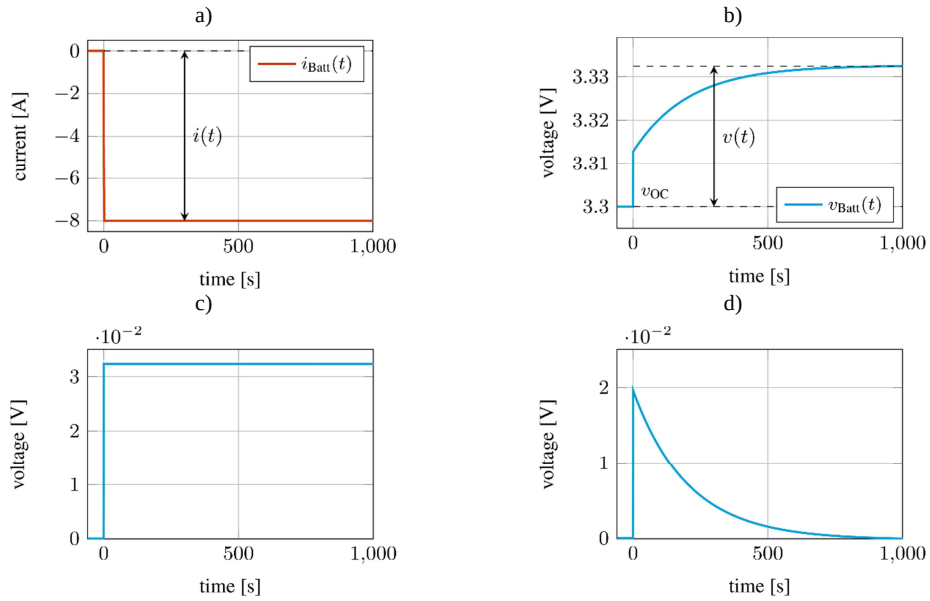

Figure 2. (a): Current step with the step height $\hat{I}$ = 8 A, (b): the system step response simulated with an OTC-model, (c): voltage component $v_1(t)$, (d): the component $v_2(t)$.

From the given linearity of the Fourier transform the spectrum $\underline{V}(f)$ of the voltage $v(t)$ results as:

$$\underline{V}(f) = \underline{V}_1(f) - \underline{V}_2(f). \tag{7}$$

For the impedance spectrum $\underline{Z}(f)$ follows now the relation

$$\underline{Z}(f) = \frac{\underline{V}_1(f) - \underline{V}_2(f)}{\underline{I}(f)}. \tag{8}$$

2.2. *Simulation Results without Error Compensation*

In figure 5 the simulation results are shown. The Bode-plot depicts a big difference between the spectrum calculated by the algorithm (green dashed) and the theoretical derived spectrum (solid green) (done by the analytical Fourier transform and the equations of the OTC-model). Especially the high frequencies show a big error in phase and magnitude. Figure 3 illustrates the origin of the error occurring, using the FFT.

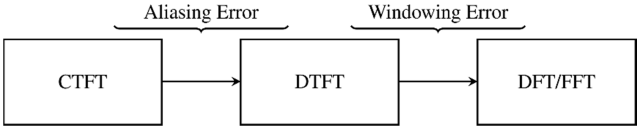

Figure 3. Error Block-Diagram.

The aliasing error yields from the discretisation of the signal which can be encountered by fulfilling the Nyquist theorem. For non-bandlimited signals a high sampling frequency will reduce the aliasing error. The windowing error can be antagonised either by applying a compensation in time domain or in frequency domain by curve fitting.

3. Error Compensation Algorithms

3.1. *Compensation in Time Domain*

The idea was developed by Nicolson in 1973. The principle is to subtract the ramp-function $p(t)$ as shown in figure 4(b) from the step-response $v(t)$ 4(a), before conducting the FFT. The ramp $p(t)$ starts at zero and goes to the negative value of the voltage $v(T_n)$ for $t = T_n$ [5]. The results of the subtracting $v'(t)$ is shown in in figure 4(c). As $v_0(t)$ is energy-limited, the split-up of the signal is now unnecessary.

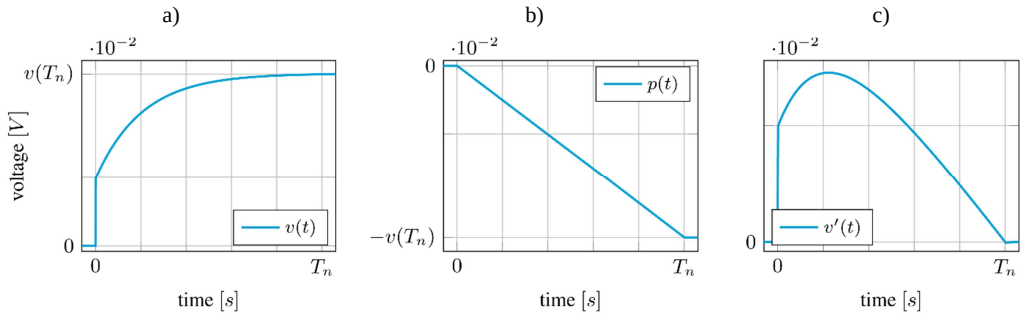

Figure 4. (a): the voltage drop *v(t)* across the impedance $\underline{Z}(f)$, (b): the ramp-function, (c): the compensated voltage $v_0(t)$.

3.2. *Compensation in frequency domain*

The idea is to approximate the analytical Fourier transformation of the voltage component $v_2(t)$, but also to keep the information about the non-linearity included in the FFT spectrum. To compensate the error in frequency domain, the FFT of $v_2(t)$ has to be adapted. This can be done by a compensation function $\underline{D}(f)$, which is multiplied by the result of the fast Fourier transformation $\underline{V}_2(f)$.

The new spectrum of the $v_2(t)$ voltage component:

$$\underline{V}'_2(f) = \underline{D}(f) \cdot \underline{V}_2(f). \tag{9}$$

$\underline{D}(f)$ is a vector of the same size as $\underline{V}_2(f)$. It contains a complex correction factor for each frequency bin. Ideally $\underline{V}'_2(f)$ yields into the continuous time Fourier transform (CTFT) of $v_2(t)$. The CTFT can be obtained using a curve fitting algorithm, where the data of $\underline{V}_2(f)$ is fitted to a behavioral description of a battery model (OTC-Model description). The Levenberg-Marquardt (LM) [6, 7] curve fitting algorithm is applied. The obtained model parameters are used to calculate the analytical Fourier transform of the $v_2(t)$ component. For the compensation factor follows:

$$\underline{D}(f) = \frac{\mathrm{CTFT}\{v_2(t)\}}{\mathrm{DTFT}\{v_2(t)\}}. \tag{10}$$

The compensated spectrum of $v_2(t)$ is then calculated by:

$$\underline{V}'_2(f) = \frac{\mathrm{CTFT}\{v_2(t)\}}{\mathrm{DTFT}\{v_2(t)\}} \cdot \underline{V}_2(f). \tag{11}$$

3.3. *Simulation Results with Error Compensation*

Exemplified for the error-compensation in frequency domain the Bode plot is shown in figure 5. The green solid line shows the analytical impedance $\underline{Z}_a(f)$ and the green dashed line the result of the method without compensation $\underline{Z}(f)$. The compensated spectrum $\underline{Z}'(f)$ is marked with yellow crosses. As you can see $\underline{Z}'(f)$

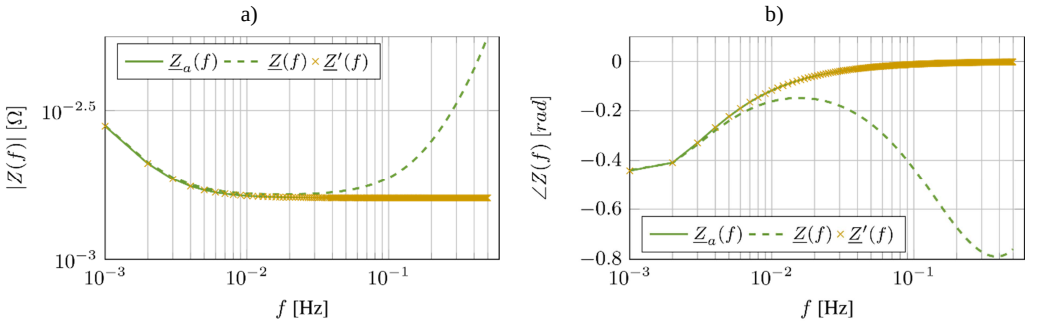

Figure 5. Bode-plot of $\underline{Z}(f)$: (a): the magnitude, (b): the phase. The green line represents the theoretical characteristic. The dashed line shows the obtained spectrum without error compensation. The yellow crosses indicate the spectrum after applying the error compensation.

almost precisely match $\underline{Z}_a(f)$. The Error Modulus (EM) averages in a value of 0.65 10^{-4} % in relation to $\underline{Z}_a(f)$. For the compensation in time domain the EM numbers in average 0.2235 %. Both theoretical results are satisfactory.

4. Application to Real Li-Ion Batteries

The theoretical approach is now applied to real Li-Ion batteries under laboratory conditions. A single measuring period for a certain operating point is composed off an ON- and an OFF-Phase followed by an electrochemical impedance spectroscopy measurement as pointed out in figure 6. 6(a) shows the current $i_{\mathrm{Batt}}(t)$ and 6(b) the voltage response $v_{\mathrm{Batt}}(t)$ of the battery. In the ON-Phase ($t_0 - t_1$) the current is switched on, in this case with a step height of $\hat{I} = -8$ A for charging mode. During this time interval the voltage changes according to the battery cell behaviour. After a certain time (~12min) the current is switched off and the voltage turns into steady state (v_{OC}).

As previously mentioned, in case of a real battery the open circuit voltage v_{OC} is not constant and changes in relation to the SOC. During the ON-Phase the dependency is assumed to be linear. As the current is zero in the OFF-Phase and before $t \leq t_0$ the open circuit voltage $v_{\mathrm{OC}}(t)$ is constant. The function is plotted in figure 6(b) (blue dashed). To get the voltage drop $v(t)$ across the impedance $\underline{Z}(f)$ the open circuit voltage has to be subtracted from $v_{\mathrm{Batt}}(t)$ as $v(t) = v_{\mathrm{OC}}(t) - v_{\mathrm{Batt}}(t)$.

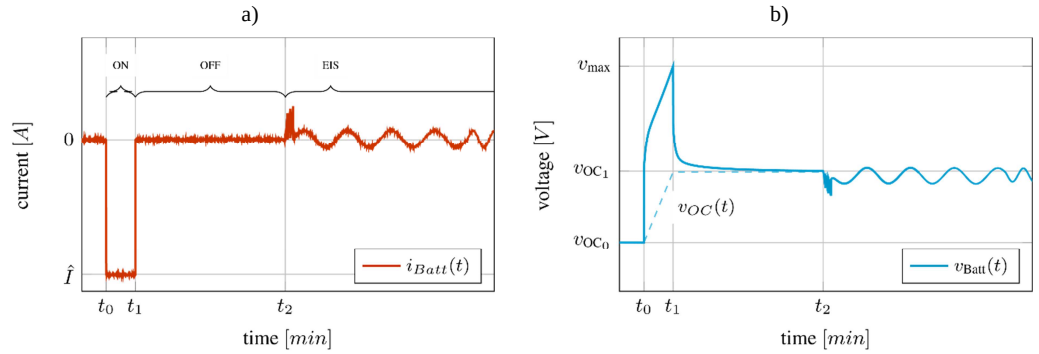

Figure 6. Measurement interval for one SOC value: (a): the battery current $i_{\mathrm{Batt}}(t)$, (b): the voltage response of the battery cell.

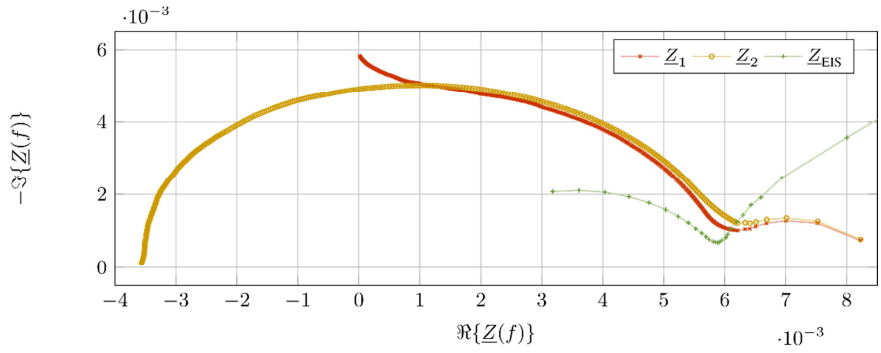

Figure 7. Nyquist plot of the obtained impedance spectra $\underline{Z}_1$ and $\underline{Z}_2$ in comparison to the reference $\underline{Z}_{\mathrm{EIS}}$ form the EIS-meter measurement.

4.1. *Verification of the Practical Results*

Two approaches are used to verify the results of the method. The first approach compares the impedance spectrum results to the impedance measurements from the EIS-meter at the same frequency bins, as shown in figure 7. $\underline{Z}_1$ represents the impedance with error compensation in time domain and $\underline{Z}_2$ with compensation in frequency domain. As you can see the obtained spectra have almost the same shape, but differ much from the reference. The second approach is to evaluate in time domain, both, the method results and the EIS-meter measurements. For the evaluation in time domain the obtained spectra are fitted to a second order fractional rational function (eq. 12), to obtain the battery model in form of the system transfer functions T_1, T_2 and T_{EIS} [8].

$$T(s)=\frac{B(s)}{A(s)}=\frac{b_1 s^2+b_2 s+b_3}{a_1 s^2+a_2 s+a_3} \quad ,s=j\omega. \tag{12}$$

The obtained battery models are now used to simulate the battery output $v_{\mathrm{Batt}}(t)$ for a stimulation signal $i_{\mathrm{Batt}}(t)$ and compared with real battery measurements for verification.

8(a) and 8(b) give the results for using the impedance spectra of $\underline{Z}_1$ and $\underline{Z}_2$. As can be seen the reconstructed

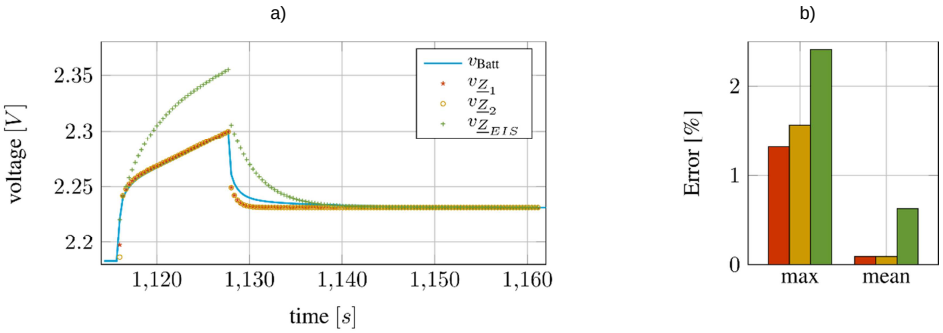

Figure 8. (a): Verification in time domain using a current-step as excitation signal. (b): shows the maximum and mean error the measured battery output voltage $v_{\mathrm{Batt}}(t)$.

voltages $v_{Z.1}$ and $v_{Z.2}$ fit almost perfectly the real cell voltage response $v_{\mathrm{Batt}}(t)$. The voltage response $v_{Z.\mathrm{EIS}}$ on the contrary deviates strongly, as can be seen by the maximum and mean error shown in figure 8(b). The error of $v_{Z1.2}$ averages in a deviation of less than 0.15% to $v_{\mathrm{Batt}}(t)$ and the evaluation of $v_{Z.\mathrm{EIS}}$ yields in almost a triple value with about 0.45% in average.

4.2. *Evaluation of the Models using a General Test Profile*

To evaluate the models and therefore the obtained impedances $\underline{Z}_{1.2}$ and $\underline{Z}_{\mathrm{EIS}}$ the simulation is repeated with a different stimulation signal. The used test profile is shown in figure 9(a). It covers the general operating modes of a battery: an increasing current (ramp) and a continuous current of different values for discharging and charging.

This profile is first applied to a real battery and the response is measured (cf. figure 9(b)) and later it is employed to the previously achieved battery models (T_1, T_2 and T_{EIS}). The trend of $v_{\mathrm{OC}}(t)$ is shown in figure 9(b). The model outputs and the evaluation results are shown in figure 9(c) and (d) for algorithm 1 and 2 respectively. The deviation to the measured voltage response $v_{\mathrm{Batt}}(t)$ has increased compared to the evaluation using a current step as stimulus (cf. figure 8), but is still less than the targeted 5% maximum error. Again the reconstruction using T_{EIS} produces the biggest mean error.

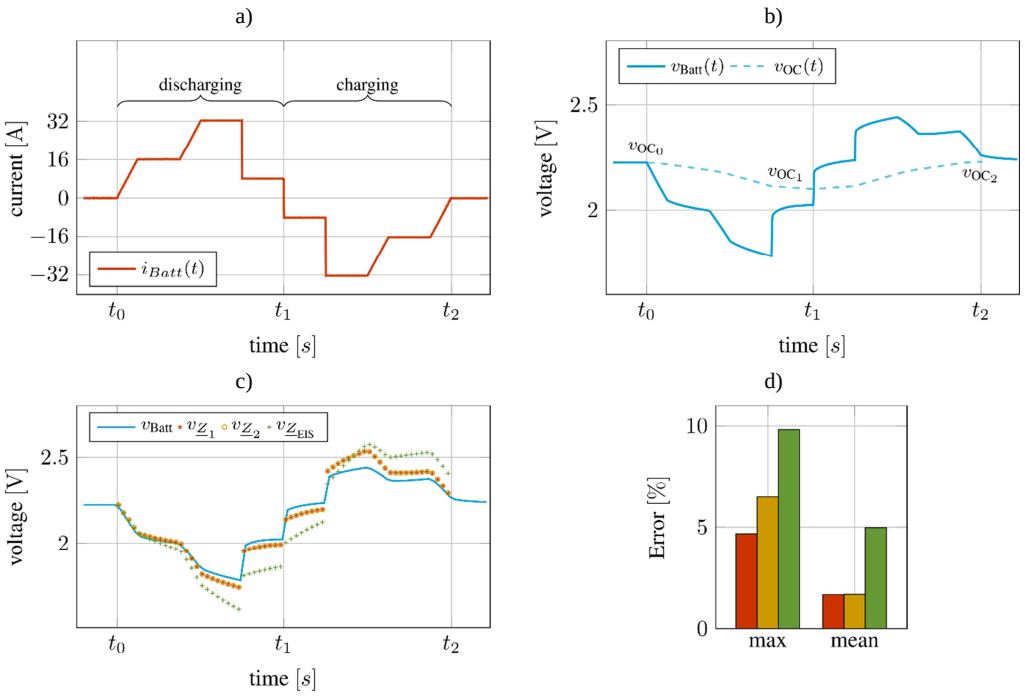

Figure 9. Measuring Period for one SOC value: (a): the current $i_{Batt}(t)$, (b): the voltage response of the battery cell, (c): the measured voltage response compared to the simulated one using the general test profile, (d): the relative max and mean error.

5. Discussion

All together 53 measuring intervals within 13 series of measurements for different SOC-values, currents $\hat{I}$, temperatures T and sampling frequencies F_s for charging and discharging mode were considered in the investigation. It was found out, that best accuracies were obtained in the mid-SOC range. The relation of the precision and the SOC value can be explained by the increasing non-linearity of the battery close to the upper and lower limits (0% and 100% SOC respectively). This behavior can be ascribed to the assumption made regarding the linear relation of the SOC and the open circuit voltage. It could be ascertained that the current amplitude $\hat{I}$ has no significant effect on the accuracy, which allows the application to battery arrays. It was found out, that the OFF-phase investigation provides better results compared to the ON-phase. This is again founded in the assumed linearity, which does not always apply. Additionally the SOC is constant for the OFF-phase. From time domain investigation also follows, that both error compensation algorithms in quiet similar accuracies. At which the error compensation in frequency domain offers the greatest flexibility, as it is not bounded to a step and a step-response analysis.

6. Conclusion

Overall the idea to determine the impedance of a Li-Ion battery using methods of digital signal processing could be implemented and verified with good results and accuracies of less than the targeted maximum deviation of 5%. The introduced algorithms are robust and produce reliable impedance spectra for all investigated operating points. The best accuracies are achieved within the middle SOC range. By the way it was depict that the EIS-meter measurements are not sufficiently accurate for low frequencies. The obtained results and experiences are a good basis for further investigation and the first step in the direction of online model identification.

Acknowledgements

The authors wish to thank the Federal Ministry of Economics of Germany for the financial support by the research project IRENE (Integration of Renewable Energy and Electric Mobility). Further many thanks to Prof. Dr.-Ing. Dr. h.c. H. Biechl, director of the Institute for Electrical Power Systems, for his support.

Estonian partner research work has been supported by Estonian Ministry of Education and Research (Project SF0140016s11).

References

[1] Bischof H. and Biechl H., Messtechnische Ermittlung von Systemübertragungsfunktionen aus transienten Übergangsverläufen von Systemanregung und - antwort - Anwendung auf Synchronmaschinen. In etzArch.10 1987, pages 47–51.
[2] Marko H., Methoden der Systemtheorie: die Spektraltransformationen und ihre Anwendungen. Springer, 1977.
[3] Macdonald D. D., Reflections on the history of electrochemical impedance spectroscopy. Electrochimica Acta 2006, 51:1376 – 1388.
[4] Chang B. Y. and Park S. M., Electrochemical impedance spectroscopy. Annual Review of Analytical Chemistry 2010, 3(1):207–229.
[5] Nicolson A.M., Forming the fast fourier transform of a step response in time-domain metrology. Electronics Letters 1973, 9(14):317–318.
[6] Levenberg K., A method for the solution of certain non-linear problems in least squares. Quarterly Journal of Applied Mathmatics 1944, II(2):164–168.
[7] Gavin H., The Levenberg-Marquardt method for nonlinear least squares curve-fitting problems. Department of Civil and Environmental Engineering, Duke University, September 2011.
[8] A. Rahmoun, H. Biechl, and A. Rosin. Evaluation of equivilant circuit diagrams and transfer functions for modeling of lithium-ion batteries. 2013.

PAPER- VIII A. Armstorfer, N. Beg, A. Rahmoun, A. Rosin, and H. Biechl, “Mathematical Modeling and Evaluation of a Microgrid Demonstrator in Island Mode,” in Conference on Sustainable Energy Supply and Energy Storage Systems NEIS 2017, 2017.

Mathematical Modeling and Evaluation of a Microgrid Demonstrator in Island Mode

Andreas Armstorfer[1,2], Nauman Beg[1], Ahmad Rahmoun[1,2], Argon Rosin[2], and Helmuth Biechl[1,2]
[1]Institute of Electrical Power Systems (IEES), University of Applied Sciences Kempten, Kempten, Germany
[2]School of Engineering, Tallinn University of Technology, Tallinn, Estonia*

Abstract

The research work presents an approach to set-up simplified mathematical models of microgrid components based on detailed models. The verification is done by a comparison with measurement results of a real system. Using simplified models allows an accurate analysis and optimization of the dynamic behavior of existing as well as planned microgrids. The paper shows simulation and measurement results for different combinations of microgrid components in island mode operation.

1 Introduction

Microgrids in island mode consisting of renewable energy sources, battery storage systems and gensets require droop control of voltage and frequency [1]. In the research project IREN2 [2, 3] funded by the German Federal Ministry of Economic Affairs and Energy (BMWi), a microgrid demonstrator is established to investigate the upcoming challenges in distribution grids due to the increase in small decentralized generation units (DGs) which will eventually replace conventional power plants. The demonstrator is set-up in Wildpoldsried, a village located in the southern Germany with a high amount of renewable energy generation. The demonstrator consists of a Li-Ion Battery Energy Storage System (BESS) with a maximum power of 300kVA and an energy capacity of 170kWh, two gensets with 100kVA resp. 500kVA rated power as well as a 150kW unsymmetrical ohmic load. Furthermore, a back-to-back voltage source converter (B2B-VSC) with a maximum power of 500kVA is used to emulate the volatile photovoltaic (PV) in-feed, specific load profiles or an unlimited energy storage system. The BESS, the gensets as well as the B2B-VSC can be operated in grid forming or grid following mode. With the global objective of a stable microgrid operation, a detailed model of each microgrid component is developed to evaluate fast dynamics as well as steady state behavior. To facilitate system level simulations, simplified models for each component with various levels of complexity need to be developed under consideration of the required applications. Realistic practical scenarios are defined using different combinations of microgrid components of the demonstrator under various operation modes. Further, a comparison between simulation and measurements is shown.

*The Estonian partner work was supported by the Estonian Centre of Excellence in Zero Energy and Resource Efficient Smart Buildings and Districts ZEBE, grant 2014-2020.4.01.15-0016 funded by European Regional Development Fund.

In section 2, the structure and specifications of the real microgrid components are presented as well as the simplification procedure for the developed electrical models. An overview of the control structure is also briefly discussed. Section 3 presents the simulation setup in the software PSCAD for the defined scenarios which refer to the discussed microgrid application. A comparison between simulation results and actual measurements at the demonstrator is shown and discussed. Finally, section 4 outlines further challenges and investigations regarding stable and optimum operation of future microgrids.

2 Microgrid components overview

2.1 Back-2-Back VSC (B2B-VSC)

A 500kVA B2B-VSC described in section 1 which interlinks the 20kV MV grid with the 400V LV microgrid is developed specifically for the discussed demonstration setup and serves multiple purposes. It is a 4 quadrant converter which is able to control active and reactive power flow between MV and LV grids. It can also emulate a storage system with infinite capacity or track a given load profile (P and Q) to generate PV in-feed into the microgrid.

Figure 1 shows an overview of the B2B-VSC including the MV resp. LV side. The VSCs of the B2B unit are connected to the 20kV MV grid resp. 400V LV microgrid through an AC filter and a Δ-Y transformer. Converter parameters along with the MV and LV side transformer specifications are summarized in **Table 1** and **Table 2** respectively. The MV VSC regulates the DC link voltage whereas the LV VSC has a droop control to regulate the microgrid voltage and frequency in grid forming mode. The control structure of the DC link voltage controller in the MV VSC comprises of a non-linear cascaded control scheme that is linearized around the operation DC link voltage. It is discussed in detail in [4, 5].

The detailed model of the B2B-VSC is simplified relative

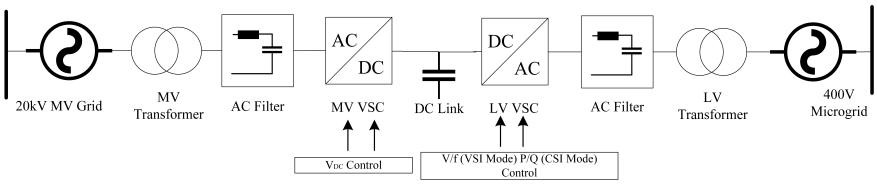

Figure 1 Overview of B2B-VSC

Table 1 B2B-VSC system parameters

Converter specifications	
Parameter	**Value**
Converter rating [S_r]	500kVA
Switching frequency [f_{sw}]	4kHz
Nominal voltage [$V_{nom,LL}$]	400V
DC link voltage [V_{DC_o}]	640V

Table 2 MV and LV VSC transformer parameters

LV 0.369kV/0.4kV Δ-Y transformer parameters	
Parameter	**Value**
Rating [$S_{r,LV}$]	750kVA
u_k	6%
P_{copper}	0.00888pu
$P_{no-load}$	0.00127pu
MV 0.4kV/20kV Y-Δ transformer parameters	
Parameter	**Value**
Rating [$S_{r,MV}$]	600kVA
u_k	6%
P_{copper}	0.00888pu
$P_{no-load}$	0.00127pu

to the 400V microgrid side by modeling the LV VSC with an ideal 3-phase AC voltage source and a lumped series impedance. The lumped impedance is the sum of the LV transformer winding resistance and the leakage inductance as well as the AC filter series impedance. It is given by

$$\begin{aligned} R_{lumped} &= R_{filter} + R_{LV,trans} \\ L_{lumped} &= L_{filter} + L_{LV,trans} \end{aligned} \tag{1}$$

MV VSC and its disturbances on the LV VSC are ignored for simplification reasons. The simplified model is shown in **Figure 2** and the lumped impedance parameters are summarized in **Table 3**.

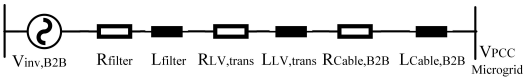

Figure 2 Simplified model of B2B-VSC

Table 3 Lumped parameters for simplified B2B-VSC model (400V microgrid side)

Parameter	**Value**
R_{lumped}	2.1565mΩ
L_{lumped}	152.24μH

The B2B-VSC can operate both in grid forming (VSI mode) or in grid following mode (CSI mode). In CSI mode, the B2B-VSC can operate as a grid following component to track P and Q set-points. The control structure in CSI mode is discussed in detail in [4]. In VSI mode, the converter tracks frequency and voltage set-points provided by the P/f resp. Q/V droop characteristics. A brief overview of the control structure in VSI mode based on peak voltage control in [6] is shown in **Figure 3**. The output active power P_1 and reactive power Q_1 of the B2B-VSC are used for the frequency and voltage droop curves which deliver the set-point frequency and voltage respectively. Value of the set-point voltage is passed to a *PI* controller after smoothing which regulates the actual output voltage of the inverter. The set-point frequency is passed to an integrator which generates the required phase of the inverter output voltage.

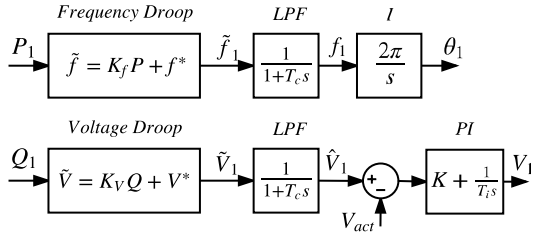

Figure 3 Frequency and voltage droop control structure

Where,

K_f P/f droop slope given in Hz/kW
K_V Q/V droop slope given in $V/kvar$
T_c Smoothing time constant
f^* Reference frequency under no load
V^* Reference voltage under no load

2.2 Battery Energy Storage System (BESS)

2.2.1 BESS Structure

The BESS consists of six strings connected in parallel as shown in **Figure 4**. Each two strings are connected to one of the three Lithium-Ion (Li-Ion) batteries. The first three strings S_1, S_2 and S_3 are connected to the first matching transformer (MT_1) whereas the next three strings S_4, S_5 and S_6 are connected to the second matching transformer (MT_2). Two isolating transformers IT_1,IT_2 are used to avoid circulating currents in the circuit of S_1 and S_6 as well as in the circuit of S_2 and S_5 which are connected to the same dc circuit.

The three phase two-winding matching transformer is used

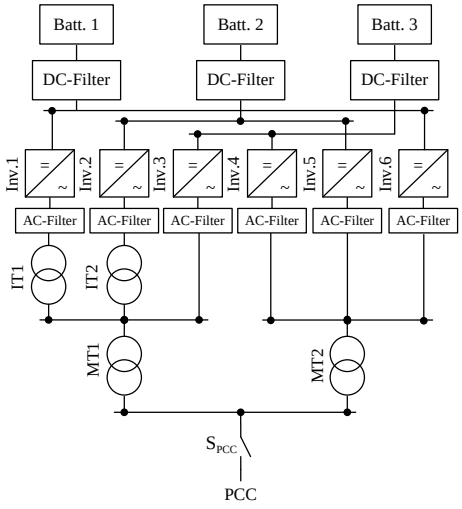

Figure 4 Structure of the BESS

Table 4 Specifications of the matching and isolating transformers.

257V/400V Δ-Y matching transformer	
Parameter	**Value**
Rating $[S_{r,LV}]$	165kVA
u_k	4.3%
P_{copper}	0.008484pu
$P_{no-load}$	0.002424pu
260V/260V Δ-Δ isolating transformer	
Parameter	**Value**
Rating $[S_{r,MV}]$	55kVA
u_k	3.73%
P_{copper}	0.021545pu
$P_{no-load}$	0.0029091pu

to adapt the inverter's low output voltage to the voltage of the LV grid. The specifications of both matching and isolating transformers are given in **Table 4**.

Each string consists mainly of a 3-phase inverter with a rated power of $55kVA$ followed by a *LC* filter in order to reduce current harmonics injected into the grid. The *LC* filter parameters are given in **Table 5**. The control structure for each string in VSI mode is similar to that described in section 2.1.

2.2.2 BESS Simulation Model

Due to the complex structure of the BESS, having a detailed model which takes into account the semiconductors of the inverter is only required for evaluating short time transients [7]. For applications where long time simulations ($T_{sim} > 10s$) are needed, a simplified model **(Figure 5)** consisting of a controlled voltage source (V_{eq}, f_{eq})

Table 5 LC-Filter specifications.

Parameter	**Value**
Serial inductance L_F	$160\mu H$
Serial resistance R_F	$16.4m\Omega$
Parallel capacitor C_F	$3.5\ \mu F$

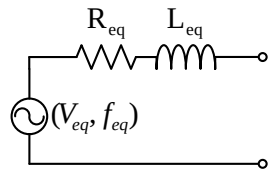

Figure 5 BESS equivalent model in VSI mode

and an equivalent impedance $(Z_{eq} = R_{eq} + jX_{eq})$ is extracted and implemented in PSCAD. The equivalent voltage and frequency (V_{eq} resp. f_{eq}) are controlled using the same droop curves $V_{eq} = K_V * (Q - Q_0) + V_0$ and $f_{eq} = K_f * (P - P_0) + f_0$ applied to the total active and reactive power (P_{out}, Q_{out}) of the BESS. The equivalent droop gains are defined under the assumption that the droop gains are equal for all strings, and they can be calculated based on equation 2. Based on this assumption, the output active and reactive power of the BESS is distributed equally on all strings in steady state operation. Therefore, the equivalent impedance can be calculated by $Z_{eq} = Z_1 \parallel Z_2 \parallel \cdots \parallel Z_6$. The parameters of the equivalent impedance are summarized in **Table 6**.

$$K_f[Hz/kW] = \frac{1}{K_p} \ \ where \quad K_p[kW/Hz] = \sum_{i=1}^{6} k_p^i = 6 \cdot k_p$$
$$K_V[V/kvar] = \frac{1}{K_q} \ \ where \quad K_q[kvar/V] = \sum_{i=1}^{6} k_q^i = 6 \cdot k_i \tag{2}$$

Table 6 Equivalent impedance of BESS

Parameter	**Value**
Serial inductance L_{eq}	$81\mu H$
Serial resistance R_{eq}	$7.7m\Omega$

2.3 Genset

A mathematical simulation model for a bio-fuel based genset in the discussed demonstrator setup is established. It consists of a prime mover (diesel engine) and a direct coupled synchronous machine. The dynamic behavior of the rotating system is mainly influenced by the inertia of the complete drive system whereas the voltage dynamics are influenced by the synchronous machine characteristics. The mathematical model of the generator is based on Park's equations. A subset of parameters is shown in **Table 7**. The frequency control of the genset is realized by a PI controller with droop characteristics which outputs the set-point torque T_m for the prime mover as shown in **Figure 6**. Moreover, **Figure 7** shows the genset's voltage control with droop behavior which controls the current I_f in the

excitation winding. The frequency droop gain K_f is defined in $[Hz/kW]$ whereas the voltage droop gain K_V is set in $[V/kvar]$. Further, the frequency and voltage set-point at no load operation are defined as f^* resp. V^*_{LN}. P_{out} and Q_{out} are the actual active resp. reactive power measured at the PCC of the genset.

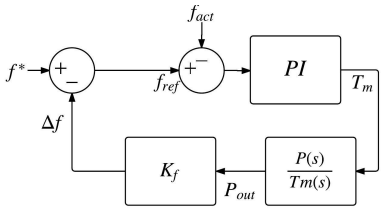

Figure 6 Frequency control including P/f droop

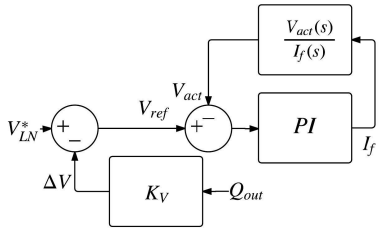

Figure 7 Voltage control including Q/V droop

Table 7 Subset of model parameters of the synchronous generator

Parameter	Value
Apparent power S_r	135kVA
Nominal voltage $V_{nom,LN}$	230V
Base angular frequency ω	314 rad/s
Inertia constant H	0.5s
Iron loss resistance R_{Fe}	300pu
Armature resistance R_a	0.013pu
Unsaturated d-axis reactance x_d	2.2pu
Unsaturated q-axis reactance x_q	1.36pu
Transient d-axis reactance x'_d	0.154pu
Sub-transient d-axis reactance x''_d	0.076pu
Sub-transient q-axis reactance x''_q	0.284pu
Transient d-axis time constant T'_d	0.039s
Sub-transient d-axis time constant T''_d	0.0085s

3 Simulation and Measurements

An overview of the demonstrator site is shown in **Figure 8**. Measurements are only taken for the demonstrator area shown in **Figure 8**. This means that the switch S_1 is open and isolates the demonstrator site from the residential area. The cable impedance between the components is ignored which effects to a greater extent the reactive power flow

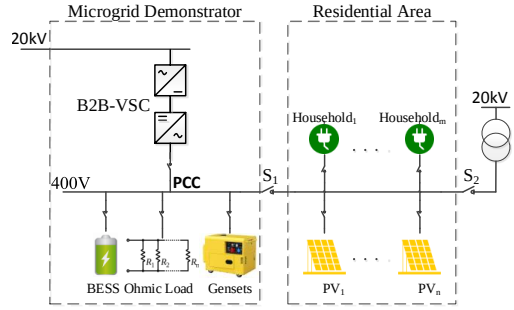

Figure 8 Demonstrator overview

between the components. This will be briefly explained during the discussion of the results. The case scenarios tested are given as follows:

Scenario 1: (SC1) BESS and B2B-VSC in VSI mode with an applied active load profile on the load bank

Scenario 2: (SC2) BESS and genset in VSI mode with an applied active load profile on the load bank

Scenario 3: (SC3) BESS, B2B-VSC and genset in VSI mode with an applied active load profile on the load bank

Scenario 4: (SC4) BESS and genset in VSI mode and the B2B-VSC is in CSI mode with a given active power generation profile and a base load of 48kW at the point of common coupling (PCC)

The applied load profile for passive load at the *PCC* in scenario 1, 2 and 3 is shown in **Figure 9**. In **Figure 10**, the active power generation profile of the B2B-VSC is depicted. Droop parameters of all components are fixed for all scenarios. They are summarized in **Table 8**.

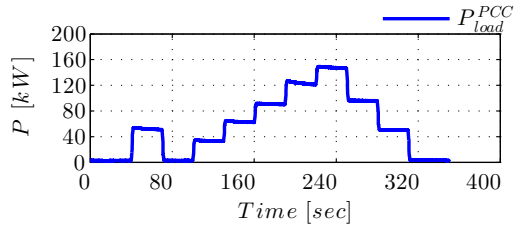

Figure 9 Load profile in SC1, SC2 and SC3

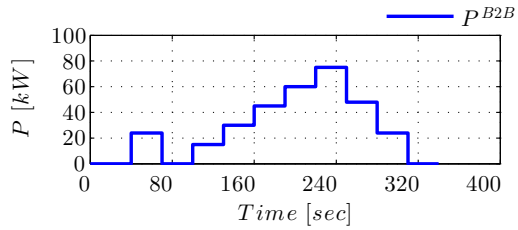

Figure 10 Generation profile of B2B-VSC in SC4

In SC1, BESS and B2B-VSC are working in VSI mode. Profiles for the output active power P, terminal voltage

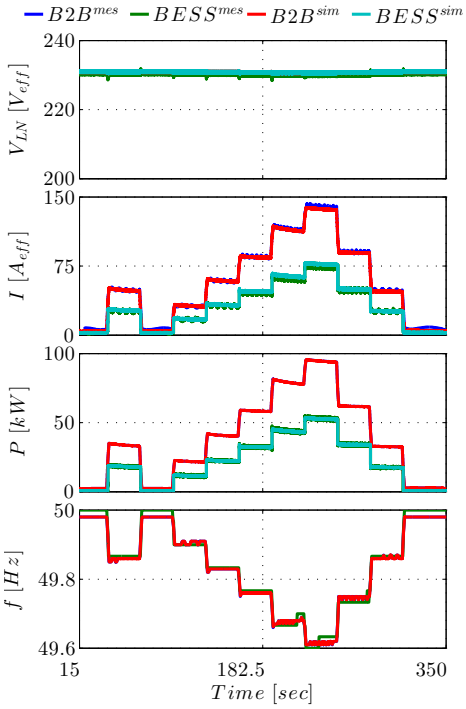

Figure 11 SC1- Measurement and simulation results

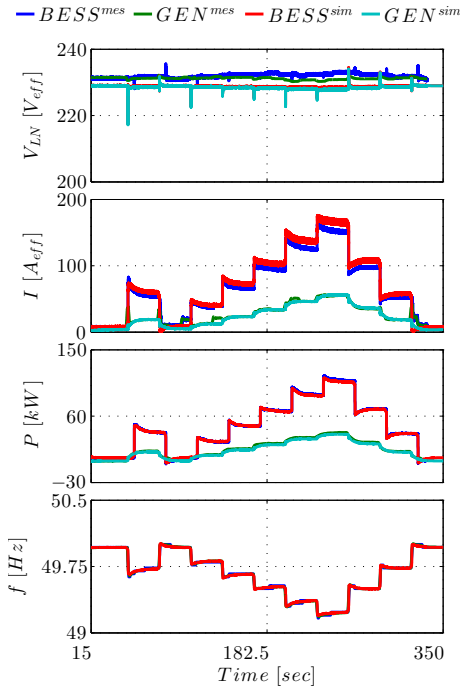

Figure 12 SC2- Measurement and simulation results

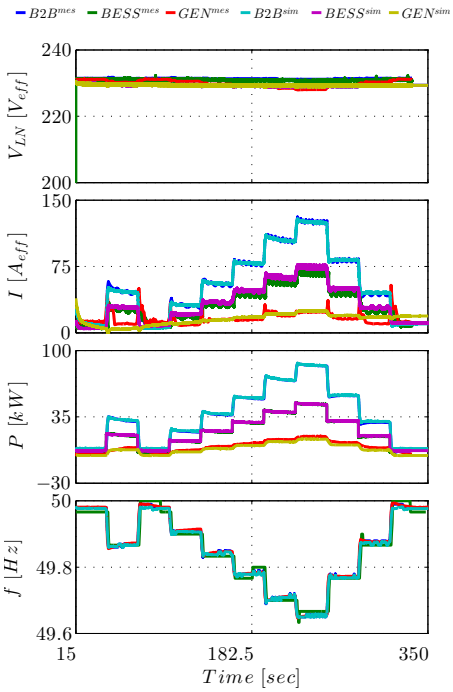

Figure 13 SC3- Measurement and simulation results

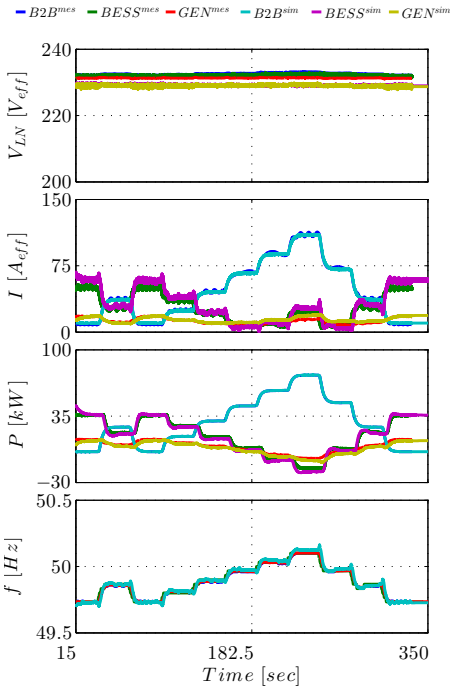

Figure 14 SC4- Measurement and simulation results

Table 8 Droop parameters

Parameter	B2B-VSC	BESS	Genset
K_f $[Hz/kW]$	0.004	0.0067	0.02
K_V $[V/kvar]$	0.02	0.0333	0.05
f^* $[Hz]$	50	50	50
V^*_{LN} $[V]$	230	230	230
T_c $[ms]$	100	100	x

V_{rms}, output current I_{rms} as well as frequency f for both simulations and measurements are shown in **Figure 11** which matches quite closely. In **Figure 12** (SC2), the deviation between the simulation and measured results for current at high loads is due to the cable impedance mismatch in the simulation model between the component terminals and the *PCC*. This results in additional reactive power flow between the components. To compensate it, the set point voltage $\hat{V}$ of individual components can be adjusted in the simulation model. During low loads, voltage drop in the cable impedance is insignificant and hence simulation and measured values are close to each other. In **Figure 13** (SC3), small spikes can be observed in the measured currents of the genset during load steps. It is due to the adjustment of its terminal voltage to minimize reactive power flow which causes abrupt current change. Results for SC4 are shown in **Figure 14** where the B2B-VSC covers a part of the base load (48kW) according to its generation power profile. The residual load is distributed between BESS and genset according to their droop curves. The presented results clearly demonstrates the load sharing among the participating components.

4 Summary and Conclusions

The presented results of the different quasi-stationary scenarios confirm the validity of the system approximation when using simplified component models of the single components. Values of maximum relative error given by equation 3 for important quantities are summarized in **Table 9**. A higher value of ΔI_{max} in SC3 and SC4 is caused by the relatively high reactive current mismatch between simulation and measurement values in the case of small active load conditions. Load distribution between components in relation to their droop parameters shows proper working of the droop control. The aspect of reactive power mismatch between simulation and measurement is caused by the cable impedance between components and *PCC* which is not considered in the simulation. The effect of short time dynamics on the system stability as well as stability issues during parallel operation of components will be investigated in the future work.

$$\Delta X_{max}[\%] = \frac{max|X_{sim} - X_{mes}|}{|X_{mes,pk}|}.100 \qquad (3)$$

Table 9 Maximum relative error

Scenario 1			
Relative error	**B2B-VSC** $[\%]$	**BESS** $[\%]$	**Genset** $[\%]$
ΔP_{max}	0.7	1.03	x
Δf_{max}	0.02	0.02	x
ΔV_{max}	0.17	0.3	x
ΔI_{max}	4	7.47	x
Scenario 2			
ΔP_{max}	x	2.4	0.71
Δf_{max}	x	0.06	0.04
ΔV_{max}	x	1.7	1.166
ΔI_{max}	x	4.9	2.074
Scenario 3			
ΔP_{max}	3.4	4.89	16.6
Δf_{max}	0.02	0.02	0.02
ΔV_{max}	0.95	0.91	0.79
ΔI_{max}	2.27	7.5	25.31
Scenario 4			
ΔP_{max}	0	10.2	18.6
Δf_{max}	0.04	0.04	0.06
ΔV_{max}	1.63	1.334	0.951
ΔI_{max}	2.57	14.9	26.5

5 Literature

[1] J. Stanojevic, A. Djordjevic, M.Mitrovic,"Influence of Battery Energy Storage System on Generation Adequacy and System Stability in Hybrid Micro Grids" in Environment Friendly Energies and Applications (EFEA) 2016, 2016

[2] R. Köberle, K. Mayr, B. Rindt, T. Sowa, D. Buchstaller, A. Armstorfer, and H. Biechl, "IREN2: Zukunftsfähige Netze zur Integration Regenerativer Energiesysteme," in Von Smart Grids zu Smart Markets 2015, 2015.

[3] "IREN2 official website." [Online]. Available: www.iren2.de.

[4] N. Beg, A. Rahmoun, A. Armstorfer, A. Rosin, and H. Biechl, "Determination methods for controller parameters of back-to-back converters in electric power grids," in 2016 Electric Power Quality and Supply Reliability (PQ), 2016, pp. 157–164.

[5] C. Bajracharya, M. Molinas, "Understanding of tuning techniques of converter controllers for VSC/HVDC," in Nordic Workshop on Power and Industrial Electronics 2008, 2008.

[6] Siemens, "SINAMICS S120/S150," Listenhandbuch, pp. 2152–2153

[7] A. Rahmoun, A. Armstorfer, A. Rosin, and H. Biechl, "Modelling and Simulation of an Energy Storage System for a Smart Grid Including Power Electronics and Battery Model," in IRES 2015 Poster Exhibition, 2015.

DISSERTATIONS DEFENDED AT TALLINN UNIVERSITY OF TECHNOLOGY ON *POWER ENGINEERING, ELECTRICAL ENGINEERING, MINING ENGINEERING*

1. **Jaan Tehver**. Boiling on Porous Surface. 1992.
2. **Aleksandrs Cars**. Woodhips Combustion Technology. 1992.
3. **Endel Risthein**. Electricity Supply of Industrial Plants. 1993.
4. **Tõnu Trump**. Some New Aspects of Digital Filtering. 1993.
5. **Vello Sarv.** Synthesis and Design of Power Converters with Reduced Distortions Using Optimal Energy Exchange Control. 1994.
6. **Ivan Klevtsov**. Strained Condition Diagnosis and Fatigue Life Prediction for Metals under Cyclic Temperature Oscillations. 1994.
7. **Ants Meister**. Some Phase-Sensitive and Spectral Methods in Biomedical Engineering. 1994.
8. **Mati Meldorf**. Steady-State Monitoring of Power System. 1995.
9. **Jüri-Rivaldo Pastarus**. Large Cavern Stability in the Maardu Granite Deposit. 1996.
10. **Enn Velmre**. Modeling and Simulation of Bipolar Semiconductor Devices. 1996.
11. **Kalju Meigas**. Coherent Photodetection with a Laser. 1997.
12. **Andres Udal**. Development of Numerical Semiconductor Device Models and Their Application in Device Theory and Design. 1998.
13. **Kuno Janson**. Paralleel- ja järjestikresonantsi parameetrilise vaheldumisega võrgusageduslik resonantsmuundur ja tema rakendamine. 2001.
14. **Jüri Joller**. Research and Development of Energy Saving Traction Drives for Trams. 2001.
15. **Ingo Valgma**. Geographical Information System for Oil Shale Mining – MGIS. 2002.
16. **Raik Jansikene**. Research, Design and Application of Magnetohydrodynamical (MHD) Devices for Automation of Casting Industry. 2003.
17. **Oleg Nikitin**. Optimization of the Room-and-Pillar Mining Technology for Oil-Shale Mines. 2003.
18. **Viktor Bolgov**. Load Current Stabilization and Suppression of Flicker in AC Arc Furnace Power Supply by Series-Connected Saturable Reactor. 2004.

19. **Raine Pajo**. Power System Stability Monitoring – an Approach of Electrical Load Modelling. 2004.

20. **Jelena Shuvalova**. Optimal Approximation of Input-Output Characteristics of Power Units and Plants. 2004.

21. **Nikolai Dorovatovski**. Thermographic Diagnostics of Electrical Equipment of Eesti Energia Ltd. 2004.

22. **Katrin Erg**. Groundwater Sulphate Content Changes in Estonian Underground Oil Shale Mines. 2005.

23. **Argo Rosin**. Control, Supervision and Operation Diagnostics of Light Rail Electric Transport. 2005.

24. **Dmitri Vinnikov**. Research, Design and Implementation of Auxiliary Power Supplies for the Light Rail Vehicles. 2005.

25. **Madis Lehtla**. Microprocessor Control Systems of Light Rail Vehicle Traction Drives. 2006.

26. **Jevgeni Šklovski**. LC Circuit with Parallel and Series Resonance Alternation in Switch-Mode Converters. 2007.

27. **Sten Suuroja**. Comparative Morphological Analysis of the Early Paleozoic Marine Impact Structures Kärdla and Neugrund, Estonia. 2007.

28. **Sergei Sabanov**. Risk Assessment Methods in Estonian Oil Shale Mining Industry. 2008.

29. **Vitali Boiko**. Development and Research of the Traction Asynchronous Multimotor Drive. 2008.

30. **Tauno Tammeoja**. Economic Model of Oil Shale Flows and Cost. 2008.

31. **Jelena Armas**. Quality Criterion of road Lighting Measurement and Exploring. 2008.

32. **Olavi Tammemäe**. Basics for Geotechnical Engineering Explorations Considering Needed Legal Changes. 2008.

33. **Mart Landsberg**. Long-Term Capacity Planning and Feasibility of Nuclear Power in Estonia under Certain Conditions. 2008.

34. **Hardi Torn**. Engineering-Geological Modelling of the Sillamäe Radioactive Tailings Pond Area. 2008.

35. **Aleksander Kilk**. Paljupooluseline püsimagnetitega sünkroongeneraator tuuleagregaatidele. 2008.

36. **Olga Ruban**. Analysis and Development of the PLC Control System with the Distributed I/Os. 2008.

37. **Jako Kilter**. Monitoring of Electrical Distribution Network Operation. 2009.

38. **Ivo Palu**. Impact of Wind Parks on Power System Containing Thermal Power Plants. 2009.

39. **Hannes Agabus**. Large-Scale Integration of Wind Energy into the Power System Considering the Uncertainty Information. 2009.

40. **Kalle Kilk**. Variations of Power Demand and Wind Power Generation and Their Influence to the Operation of Power Systems. 2009.

41. **Indrek Roasto**. Research and Development of Digital Control Systems and Algorithms for High Power, High Voltage Isolated DC/DC Converters. 2009.

42. **Hardi Hõimoja**. Energiatõhususe hindamise ja energiasalvestite arvutuse metoodika linna elektertranspordile. 2009.

43. **Tanel Jalakas**. Research and Development of High-Power High-Voltage DC/DC Converters. 2010.

44. **Helena Lind**. Groundwater Flow Model of the Western Part of the Estonian Oil Shale Deposit. 2010.

45. **Arvi Hamburg**. Analysis of Energy Development Perspectives. 2010.

46. **Mall Orru**. Dependence of Estonian Peat Deposit Properties on Landscape Types and Feeding Conditions. 2010.

47. **Erik Väli**. Best Available Technology for the Environmentally Friendly Mining with Surface Miner. 2011.

48. **Tarmo Tohver**. Utilization of Waste Rock from Oil Shale Mining. 2011.

49. **Mikhail Egorov**. Research and Development of Control Methods for Low-Loss IGBT Inverter-Fed Induction Motor Drives. 2011.

50. **Toomas Vinnal**. Eesti ettevõtete elektritarbimise uurimine ja soovituste väljatöötamine tarbimise optimeerimiseks. 2011.

51. **Veiko Karu**. Potential Usage of Underground Mined Areas in Estonian Oil Shale Deposit. 2012.

52. **Zoja Raud**. Research and Development of an Active Learning Technology for University-Level Education in the Field of Electronics and Power Electronics. 2012.

53. **Andrei Blinov**. Research of Switching Properties and Performance Improvement Methods of High-Voltage IGBT based DC/DC Converters. 2012.

54. **Paul Taklaja**. 110 kV õhuliinide isolatsiooni töökindluse analüüs ja töökindluse tõstmise meetodid. 2012.

55. **Lauri Kütt**. Analysis and Development of Inductive Current Sensor for Power Line On-Line Measurements of Fast Transients. 2012.

56. **Heigo Mõlder**. Vedelmetalli juhitava segamisvõimaluse uurimine alalisvoolu kaarleekahjus. 2012.

57. **Reeli Kuhi-Thalfeldt**. Distributed Electricity Generation and its Possibilities for Meeting the Targets of Energy and Climate Policies. 2012.

58. **Irena Milaševski**. Research and Development of Electronic Ballasts for Smart Lighting Systems with Light Emitting Diodes. 2012.

59. **Anna Andrijanovitš**. New Converter Topologies for Integration of Hydrogen Based Long-Term Energy Storages to Renewable Energy Systems. 2013.

60 **Viktor Beldjajev**. Research and Development of the New Topologies for the Isolation Stage of the Power Electronic Transformer. 2013.

61. **Eduard Brindfeldt**. Visually Structured Methods and Tools for Industry Automation. 2013.

62. **Marek Mägi**. Development and Control of Energy Exchange Processes Between Electric Vehicle and Utility Network. 2013.

63. **Ants Kallaste**. Low Speed Permanent Magnet Slotless Generator Development and Implementation for Windmills. 2013.

64. **Igor Mets**. Measurement and Data Communication Technology for the Implementation in Estonian Transmission Network. 2013.

65. **Julija Šommet**. Analysis of Sustainability Assessment in Carbonate Rock Quarries. 2014.

66. **Tanel Kivipõld**. Real-Time Electricity Tariff System for Retail Market. 2014.

67. Priit Uuemaa. Industrial CHP Optimal Management Model in the Energy Market under Incomplete Information. 2014.

68. **Anton Rassõlkin**. Research and Development of Trial Instrumentation for Electric Propulsion Motor Drives. 2014.

69. **Toomas Vaimann**. Diagnostics of Induction Machine Rotor Faults Using Analysis of Stator Signals. 2014.

70. **Aivar Auväärt**. Development of Energy Reserve Optimization Methodology for Households with Renewable Power Systems. 2014.

71. **Raivo Attikas**. Modelling of Control Systems and Optimal Operation of Power Units in Thermal Power Plants. 2014.

72. **Liisa Liivik**. Semiconductor Power Loss Reduction and Efficiency Improvement Techniques for the Galvanically Isolated Quasi-Z-Source DC-DC Converters. 2015.

73. **Victor Astapov**. Technical-Economic Analysis of Distributed Generation Units in Power Systems. 2015.

74. **Tiit Hõbejõgi**. Possibilities to Optimize Low Voltage Network Investments in Rural Areas. 2016.

75. **Märt Ots**. Practical Implementation of Price Regulation in Energy Sector. 2016.

76. **Ilja Bakman**. High-Efficiency Predictive Control of Centrifugal Multi-Pump Stations with Variable-Speed Drives. 2016.

77. **René Nukki**. Research and Development of Exterior-Rotor Permanent Magnet Synchronous Machines for Light Aerial Vehicles. 2016.

78. **Imre Drovtar**. Demand Side Management Possibilities and Viability for Voltage Support Services in Estonia. 2016.

79. **Andrii Chub**. Research, Design and Implementation of Galvanically Isolated Impedance-Source DC-DC Converters. 2016.

80. **Jaan Niitsoo**. Residential Grids Power Quality Analyses Concerning Nonlinear Consumer Loads and PV Panels. 2016.

81. **Einari Kisel**. Indicators for Assessing the Quality of an Energy Policy. 2017.

82. **Denis Lebedev**. Research and Development of Storage Based Energy Management System for Households. 2017

83. **Oleg Kudrjavtsev**. Design and Optimization of Permanent Magnet Generator with Outer Rotor for Wind Turbine Application. 2017.

84. **Levon Gevorkov**. Simulation and Experimental Study on Energy Management of Circulating Centrifugal Pumping Plants with Variable Speed Driver. 2017.